Alma Mater Studiorum - Università di Bologna

DOTTORATO DI RICERCA IN
ASTRONOMIA

Ciclo XXIX

Settore Concorsuale di afferenza: 02/C1
Settore Scientifico disciplinare: FIS/05

COSMOLOGICAL CONSTRAINTS ON COSMIC INFLATION AND SCALAR-TENSOR DARK ENERGY MODELS FROM CMB ANISOTROPIES AND GALAXY CLUSTERING

Presentata da: Dr. Mario Ballardini

Coordinatore Dottorato:
Chiar.mo Prof.
Francesco Ferraro

Relatore:
Chiar.mo Prof.
Lauro Moscardini

Correlatore:
Dr. Fabio Finelli

Esame finale anno 2016

Contents

Introduction

During the past 18 years, several observations have deeply changed cosmology, turning it into a data-driven high-precision science and establishing it as a powerful probe of fundamental physics fully complementary to particle physics. Thanks to the precise measurement of the Cosmic Microwave Background (CMB) temperature and polarization anisotropies by *Planck* and other experiments, and to new Large Scale Structure (LSS) data by SDSS, cosmological parameters are now known at the percent level.

One of the outstanding questions which cosmology can address is to probe the energy scale and the physics of cosmic inflation, the epoch of nearly exponential expansion in the very early Universe, which flattens the spatial geometry and dilutes away any possible pre-existing relics prior to inflation such as topological defects. In its simplest realization, the nearly exponential expansion of inflation is driven by a scalar field ϕ slowly rolling down a sufficiently flat potential $V(\phi)$. During inflation, quantum fluctuations in the scalar field and in the metric are amplified and stretched to density fluctuations and gravitational waves on cosmological scales, respectively. Measurement of CMB anisotropies such as *Planck* has contributed significantly to determine the current understanding of cosmic inflation. The tight constraint on spatial curvature and on isocurvature fluctuations, the measurement of the bispectral non-Gaussianity parameters $f_{\rm NL}$ consistent with zero are in agreement with the predictions for the simplest single field slow-roll inflationary models. The last key prediction of inflation that still remains untested is the presence of a stochastic background of primordial GWs: tighter and tigher bounds on primordial B-mode polarization are set by ground experiments such as BICEP2 and Keck-Array in combination with the high frequency measurements of the dust polarization by *Planck*. In this exciting and evolving observational context it is interesting to consider two complementary approaches. Since simple models of single field slow-roll inflation provide a good fit to the data, in the first approach it is interesting to ask ourselves which are the favourite potentials for the inflaton, keeping into account our ignorance on the process which leads to the thermalization of the Universe after inflation. As we will see it is an exciting time since *Planck* data have been able to rule out a host of once popular, textbook examples of inflation models such as those based upon a monomial potential, $V(\phi) \propto \phi^n$, with $n \geq 2$. As a second and complementary approach, it is instead interesting to carefully

investigate the statistical significance of the deviations from a simple power-law for density fluctuations supported by the *Planck* CMB power spectrum in temperature and polarization. These deviations from a simple power-law spectrum can be easily accommodated in models of inflation with temporary violation of the slow-roll condition which have drawn a lot of attention in the theoretical cosmology community. We will report a careful comparison of these predictions with *Planck* data including a calculation of the Bayesian evidence. We will then quantify how the clustering of future galaxy surveys can add complementary information to CMB anisotropies.

Cosmology is almost unique in providing clues on the nature of the current acceleration of the Universe, which was awarded by a Nobel prize to Saul Perlmutter, Brian P. Schmidt and Adam G. Riess for the discovery of the accelerating expansion of the Universe through observations of distant supernovae.

The discovery of such recent acceleration of the Universe has contributed to the definition of the concordance ΛCDM model which is still sufficient to fit a host of different cosmological observations. Also in this case, the simplest among the possible several explanations of the late-time acceleration, a cosmological constant, is currently the dominant paradigm. Models can be divided in two broad classes, such as dark energy, where a new matter component is added to the Einstein equations, and modified gravity, in which Einstein gravity is extended. The higher and higher precision of cosmological data drives either an effort in the construction of the theoretical models and in the accuracy of their predictions of cosmological observables. Since data are currently compatible with a cosmological constant, in this thesis we have taken the approach to study a particular class of simple models of scalar-tensor dark energy models, within induced gravity or Brans-Dicke gravity, which contain just an additional parameter with respect to the six of the concordance ΛCDM model. Therefore, these models are highly predictive. In order to establish a methodology rooted in the nowadays era of precision cosmology we will avoid the use of approximate phenomenological parametrizations to describe these models and we will use exact numerical evolution for the background cosmology and the corresponding linear fluctuations.

The thesis is organized as follows.

CHAPTER ONE We introduce the basic concepts of relativistic cosmology, the success and the puzzles of the Big Bang cosmological model. We introduce the Robertson-Walker metric and the Friedmann-Lemeitre equations to describe homogeneous and isotropic universes. We review the basic aspects of cosmic inflation as driven by a slowly rolling scalar field. We then give a general introduction on dark energy with an emphasis on scalar-tensor theories, and in particular induced gravity, as an example of modified gravity.

CHAPTER TWO We review the relativistic theory of cosmological perturbations and we then introduce the equations for gauge-invariant scalar field fluctuations and tensor perturbations, which are at the core of inflationary predictions.

After the derivation of the curvature and tensor power spectra from inflation, we provide a detailed calculation for the scalar spectral index $n_{\rm s}$ and the tensor-to-scalar ratio r, in the slow-roll approximation, for a selection of single field inflationary models (which will be used later in the analysis with *Planck* data in chapter 4).

Then, we introduce the framework of inflationary models with temporary violation of the slow-roll conditions. We review the derivation of the power spectrum of curvature perturbations for a model with a discontinuity in the first derivative of the potential originally introduced by Starobinsky. We then discuss the observational degeneracies between a discontinuity in the first derivative of the potential and in the first derivative of the speed of sound in the power spectrum.

CHAPTER THREE We review the basic concepts of the CMB temperature and polarization angular power spectra, the galaxy power spectra and the Fisher approach.

CHAPTER FOUR After a brief overview of the *Planck* mission and of the main cosmological results of *Planck* 2015 data release, we discuss in more details the implications of *Planck* 2015 data in the following topics: inflationary physical parameters and slow-roll parameters, Bayesian comparison of single field inflationary models taking into account reheating uncertainties, *Planck* results on parametrized features which are the topics I have contributed in the *Planck* 2015 paper on inflation. We then summarize the *Planck* 2015 constraints on induced gravity dark energy models with monomial potentials.

CHAPTER FIVE We present the forecast for inflationary models with primordial features motivated by the *Planck* 2015 analysis by combining the clustering power spectrum of future galaxy surveys with CMB angular power spectrum information.

We then present our conclusions.

1 The quantum origin of the Universe and its late-time acceleration

Current observational data suggest that there are two different stages during which the Universe is accelerating.

The global properties of the Universe and the origin of the structures are provided by an accelerating stage in the early Universe known as cosmic inflation, introduced to solve the puzzles of the standard cosmological model.

Observations at low redshift strongly suggest that its density is dominated by dark energy (DE) with properties similar to a cosmological constant: this is the second stage of acceleration.

In this chapter, we describe the essential concepts of the standard cosmological model. We refer the reader to several review articles and books for further information [1–3]

1.1 Basics of the standard cosmological model of the Big Bang

The formulation of the Big Bang model goes back to the 1940s thanks to the work of George Gamow and his collaborators, Ralph Alpher and Robert Herman. In order to explain the formation of the light elements, they introduced an early phase during which the Universe was very hot and dense. After this *hot phase*, the Universe has expanded and has cooled to its present state [4, 5]. As direct consequence of the Big Bang model, Alpher and Herman predicted the existance of a Cosmic Microwave Background (CMB) radiation [6, 7] of 5 K.

The discovery of the CMB radiation by Arno Penzias and Robert Woodrow Wilson in 1965 [8, 9], the measurement of its temperature (approximately 3 K), and its subsequent interpretation as the relic radiation from a thermal phase of the Universe [10] confirmed the Big Bang as the standard cosmological model. The measurement performed by Penzias and Wilson has been confirmed and refined over the years, by many ground-based, sub-orbital, and space experiments which have strongly constrained the physics

of the early Universe and the evolution of the primordial perturbations.

More recent measurements of the local Universe have indicated the presence of an accelerated stage of the Universe beyond the Einstein-de Sitter model. The evidence of the acceleration is now supported by many types of observations, such as from Supernovae type Ia (SN Ia) [11, 12], CMB anisotropies [13, 14] and from Baryon Acoustic Oscillation (BAO) [15]. This acceleration can be explained by the existence of a cosmological constant or an unusual form of matter. This nature will be well characterized by the next generation of galaxy and radio surveys that will open a new observational window on the near Universe, i.e. $z \sim [0, 10]$, and on the non-linear regime of structure formation.

In this section we introduce the basics for the description of a homogeneous and isotropic cosmology: the Robertson-Walker metric and the Friedmann-Lemaître equations.

1.1.1 The Robertson-Walker metric

In order to reproduce the observed homogeneity and isotropy, we can describe our Universe with the Robertson-Walker (RW) metric [16–19]:

$$\mathrm{d}s^2 = -\mathrm{d}t^2 + a^2(t)\left[\frac{\mathrm{d}r^2}{1-Kr^2} + r^2\left(\mathrm{d}\theta^2 + \sin^2\theta\mathrm{d}\phi^2\right)\right], \tag{1.1}$$

where t is the *cosmic time*, measured by clocks moving with the fluid element, $a(t)$ is the *scale factor*, K is the *spatial curvature* which can assume only the values $\pm 1,\ 0$ corresponding to closed/open or spatially flat geometries, and (r, θ, ϕ) are the comoving (polar) coordinates. Another useful time variable is the *conformal time*, defined as:

$$\mathrm{d}\eta = \frac{\mathrm{d}t}{a(t)}, \tag{1.2}$$

that allows to rewrite the Eq. (1.1) for the RW metric as:

$$\mathrm{d}s^2 = -a^2(\eta)\left[\mathrm{d}\eta^2 - \frac{\mathrm{d}r^2}{1-Kr^2} - r^2\left(\mathrm{d}\theta^2 + \sin^2\theta\mathrm{d}\phi^2\right)\right]. \tag{1.3}$$

We will also use the *redshift*, more directly connected to observations and defined as:

$$1 + z \equiv \frac{a_0}{a(t)}, \tag{1.4}$$

where $a_0 \equiv a(t_0)$ indicates the value of the scale factor today. Hereafter, we will consider $a_0 = 1$.

1.1.2 The Friedmann-Lemaître equations of motion

The cosmological equations of motion are derived assuming that gravity is described by Einstein's theory of General Relativity (GR) [20] which relates the geometrical properties of the space-time to the energy-momentum tensor (EMT) $T_{\mu\nu}$, describing the content of the Universe:

$$R_{\mu\nu} - \frac{1}{2} R g_{\mu\nu} = \frac{1}{M_{\rm pl}^2} T_{\mu\nu} + \Lambda g_{\mu\nu} \,, \tag{1.5}$$

where $R_{\mu\nu}$ is the Ricci tensor, R is the Ricci scalar, $g_{\mu\nu}$ is the metric tensor and Λ the cosmological constant. [1] The EMT for a perfect fluid can be described as:

$$\begin{aligned} T_{\mu\nu} &= p g_{\mu\nu} + (p+\rho) u_\mu u_\nu \\ &= \mathrm{diag}(\rho, p, p, p) \,, \end{aligned} \tag{1.6}$$

where ρ is the total energy density of the Universe, p is its total pressure and u_μ is the fluid 4-velocity. By combining Eq. (1.5) with Eq. (1.6) we obtain the Friedmann-Lemaître (FL) equations [21, 22]:

$$\left(\frac{\dot{a}}{a}\right)^2 \equiv H^2 = \frac{1}{3M_{\rm pl}^2}\rho + \frac{\Lambda}{3} - \frac{K}{a^2} \,, \tag{1.7a}$$

$$\frac{\ddot{a}}{a} \equiv \dot{H} + H^2 = -\frac{1}{6M_{\rm pl}^2}(\rho + 3p) + \frac{\Lambda}{3} \,, \tag{1.7b}$$

where H is the Hubble parameter which rules the evolution of the scale factor and gives the expansion rate of the Universe. Here $\dot{}$ defines the derivatives with respect to the cosmic time (1.2). For the X component, we define the *density parameter* Ω_X as the ratio between its energy density and the critical density of the Universe (assuming a reference value for the Hubble parameters $H_0 \simeq 67$ km s^{-1} Mpc^{-1}, according to Refs. [23, 24]):

$$\rho_{\rm cr} \equiv 3M_{\rm pl}^2 H^2 \simeq 0.84 \times 10^{-28} \mathrm{g/cm}^3 \,. \tag{1.8}$$

The FL Eq. (1.7a) can be rewritten to carry off the curvature of the Universe to the total energy density as:

$$\Omega_{\rm tot} - 1 = \frac{K}{a^2 H^2} \,, \tag{1.9}$$

[1] In our notation the reduced Planck mass is defined as $M_{\rm pl} \equiv 1/\sqrt{8\pi G} = 2.435 \times 10^{18}$ GeV/c^2.

where the total energy density is the sum of all the contributions from matter (with zero pressure, baryon and CDM), the relativistic components (radiation, neutrinos), and from the cosmological constant ($\Omega_\Lambda \equiv \Lambda/3M_{\rm pl}^2$).

Differentiating with respect to the time Eq. (1.7a) we obtain the *continuity equation*:

$$\dot{\rho} + 3H(1+w)\rho = 0\,. \tag{1.10}$$

where we have introduced the *parameter of state* w ($w = p/\rho$). If we consider matter, i.e. $w \simeq 0$, the continuity equation leads to $\rho_{\rm m} \propto a^{-3}$; for radiation, i.e. $w = 1/3$, Eq. (1.10) leads to $\rho_{\rm r} \propto a^{-4}$. This implies that the early Universe is dominated by radiation since $a \to 0$, and then, after equality between the matter and radiation density at $z_{\rm eq} \simeq 3400$, by matter.

We can also define an effective energy density and pressure for the cosmological constant as:

$$\rho_\Lambda = -p_\Lambda = M_{\rm pl}^2\Lambda\,. \tag{1.11}$$

A universe dominated by a cosmological constant was described for the first time by Willen de Sitter in the 1917 [25]. The de Sitter Universe is a cosmological model with no matter ($\rho = 0$, $p = 0$) and flat ($K = 0$). A positive cosmological constant plays the role of a repulsive gravitational constant and drives the universe into an expansion phase with an exponential scale factor, i.e. $a(t) \propto e^{\sqrt{\frac{\Lambda}{3}}t}$.

The generalization to the multi-component case of the Friedmann's Eq. (1.7a) in presence of matter, radiation, and a cosmological constant is:

$$H^2(z) = H_0^2\left[\Omega_{\rm m,0}(1+z)^3 + \Omega_{\rm r,0}(1+z)^4 + \Omega_{\Lambda,0} + (1-\Omega_{\rm m,0}-\Omega_{\rm r,0}-\Omega_{\Lambda,0})(1+z)^2\right]\,, \tag{1.12}$$

where the last term on the right hand side (rhs) is equal to zero for a flat universe.

1.2 Problems

Despite the great achivements of the Big Bang model described in Sec. 1.1 some conceptual problems remain. These problems consist in the explanation of cosmological observations under general initial conditions (the cosmological horizon, the flatness of the Universe, the excessive degree of homogeneity and isotropy of the Universe, ...). Other important open problems are connected to theoretical physics (unification

of gravity and quantum mechanics, ...), and also particle physics (the origin of the baryon asymmetry, the nature of the dark matter, the presence of extra relics, ...).

Now, we will discuss the conceptual problems of the Big Bang cosmology.

1.2.1 The horizon problem

The distance travelled by a photon, calculated by solving the radial equation of motion $\mathrm{d}s^2 = 0$, represents the maximum causal connection between two points in the space-time, called *comoving particle horizon*, defined as:

$$\chi(t) = \int_0^t \frac{dt'}{a(t')}\,, \tag{1.13}$$

that corresponds to the *comoving distance* between a distant emitter and us.

The Hubble radious at the time of the formation of the CMB, at $z \simeq 1090$ (the last scattering surface), was roughly 100 Mpc, corresponding to an angle of around 1°. Therefore two points on the last scattering surface separated by more than 1° have never been in causal contact betweem them.

How can we explain the level of homogeneity and isotropy of the observed Universe in the CMB pattern? This is the *horizon problem*.

For a universe dominated by a fluid with a costant equation of state we have for the comoving Hubble radius (which is the inverse of the Hubble distance, by governing causality):

$$1/aH = a^{\frac{1+3w}{2}}/H_0\,, \tag{1.14}$$

and the comoving particle horizon is:

$$\chi(t) = \frac{2}{1+3w}\frac{1}{aH} = \frac{2}{(1+3w)H_0}a^{\frac{1+3w}{2}}\,. \tag{1.15}$$

In order to solve the horizon problem we need to postulate a stage in which the comoving particle horizon and the Hubble radius behave differently to reduce the Hubble radius in the early Universe by violating the strong energy condition (SEC), i.e. :

$$1 + 3w > 0\,. \tag{1.16}$$

1.2.2 The flatness problem

As from Eq. (1.9), $\Omega_{\mathrm{tot}} = 1$ is an unstable fixed point for an expanding universe. Therefore, the current measurments leading to $\Omega_{\mathrm{tot}} \sim 1$ at percent level require Ω_{tot}

extremely close to one in the past. If we extimate the difference between the curvature in the early Universe, e.g. $T_{\rm early} \simeq 10^{15}$ GeV, and the curvature today, i.e. $T_0 \simeq 10^{-3}$ eV, we obtain a tiny number:

$$\frac{|\Omega_{\rm early} - 1|}{|\Omega_0 - 1|} \approx \left(\frac{a_{\rm early}}{a_0}\right)^2 \sim \left(\frac{T_0}{T_{\rm early}}\right)^2 \sim 10^{-54}\,. \tag{1.17}$$

The flatness problem is connected to the *entropy problem*. Under the hypothesis of adiabatic expansion of the Universe, the Eq. (1.9) during radiation domination gives:

$$\Omega_{\rm tot} - 1 \approx \frac{K M_{\rm pl}^2}{S^{2/3} T^2}\,, \tag{1.18}$$

which corresponds to a universe with an incredibly large amount of entropy at that time.

1.2.3 Extra relics

The abundance of relics predicted in theories beyond the Standard Model (SM) of particle physics exceed the bounds from current observations.

In the standard cosmological model, this problem was originally associated to the specific case of the magnetic monopole, *the cosmological monopole problem*.

Certain grand unified gauge theories (GUT) predict that the standard models $SU(3)\times SU(2)\times U(1)$ arose from the breaking of an original simple symmetry group, e.g. $SU(5)$. Assuming such a type of symmetry, during its evolution, the Universe should suffer a spontaneous breaking of a GUT symmetry at $T_{\rm GUT} \gg T_{\rm SM}$, and an abundance of monopoles larger than the current measurements should be generated.

1.2.4 Cosmological perturbations

The Big Bang model does not provide a causal mechanism of the generation of primordial inhomogeneities.

These inhomogeneities are responsible for the anisotropies of the CMB and for the overdensities that we observe today in the Large Scale Structure (LSS) matter distribution.

1.3 Cosmic inflation

In contrast with the success of the Big Bang model, which describes the Universe after nucleosynthesis, the knowledge of the early Universe is more puzzling. The addition

of a new phase before nucleosynthesis, during which the Universe went through an accelerated expansion, was proposed to solve some problems and the initial fine-tuning required by the Big Bang model, and only almost twenty years after this theory was proposed, cosmological observations became precise enough to test these ideas.

1.3.1 Conditions for inflation

The theory of cosmic inflation has been proposed in order to solve some of the problems of the Big Bang model. It is defined as the phase during which the scale factor of the Universe is accelerating:

$$\ddot{a} > 0\,, \tag{1.19}$$

which corresponds to the fact that the comoving Hubble length, i.e. $1/aH$, is decreasing with time. Decreasing the Hubble radius in the early Universe requires a SEC violation according to Eq. (1.16).

Thanks to this condition it is possible to solve the problems of the Big Bang model previously mentioned: the comoving horizon is reduced well inside the Hubble radius, $\Omega_{\rm tot}$ is driven to 1, classical inhomogeneities and relic abundances produced before inflation are diluited and pushed outside the observable scales we can probe with CMB and LSS.

By combining Eq. (1.10) with Eq. (1.19) we obtain that the condition to have inflation correnspponds to the negative pression of a fluid that dominates the Universe, since:

$$\rho + 3p < 0\,, \tag{1.20}$$

assuming for simplicity $K = 0$.

There are a lot of possible solutions that satisfy the inflationary condition. The archetypal example is the de Sitter expansion governed by the space-time metric:

$$\mathrm{d}s^2 = dt^2 - e^{2Ht}\mathrm{d}\mathbf{x}^2\,, \tag{1.21}$$

characterized by the exponential scale factor which is a self-consistent solution for a de Sitter universe, as we have seen. However, realistic inflationary models usually predict a deviation from the exact de Sitter expansion, since inflation must come to an end.

In order to solve the *horizon problem* we need an observed comoving radius smaller than the one at the beginning of inflation:

$$\frac{a_0 H_0}{a_{\rm end} H_{\rm end}} \sim \frac{a_0}{a_{\rm end}} \left(\frac{a_{\rm end}}{a_0}\right)^2 \sim \frac{T_0}{T_{\rm end}} \sim \frac{10^{-3}\ \text{eV}}{10^{15}\ \text{GeV}} \sim 10^{27}\,. \tag{1.22}$$

The most common way for this to emerge is to have $H \simeq$ const during inflation, so that:

$$\ln\left(\frac{a_{\rm end}}{a_{\rm in}}\right) > 62\,. \tag{1.23}$$

Moreover, we have to add to the puzzle a non-adiabatic period, between the end of inflation and the radiation-dominated phase where a large entropy is generated under the form of relativistic degrees of freedom.

1.3.2 The physics of inflation

Many properties for a matter component with a negative pressure can be reproduced by a scalar field, as the one connected to the Higgs particle. In a homogeneous universe, the scalar field is a function of time only.

We can describe a universe filled by a scalar field ϕ from the generic action:

$$\mathcal{S} = \int {\rm d}^4x\,\sqrt{-g}\left[\frac{M_{\rm pl}^2}{2}R + P(\chi,\phi)\right]\,, \tag{1.24}$$

where $P(\chi,\phi)$ is the matter Lagrangian and plays the role of pressure, and $2\chi = -(\nabla\phi)^2$ is the kinetic term. The simplest case for a single scalar field action with its linear derivative with standard kinetic term is $P = \chi - V(\phi)$, which corresponds to an energy density and pressure given by:

$$\rho_\phi = \frac{1}{2}\dot\phi^2 + V(\phi)\,, \tag{1.25a}$$

$$p_\phi = \frac{1}{2}\dot\phi^2 - V(\phi)\,. \tag{1.25b}$$

The equations of FL (1.7a)-(1.7b) for an expanding universe and the continuity equation (1.10) containing a homogeneous scalar field read:

$$H^2 = \frac{1}{3M_{\rm pl}^2}\left[\frac{1}{2}\dot\phi^2 + V(\phi)\right]\,, \tag{1.25c}$$

$$\dot H = -\frac{\dot\phi}{2M_{\rm pl}^2}\,, \tag{1.25d}$$

$$\ddot\phi + 3H\dot\phi = -V_{,\phi}\,, \tag{1.25e}$$

where we assume a spatially flat universe ($K = 0$). The third equation corresponds to the standard Klein-Gordon (KG) equation of the dynamic of a scalar field. The condition for inflation, Eq. (1.20), reads:

$$\dot{\phi}^2 < V(\phi)\,, \tag{1.26}$$

which means that we will have inflation whenever the potential energy dominates over the total budget. This should be provided by a flat enough potential, so that the scalar field is expected to roll slowly. Assuming only models with a single scalar field and a standard kinetic term, the *model* is given, and so all its predictions, by choosing the potential $V(\phi)$.

Another important quantity is the amount of inflation, the so called *number of e-folds*, defined as:

$$N \equiv \ln \frac{a(t_{\rm end})}{a(t_{\rm ini})} = \int_{t_{\rm ini}}^{t_{\rm end}} {\rm d}t\, H\,. \tag{1.27}$$

If this number is sufficiently large, i.e. if inflation holds for enough time, the horizon, the flatness, and the monopole problems can be solved.

1.3.3 Slow-roll dynamics

With the single scalar field Lagrangian defined above, it is possible to introduce a set of parameters to describe the behaviour of the scalar field ϕ during inflation and derive the observable quantities. It is possible to parametrize the dynamic of the inflaton with the Hubble Flow Functions (HFFs) which are defined by the hierarchy equation:

$$\epsilon_{\rm n+1} = \frac{{\rm d}\,|\ln \epsilon_{\rm n}|}{{\rm d}\,N}\,, \tag{1.28}$$

with initial value:

$$\epsilon_0 \equiv \frac{H_{\rm in}}{H}\,. \tag{1.29}$$

In order to satisfy the inflationary conditions introduced before we have from Eq. (1.20):

$$\epsilon_1 \equiv -\frac{\dot{H}}{H^2} < 1\,. \tag{1.30}$$

Moreover, ϵ_1 has to remain small for a sufficient time in order to solve the horizon problem, hence the fractional change of ϵ_1 is measured by the second HFF:

$$\epsilon_2 \equiv \frac{\dot{\epsilon}_1}{H\epsilon_1}\,, \tag{1.31}$$

and for this reason, we require $|\epsilon_2| < 1$. For the standard case of a single scalar field with canonical kinetic term in the Lagrangian, inflation occurs if the kinetic energy gives a small contribution to the total energy density and persists if the acceleration of the scalar field is small:

$$\epsilon_1 = \frac{\dot{\phi}^2/2}{M_{\rm pl}^2 H^2} \ll 1\,, \qquad\qquad |\epsilon_2| = \left|\frac{2\ddot{\phi}}{H\dot{\phi}}\right| \ll 1\,, \tag{1.32}$$

which implies:

$$\dot{\phi} \ll 2V\,, \qquad\qquad 3H\dot{\phi} \simeq -V_{,\phi} \quad (\ddot{\phi} < V_{,\phi})\,. \tag{1.33}$$

These two conditions summarize the *slow-roll approximation*. Under the validity of the slow-roll conditions, Eq. (1.27) for the number of e-folds can be approximated as:

$$N = \int {\rm d}t\, H = \int \frac{1}{\sqrt{2\epsilon_1}} \frac{|{\rm d}\phi|}{M_{\rm pl}} \simeq \int_{\phi_{\rm ini}}^{\phi_{\rm end}} {\rm d}\phi\, \frac{V}{V_{,\phi}}\,. \tag{1.34}$$

The potential slow-roll parameters represent an alternative parameterization of the HFFs [26]:

$$\epsilon_V \equiv \frac{M_{\rm pl}^2}{2}\frac{V_{,\phi}^2}{V^2}\,, \tag{1.35a}$$

$$\eta_V \equiv M_{\rm pl}^2 \frac{V_{,\phi\phi}}{V}\,, \tag{1.35b}$$

$$\xi_V^2 \equiv M_{\rm pl}^4 \frac{V_{,\phi\phi\phi}V_{,\phi}}{V^2}\,. \tag{1.35c}$$

It is important to note that this second hierarchy of potential slow-roll parameters is

"exactly" given in form of the HFFs:

$$\epsilon_V = \epsilon_1 \frac{\left(1 - \frac{\epsilon_1}{3} + \frac{\epsilon_2}{6}\right)^2}{\left(1 - \frac{\epsilon_1}{3}\right)^2}\,, \tag{1.36a}$$

$$\eta_V = \frac{2\epsilon_1 - \frac{\epsilon_2}{2} - \frac{2\epsilon_1^2}{3} + \frac{5\epsilon_1\epsilon_2}{6} - \frac{\epsilon_2^2}{12} - \frac{\epsilon_2\epsilon_3}{6}}{1 - \frac{\epsilon_1}{3}}\,, \tag{1.36b}$$

$$\begin{aligned}\xi_V^2 =& \frac{1 - \frac{\epsilon_1}{3} + \frac{\epsilon_2}{6}}{\left(1 - \frac{\epsilon_1}{3}\right)^2}\left(4\epsilon_1^2 - 3\epsilon_1\epsilon_2 + \frac{\epsilon_2\epsilon_3}{2} - \epsilon_1\epsilon_2^2\right.\\ &\left. + 3\epsilon_1^2\epsilon_2 - \frac{4}{3}\epsilon_1^3 - \frac{7}{6}\epsilon_1\epsilon_2\epsilon_3 + \frac{\epsilon_2^2\epsilon_3}{6} + \frac{\epsilon_2\epsilon_3^2}{6} + \frac{\epsilon_2\epsilon_3\epsilon_4}{6}\right)\,.\end{aligned} \tag{1.36c}$$

It is possible to approximate the slow-roll potential parameters in terms of the HFFs, and vice versa. Applying the slow-roll approximation to the Friedmann Eq. (1.25c). At the leading order we have:

$$H^2 \simeq \frac{V}{3M_{\rm pl}^2}\,, \tag{1.37}$$

and so:

$$\epsilon_{\rm V} \simeq \epsilon_1\,, \tag{1.38a}$$

$$\eta_{\rm V} \simeq 2\epsilon_1 - \frac{\epsilon_2}{2}\,, \tag{1.38b}$$

$$\xi_{\rm V}^2 \simeq 4\epsilon_1^2 - \frac{\epsilon_1\epsilon_2}{3} + \frac{\epsilon_2\epsilon_3}{2}\,, \tag{1.38c}$$

and to derive the next-to-leading order is enough to use:

$$H^2 \simeq \frac{V}{3M_{\rm pl}^2}\left(1 - \frac{\epsilon_1}{3}\right)^{-1}\,, \tag{1.39}$$

instead of Eq. (1.37).

To describe the effects due to a non-standard kinetic term we have also to introduce, together with the HFFs, the speed of sound and its derivatives, that can be expressed for a generic matter Lagrangian as [27, 28]:

$$c_{\rm s}^2 \equiv \frac{P_{,\chi}}{P_{,\chi} + 2\chi P_{,\chi\chi}}\,, \tag{1.40}$$

$$s \equiv \frac{\dot{c}_{\rm s}}{H c_{\rm s}}\,. \tag{1.41}$$

1.3.4 The first models of inflation

The first model of inflation was proposed by Alexei Starobinsky in 1980 [29]. It is based on the inverstigation of the conformal anomaly in quantum field theory in curved space-times. By taking into account higher order terms in the curvature, motivated by one-loop quantum effects, the model provides a way to generate a nearly de Sitter stage and terminate the inflationary epoch with an isotropic, homogeneous universe. In this model it was also predicted gravitational waves (GW) with a flat spectrum [30].

The mechanism of production of adiabatic perturbations of the metric with a flat spectrum, responsible for the observed CMB anisotropies and LSS of the Universe, was proposed by Viatcheslav Fyodorovich Mukhanov and G. V. Chibisov, in the context of the model proposed by Starobinsky, in 1981 [31]. Afterwards, Starobinsky predicted the amount of gravitational waves in this model [32].

Another simple model, based on a scalar field, was proposed by Alan Guth in 1981 [33]. His model, now called *old inflation*, is based on the idea of the decay of a so-called false vacuum into bubbles of true vacuum. Even if it provides a mechanism for inflation to begin and a possible solution to the horizon and flatness problems, the first formulation by Guth gives no consistent way to end the inflation according to the observations, the so called *graceful exit problem*. In fact, the universe after the phase transition in this scenario becomes extremely inhomogeneous [34, 35].

The solution was found in 1981-1982 by Andrei Linde with the invention of the *new inflation* theory [36, 37]; few month later, the same result was also obtained by Andreas Albrecht and Paul J. Steinhardt [38]. Starting from either a false vacuum or an ustable state, the inflaton field slowly rolls down to the minimum of its effective potential.

Even the new inflation has few problems. In fact it only works if the effective potential of the field has a very flat plateau near $\phi = 0$. Moreover, the physics of the phase transitions, the base for both old and new inflation, requires an initial thermal equilibrium with other matter fields (in most versions the inflaton field is very weakly coupled to other fields) and this is problematic [39].

In 1983 the *chaotic inflation* scenario was proposed by Linde [40]. This scenario resolves all problems of both old and new inflation: the requirement of a universe in thermal equilibrium from the very beginning, the requirement of homogeneity until the end of inflation, and the conceptual problem about the phase of the universe before this phase transition. Chaotic inflation occurs in all theories where the potential has a sufficiently flat region, which allows the existence of the slow-roll regime [40], indipendently from the simplicity or not of the potential and independently from the presence of thermal equilibrium in the early universe.

1.4 The end of inflation and reheating

The theory of reheating of the Universe after inflation is an important part of cosmic inflation, since connects the quantum regime of inflation to the thermal equilibrium of Big Bang cosmology. In the stage of reheating the inflaton decays into SM particles or particles which then decay into those.

One of the first and more intuitive approach to inflaton decay is the perturbative approach [41]. We assume that the inflaton field is coupled to another scalar field χ through an interacting term:

$$-g\sigma\phi\chi^2\,, \tag{1.42}$$

where g is a dimensionless coupling constant and σ is a mass scale, then the decay rate of the inflaton into χ pairs is given by:

$$\Gamma_{\phi\to\chi\chi} = \frac{g^2\sigma^2}{8\pi m}\,, \tag{1.43}$$

where m is the inflaton mass. The energy loss due to the particles production can be taken into account by adding a friction term into the KG Eq. (1.25e) like:

$$\ddot{\phi} + (3H + \Gamma)\,\dot{\phi} + V_{,\phi} = 0\,, \tag{1.44}$$

and becames relevant when $H \simeq \Gamma$, which also determinates the temperature of the SM fields after energy transfer:

$$T_{\rm R} \sim \sqrt{\Gamma M_{\rm pl}}\,. \tag{1.45}$$

In general, the physics of reheating may be more complicated because of the non-linear backreaction, the non-perturbative nature of rescattering, and because it requires to know all the couplings between the inflaton field and the other fields in the SM. For this reason, the reheating phase can be described phenomenologically by two parameters: the number of e-folds between the end of inflation and the beginning of the radiation phase, i.e. $N_{\rm reh}$, and the average equation of state during the reheating phase, i.e. $w_{\rm reh}$.

1.4.1 Amount of inflation

We can find an expression for Eq. (1.27) after the identification of the different relevant phases of the Universe, assuming instantaneous transitions between them.

We start by considering a wavenumber $k = aH$ which crosses the horizon during inflation:

$$\frac{k}{a_0 H_0} = \frac{a_k H_k}{a_0 H_0} = \frac{a_k}{a_{\rm end}} \frac{a_{\rm end}}{a_{\rm reh}} \frac{a_{\rm reh}}{a_0} \frac{H_k}{H_0} \,. \tag{1.46}$$

The definition of energy density and entropy density [42], for particles in thermal equilibrium is:

$$\rho_{\rm x} = \frac{\pi^2}{30} g_{\rm x}(T) T_{\rm x}^4 \,, \tag{1.47}$$

$$s_{\rm x} = \frac{2\pi^2}{45} g_{\rm x}(T) T_{\rm x}^3 \,, \tag{1.48}$$

and assuming the conservation of entropy it is possible to manipulate the various terms of Eq. (1.46). The first term on the rhs of Eq. (1.46) is defined as:

$$N(k) \equiv \ln \left(\frac{a_{\rm end}}{a_k} \right) \,, \tag{1.49}$$

and represents the number of e-folds between the time at which the comoving wavenumber k crossing the comoving Hubble radius and the end of inflation.

The second term on the rhs of Eq. (1.46) expresses the amout of time between the end of inflation and the beginning of the radiation-dominated phase, i.e. the reheating phase. We can introduce a new number of e-folds defined as:

$$N_{\rm reh} \equiv \ln \left(\frac{a_{\rm reh}}{a_{\rm end}} \right) \,, \tag{1.50}$$

or, starting from the energy conservation described in Eq. (1.10) and assuming an unknown cosmic fluid during reheating with an average equation of state parameter $w_{\rm reh}$:

$$\begin{aligned} \rho_{\rm reh} &= \rho_{\rm end} \exp \left\{ 3 \int \frac{{\rm d}a}{a} (1 + w_{\rm reh}(a)) \right\} \\ &= \rho_{\rm end} \exp \left\{ -3 \int_{N_{\rm end}}^{N} dN' \left[1 + w_{\rm reh}(N') \right] \right\} \\ &= \rho_{\rm end} \exp \left\{ -3 N_{\rm reh} (1 + \bar{w}_{\rm reh}) \right\} \,, \end{aligned} \tag{1.51}$$

in order to connect the end of inflation to the radiation-dominated phase. If we assume instant reheating, $N_{\rm reh} = 0$ and $w_{\rm reh} = 1/3$.

The third term on the rhs of Eq. (1.46) can be derived from the entropy conservation between the reheating phase and the radiation-dominated phase from:

$$g_{\rm reh}T_{\rm reh}^3 = \left(\frac{a_0}{a_{\rm reh}}\right)^3 \left(2 + \frac{7}{8}2\frac{4}{11}N_{\rm eff}\right) T_{\gamma,0}^3\,, \tag{1.52}$$

where $N_{\rm eff}$ is the effective number of neutrino species in the Universe. We use as standard value $N_{\rm eff} = 3.046$ which takes into account that neutrino decoupling was not quite completed when e^+e^- pairs annihilation began. Here $g_{\rm reh}$ is the number of effective degree of freedom at reheating, i.e. $g_* = g_{\rm B} + 7g_{\rm F}/8$. At $T \gtrsim 100$ MeV all the particles of the SM are relativistic and hence $g_* = 106.75$. All the degrees of freedom in the Minimal Supersymmetric SM (MSSM) give $g_* = 228.75$ for $T \gtrsim 1$ TeV. Using the definition of energy density we can express the reheating temperature like:

$$T_{\rm reh}^4 = \frac{30}{\pi g_{\rm reh}}\rho_{\rm end}e^{-3N_{\rm reh}(1+w_{\rm reh})}\,, \tag{1.53}$$

and plugging that into Eq. (1.52) to get:

$$\frac{a_{\rm reh}}{a_0} = \left(2 + \frac{7}{11}N_{\rm eff}\right)^{1/3} \frac{T_{\gamma,0}}{g_{\rm reh}^{12}} \left(\frac{\pi^2}{30}\rho_{\rm end}\right)^{1/4} e^{\frac{3}{4}N_{\rm reh}(1+w_{\rm reh})}\,. \tag{1.54}$$

We obtain finally:

$$N(k) = -\ln\left(\frac{k}{a_0H_0}\right) - \frac{1}{12}\ln\left(g_{\rm reh}\right) + \frac{1}{4}\ln\left(\frac{\rho(k)}{M_{\rm pl}^4\rho_{\rm end}}\right) - \frac{1-3w_{\rm reh}}{4}N_{\rm reh} + G(N_{\rm eff}, H_0)\,, \tag{1.55}$$

where we used Eq. (1.7a). We collect all the numerical factor in:

$$G(N_{\rm eff}, H_0) = \frac{1}{3}\ln\left(2 + \frac{7}{11}N_{\rm eff}\right) + \frac{1}{4}\ln\left(\frac{T_{\gamma,0}^4\pi^2}{270H_0^4}\right)\,, \tag{1.56}$$

which correspond for our choice of parameters to [2]:

$$\frac{1}{3}\ln\left(2 + \frac{7}{11}3.046\right) + \frac{1}{4}\ln\left(\frac{(2.7255\text{ K} \times k_B)^4\pi}{540(67\text{ km/s/Mpc} \times \hbar)^4}\right) \simeq 66.9\,. \tag{1.57}$$

We show in Fig. (1.1) the weak dependence of Eq. (1.57) from the three cosmological parameters $N_{\rm eff}, H_0, T_{\gamma,0}$.

[2] From http://pdg.lbl.gov/2015/reviews/rpp2015-rev-phys-constants.pdf:
1 pc = $3.08567758130573 \times 10^{16}$ m,
$k_B = 8.61673324(78) \times 10^{-5}$ eV/K,
$h = 6.1582119514(40) \times 10^{-16}$ eV s.

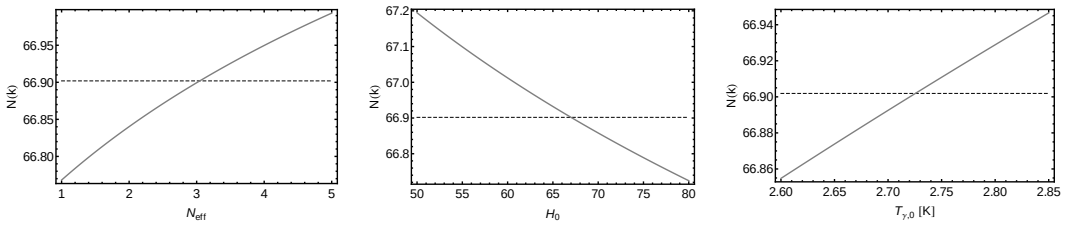

Figure 1.1: We show the minor dependence of Eq. (1.55) from $N_{\rm eff}$ (left panel), H_0 (central panel), and $T_{\gamma,0}$ (right panel).

The first term in Eq. (1.55) depends on the scale k at which the primordial power spectrum is computed and usually correnspponds to:

$$-\log\left(\frac{k}{67/299792.458}\right) \simeq \begin{cases} -5.4 & \text{for} \quad k_* = 0.05\ \text{Mpc}^{-1}\,, \\ -2.2 & \text{for} \quad k_* = 0.002\ \text{Mpc}^{-1}\,. \end{cases} \tag{1.58}$$

The second term in Eq. (1.55) gives a very small contribution to the total number of e-folds:

$$-\frac{1}{12}\ln\left(g_{\rm reh}\right) \simeq \begin{cases} -0.39, & \text{for} \quad g_* = 106.75\,, \\ -0.45, & \text{for} \quad g_* = 228.75\,, \\ -0.58, & \text{for} \quad g_* = 10^3\,. \end{cases} \tag{1.59}$$

So for example, if we consider the pivot scale for the primordial power spectra (PPS) to be $k_* = 0.002\ \text{Mpc}^{-1}$ and an effective number of bosonic degrees of freedom during the reheating phase of $g_* = 10^3$ (see [43, 44]), we get:

$$N_{0.002} = 64.1 + \frac{1}{4}\ln\left(\frac{\rho_{0.002}}{M_{\rm pl}^4\rho_{\rm end}}\right) - \frac{1-3w_{\rm reh}}{4}N_{\rm reh}\,. \tag{1.60}$$

1.5 Late-time acceleration

Current observations confirmed the ΛCDM model as the standard cosmological model. Both the two accelerations of the Universe could be explained as the Universe was dominated by the potential of a scalar field (obviously the potential having a very different amplitude and scale).

A cosmological constant Λ is just the simplest and minimal candidate of DE. We choose to classify mechanisms to explain the origin of the DE in two broad classes:

the first one is based on specific form of matter, and the second one is based on the modification of gravity. In both classes the DE equation of state changes in time, by which the models can be distinguished from the ΛCDM model.

1.5.1 Quintessence

A class of models of DE which has drawn much attention is that of *quintessence*, which proposes a dynamical, time-evolving form of DE. In these models, the accelerated expansion is driven by a scalar field minimally coupled to the Ricci scalar. The general action for quintessence is [45] (see also [46] for a textbook):

$$\mathcal{S} = \int \mathrm{d}^4x \sqrt{-g} \left[\frac{R}{16\pi G} - \frac{1}{2}\partial_\mu\phi\partial^\mu\phi - V(\phi) + \mathcal{L}_\mathrm{m} \right] , \tag{1.61}$$

which gives the EMT for the field ϕ:

$$T^{(\phi)}_{\mu\nu} = \partial_\mu\phi\partial_\nu\phi + \left(\frac{1}{2} g^{\alpha\beta}\partial_\alpha\phi\partial_\beta\phi - V(\phi) \right) g_{\mu\nu} \, . \tag{1.62}$$

Assuming an homogeneus field the equation of motion becomes:

$$\ddot{\phi} + 3H\dot{\phi} + \frac{dV}{d\phi} = 0 \, . \tag{1.63}$$

Here the Hubble parameter H acts as a damping term on the field ϕ. The equation of state for the scalar field is:

$$\omega_\phi = \frac{p_\phi}{\rho_\phi} = \frac{\frac{1}{2}\dot{\phi}^2 - V(\phi)}{\frac{1}{2}\dot{\phi}^2 + V(\phi)} \, , \tag{1.64}$$

where we see that $-1 \leq \omega_\phi \leq 1$, depending on the potential and the kinetic energy of ϕ. The field tends to roll down the potential, its motion being slow down by the term $3H\dot{\phi}$. Therefore, if the potential is not steep, the field rolls down it very slowly, yielding to $\dot{\phi} \ll V(\phi)$. Under this condition, the equation of state becomes $\omega_\phi < -\frac{1}{3}$, thus allowing an accelerated expansion since $\omega_\phi \sim -1$. The behaviour of the field should be independent of the initial conditions in order to avoid the fine tuning problems. Also, to be compatible with the observations, the effects of the scalar field on the evolution of the Universe should be negligible in past epochs. These conditions should be satisfied by the potential of the field, thus the choice of its form has to be carefully studied.

There exists a category of solutions, so-called tracker solutions, that satisfies all these conditions: these are attractor-like solutions in the sense that for a wide range of initial

conditions the field approaches the same evolution during the radiation-dominated phase. Example of this tracker potentials are [47]:

$$V = M^4 \left(e^{\frac{M_{\rm pl}}{\phi}} - 1 \right) , \tag{1.65a}$$

$$V = \frac{M^{4+\alpha}}{\phi^\alpha} , \tag{1.65b}$$

where $\alpha > 0$ and M are both free parameters. Also, a subclass of quintessence models exists in which there is no potential term: these are called k-essence models since the field contributes only with a kinetic term. In these models the accelerated expansion of the Universe is driven by the scalar field's kinetic energy rather than the potential energy [48]. The FL equations for general quintessence models are [49]:

$$H^2 = \frac{1}{3M_{\rm pl}} \left[\sum_{\rm i} \rho_{\rm i} + \frac{1}{2}\dot{\phi} + V(\phi) \right] , \tag{1.66a}$$

$$\dot{H} = -4\pi G \left[\sum_{\rm i} (\rho_{\rm i} + p_{\rm i}) + \dot{\phi}^2 \right] . \tag{1.66b}$$

1.5.2 Scalar-tensor theories

The scalar-tensor theories of gravity are some of the most established and well studied alternative theories of gravity. The scalar-tensor theory was conceived originally by Pascaul Jordan in 1955 [50], who proposed to embed a four-dimensional curved manifold in five-dimentional flat space-time by adding a scalar field. This setting enabled to describe a space-time dependent gravitational constant, in accordance with Dirac's argument that the gravitational constant should be time-dependent [51, 52]. Jordan's effort was taken over by Carl Henry Brans and Robert Henry Dicke in 1961 [53]. They demanded that the matter part of the Lagrangian be decoupled from the scalar field as an implementation of their requirement that the *weak equivalence principle* (WEP) be respected.

Jordan-Brans-Dicke (JBD) theory is among the simplest extentions of GR depending on one additional parameter only. In addition to the metric, the gravitational field is further mediated by a scalar field whose inverse plays the role of a spacetime-varying gravitational costant. The action for JBD theory is given by:

$$\mathcal{S} = \int {\rm d}^4x\sqrt{-g} \left[\frac{1}{16\pi G} \left(\phi R - \frac{\omega}{\phi} \nabla_\mu \phi \nabla^\mu \phi + \mathcal{L}_{\rm m} \right) \right] , \tag{1.67}$$

written in the *Jordan frame* (JF). Here ϕ is the Brans-Dicke (BD) field, which gives the strength of the gravitational field, ω is a coupling constant. In the limit of large ω, the kinetic term becomes large and the energetically favoured situation is that ϕ be constant, recovering general relativity. One way to rewriting this action is simply to redefine the BD field in order to recover the standard kinetic term for a scalar action; this is possible by defining a new field and coupling parameter as:

$$\sigma^2 = \frac{\phi}{\xi} M_{\rm pl}^2 \,, \tag{1.68}$$

$$\xi = \frac{1}{4\omega} \,, \tag{1.69}$$

to give:

$$\mathcal{S} = \int \mathrm{d}^4x \sqrt{-g} \left(\frac{\xi \sigma^2 R}{2} - \frac{g^{\mu\nu}}{2} \partial_\mu \sigma \partial_\nu \sigma + \mathcal{L}_{\rm m} \right) . \tag{1.70}$$

In its original formulations, JBD theory was modelled without a cosmological constant. An alternative to the addition of a cosmological constant is to consider a potential term for the scalar field. *Induced gravity* (IG), in the context of late-time cosmology, is a BD like model where the effective cosmological constant is generated from the scalar potential. The action in Eq. (1.70), which contains only dimensionless parameters, was introduced to generate the gravitational constant and inflation by spontaneous breaking of scale invariance in absence of matter [54]. In the context of late cosmology, this action was studied in Refs. [55, 56] to reduce the time dependence of the effective gravitational constant in the original BD model (i.e. with a vanishing potential [53]) and to generate an effective cosmological constant.

The addition of a potential term in Eq. (1.70) is important for the global dynamics of the model and modifies the original BD attractor with power-law time dependence of the scalar field in presence of non-relativistic matter, i.e. $a(t) = (t/t_0)^{(2\omega_{\rm BD}+2)/(3\omega_{\rm BD}+4)}$ and $\Phi = \Phi_0 (t/t_0)^{2/(3\omega_{\rm BD}+4)}$. At recent times, the potential term drives the Universe into acceleration and Einstein gravity plus a cosmological constant with a time-independent value of the scalar field emerges as an attractor among homogeneous cosmologies for the model in Eq. (1.70). In Ref. [57] it was shown how the background cosmology of these types of models is consistent with observations with $\gamma \ll 1$. Part of the original work of this thesis is to quantify these bounds with current observations of CMB and LSS.

The FL and the KG equations for IG in a flat RW metric are respectively:

$$H^2 + 2H\frac{\dot{\sigma}}{\sigma} = \frac{\sum_{\rm i}\rho_{\rm i} + V(\sigma)}{3\gamma\sigma^2} + \frac{\dot{\sigma}^2}{6\gamma\sigma^2}\,, \tag{1.71}$$

$$\ddot{\sigma} + 3H\dot{\sigma} + \frac{\dot{\sigma}^2}{\sigma} + \frac{1}{(1+6\gamma)}\Big(V_{,\sigma} - \frac{4V}{\sigma}\Big) = \frac{1}{(1+6\gamma)}\frac{\sum_{\rm i}(\rho_{\rm i} - 3p_{\rm i})}{\sigma}\,, \tag{1.72}$$

once the Einstein trace equation:

$$-\gamma\sigma^2 R = T - (1+6\gamma)\partial_\mu\sigma\partial^\mu\sigma - 4V - 6\gamma\sigma\Box\sigma\,, \tag{1.73}$$

is used. In the above $V_{,\sigma}$ denotes the derivative of the potential $V(\sigma)$ with respect to σ, the index i runs over all fluid components, i.e. baryons, CDM, photons and neutrinos. The effective potential in Eq. 1.72 vanishes for $n = 4$.

In absence of matter, exact solutions with an accelerated expansion exist for monomial potentials $V(\sigma) = \lambda_n\sigma^n$ within IG [58] (for earlier works see Ref. [59]). Solutions with $a(t) \sim t^p$ (with $t > 0$ and $p > 1$) exist:

$$p = 2\frac{1 + (n+2)\gamma}{(n-4)(n-2)\gamma}\,, \tag{1.74}$$

$$\sigma(t) = \frac{c_0}{t^{\frac{2}{(n-2)}}}\,, \tag{1.75}$$

with $4 < n < 4 + \sqrt{2(6 + 1/\gamma)}$ or $4 - \sqrt{2(6 + 1/\gamma)} < n < 2$ and c_0 is an integration constant. The special cases with $n = 2\,, 4$ (which correspond to poles in the above equations) correspond to a de Sitter solution having $a(t) \propto e^{Ht}$. However for these two special cases, the time evolution for the scalar field is different, being σ time dependent for $n = 2$ and constant in time for $n = 4$.

As in [60], we consider the present value for the scalar field consistent with the gravitational constant $G = 6.67\times10^{-8}$ cm^3 g^{-1} s^{-2} measured in laboratory Cavendish-type:

$$\gamma\sigma_0^2 = \frac{1}{8\pi G}\frac{1+8\gamma}{1+6\gamma}\,. \tag{1.76}$$

In Fig. 1.2 several quantities are plotted versus the scale factor a for $\gamma = 10^{-3}$ and for different values of n, within the assumption of Eq. 1.76. In the upper left panel, the evolution of σ/σ_0 is plotted up to $a = 10$ in order to show the dependence on n of the future single field attractor of Eq. 1.75. In the upper right panel we show the parameter of state $w_{\rm DE}$ of the effective DE component corresponding to Einstein gravity with a

Newton's constant given by the current value of the scalar field, i.e. $8\pi G_{\rm N} = (\gamma\sigma_0^2)^{-1}$ as introduced in [61]: also in this case we extend the plot up to $a = 10$ to show that $w_{\rm DE} \simeq -1$ for values of γ compatible with observations [60]. In the lower left panel we show the evolution of the critical densities $\Omega_{\rm i}$, always corresponding to an Einstein gravity system with a Newton's constant given by the current value of the scalar field defined in [60]. In the lower right panel, we show explicitly the evolution of $G_{\rm N}(a)/G_{\rm N} \equiv \sigma_0^2/\sigma^2$; it is clear that in this class of models the effective Newton's constant (the effective Planck mass $M_{\rm pl}^2(a) = \gamma\sigma^2(a)$) decreases (increases) with time.

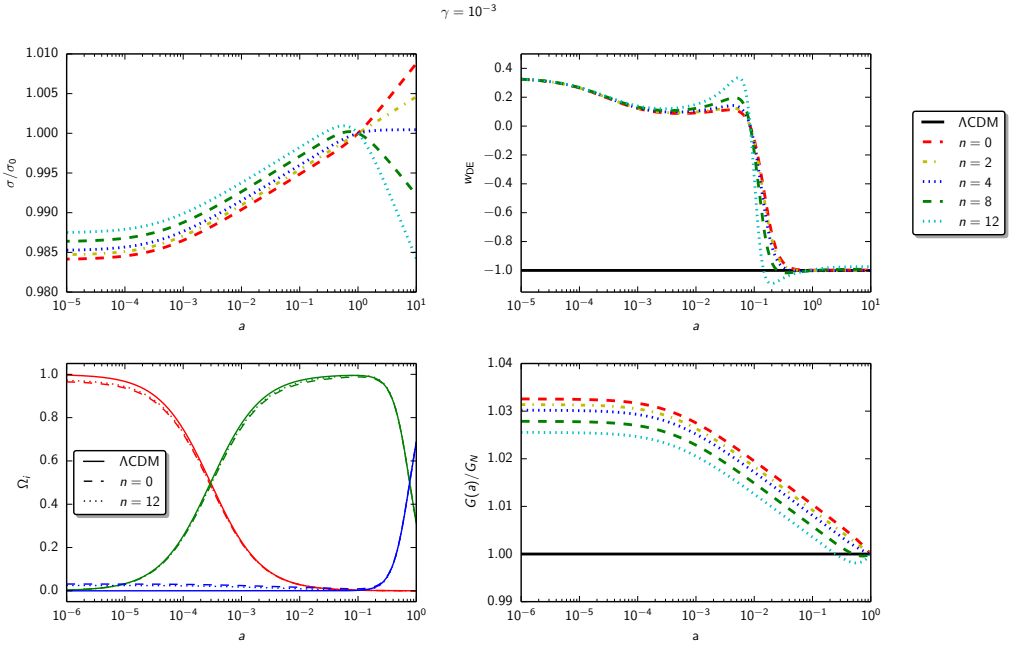

Figure 1.2: Evolution of σ/σ_0 (upper left panel), $w_{\rm DE}$ (upper right panel), and $G_{\rm N}(a)/G_{\rm N} \equiv \sigma_0^2/\sigma^2$ (lower right panel) as function of the scale factor a for $\gamma = 10^{-3}$ and different values of n. In the lower left panel we show the critical densities $\Omega_{\rm i}$: radiation in red, matter in green and effective DE in blue. See text for more details. Taken from [62].

So far many healthy extensions of GR are based on the inclusion of a scalar degree of freedom which go beyond the original JBD theory, Galileon models [63], Hordenski theories [64, 65], and theories beyond Hordenski [66, 67].

By considering the most general scalar-tensor Lagrangian [67]:

$$L_2^\phi \equiv G_2(\phi,\chi)\,, \tag{1.77}$$

$$L_3^\phi \equiv G_3(\phi,\chi)\Box\phi\,, \tag{1.78}$$

$$\begin{aligned} L_4^\phi \equiv\ & G_4(\phi,\chi)^{(4)}R - 2G_{4,\chi}(\phi,\chi)\left(\Box\phi^2 - \phi^{,\mu\nu}\phi_{,\mu\nu}\right) \\ & + F_4(\phi,\chi)\epsilon^{\mu\nu\rho}{}_\sigma\epsilon^{\mu'\nu'\rho'\sigma}\phi_{,\mu}\phi_{,\mu'}\phi_{,\nu\nu'}\phi_{,\rho\rho'}\,, \end{aligned} \tag{1.79}$$

$$\begin{aligned} L_5^\phi \equiv\ & G_5(\phi,\chi)^{(4)}G_{\mu\nu}\phi^{,\phi\nu} + \frac{1}{3}G_{5,\chi}(\phi,\chi)\left(\Box\phi^3 - 3\Box\phi\phi_{,\mu\nu}\phi^{,\mu\nu} + 2\phi_{,\mu\nu}\phi^{,\mu\rho}\phi^{,\nu}{}_{,\sigma}\right) \\ & + F_5(\phi,\chi)\epsilon^{\mu\nu\rho\sigma}\epsilon^{\mu'\nu'\rho'\sigma'}\phi_{,\mu}\phi_{,\mu'}\phi_{,\nu\nu'}\phi_{,\rho\rho'}\phi_{,\sigma\sigma'}\,, \end{aligned} \tag{1.80}$$

IG results as a basic and testable example of this class of theories where only two of the seven free functions are non-zero, i.e.:

$$G_2(\phi,\chi) = \chi - V(\phi)\,, \tag{1.81}$$

$$G_4(\phi,\chi) = \frac{\gamma\phi^2}{2}\,. \tag{1.82}$$

It is important to test the *exact* theoretical predictions of this important subclass of the theories beyond Hordenski, since few extra parameters beyond ΛCDM can be constrained by current cosmological observations.

2 Key predictions for inflation and inflationary models

In this chapter we introduce the essential concepts of cosmological inflation. We will consider single-field slow-roll models of inflation and study both scalar and tensor fluctuations. After an introduction of the important concepts, such as the theory of cosmological perturbations in terms of GR and the relations between the gravitational potentials and the primordial power spectra, we will proceed to a more technical definition of the relevant quantities that will be used and studied in the next chapters. We refer the reader to several review articles and books for further informations [1–3, 68].

2.1 Relativistic perturbation theory

The goal of cosmological perturbation theory is to relate the physics of the early Universe (e.g. inflation) to CMB anisotropy and LSS and to provide the initial conditions for numerical simulations of structure formation. The physics during the period from the end of inflation to the beginning of non-linear gravitational collapse is complicated by relativistic effects but greatly simplified by the small amplitude of perturbations. Thus, an essentially complete and accurate treatment of relativistic perturbation evolution is possible, at least in the context of simple fluctuation models like inflation.

In the following we denote with an overline the unperturbed quantity so that a generic quantity is:

$$A = \overline{A} + \delta A \,. \tag{2.1}$$

2.1.1 Perturbations of the metric

First, we must specify the form of the metric, taking into account perturbations around a homogeneous, flat universe described by:

$$\mathrm{d}s^2 = a^2(\eta) \left[-\mathrm{d}\eta^2 + \delta_{\mathrm{ij}} \, \mathrm{d}x^{\mathrm{i}} \mathrm{d}x^{\mathrm{j}} \right] , \tag{2.2}$$

which takes the general form to first-order in perturbations:

$$\mathrm{d}s^2 = a^2(\eta)\left\{-(1+2A)d\eta^2 + 2B_{\mathrm{i}}\,\mathrm{d}\eta\,\mathrm{d}x^{\mathrm{i}} + [(1+2C)\delta_{\mathrm{ij}} + h_{\mathrm{ij}}]\;\mathrm{d}x^{\mathrm{i}}\mathrm{d}x^{\mathrm{j}}\right\}. \tag{2.3}$$

The tensor h_{ij} is symmetric by costruction and the perturbed metric tensor in matrix form reads as:

$$g_{\mu\nu} = a^2\begin{pmatrix} -(1+2A) & B_{\mathrm{i}} \\ B_{\mathrm{i}} & (1+2C)\delta_{\mathrm{ij}} + h_{\mathrm{ij}} \end{pmatrix}, \tag{2.4}$$

and the controvariant metric tensor:

$$g^{\mu\nu} = a^{-2}\begin{pmatrix} -(1-2A) & B^{\mathrm{i}} \\ B^{\mathrm{i}} & (1-2C)\delta^{\mathrm{ij}} - h^{\mathrm{ij}} \end{pmatrix}. \tag{2.5}$$

A 4D tensor has in principle 16 independent components. However, since the metric tensor is symmetric, only 10 are distinct: 1 comes from A, 3 from B_{i}, and 6 from the symmetric tensor field $(1+2C)\delta_{\mathrm{ij}} + h_{\mathrm{ij}}$.

In order to keep track more efficiently of the equations, it is more useful to rewrite Eq. (2.3) as:

$$\begin{aligned}\mathrm{d}s^2 = a^2(\eta)\Big\{ &-(1+2A)\mathrm{d}\eta^2 + 2(\partial_{\mathrm{i}}B + \hat{B}_{\mathrm{i}})\,\mathrm{d}\eta\,\mathrm{d}x^{\mathrm{i}} \\ &+ \left[(1+2C)\delta_{\mathrm{ij}} + 2\partial_{\langle\mathrm{i}}\partial_{\mathrm{j}\rangle}E + 2\partial_{(\mathrm{i}}\hat{E}_{\mathrm{j})} + 2\hat{E}_{\mathrm{ij}}\right]\;\mathrm{d}x^{\mathrm{i}}\mathrm{d}x^{\mathrm{j}}\Big\},\end{aligned} \tag{2.6}$$

where we used the scalar-vector-tensor (SVT) decomposition to achieve the above result (see Ref. [3] for details).

Due to the general covariance of the Einstein equations and conservation laws, GR is invariant under a general coordinate transformation:

$$x^\mu \to \tilde{x}^\mu = x^\mu + \xi^\mu, \tag{2.7}$$

where $|\xi^\mu| \ll 1$ and the vector part of the tensor ξ^μ can be decomposed in a scalar part, and a divergenceless vector part, i.e.:

$$\xi^0 = T, \tag{2.8}$$

$$\xi^{\mathrm{i}} = \hat{L}^{\mathrm{i}} + \partial^{\mathrm{i}}L, \tag{2.9}$$

implying that preferred coordinate systems do not exist. For example, since the metric tensor transforms as:

$$\tilde{g}_{\mu\nu} = \frac{\partial x^\alpha}{\partial\tilde{x}^\mu}\frac{\partial x^\beta}{\partial\tilde{x}^\nu}\,g_{\alpha\beta}, \tag{2.10}$$

its time-time component transforms as:

$$\begin{aligned} g_{00} &= -a^2(\eta)(1+2A) \\ &= \frac{\partial \tilde{x}^\alpha}{\partial x^0}\,\frac{\partial \tilde{x}^\beta}{\partial x^0}\,\tilde{g}_{\alpha\beta} \\ &\simeq \frac{\partial \tilde{x}^0}{\partial x^0}\,\frac{\partial \tilde{x}^0}{\partial x^0}\,\tilde{g}_{00} \\ &\simeq (\delta^0_0 + T')^2\left[-a^2(\tilde{\eta})(1+2\tilde{A})\right] \\ &\simeq -(1+2T')a^2(\tau)(1+2\mathcal{H}\,T)(1+2\tilde{A}) \\ &\simeq -a^2(\eta)(1+2\tilde{A}+2\mathcal{H}T+2T')\,, \end{aligned} \tag{2.11}$$

where $\mathcal{H}$ is the Hubble parameter in conformal time, i.e. $\mathcal{H} = aH$. The $\simeq$ means that we drop all the terms of second-order in ξ, and higher order terms.

In a similar way all the coefficients of Eq. (2.6) are computed:

$$\tilde{A} = A - T' - \mathcal{H}T\,, \tag{2.12}$$

$$\tilde{B} = B + T - L'\,, \qquad \tilde{\hat{B}}_{\rm i} = \hat{B}_{\rm i} - \hat{L}'_{\rm i}\,, \tag{2.13}$$

$$\tilde{C} = C - \mathcal{H}T - \frac{1}{3}\,\nabla^2 L\,, \tag{2.14}$$

$$\tilde{E} = E - L\,, \qquad \tilde{\hat{E}}_{\rm i} = \hat{E}_{\rm i} - \hat{L}_{\rm i}\,, \qquad \tilde{\hat{E}}_{\rm ij} = \hat{E}_{\rm ij}\,. \tag{2.15}$$

Since the existence of this freedom, it is useful to define a set of quantities which do not change under gauge tranformation, the so called *gauge-invariant*, that can be built up using these relations:

$$\Psi \equiv A + \mathcal{H}(B - E') + (B - E')'\,, \tag{2.16}$$

$$\Phi \equiv -C - \mathcal{H}(B - E') + \frac{1}{3}\,\nabla^2 E\,, \tag{2.17}$$

known as *Bardeen potentials* [69].

A commonly used gauge is the Newtonian one, defined as:

$$B = 0 = E\,, \tag{2.18}$$

and in this gauge the line element (2.6) becomes:

$$\mathrm{d}s^2 = a^2(\eta)\left[-(1+2\Psi)\mathrm{d}\eta^2 + (1-2\Phi)\delta_{\rm ij}\right]\,. \tag{2.19}$$

2.1.2 Perturbations of Einstein tensor

With the relations (2.19) for the perturbed metric in the Newtonian gauge, we can derive the perturbed equations of the Einstein tensor, defined as:

$$G_{\mu\nu} \equiv R_{\mu\nu} - \frac{1}{2} g_{\mu\nu} R \,. \tag{2.20}$$

Both the Ricci tensor and the Ricci scalar in Eq. (2.20) can be derived from the Riemann tensor:

$$R^{\mu}{}_{\nu\rho\sigma} = \partial_\rho \Gamma^{\mu}_{\nu\sigma} - \partial_\sigma \Gamma^{\mu}_{\nu\rho} + \Gamma^{\lambda}_{\nu\sigma}\Gamma^{\mu}_{\lambda\rho} - \Gamma^{\lambda}_{\nu\rho}\Gamma^{\mu}_{\lambda\sigma} \,, \tag{2.21}$$

that gives:

$$R_{\mu\nu} \equiv R^{\lambda}{}_{\lambda\mu\nu} \,, \tag{2.22}$$
$$R \equiv g^{\mu\nu} R_{\mu\nu} \,. \tag{2.23}$$

Therefore, the components of the Einstein tensor are directly computed from the Christoffel symbol for a given metric:

$$\Gamma^{\rho}_{\mu\nu} \equiv \frac{1}{2} g^{\rho\sigma} \left[\partial_\mu g_{\nu\sigma} \partial_\nu g_{\sigma\mu} - \partial_\sigma g_{\mu\nu} \right] \,. \tag{2.24}$$

Now, from Eq. (2.19) the components of the Christoffel symbol in Newtonian gauge are:

$$\Gamma^{0}_{00} = \mathcal{H} + \Psi' \,, \tag{2.25}$$
$$\Gamma^{0}_{0\mathrm{i}} = \partial_{\mathrm{i}} \Psi \,, \tag{2.26}$$
$$\Gamma^{\mathrm{i}}_{00} = \partial^{\mathrm{i}} \Psi \,, \tag{2.27}$$
$$\Gamma^{0}_{\mathrm{ij}} = \delta_{\mathrm{ij}} \left[\mathcal{H} - 2\mathcal{H}(\Psi + \Phi) - \Phi' \right] \,, \tag{2.28}$$
$$\Gamma^{\mathrm{i}}_{\mathrm{j}0} = \delta^{\mathrm{i}}_{\mathrm{j}} (\mathcal{H} - \Phi') \,, \tag{2.29}$$
$$\Gamma^{\mathrm{i}}_{\mathrm{jk}} = -(\delta^{\mathrm{i}}_{\mathrm{j}} \partial_{\mathrm{k}} \Phi + \delta^{\mathrm{i}}_{\mathrm{k}} \partial_{\mathrm{j}} \Phi) + \delta_{\mathrm{jk}} \partial^{\mathrm{i}} \Phi \,. \tag{2.30}$$

The computation of the components of the Ricci tensor and of the Ricci scalar is quite

easy, so we simply write the main stages:

$$R_{00} = -3\mathcal{H}' + \nabla^2\Psi + 3\mathcal{H}(\Phi' + \Psi') + 3\Phi'' \,, \tag{2.31}$$

$$R_{0\mathrm{i}} = 2\partial_\mathrm{i}\Phi' + 2\mathcal{H}\partial_\mathrm{i}\Psi \,, \tag{2.32}$$

$$\begin{aligned} R_{\mathrm{ij}} = {} & \delta_{\mathrm{ij}}\left[\mathcal{H}' - 2\mathcal{H}'(\Phi + \Psi) - \mathcal{H}\Psi' - 5\mathcal{H}\Phi' - \Phi'' + \nabla^2\Phi + 2\mathcal{H}^2 - 4\mathcal{H}^2(\Phi + \Psi)\right] \\ & + \partial_\mathrm{i}\partial_\mathrm{j}(\Phi - \Psi) \,, \end{aligned} \tag{2.33}$$

$$\begin{aligned} R = {} & g^{00}R_{00} + g^{\mathrm{ij}}R_{\mathrm{ij}} \\ = {} & \frac{1}{a^2}\left[6(\mathcal{H}' + \mathcal{H}^2) - 2\nabla^2\Psi + 4\nabla^2\Phi - 12\Psi(\mathcal{H}' + \mathcal{H}^2) - 6\Phi'' - 6\mathcal{H}(\Psi' + 3\Phi')\right] . \end{aligned} \tag{2.34}$$

We can now derive the components of the Einstein tensor $G_{\mu\nu}$:

$$G_{00} = 3\mathcal{H}^2 + 2\nabla^2\Phi - 6\mathcal{H}\Phi' \,, \tag{2.35}$$

$$G_{0\mathrm{i}} = 2\partial_\mathrm{i}(\Phi' + \mathcal{H}\Psi) \,, \tag{2.36}$$

$$\begin{aligned} G_{\mathrm{ij}} = {} & \delta_{\mathrm{ij}}\left[\nabla^2(\Psi - \Phi) + 2\Phi'' - (2\mathcal{H}' + \mathcal{H}^2) + 2(2\mathcal{H}' + \mathcal{H}^2)(\Phi + \Psi) + 2\mathcal{H}\Psi' + 4\mathcal{H}\Phi'\right] \\ & + \partial_\mathrm{i}\partial_\mathrm{j}(\Phi - \Psi) \,. \end{aligned} \tag{2.37}$$

2.1.3 Perturbations of the energy-momentum tensor

In order to find the first-order perturbation for the EMT for a perfect fluid (1.6), we start by perturbing the relation:

$$\overline{g}_{\mu\nu}\overline{u}^\mu\overline{u}^\nu = -1 \,, \tag{2.38}$$

which gives:

$$0 = \overline{g}_{\mu\nu}(\overline{u}^\mu\delta u^\nu + \overline{u}^\nu\delta u^\mu) + \overline{u}^\mu\overline{u}^\nu\delta g_{\mu\nu} = \overline{u}^\mu\overline{u}^\nu\delta g_{\mu\nu} + 2\,\overline{u}_\mu\delta u^\mu \,. \tag{2.39}$$

Taking into account that the unperturbed 4-velocity is $\overline{u}^\mu = \delta^\mu_0/a$ and the components of the perturbed metric are given by Eq. (2.4), we derive from Eq. (2.39):

$$\delta u^0 = -\frac{A}{a} \,. \tag{2.40}$$

Defining $\delta u^\mathrm{i} = v^\mathrm{i}/a$ we obtain:

$$u^\mu = \frac{1}{a}\left(1 - A,\, v^\mathrm{i}\right) \tag{2.41}$$

The first-order perturbation in $T_{\mu\nu}$ is:

$$\delta T^{\mu}{}_{\nu} = \delta^{\mu}{}_{\nu}\delta p + (\delta p + \delta\rho)\overline{u}^{\mu}\overline{u}_{\nu} + (\overline{p} + \overline{\rho})(\overline{u}^{\mu}\delta u_{\nu} + \overline{u}_{\nu}\delta u^{\mu})\,, \tag{2.42}$$

and, combining with Eq. (2.41), the components read:

$$\delta T^{0}{}_{0} = -\delta\rho\,, \tag{2.43}$$
$$\delta T^{0}{}_{i} = (\overline{\rho} + \overline{p})(v_{\mathrm{i}} + B_{\mathrm{i}})\,, \tag{2.44}$$
$$\delta T^{\mathrm{i}}{}_{0} = -(\overline{\rho} + \overline{p})v^{\mathrm{i}} \equiv -q^{\mathrm{i}}\,, \tag{2.45}$$
$$\delta T^{\mathrm{i}}{}_{\mathrm{j}} = \delta^{\mathrm{i}}_{\mathrm{j}}\,\delta p\,. \tag{2.46}$$

The elements of the full EMT finally are:

$$T_{00} = g_{00}\,T^{0}{}_{0} = a^2(1+2\Phi)\overline{\rho}(1+\delta) = a^2\overline{\rho}(1+\delta+2\Phi)\,, \tag{2.47}$$
$$T_{\mathrm{ii}} = g_{\mathrm{ij}}\,T^{\mathrm{j}}{}_{\mathrm{i}} = a^2\delta_{\mathrm{ij}}(1-2\Phi)\delta^{\mathrm{j}}_{\mathrm{i}}(\overline{p}+\delta p) = a^2(\overline{p}+\delta p-2\Phi)\,, \tag{2.48}$$
$$T_{0\mathrm{i}} = g_{00}T^{0}{}_{\mathrm{i}} = -a^2\,q_{\mathrm{i}}\,, \tag{2.49}$$
$$T_{\mathrm{i}\neq\mathrm{j}} = 0\,. \tag{2.50}$$

As for the metric tensor, we can now find a gauge-invariant quantity in order to describe the perturbations of the EMT. In a new coordinate frame $\tilde{x}^{\mu}$, the EMT trasforms as:

$$\tilde{T^{\mu}}{}_{\nu} = \frac{\partial\tilde{x}^{\mu}}{\partial x^{\alpha}}\,\frac{\partial x^{\beta}}{\partial\tilde{x}^{\nu}}\,T^{\alpha}{}_{\beta}\,. \tag{2.51}$$

Using Eqs. (2.8)-(2.9) the perturbed part of the EMT in the new coordinates frame is:

$$\delta\tilde{T^{\mu}}{}_{\nu} = \delta T^{\mu}{}_{\nu} - \overline{T}^{\mu}{}_{\nu,\gamma}\,\xi^{\gamma} + \overline{T}^{\gamma}{}_{\nu}\,\xi^{\mu}{}_{,\gamma} - \overline{T}^{\mu}{}_{\gamma}\,\xi^{\gamma}{}_{,\nu}\,, \tag{2.52}$$

and we obtain the explicit components:

$$\delta\tilde{\rho} = \delta\rho - \overline{\rho}'\,T\,, \tag{2.53}$$
$$\delta\tilde{p} = \delta p - \overline{p}'\,T\,, \tag{2.54}$$
$$\tilde{q}^{\mathrm{i}} = q^{\mathrm{i}} + (\overline{\rho}+\overline{p})L^{\mathrm{i}}\,, \tag{2.55}$$
$$\tilde{v}^{\mathrm{i}} = v^{\mathrm{i}} + L^{\mathrm{i}}\,. \tag{2.56}$$

We define the *comoving-gauge density perturbation*:

$$\Delta \equiv \delta + \frac{\overline{\rho}'}{\overline{\rho}}(B+v)\,, \tag{2.57}$$

where $\delta \equiv \delta\rho/\bar{\rho}$ is the *density contrast*.

We can now derive for completeness the equations for the evolution of a generic uncoupled species governed by the EMT (1.6), starting from the continuity equation $\nabla_\mu T^\mu{}_\nu = 0$.

From the time-component we obtain:

$$\begin{aligned} 0 &= T^\mu{}_{0,\mu} + \Gamma^\mu_{\alpha\mu} T^\alpha{}_0 - \Gamma^\alpha_{\mu 0} T^\mu{}_\alpha \\ &= -\left[\overline{\rho}' + \delta\rho' + \partial_i q^i + 3(\mathcal{H} - \Phi')(\overline{\rho} + \overline{p}) + 3\mathcal{H}(\delta\rho + \delta p)\right] , \end{aligned} \tag{2.58}$$

which corresponds to the relativistic version of the continuity equation:

$$\delta' + 3\mathcal{H}\delta\left(\frac{\delta P}{\delta\rho} - \frac{\overline{p}}{\overline{\rho}}\right) + \left(1 + \frac{\overline{p}}{\overline{\rho}}\right)\left(\nabla\cdot\boldsymbol{v} - 3\Phi'\right) = 0\,. \tag{2.59}$$

From the spatial-component of the continuity equation:

$$\begin{aligned} 0 &= T^\mu{}_{\mathrm{i},\mu} + \Gamma^\mu_{\alpha\mu} T^\alpha{}_i - \Gamma^\alpha_{\mu\mathrm{i}} T^\mu{}_\alpha \\ &= q_\mathrm{i}' + \partial_\mathrm{i}\delta p + 4q_\mathrm{i}\mathcal{H} + (\overline{\rho} + \overline{p})\partial_\mathrm{i}\Psi\,, \end{aligned} \tag{2.60}$$

which gives:

$$\boldsymbol{v}' + \mathcal{H}\boldsymbol{v} - 3\mathcal{H}\frac{\overline{p}'}{\overline{\rho}'}\boldsymbol{v} + \frac{\nabla\delta p}{\overline{\rho} + \overline{p}} + \nabla\Psi = 0\,. \tag{2.61}$$

Eqs. (2.59)-(2.61) need to be modified for individual components if the components interact with each other. An example is the baryonic fluid which couples to the photons before recombination via Thomson scattering in the so called *tight-coupling approximation*.

For adiabatic primordial perturbations, the equations above simplify since:

$$\delta p = c_\mathrm{s}\delta\rho\,, \tag{2.62}$$

where $c_\mathrm{s}^2 = \mathrm{d}p/\mathrm{d}\rho = w + \rho\mathrm{d}w/\mathrm{d}\rho$ is the *adiabatic speed of sound* squared. Since the photons and the baryons have $w = \text{const}$:

$$\frac{\delta p}{\delta\rho} = w\,. \tag{2.63}$$

2.1.4 Perturbed Einstein equations

Now that we have the perturbed equations for both the Einstein tensor and the EMT, we can write the Einstein equations explicitly.

The time-time component, combining Eq. (2.35) with Eq. (2.47), is:

$$3\mathcal{H}^2 + 2\nabla^2\Phi - 6\mathcal{H}\Phi' = 8\pi G a^2 \overline{\rho}(1 + \delta + 2\Phi)\,. \tag{2.64}$$

We can now split the above equation in the unperturbed zero-order part, which gives the usual FL equation:

$$\mathcal{H}^2 = \frac{8\pi G}{3}\,\overline{\rho} a^2\,, \tag{2.65}$$

and in the perturbed first-oder part:

$$\nabla^2\Phi = 4\pi G a^2 \delta + 3\mathcal{H}(\Phi' + \mathcal{H}\Phi)\,. \tag{2.66}$$

The diagonal space-space components, i.e. $\mathrm{i} = \mathrm{j}$, combining Eq. (2.37) with Eq. (2.48), are:

$$2\Phi'' - (2\mathcal{H}' + \mathcal{H}^2) + 4(2\mathcal{H}' + \mathcal{H}^2)\Phi + 6\mathcal{H}\Phi' = 8\pi G a^2(\overline{p} + \delta p - 2\overline{p}\,\Phi)\,. \tag{2.67}$$

Again, at the unperturbed order we find:

$$2\mathcal{H}' + \mathcal{H}^2 = -8\pi G a^2 \overline{p}\,, \tag{2.68}$$

and at first-oder:

$$\Phi'' + 3\mathcal{H}\Phi' + (2\mathcal{H}' + \mathcal{H}^2)\Phi = 4\pi G a^2 \delta p\,. \tag{2.69}$$

The time-space component, combining Eq. (2.36) with Eq. (2.49), is:

$$\partial_{\mathrm{i}}(\Phi' + \mathcal{H}\Phi) = -4\pi G a^2 q_{\mathrm{i}}\,, \tag{2.70}$$

that we can rewrite after integration, assuming that the potentials are regular at infinity, as:

$$\Phi' + \mathcal{H}\Phi + 4\pi G a^2 v(\overline{\rho} + \overline{p}) = 0\,. \tag{2.71}$$

The non-diagonal space-space components, i.e. $\mathrm{i} \neq \mathrm{j}$, combining Eq. (2.37) with Eq. (2.50), are:

$$\partial_{\mathrm{i}}\partial_{\mathrm{j}}(\Phi - \Psi) = 0\,, \tag{2.72}$$

and assuming again the decaying at infinity, we find that in GR:

$$\Phi = \Psi \,. \tag{2.73}$$

Substituing in Eq. (2.66) Eq. (2.71) and the definition of the comoving-gauge density perturbation (2.57), we can recast this equation:

$$\nabla^2 \Phi = 4\pi G a^2 \overline{\rho} \Delta \,. \tag{2.74}$$

2.2 Curvature perturbation

We now define a new fundamental quantity for later considerations: the *comoving curvature perturbation*.

The Ricci scalar can be expressed for the generic perturbed metric (2.6) on a constant hypersurface as:

$${}^{(3)}R = \frac{1}{a^2}\left[\partial_a(\delta^{\mathrm{ij}}\,{}^{(3)}\Gamma^a_{\mathrm{ij}}) - \partial^{\mathrm{i}}\,{}^{(3)}\Gamma^{\mathrm{a}}_{\mathrm{ia}}\right] , \tag{2.75}$$

from which:

$$a^2\,{}^{(3)}R = -4\nabla^2\left(C - \frac{\nabla^2 E}{3}\right) \equiv 4\nabla^2 \mathcal{K} \,. \tag{2.76}$$

$\mathcal{K}$ is called *curvature perturbation* which allows us to define the comoving curvature perturbation $\mathcal{R}$, the curvature perturbation in the *comoving gauge*, characterized by $B^{\mathrm{i}} = 0 = q^{\mathrm{i}}$.

We manipulate $\mathcal{R}$ by adding a linear combination of B and q, that vanish in the comoving gauge, in order to build a gauge-invariant quantity:

$$\mathcal{R} \equiv -C + \frac{\nabla^2 E}{3} - \mathcal{H}(B + v) \,. \tag{2.77}$$

The comoving curvature perturbartion in Newtonian gauge, by appling the condition (2.18), is:

$$\mathcal{R} = \Psi - \mathcal{H} v \,. \tag{2.78}$$

Thanks to the Einstein Eq. (2.71) and to the FL Eq. (1.7), we rewrite the comoving curvature perturbation into:

$$\begin{aligned} \mathcal{R} &= \Psi + \mathcal{H}\,\frac{2(\Psi' + \mathcal{H}\Psi)}{3\mathcal{H}^2(1+w)} \\ &= \Psi + \frac{2}{3}\,\frac{\Psi' + \mathcal{H}\Psi}{\mathcal{H}(1+w)} \,. \end{aligned} \tag{2.79}$$

2.3 The Mukhanov equation

We can now apply the formulation of relativistic perturbation theory to a scalar field model. In particular, we consider the generic scalar Lagrangian:

$$\mathcal{L} = P(\chi, \phi)\,, \tag{2.80}$$

where χ is defined as the standard kinetic term:

$$\chi \equiv -\frac{1}{2} g^{\mu\nu} \partial_\mu \phi \, \partial_\nu \phi\,. \tag{2.81}$$

The EMT for this Lagrangian is:

$$\begin{aligned} T_{\mu\nu} =& -\frac{\delta P}{\delta \partial^\mu \phi} \partial_\nu \phi + g_{\mu\nu} P\,, \\ =& g_{\mu\nu} P + P_{,\chi} \partial_\mu \phi \partial_\nu \phi\,, \end{aligned} \tag{2.82}$$

from which we recover the standard expression for the perfect fluid (1.6) by identifying:

$$p = P(\chi, \phi)\,, \tag{2.83}$$

$$\rho = 2\chi P_{,\chi} - P\,, \tag{2.84}$$

$$u_\mu = \frac{\partial_\mu \phi}{\sqrt{2\chi}}\,. \tag{2.85}$$

We perturb the scalar field as:

$$\phi(\eta, \boldsymbol{x}) = \overline{\phi}(\eta) + \delta\phi(\eta, \boldsymbol{x})\,, \tag{2.86}$$

so that the kinetic term in Newtonian gauge becomes:

$$\begin{aligned} \chi &= -\frac{1}{2} g^{\mu\nu} \partial_\mu \overline{\phi} \, \partial_\nu \overline{\phi} - g^{\mu\nu} \partial_\mu \overline{\phi} \, \partial_\nu \delta\phi \\ &= -\frac{1}{2} g^{00} \overline{\phi}'^2 - g^{00} \overline{\phi}' \delta\phi' \\ &= \frac{1}{a^2} \left(\frac{\overline{\phi}'^2}{2} + \overline{\phi}' \delta\phi' - \overline{\phi}'^2 \Psi \right) \equiv \overline{\chi} + \delta\chi\,, \end{aligned} \tag{2.87}$$

and the first-order perturbation of the kinetic term is:

$$\delta\chi = \frac{1}{a^2} \left(\overline{\phi}' \delta\phi' - \overline{\phi}'^2 \Psi \right) = 2\overline{\chi} \left(\frac{\delta\phi'}{\overline{\phi}'} - \Psi \right)\,. \tag{2.88}$$

For the EMT, since we are dealing with a perfect fluid, we have:

$$\delta T^0{}_0 = -\delta\rho\,, \tag{2.89}$$

that can be calculated as:

$$\begin{aligned}
\delta\rho &= \rho_{,\chi}\delta\chi + \rho_{,\phi}\delta\phi = \rho_\chi\left(\delta\chi - \overline{\chi}'\,\frac{\delta\phi}{\overline{\phi}'}\right) - 3\,\mathcal{H}(P+\rho)\frac{\delta\phi}{\overline{\phi}'} \\
&= \frac{P+\rho}{c_\mathrm{s}^2}\left(\frac{\delta\phi'}{\overline{\phi}'} - \Psi - \frac{\overline{\phi}''}{\overline{\phi}'^2}\,\delta\phi + \mathcal{H}\,\frac{\delta\phi}{\overline{\phi}'}\right) - 3\,\mathcal{H}(P+\rho)\frac{\delta\phi}{\overline{\phi}'} \\
&= \frac{P+\rho}{c_\mathrm{s}^2}\left[\frac{\mathrm{d}}{\mathrm{d}\tau}\left(\frac{\delta\phi}{\overline{\phi}'}\right) + \mathcal{H}\,\frac{\delta\phi}{\overline{\phi}'} - \Psi\right] - 3\,\mathcal{H}(P+\rho)\frac{\delta\phi}{\overline{\phi}'}\,,
\end{aligned} \tag{2.90}$$

where we used Eq. (1.40) which defines the speed of sound.

The expression for $\delta T^0{}_\mathrm{i}$, instead, is simpler to be derived:

$$\begin{aligned}
T^0{}_\mathrm{i} &= -\frac{1}{a^2}(1-2\Psi)(P+\rho)u_0 u_\mathrm{i} \\
&= -\frac{1}{a^2}(1-2\Psi)(P+\rho)\frac{\partial_0\phi\,\partial_\mathrm{i}\phi}{2\chi} \\
&= -\frac{1}{a^2}(P+\rho)\frac{\overline{\phi}'\,\partial_\mathrm{i}\delta\phi}{2\overline{\chi}} \\
&= -(P+\rho)\frac{\partial_\mathrm{i}\delta\phi}{\overline{\phi}'} \\
&= \delta T^0{}_\mathrm{i}\,.
\end{aligned} \tag{2.91}$$

Since it is first-order in perturbations, and comparing with Eq. (2.45) we find:

$$v = -\frac{\delta\phi}{\overline{\phi}'}\,, \tag{2.92}$$

and then from Eq. (2.78):

$$\mathcal{R} = \Psi + \mathcal{H}\frac{\delta\phi}{\overline{\phi}'}\,. \tag{2.93}$$

Now, combining the Eqs. (2.35)-(2.36)-(2.37), previously calculated for the Einstein tensor, with the Eqs. (2.89)-(2.91), for the EMT of the Lagrangian (2.80), we just obtain the Einstein equations.

The non-diagonal space-space components, i.e. $\mathrm{i} \neq \mathrm{j}$, are again:

$$\partial_{\mathrm{i}}\partial_{\mathrm{j}}(\Phi - \Psi) = 0\,, \tag{2.94}$$

and assuming the regularity of the potentials:

$$\Phi = \Psi\,. \tag{2.95}$$

If the potentials are sufficiently regular, and so allow us to drop their spatial derivatives, the time-space components become:

$$\Psi' + \mathcal{H}\Psi = 4\pi G a^2 (P+\rho)\frac{\delta\phi}{\overline{\phi}'}\,, \tag{2.96}$$

which can be written in the equivalent form:

$$\frac{\mathrm{d}}{\mathrm{d}\tau}\left(\frac{a^2\Psi}{\mathcal{H}}\right) = \frac{4\pi G a^4 (P+\rho)}{\mathcal{H}^2}\left(\mathcal{H}\frac{\delta\phi}{\overline{\phi}'} + \Psi\right)\,. \tag{2.97}$$

The time-time component, at first-order in perturbation theory is:

$$\begin{aligned}\nabla^2\Psi - 3\mathcal{H}\left(\Psi' + \mathcal{H}\Psi\right) &= \nabla^2\Psi - \cancel{12\mathcal{H}\pi G a^2 (P+\rho)\frac{\delta\phi}{\overline{\phi}'}} \\ &= 4\pi G a^2\left\{\frac{P+\rho}{c_{\mathrm{s}}^2}\left[\frac{\mathrm{d}}{\mathrm{d}\tau}\left(\frac{\delta\phi}{\overline{\phi}'}\right) + \mathcal{H}\frac{\delta\phi}{\overline{\phi}'} - \Psi\right] - \cancel{3\,\mathcal{H}(P+\rho)\frac{\delta\phi}{\overline{\phi}'}}\right\}\,,\end{aligned} \tag{2.98}$$

and using again (2.96) together with Eq. (1.7b):

$$\begin{aligned}\nabla^2\Psi &= \frac{4\pi G a^2(P+\rho)}{c_{\mathrm{s}}^2}\left[\frac{\mathrm{d}}{\mathrm{d}\tau}\left(\frac{\delta\phi}{\overline{\phi}'}\right) + \mathcal{H}\frac{\delta\phi}{\overline{\phi}'} - \Psi\right] \\ &= \frac{4\pi G a^2(P+\rho)}{\mathcal{H}c_{\mathrm{s}}^2}\left[\mathcal{H}\frac{\mathrm{d}}{\mathrm{d}\tau}\left(\frac{\delta\phi}{\overline{\phi}'}\right) + \Psi' + \mathcal{H}'\frac{\delta\phi}{\overline{\phi}'}\right] \\ &= \frac{4\pi G a^2(P+\rho)}{\mathcal{H}c_{\mathrm{s}}^2}\frac{d}{d\tau}\left[\mathcal{H}\frac{\delta\phi}{\overline{\phi}'} + \Psi\right] \\ &= \frac{4\pi G a^2(P+\rho)}{\mathcal{H}c_{\mathrm{s}}^2}\mathcal{R}'\,,\end{aligned} \tag{2.99}$$

this relation, thanks to the Friedmann equations, can be rewritten in Fourier space as:

$$\frac{3}{2}(1+w)\mathcal{R}'_{\boldsymbol{k}} = -\frac{c_{\mathrm{s}}^2 k^2}{\mathcal{H}}\,\Psi_{\boldsymbol{k}}\,. \tag{2.100}$$

This equation is fundamental, since it ensures that on super-horizon scales (i.e. with $k \ll \mathcal{H}$) the comoving curvature perturbation is almost constant (it is *frozen*).

Another set of useful variables is:

$$z \equiv \frac{a^2\sqrt{P+\rho}}{\mathcal{H}c_\mathrm{s}}\,, \tag{2.101}$$

$$\theta \equiv \frac{1}{zc_\mathrm{s}} = \frac{\mathcal{H}}{a^2\sqrt{P+\rho}}\,, \tag{2.102}$$

and:

$$v \equiv z\mathcal{R} = \frac{a^2\sqrt{P+\rho}}{\overline{\phi}'c_\mathrm{s}}\left(\delta\phi + \frac{\overline{\phi}'}{\mathcal{H}}\Psi\right)\,, \tag{2.103}$$

$$u \equiv \frac{\Psi}{4\pi\sqrt{P+\rho}}\,, \tag{2.104}$$

where Eq. (2.103) is the *Mukhanov variable* [70, 71]. With these quantities, the two Einstein's equations (2.96)-(2.99) become:

$$\nabla^2 u = \frac{z}{c_\mathrm{s}}\left(\frac{v}{z}\right)'\,, \tag{2.105}$$

$$v = \frac{\theta}{c_\mathrm{s}}\left(\frac{u}{\theta}\right)'\,, \tag{2.106}$$

that combined give in Fourier space:

$$v_{\boldsymbol{k}}'' + \left(c_\mathrm{s}^2k^2 - \frac{z''}{z}\right)v_{\boldsymbol{k}} = 0\,, \tag{2.107}$$

which is the *generalized Mukhanov equation* [70, 71].

2.4 Spectrum of curvature perturbation

We now quantize the Mukhanov variable v, introduced in the previous section. The results obtained recall the standard quantization of the harmonic oscillator (see for instance Ref. [72]).

To quantize the system, we promote v and its canonical momentum $\pi \equiv \delta\mathcal{L}/\delta v = v'$ to operators $\hat{v}$ and $\hat{\pi}$, and impose the usual commutation relations:

$$[\hat{v}(\eta,\mathbf{x}),\hat{\pi}(\eta,\mathbf{y})] = \imath\delta_\mathrm{D}^{(3)}(\mathbf{x}-\mathbf{y}))\,, \tag{2.108}$$

$$[\hat{v}(\eta,\mathbf{x}),\hat{v}(\eta,\mathbf{y})] = 0\,, \tag{2.109}$$

$$[\hat{\pi}(\eta,\mathbf{x}),\hat{\pi}(\eta,\mathbf{y})] = 0\,. \tag{2.110}$$

By writing in Fourier space we have:

$$\hat{v}_{\mathbf{k}} = v_{\mathbf{k}}\hat{a}_{\mathbf{k}} + v^{*}_{\mathbf{k}}\hat{a}^{\dagger}_{\mathbf{k}}\,, \tag{2.111}$$

where the annihilation and creation operators satisfy the commutation relation:

$$\left[\hat{a}_{\mathbf{k}}, \hat{a}^{\dagger}_{\mathbf{k}'}\right] = (2\pi)^3\delta^{(3)}_{\mathrm{D}}(\mathbf{k}-\mathbf{k}')\,, \tag{2.112}$$

$$[\hat{a}_{\mathbf{k}}, \hat{a}_{\mathbf{k}'}] = 0\,, \tag{2.113}$$

$$\left[\hat{a}^{\dagger}_{\mathbf{k}}, \hat{a}^{\dagger}_{\mathbf{k}'}\right] = 0\,, \tag{2.114}$$

plus the condition on the mode functions $W[v_{\mathbf{k}}, v'_{\mathbf{k}}] = \imath$. It is useful to express the time-dependent frequency of Eq. (2.107):

$$\omega^2_k(\eta) = c^2_{\mathrm{s}}k^2 - \frac{z''}{z}\,, \tag{2.115}$$

in terms of the HFFs recasting z as:

$$z = \frac{aM_{\mathrm{pl}}}{c_{\mathrm{s}}}\sqrt{2\epsilon_1}\,. \tag{2.116}$$

The result of the exact expression is:

$$\frac{z''}{z} = a^2H^2\left[2-\epsilon_1+\frac{3\epsilon_2}{2}-3s-\frac{\epsilon_1\epsilon_2}{2}+\epsilon_1 s-\epsilon_2 s+\frac{{\epsilon_2}^2}{4}+s^2+\frac{\epsilon_2\epsilon_3}{2}-\frac{\dot{s}}{H}\right]. \tag{2.117}$$

We now look for a solution for the Mukhanov equation during a phase of slow-roll, with a constant speed of sound. At first-order in HFFs, we have:

$$\begin{aligned}\frac{z''}{z} &\approx a^2H^2\left[2-\epsilon_1+\frac{3\epsilon_2}{2}\right]\\ &\approx \frac{1}{\eta^2}\left[2-\epsilon_1+\frac{3\epsilon_2}{2}\right] = \frac{\nu^2-1/4}{\eta^2}\,,\end{aligned} \tag{2.118}$$

where we used $aH \simeq -1/(1-\epsilon_1)\eta$ [73]. The Eq. (2.107) admits, for ϵ_1 almost constant, the solution:

$$v_{\boldsymbol{k}}(\eta) \equiv -\frac{\sqrt{-\pi\eta}}{2}\left[\alpha_k H^{(1)}_{\nu}(-c_{\mathrm{s}}k\eta) + \beta_k H^{(2)}_{\nu}(-c_{\mathrm{s}}k\eta)\right], \tag{2.119}$$

where $H^{(1,2)}_{\nu}(x)$ are the Hankel functions of the first and second kind [74], with α_k and β_k the *Bogoliubov coefficients*. Here we defined $x \equiv -c_{\mathrm{s}}k\eta$.

At sufficiently early times, all the modes where deep inside the horizon, which means that $k \gg aH = \mathcal{H}$, which correnspponds to $|k\eta| \gg 1$. Since for a quasi de Sitter expansion $\eta = -1/aH$, in the inflationary slow-roll scenario, early times correspond to infinite negative conformal time. Thus, at zero-order in HFF, in the remote past:

$$\omega_k^2 \approx c_\mathrm{s}^2 k^2 - \frac{2}{\eta^2} \xrightarrow{\eta \to -\infty} c_\mathrm{s}^2 k^2 \,, \tag{2.120}$$

where Eq. (2.117) for slowly varying slow-roll parameters has been used.

In this limit, the Mukhanov equation (2.107) has two independent solutions $v_{\boldsymbol{k}} \propto e^{\pm i c_\mathrm{s} k \eta}$; however, we can consider only the growing mode $v_{\boldsymbol{k}} \propto e^{-i c_\mathrm{s} k \eta}$.

To get an explicit expression for such a mode, we exploit the normalization condition on the Wronskian, i.e. $W[v, v'] = 1$. As a consequence, we find out that at very early times:

$$v_{\boldsymbol{k}}(\eta) = \frac{e^{-i c_\mathrm{s} k \eta}}{\sqrt{2 c_\mathrm{s} k}} \,. \tag{2.121}$$

This defines a preferable set of mode function and a unique vacuum, called *Bunch-Davies vacuum* [75]. Eq. (2.121) is nothing but a plane wave which propagates in Minkowski space-time.

Imposing the Bunch-Davies vacuum solution at early times, at first-order in HFFs we find:

$$v_{\boldsymbol{k}}(\eta) = -\frac{\sqrt{-\pi\eta}}{2} H_\nu^{(1)}(-c_\mathrm{s} k \eta) \,. \tag{2.122}$$

For $\nu = 3/2$ we fall into the de Sitter solution and then:

$$\begin{aligned} v_{\boldsymbol{k}}(\eta) &= \frac{-i}{\sqrt{2k^3 c_\mathrm{s}^3}} \frac{1 + i c_\mathrm{s} k \eta}{\eta} e^{-i c_\mathrm{s} k \eta} \\ &= \frac{e^{-i c_\mathrm{s} k \eta}}{\sqrt{2 c_\mathrm{s} k}} \left(1 - \frac{i}{c_\mathrm{s} k \eta}\right) . \end{aligned} \tag{2.123}$$

Now that we have an expression for $v_{\mathbf{k}}$, we are able to define a quantity which will become fundamental later: the *primordial power spectrum of curvature perturbation* (PPS).

The two-point correlation function of $\hat{v}_{\mathbf{k}}$ is defined in terms of the power spectrum

as:

$$\begin{aligned}\langle\hat{v}_{\mathbf{k}}\hat{v}_{\mathbf{k}'}\rangle &\equiv \langle 0|\left(v_{\mathbf{k}}(\eta)a_{\mathbf{k}}+v^{*}_{\mathbf{k}}(\eta)a^{\dagger}_{\mathbf{k}}\right)\left(v_{\mathbf{k}'}(\eta)a_{\mathbf{k}'}+v^{*}_{\mathbf{k}'}(\eta)a^{\dagger}_{\mathbf{k}'}\right)|0\rangle \\ &= v_{\mathbf{k}}v^{*}_{\mathbf{k}'}\langle 0|a_{\mathbf{k}}a^{\dagger}_{\mathbf{k}}|0\rangle \\ &= v_{\mathbf{k}}v^{*}_{\mathbf{k}'}\langle 0|\left[a_{\mathbf{k}},a^{\dagger}_{\mathbf{k}}\right]|0\rangle \\ &= (2\pi)^{3}\delta^{(3)}_{\mathrm{D}}(\mathbf{k}-\mathbf{k}')|v_{\mathbf{k}}|^{2} \\ &\equiv P_{v}(k)\,(2\pi)^{3}\delta_{\mathrm{D}}(\mathbf{k}-\mathbf{k}')\,, \end{aligned} \tag{2.124}$$

and the power spectrum for the curvature perturbations is:

$$P_{\mathcal{R}}(k)\equiv\langle\hat{\mathcal{R}}_{\mathbf{k}}\hat{\mathcal{R}}_{\mathbf{k}'}\rangle=\frac{P_{v}(k)}{z^{2}}\,. \tag{2.125}$$

It is also useful to define a *dimensionless power spectrum* $\mathcal{P}_{\mathcal{R}}(k)$ as:

$$\mathcal{P}_{\mathcal{R}}(k)\equiv\frac{k^{3}}{2\pi^{2}}\,P_{\mathcal{R}}(k)=\frac{k^{3}}{2\pi^{2}}\,|\mathcal{R}_{\boldsymbol{k}}|^{2}\,. \tag{2.126}$$

From Eq. (2.123) we find:

$$\mathcal{P}_{\mathcal{R}}(k)=\frac{H^{2}}{8\pi^{2}M^{2}_{\mathrm{pl}}\epsilon_{1}c_{\mathrm{s}}}\left[1+\left(\frac{c_{\mathrm{s}}k}{aH}\right)^{2}\right]\xrightarrow{k\eta\ll 1}\frac{H^{2}}{8\pi^{2}M^{2}_{\mathrm{pl}}\epsilon_{1}c_{\mathrm{s}}}\,. \tag{2.127}$$

Since we know that on super-horizon scales the comoving curvature perturbation $\mathcal{R}$, and consequently the power spectrum, are almost constant, the latter equation can be evaluated at horizon crossing, i.e. $k=aH$.

At the horizon crossing the PPS is purely a function of k. Hence, the simplest way to parametrize the PPS, taking into account a slight deviation from scale-invariance, is:

$$\mathcal{P}_{\mathcal{R}}(k)\equiv A_{\mathrm{s}}\left(\frac{k}{k_{*}}\right)^{n_{\mathrm{s}}-1}\,, \tag{2.128}$$

where k_{*} is a reference scale, n_{s} is called *scalar spectral index*, and the amplitude is given by:

$$A_{\mathrm{s}}=\frac{H^{2}}{8\pi^{2}M^{2}_{\mathrm{pl}}\epsilon_{1}c_{\mathrm{s}}}\,. \tag{2.129}$$

If $n_{\rm s}$ has no wavelength dependence, i.e. no running, it can be determined as:

$$\begin{aligned} n_{\rm s} - 1 &= \frac{{\rm d}\ln \mathcal{P}_{\mathcal{R}}}{{\rm d}\ln k} \\ &= \frac{{\rm d}\ln \mathcal{P}_{\mathcal{R}}}{{\rm d}N}\frac{{\rm d}N}{{\rm d}\ln k} \\ &= \left(2\frac{{\rm d}\ln H}{{\rm d}N} - \frac{{\rm d}\ln \epsilon_1}{{\rm d}N} - \frac{{\rm d}\ln c_{\rm s}}{{\rm d}N}\right)\frac{{\rm d}N}{{\rm d}\ln k} \\ &= (-2\epsilon_1 - \epsilon_2 - s)\frac{{\rm d}N}{{\rm d}\ln k} \\ &= (-2\epsilon_1 - \epsilon_2 - s)\left[\frac{\rm d}{{\rm d}N}(N + \ln H)\right]^{-1} \\ &\approx (-2\epsilon_1 - \epsilon_2 - s)(1 + \epsilon_1) \\ &\approx (-2\epsilon_1 - \epsilon_2 - s)\,, \end{aligned} \tag{2.130}$$

from which it is clear that the slow-roll parameters are responsible for the deviation from scale invariance.

2.5 Tensor modes

The same formalism for the scalar fluctuations can be applied to compute the quantum generation of tensor perturbations.

In Fourier space, a symmetric, transverse, and traceless tensors can be written:

$$h_{\rm ij}(\eta, \mathbf{x}) = \int {\rm d}^3k \sum_{\gamma=+,\times} \epsilon^{\gamma}_{\rm ij}(k) h_{\mathbf{k},\gamma}(\eta) e^{\imath \mathbf{k}\cdot\mathbf{x}}\,, \tag{2.131}$$

where $\epsilon^{\alpha}_{\rm ij} = \epsilon^{\alpha}_{\rm ji}$, $\epsilon^{\alpha}_{\rm ii} = k^{\rm i}\epsilon^{\alpha}_{\rm ij} = 0$, and $\epsilon^{\alpha}_{\rm ij}\epsilon^{\beta}_{\rm ij} = 2\delta_{\alpha\beta}$.

From Einstein equation, it can be shown that each polarization state of GWs satisfy: it can be show that $h_{\mathbf{k},\gamma}$, satisfy the equations:

$$v''_{\mathbf{k},\gamma} + \left(k^2 - \frac{a''}{a}\right) v_{\mathbf{k},\gamma} = 0 \tag{2.132}$$

where we have adopted the normalization for the tensor mode function $v_{\mathbf{k},\gamma} \equiv aM_{\rm pl}h_{\mathbf{k},\gamma}/2$. Eq. (2.132) is the same as the Mukhanov equation with $z''/z \to a''/a$ and $c_{\rm s} = 1$. For this reason, we do not repeat here the full calculation, but we only present the main results.

In analogy with what we have done in the previous section, the quantity a''/a can be recast as:

$$\begin{aligned}\frac{a''}{a} &= \frac{1}{\eta^2}(2+3\epsilon_1) \\ &= \frac{4\nu_t - 1}{4\eta^2}\,,\end{aligned} \tag{2.133}$$

where $\nu_t \equiv \epsilon_1 + 3/2$. Therefore, the solution $\tilde{v}_{\mathbf{k}}$ is the same for both the polarizations, and it is equal to (2.122), with the substitutions $c_{\rm s} \to 1$ and $\nu \to \nu_t$.

The dimentionless power spectrum $\mathcal{P}_h(k)$ on superhorizon scales, at the leading order in HFFs, is:

$$\begin{aligned}\mathcal{P}_h(k) &\equiv \frac{k^3}{2\pi^2}|h_{\rm ij}(\boldsymbol{k})|^2 \\ &= \frac{k^3}{2\pi^2}\sum_{\alpha,\beta} e^{\alpha}_{\rm ij} e^{\beta\,*}_{\rm ij}\, v_{\mathbf{k},\alpha} v^*_{\mathbf{k},\beta} \\ &= \frac{k^3}{2\pi^2}\, 4|\tilde{v}_{\boldsymbol{k}}|^2\, \frac{2}{a^2 M_{\rm pl}^2} \\ &\approx \frac{2H^2}{\pi^2 M_{\rm pl}^2}\,.\end{aligned} \tag{2.134}$$

Assuming a power-law spectrum for GWs:

$$\mathcal{P}_h(k) \equiv A_{\rm t}\left(\frac{k}{k_*}\right)^{n_{\rm t}}\,, \tag{2.135}$$

where the *tensor spectral index* is given by:

$$n_{\rm t} \equiv \frac{{\rm d}\ln \mathcal{P}_h}{{\rm d}\ln k} = 2\frac{\dot{H}}{H^2}(1+\epsilon_1) \approx -2\epsilon_1\,, \tag{2.136}$$

and the amplitude by:

$$A_{\rm t} = \frac{2H^2}{\pi^2 M_{\rm pl}^2}\,. \tag{2.137}$$

In the case of tensor perturbations, the scale invariance is characterized by $n_{\rm t} = 0$, since $\epsilon_1 \to 0$.

For single-field inflationary models, an important quantity is the so called *tensor-to-scalar ratio* (the ratio of the GW amplitude to that of the scalar curvature fluctuations at a given pivot scale $k_* = 0.05$ Mpc^{-1}), which is defined as

$$r \equiv \frac{A_{\rm t}}{A_{\rm s}} \,. \tag{2.138}$$

Combining Eqs. (2.129) and (2.137), the so called consistency condition between the tensor-to-scalar ratio and the tensor spectral index holds:

$$r \approx 16\epsilon_1 \,, \tag{2.139}$$

$$\approx -8 n_{\rm t} \,. \tag{2.140}$$

The above relation holds to first order in the slow-roll parameters, and a modified one is needed to second order. When the inflaton has non-trivial speed of sound, the first order consistency condition in (2.139) is modified as:

$$r \approx 16 c_{\rm s} \epsilon_1 \,. \tag{2.141}$$

2.6 Predictions for selected inflationary models

In the following we derive and discuss the predictions for a selection of slow-roll inflationary models [44]. Given the relation between the number of e-folds during inflation and the post-inflationary expansion, the values of $n_{\rm s}$ and r, relevant for the CMB measurements, are given for choice of inflationary models. The theoretical uncertainty in the number of e-folds is important at a quantitative level and needs therefore to be taken into account.

In order to better connect the physics of the model to Eq. (1.55) it is useful to rewrite the third term on the rhs as:

$$\begin{aligned}
\frac{\rho(k)}{M_{\rm pl}^4 \rho_{\rm end}} &= \frac{3V(k)}{3-\epsilon_1(k)} \frac{3-\epsilon_1^{\rm end}}{3V_{\rm end}} \frac{1}{M_{\rm pl}^4} \\
&= \frac{3}{3-\epsilon_1(k)} H^2(k) \left[3-\epsilon_1(k)\right] M_{\rm pl}^2 \frac{3-\epsilon_1^{\rm end}}{3V_{\rm end}} \frac{1}{M_{\rm pl}^4} \\
&= \frac{H^2(k)}{M_{\rm pl}^2 V_{\rm end}} (3-\epsilon_1^{\rm end}) \\
&= \frac{8\pi^2 \epsilon_1(k) A_{\rm s}}{V_{\rm end}} (3-\epsilon_1^{\rm end}) \,,
\end{aligned} \tag{2.142}$$

where $\epsilon_1(k) \equiv \epsilon_1(\phi(k))$ or $\epsilon_1(N(k))$, and plugging Eq. (2.142) in Eq. (1.55) we obtain the final expression [76, 77]:

$$N(k) = 66.9 - \ln\left(\frac{k}{a_0 H_0}\right) - \frac{1}{12}\ln\left(g_{\rm reh}\right) + \frac{1}{4}\ln\left(8\pi^2 A_{\rm s}\epsilon_1\right) - \frac{1-3w_{\rm reh}}{4}N_{\rm reh} + \frac{1}{4}\ln\left(\frac{3-\epsilon_1^{\rm end}}{V_{\rm end}}\right) . \tag{2.143}$$

The last term in Eq. (1.55) is usually calculated by assuming $\epsilon_1^{\rm end} = 1$ but there are few exception where this condition does not hold. For example, in *hybrid inflation* the shape of the inflaton potential can be decoupled from the exit from inflation thanks to a second field ψ. For small values of the inflaton field ϕ, the waterfall field ψ becomes tachyonic ($m_\psi < 0$) and ends inflation when $\epsilon_1(\phi) < 1$. However, these models are ruled out from *Planck* data in large portion of the parameters space [43].

2.6.1 Power-law potentials

We first investigate the class of inflationary models with a single monomial potential [40]:

$$V(\phi) = \lambda M_{\rm pl}^4 \left(\frac{\phi}{M_{\rm pl}}\right)^n , \tag{2.144}$$

where n is positive, and λ dimensionless. The HFFs are:

$$\epsilon_1 = \frac{n^2}{2x^2} , \tag{2.145}$$

$$\epsilon_2 = \frac{2n}{x^2} , \tag{2.146}$$

$$\epsilon_3 = \epsilon_2 , \tag{2.147}$$

where $x = \phi/M_{\rm pl}$. The inflation ends with the violation of the first slow-roll condition (1.30) at:

$$x_{\rm end} = \frac{n}{\sqrt{2}} , \tag{2.148}$$

which means $\phi_{\rm end} \sim M_{\rm pl}$, after which ϕ starts to oscillate around its vacuum expectation value (VEV) $\phi = 0$. In this class of models, so called *large-field inflation*, inflation occurs for large values of the inflaton $\phi > M_{\rm pl}$.

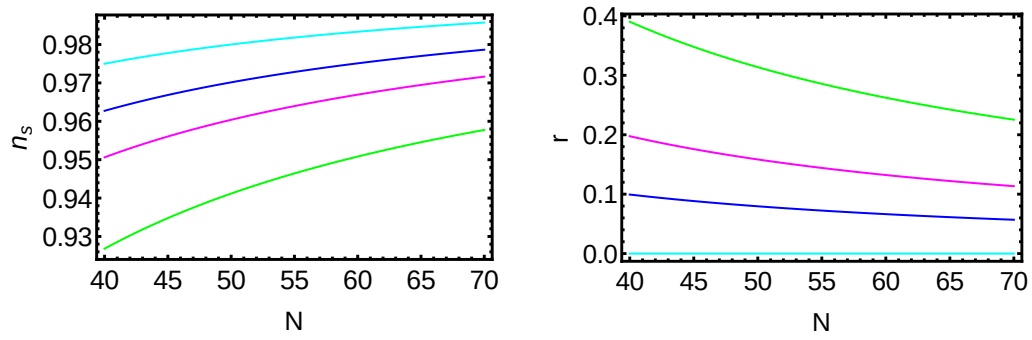

Figure 2.1: Predictions for the scalar spectral index $n_{\rm s}$ (left panel) and for the tensor-to-scalar ratio r (right panel) as function of the number of e-folds N for power-law potentials in Eq. (2.144). Different lines represent different values of n; $n = 0$ (cyan line), $n = 1$ (blue line), $n = 2$ (magenta line), and $n = 4$ (green line).

The predictions for the scalar spectral index and for the tensor-to-scalar ratio at first order in the slow-roll approximation are (see Fig. 2.1):

$$n_{\rm s} - 1 \approx -\frac{2(n+2)}{4N+n}\,, \tag{2.149a}$$

$$r \approx \frac{16n}{4N+n}\,. \tag{2.149b}$$

2.6.2 Hilltop models

In *hilltop models* [78], with potential:

$$V(\phi) \approx \Lambda^4 \left(1 - \frac{\phi^p}{\mu^p} + ...\right)\,, \tag{2.150}$$

the inflaton rolls away from an unstable equilibrium, like in the first new inflationary model [36, 38]. In Eq. (2.150) the dots indicate the effect of higher powers, which are supposed to be suppressed or to come in after the scales leave the horizon. The Eq. (2.150) is not complete close to the minimum of the potential.

The HFFs are:

$$\epsilon_1 \simeq \left(\frac{pM_{\rm pl}}{\sqrt{2}\mu}\frac{x^{p-1}}{1-x^p}\right)^2 , \tag{2.151}$$

$$\epsilon_2 \simeq 2p\left(\frac{M_{\rm pl}}{\mu}\right)^2 x^{p-2}\frac{p-1+x^p}{(1-x^p)^2} , \tag{2.152}$$

$$\epsilon_3 \simeq p\left(\frac{M_{\rm pl}}{\mu}\right)^2 x^{p-2}\frac{2x^{2p}+(p-1)(p+4)x^p+(p-1)(p-2)}{(1-x^p)^2(p-1+x^p)} , \tag{2.153}$$

where $x = \phi/\mu$, the predictions for the scalar spectral index and the tensor-to-scalar ratio at first order in the slow-roll approximation are:

$$n_{\rm s} - 1 \approx -2p(p-1)\left(\frac{M_{\rm pl}}{\mu}\right)^2 \frac{x^{p-2}}{1-x^p} - \frac{3r}{8} , \tag{2.154a}$$

$$r \approx 8p^2\left(\frac{M_{\rm pl}}{\mu}\right)^2 \frac{x^{2p-2}}{(1-x^p)^2} . \tag{2.154b}$$

In general, the trajectory cannot be analytically inverted to give the field value of $x(N)$ but we can find an exact solution for almost all integer values of p.

This class of potentials has two distinct branches: the small field scenario, when inflation occurs at $\mu \ll$, and the large field limit, when inflation occurs with $\phi \sim \mu$ and the potential can be approximated as $V(\phi) \propto \phi$, for each values of p. We consider in detail the specific cases with $p = 2$ and $p = 4$.

$\underline{p = 2}$. We choose the origin $\phi = 0$ to be a maximum of the potential with $V(\phi)$ decreasing smoothly to a minimum value of $V = 0$. Inflation with such a potential was first discussed in Ref. [79].

In the small-field limit, i.e. $\mu \ll M_{\rm pl}$, we have:

$$x_{\rm end}|_{p=2} = \frac{M_{\rm pl}}{\sqrt{2}\mu}\left[\sqrt{1+2\left(\frac{\mu}{M_{\rm pl}}\right)^2} - 1\right] , \tag{2.155}$$

$$\simeq \frac{M_{\rm pl}}{\sqrt{2}\mu} , \tag{2.156}$$

and:

$$n_{\rm s} - 1 \approx -4\frac{M_{\rm pl}^2}{\mu^2} - \frac{r}{8} , \tag{2.157a}$$

$$r \approx 16e^{-4M_{\rm pl}^2 N/\mu^2} . \tag{2.157b}$$

A *double-well potential* or a *symmetry breaking potential* $V(\phi) = \Lambda^4[1 - \phi^2/(\mu^2)]^2$ [80] can be considered as a self-consistent completion of the hilltop model with $p = 2$ in the small-field limit. However, for $\mu \gg M_{\rm pl}$ the *double-well potential* approaches $V(\phi) \propto \phi^2$.

$p = 4$. This case correnspond to the original new inflation model [38] when the symmetry $\phi \to -\phi$ and $\phi_{\rm end} \ll M_{\rm pl}$ are satisfied in order to suppress all the other terms in a power-series expansion of Eq. (2.150).

In the small-field limit we have:

$$x_{\rm end}|_{p=4} \simeq \left(\frac{\mu}{2\sqrt{2}M_{\rm pl}}\right)^{1/3}, \tag{2.158}$$

and:

$$n_{\rm s} - 1 \approx -\frac{3}{N} - \frac{r}{8}, \tag{2.159a}$$

$$r \approx \frac{1}{4N^3}\left(\frac{\mu}{M_{\rm pl}}\right)^4. \tag{2.159b}$$

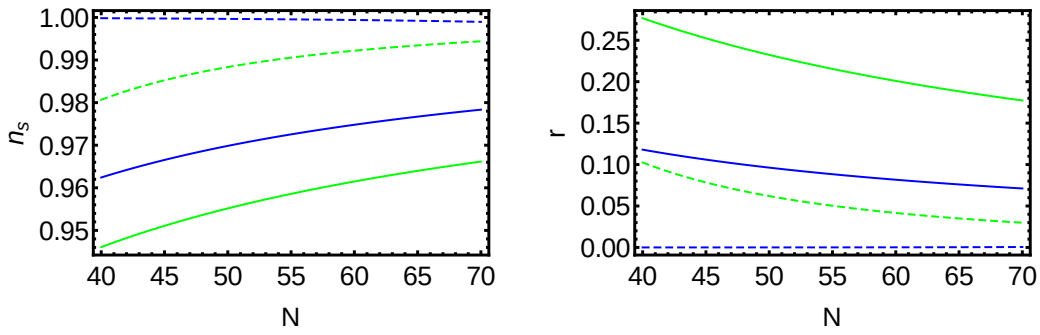

Figure 2.2: Predictions for the scalar spectral index $n_{\rm s}$ (left panel) and for the tensor-to-scalar ratio r (right panel) as function of the number of e-folds N for hilltop potentials (2.150). Different solid (dashed) lines represent different values of μ. $\mu = 10\ M_{\rm pl}$ as green line, $\mu = 100\ M_{\rm pl}$ as blue line, for $p = 4$ ($p = 2$).

We plot in Fig. 2.2 the predictions for the scalar spectral index and for the tensor-to-scalar ratio at first order in the slow-roll approximation, without any approximation in μ.

2.6.3 Natural inflation

In *natural inflation* [81, 82] a non-perturbative shift symmetry is invoked to suppress radiative corrections, leading to the periodic potential:

$$V(\phi) = \Lambda^4 \left[1 + \cos\left(\frac{\phi}{f}\right)\right] . \tag{2.160}$$

Only for $f \gtrsim 0.3 M_{\rm pl}$ the two slow-roll conditions are satisfied [81, 82]. The HFFs are:

$$\epsilon_1 = \frac{n^2}{2x^2} , \tag{2.161}$$

$$\epsilon_2 = \frac{2n}{x^2} , \tag{2.162}$$

$$\epsilon_3 = \epsilon_2 , \tag{2.163}$$

where $x = \phi/M_{\rm pl}$. By imposing $\epsilon_1^{\rm end} = 1$ we find:

$$x_{\rm end} = 2\frac{f}{M_{\rm pl}} \tan\left(\sqrt{2}\frac{M_{\rm pl}}{f}\right) . \tag{2.164}$$

The predictions for the scalar spectral index and the tensor-to-scalar ratio at first order in the slow-roll approximation are (see Fig. 2.3):

$$n_{\rm s} - 1 \approx -\left(\frac{M_{\rm pl}}{f}\right)^2 - \frac{r}{4} , \tag{2.165a}$$

$$r \approx \frac{16}{-2\left(\frac{f}{M_{\rm pl}}\right)^2 + e^{N\left(\frac{M_{\rm pl}}{f}\right)^2}\left[1 + 2\left(\frac{f}{M_{\rm pl}}\right)^2\right]} . \tag{2.165b}$$

In the limit for $f \to +\infty$, inflation occurs in the regime where ϕ is close to the minimum of the potential and the observables approach the values of $V(\phi) \propto \phi^2$:

$$n_{\rm s} - 1 \approx -\frac{4}{1 + 2N} , \tag{2.166a}$$

$$r \approx \frac{16}{1 + 2N} , \tag{2.166b}$$

the running of the spectral index is different in the two models, due to a different expression for ϵ_3, and in principle this can be used to discriminate between the two models.

For small value of f, both $n_{\rm s}$ and r decrease:

$$n_{\rm s} - 1 \approx -\frac{M_{\rm pl}^2}{f^2}\,, \tag{2.167a}$$

$$r \approx 16 e^{-\frac{N}{f^2}}\,. \tag{2.167b}$$

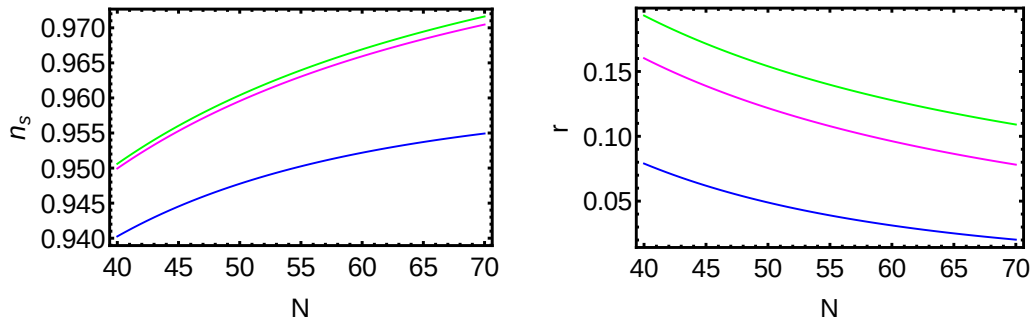

Figure 2.3: Predictions for the scalar spectral index $n_{\rm s}$ (left panel) and for the tensor-to-scalar ratio r (right panel) as function of the number of e-folds N for natural inflation (2.160). Different lines represent different values of f: $f = 5\ M_{\rm pl}$ (blue line), $f = 10\ M_{\rm pl}$ (magenta line), and $f = 30\ M_{\rm pl}$ (green line).

Note that the super-Planckian value for f required by observations is not necessarily a problem for this class of models.

When several fields $\phi_{\rm i}$ with a cosine potential as in Eq. (2.160) and scales $f_{\rm i}$ appear in the Lagrangian, an effective single field inflationary trajectory can be found for a suitable choice of parameters [83]. In such a setting, the super-Planckian value of the effective scale f required by observations, can be obtained even if the original scales statisfy $f_{\rm i} \ll M_{\rm pl}$ [83].

2.6.4 D-brane inflation

Inflation can be caused by physics in extra dimensions. If the SM of particle physics is confined to our 3-dimensional brane, the distance between our brane and anti-brane can drive inflation. We consider the following parameterization for the effective potential

driving inflation:

$$V(\phi) = \Lambda^4 \left(1 - \frac{\mu^p}{\phi^p} + ...\right) , \tag{2.168}$$

in particular $p = 2$ [84] and $p = 4$ [85, 86]. The predictions for r and n_s can be obtained from the hilltop case with the substitution $p \to -p$. For $p = 2$ the spectral index depends weakly from μ and can be approximated as $n_s - 1 \approx -3N/2$ (see Fig. 2.4).

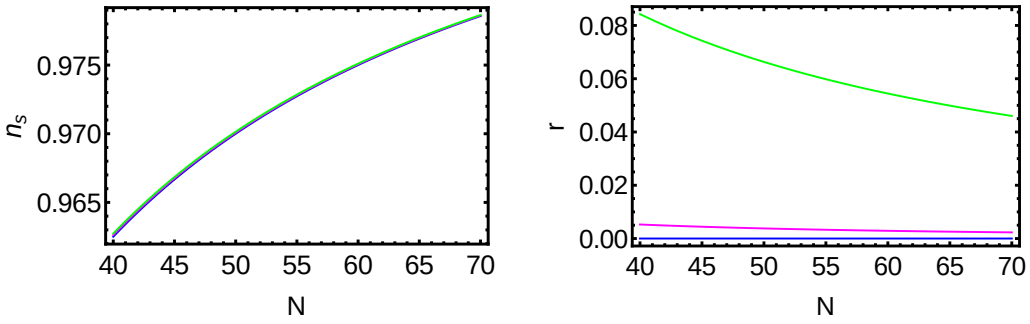

Figure 2.4: Predictions for the scalar spectral index n_s (left panel) and for the tensor-to-scalar ratio r (right panel) as function of the number of e-folds N for brane inflation (2.168) with $p = 2$. Different lines represent different values of μ: $\mu = 10^{-3}\, M_{\rm pl}$ (blue line), $\mu = M_{\rm pl}$ (magenta line), and $\mu = 10^2\, M_{\rm pl}$ (green line).

2.6.5 Potentials with exponential tails

Exponential potentials are ubiquitous in inflationary models motivated by supergravity and string theory [87–91]. We restrict ourselves to the analysis of the following class of potentials:

$$V(\phi) = \Lambda^4 \left(1 - e^{-q\phi/M_{\rm pl}} + ...\right) . \tag{2.169}$$

As for the hilltop models described earlier, the ellipsis indicates possible higher-order terms that are negligible during inflation but ensure positiveness of the potential. These

models predict:

$$n_s - 1 \approx \frac{r}{8}\left[-1 + 2W_{-1}\left(-e^{-1-\frac{q}{2}\left(\sqrt{2}+2Nq\right)}\left(1+\frac{q}{\sqrt{2}}\right)\right)\right], \tag{2.170a}$$

$$r \approx \frac{8q^2}{\left[1+W_{-1}\left(-e^{-1-\frac{q}{2}\left(\sqrt{2}+2Nq\right)}\left(1+\frac{q}{\sqrt{2}}\right)\right)\right]^2}, \tag{2.170b}$$

where W is the Lambert's function.

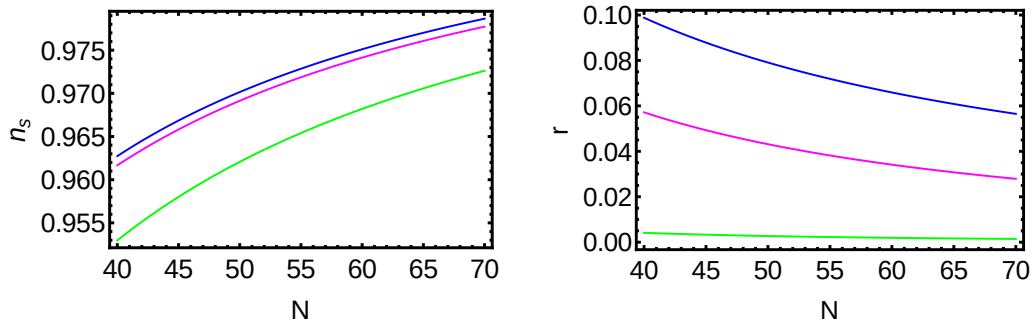

Figure 2.5: Predictions for the scalar spectral index n_s (left panel) and for the tensor-to-scalar ratio r (right panel) as function of the number of e-folds N for the potentials with exponential tails (2.169). Different lines represent different values of q: $q = 10^{-3}$ (blue line), $q = 10^{-1}$ (magenta line), and $q = 1$ (green line).

The case of an exponential potential without offset $V(\phi) = \Lambda^4 e^{-\lambda\phi/M_\mathrm{pl}}$, leading to *power-law inflation* [92], is strongly disfavoured by data, since it predicts $r = -8(n_\mathrm{s}-1)$ and therefore $n_\mathrm{s} - 1 = n_\mathrm{t}$. Moreover, for this model inflation never ends, since $\epsilon_1 =$ const, and so the basic model requires some modification.

2.6.6 Spontaneously broken SUSY

Hybrid models [93, 94] predicting $n_\mathrm{s} > 1$ are strongly disfavoured by CMB data. An example of a hybrid model predicting $n_\mathrm{s} < 1$ is the case in which slow-roll inflation is driven by loop corrections in spontaneously broken supersymmetric (SUSY) GUTs [95] described by the potential:

$$V(\phi) = \Lambda^4\left[1 + \alpha_h \log(\phi/M_\mathrm{pl})\right], \tag{2.171}$$

where $\alpha_h > 0$ is a dimensionless parameter. Note that for $\alpha_h \ll 1$, this model leads to the same predictions as the power-law potential with $n \approx 0$ discassed in Sec. 2.6.1, to lowest order in the slow-roll approximation:

$$n_\mathrm{s} - 1 \approx -\frac{1}{N}\,, \tag{2.172a}$$

$$r \approx \frac{\alpha_h}{64N}\,. \tag{2.172b}$$

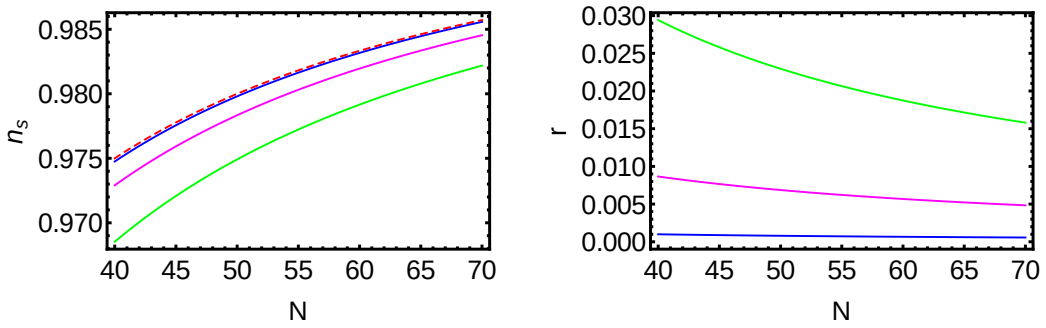

Figure 2.6: Predictions for the scalar spectral index n_s (left panel) and for the tensor-to-scalar ratio r (right panel) as function of the number of e-folds N for spontaneously broken SUSY (2.171). Different lines represent different values of α_h: $\alpha_h = 10^{-2}$ (blue line), $\alpha_h = 10^{-1}$ (magenta line), and $\alpha_h = 1$ (green line). In the panel on the left, we add the limit Eq. (2.172a) in red dashed.

2.6.7 R^2 inflation

The first inflationary model proposed [29], with action:

$$\mathcal{S} = \int \mathrm{d}^4x\, \sqrt{-g}\frac{M_\mathrm{pl}^2}{2}\left(R + \frac{R^2}{6M^2}\right)\,, \tag{2.173}$$

corresponds to the potential:

$$V(\phi) = \Lambda^4\left(1 - e^{-\sqrt{2/3}\phi/M_\mathrm{pl}}\right)^2\,, \tag{2.174}$$

in the *Einstein frame* (EF), which leads to the slow-roll predictions [31, 32]:

$$n_{\rm s} - 1 \approx -\frac{2}{N}\,, \tag{2.175a}$$

$$r \approx \frac{12}{N^2}\,. \tag{2.175b}$$

After the *Planck* 2013 data release, several theoretical developments supported the model in Eq. (2.173) beyond the original motivation of including quantum effects at one-loop [29]. No-scale supergravity [96], the large field regime of superconformal D-term inflation [97], or recent developments in minimal supergravity [98, 99] can lead to a generalization of the potential in Eq. 2.174 (see [100] for a previous embedding of R^2 inflation in $F(R)$ supergravity). The potential in Eq. (2.174) can also be generated by spontaneous breaking of conformal symmetry [101].

2.6.8 α attractors

We now study two classes of inflationary models motivated by recent developments in conformal symmetry and supergravity [102]. The first class has been motivated by considering a vector rather than a chiral multiplet for the inflaton in supergravity [103] and corresponds to the potential [102]:

$$V(\phi) = \Lambda^4 \left(1 - e^{-\sqrt{\frac{2}{3\alpha}}\frac{\phi}{M_{\rm pl}}}\right)^2 . \tag{2.176}$$

To lowest order in the slow-roll approximation, these models predict (see Fig. 2.7):

$$n_{\rm s} - 1 \approx -8\frac{1 + e^{\sqrt{\frac{2}{3\alpha}}\frac{\phi}{M_{\rm pl}}}}{3\alpha\left(1 - e^{\sqrt{\frac{2}{3\alpha}}\frac{\phi}{M_{\rm pl}}}\right)^2}\,, \tag{2.177a}$$

$$r \approx \frac{64}{3\alpha\left(1 - e^{-\sqrt{\frac{2}{3\alpha}}\frac{\phi}{M_{\rm pl}}}\right)^2}\,, \tag{2.177b}$$

on an inflationary trajectory characterized by $N \approx g(\phi/M_{\rm pl}) - g(\phi_{\rm end}/M_{\rm pl})$ with $g(x) = (3\alpha^4 e^{\sqrt{2}x/(\sqrt{3\alpha})} - \sqrt{6\alpha}x)/4$. The relation between N and ϕ can be inverted through the use of the Lambert's function, as done for other potentials [104].

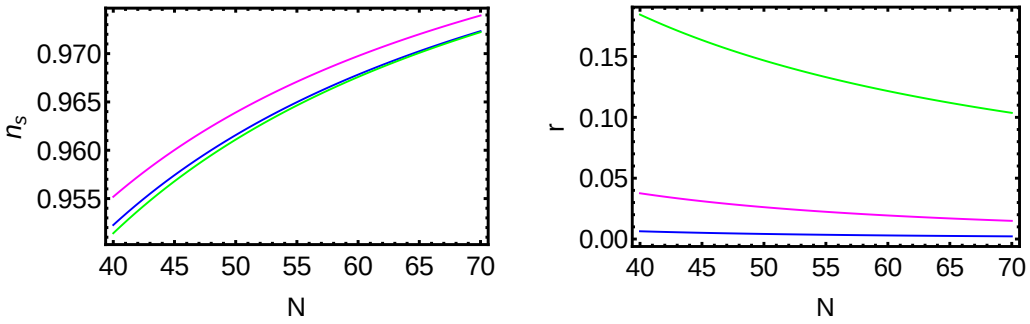

Figure 2.7: Predictions for the scalar spectral index $n_{\rm s}$ (left panel) and the tensor-to-scalar ratio r (right panel) as function of the number of e-folds N for supersymmetric α-attractors (2.176). Different lines represent different values of α: $\alpha = 1$ (blue line) which correnssponds to R^2 inflation, $\alpha = 10$ (magenta line), and $\alpha = 10^4$ (green line).

The second class of models has been called *super-conformal α-attractors* [102] and can be seen as originating from a different generating function with respect to the first class. This second class is described by the following potential [102]:

$$V(\phi) = \Lambda^4 \tanh^{2m}\left(\frac{\phi}{\sqrt{6\alpha}M_{\rm pl}}\right) . \tag{2.178}$$

This is the simplest class of models with spontaneous breaking of conformal symmetry, and for $\alpha = 1$ and $m = 1$ reduces to the original model introduced by [101]. The potential in Eq. (2.178) leads to the following slow-roll predictions [102]:

$$r \approx \frac{48\alpha m}{4mN^2 + 2Ng(\alpha, m) + 3\alpha m} , \tag{2.179}$$

$$n_s - 1 \approx \frac{-8mN - 6\alpha m + 2Ng(\alpha, m)}{4mN^2 + 2Ng(\alpha, m) + 3\alpha m} , \tag{2.180}$$

where $g(\alpha, m) = \sqrt{3\alpha(4m^2 + 3\alpha)}$. The predictions of this second class of models interpolate between those of a large-field chaotic model $V(\phi) \propto \phi^{2m}$, for $\alpha \gg 1$, and the R^2 model for $\alpha = 1$.

These two potentials (2.176)-(2.178) predict, in the limit for $\alpha \ll 1$, a tensor-to-scalar ratio smaller than the value predicted by R^2 inflation:

$$r \approx \frac{12\alpha}{N^2}\,. \tag{2.181}$$

We plot in Fig. 2.9 the 3D parameters space (r, N, α) for the supersymmetric α-model (left panel) and the 3D parameters space (r, m, α) with $N = 55$ for the superconformal α-model.

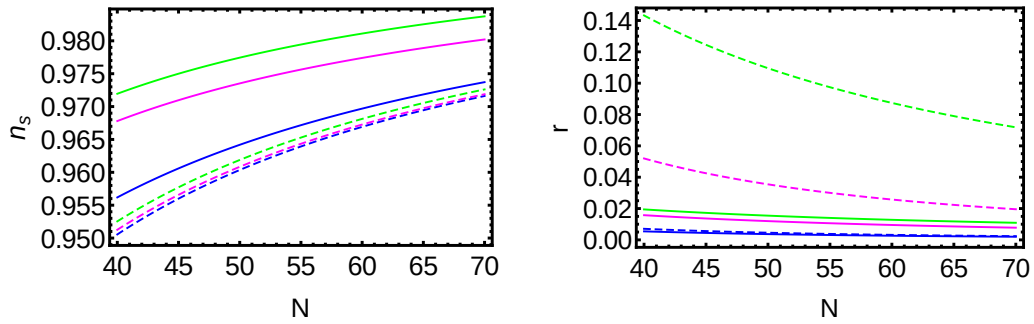

Figure 2.8: Predictions for the scalar spectral index $n_{\rm s}$ (left panel) and for the tensor-to-scalar ratio r (right panel) as function of the number of e-folds N for super-conformal α-attractors (2.178). Different solid lines represent different values of α with $m = 0.1$, and the dashed one have the same value of α with $m = 0.9$. $\alpha = 1$ (blue line) $\alpha = 10$ (magenta line), and $\alpha = 10^2$ (green line).

2.6.9 Non-minimally coupled inflaton

Inflationary predictions are quite sensitives to a non-minimal coupling, $\xi R\phi^2$, of the inflaton to the Ricci scalar. This extension can be applied to all the potentials considered so far and is supported by the inclusion of quantum corrections. We start with a generalized action:

$$\mathcal{S} = \int d^4\sqrt{-g}\left[\frac{1}{2}F(\phi)R - \frac{1}{2}\omega(\phi)\left(\nabla\phi\right)^2 - V(\phi)\right]\,. \tag{2.182}$$

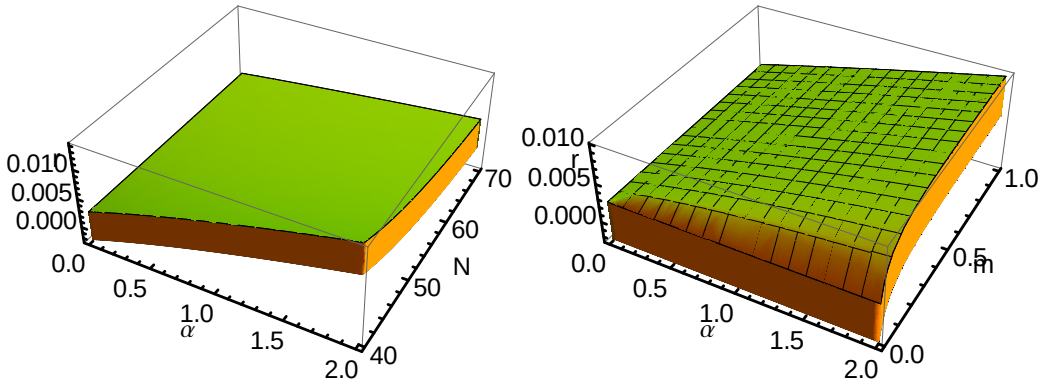

Figure 2.9: Predictions for tensor-to-scalar ratio r for the supersymmetric α-model (left panel), as function of the number of e-folds N and α, and for the superconformal α-model (right panel), as function of α and m with the number of e-folds fixed to N=55.

In a flat FLRW universe the background equations are:

$$H^2 = \frac{1}{6F}\left(\omega\dot{\phi}^2 + 2V - 6H\dot{F}\right), \tag{2.183}$$

$$\dot{H} = \frac{1}{2F}\left(-\omega\dot{\phi}^2 + H\dot{F} - \ddot{F}\right), \tag{2.184}$$

$$\ddot{\phi} + 3H\dot{\phi} + \frac{1}{2\omega}\left(\omega_{,\phi}\dot{\phi}^2 - F_{,\phi}R + 2V_{,\phi}\right) = 0\,. \tag{2.185}$$

The action (2.182) and the FL Eqs. (2.183) reduce to the Einstein gravity case for $F(\phi) = M_{\rm pl}^2$ and $\omega(\phi) = 1$. We are interested in studing a non-minimally coupled scalar field ϕ with a potential $V(\phi)$, in the original JF [105] [1], which is given by:

$$F(\phi) = \left(1 + \xi\frac{\phi^2}{M_{\rm pl}^2}\right) M_{\rm pl}^2\,, \tag{2.186}$$

$$\omega(\phi) = 1\,, \tag{2.187}$$

$$R = 6(2H^2 + \dot{H})\,. \tag{2.188}$$

[1] In Ref. [106] the authors cosidered the same case in the branch $\xi < 0$ and $\phi < 0$ with $F(\phi) = 1 - \xi\frac{\phi^2}{M_{\rm pl}^2}$.

In the non-minimally coupled case the background Eqs. (2.183) are written in the form:

$$H^2 = \frac{1}{6\left(1+\xi\frac{\phi^2}{M_{\rm pl}^2}\right)M_{\rm pl}^2}\left(\dot\phi^2 + 2V - 12H\xi\phi\dot\phi\right)\,, \tag{2.189}$$

$$\dot H = \frac{1}{2\left(1+\xi\frac{\phi^2}{M_{\rm pl}^2}\right)M_{\rm pl}^2}\left(-\dot\phi^2 + 2H\xi\phi\dot\phi - 2\xi\dot\phi^2 - 2\xi\phi\ddot\phi\right)\,, \tag{2.190}$$

$$\ddot\phi + 3H\dot\phi - 6\xi(\dot H + 2H^2)\phi + V_{,\phi} = 0\,, \tag{2.191}$$

and combining the above equations:

$$\dot H + 2H^2 = \frac{1}{6\left(1+\xi\frac{\phi^2}{M_{\rm pl}^2}\right)M_{\rm pl}^2}\left(-\dot\phi^2 + 4V - 6\xi\dot\phi^2\right) - \frac{\xi^2\frac{\phi^2}{M_{\rm pl}^2}}{1+\xi\frac{\phi^2}{M_{\rm pl}^2}}\left(\ddot\phi + 3H\dot\phi\right)\,, \tag{2.192}$$

$$\ddot\phi + 3H\dot\phi + \frac{\xi\frac{\phi^2}{M_{\rm pl}^2}(1+6\xi)}{1+\xi\frac{\phi^2}{M_{\rm pl}^2}(1+6\xi)}\frac{\dot\phi^2}{\phi} - \frac{4\xi\frac{\phi}{M_{\rm pl}^2}}{1+\xi\frac{\phi^2}{M_{\rm pl}^2}(1+6\xi)}V + \frac{1+\xi\frac{\phi^2}{M_{\rm pl}^2}}{1+\xi\frac{\phi^2}{M_{\rm pl}^2}(1+6\xi)}V_{,\phi} = 0\,. \tag{2.193}$$

Using the slow-roll approximation, the energy constraint and the field equation take the following form, respectively:

$$H^2 \simeq \frac{1}{3(1+\frac{\phi^2}{M_{\rm pl}^2})}\left[V - \frac{8\xi^2\frac{\phi^2}{M_{\rm pl}^2}}{1+\xi\frac{\phi^2}{M_{\rm pl}^2}(1+6\xi)}V + \frac{2(1+\xi\frac{\phi^2}{M_{\rm pl}^2})\xi\frac{\phi^2}{M_{\rm pl}^2}}{1+\xi\frac{\phi^2}{M_{\rm pl}^2}(1+6\xi)}V_{,\phi}\right]\,, \tag{2.194}$$

$$3H\dot\phi \simeq \frac{4\xi\frac{\phi}{M_{\rm pl}^2}}{1+\xi\frac{\phi^2}{M_{\rm pl}^2}(1+6\xi)}V - \frac{1+\xi\frac{\phi^2}{M_{\rm pl}^2}}{1+\xi\frac{\phi^2}{M_{\rm pl}^2}(1+6\xi)}V_{,\phi}\,. \tag{2.195}$$

We can now use the Eqs. (1.27) to derive the number of e-folds with:

$$\frac{H}{\dot\phi} \simeq \frac{1}{2}\left[-\frac{\xi\frac{\phi}{M_{\rm pl}^2}}{1+\xi\frac{\phi^2}{M_{\rm pl}^2}} - \frac{2V + 3\xi\frac{\phi}{M_{\rm pl}^2}V_{,\phi}}{V_{,\phi} - 4\xi\frac{\phi}{M_{\rm pl}^2}V + \xi\frac{\phi^2}{M_{\rm pl}^2}V_{,\phi}}\right]\,. \tag{2.196}$$

One of the most interesting effect due to $\xi \neq 0$ is to reconcile the quartic potential $V(\phi) = \lambda\phi^4/4$ with CMB observations, even for $\xi \ll 1$. The Higgs inflation model [107],

in which inflation occurs with $V(\phi) = \lambda(\phi^2 - \phi_0^2)^2/4$ and $\xi \gg 1$ for $\phi \gg \phi_0$, leads to the same predictions of the R^2 model to lowest order in the slow-roll approximation at tree level (see [108] and [109] for the inclusion of loop corrections). In oder to derive the trajectory of the scalar field we approximate the expression for the number of e-folds for $V(\phi) = \lambda\phi^4/4$ as:

$$N \simeq \frac{1}{4}\left[\frac{1+6\xi}{2}\left(\phi^2+\phi_{\rm end}^2\right) - \ln\left(\frac{1+\xi\frac{\phi_{\rm end}^2}{M_{\rm pl}^2}}{1+\xi\frac{\phi^2}{M_{\rm pl}^2}}\right)\right], \tag{2.197}$$

$$\approx \frac{1+6\xi}{8}\left(\phi^2+\phi_{\rm end}^2\right), \tag{2.198}$$

and the trajectory of the inflaton field is:

$$\phi \simeq \sqrt{\frac{8}{1+6\xi}N - \phi_{\rm end}^2}\,. \tag{2.199}$$

As for the case of R^2 inflation, we want to derive the predictions for this class of models in the EF. After performing a conformal transformation $\hat{g}_{\mu\nu} = \Omega(\phi)g_{\mu\nu}$, with $\Omega(\phi) = F(\phi)/M_{\rm pl}^2$, the action takes the form:

$$\mathcal{S} = \int {\rm d}^4x\sqrt{-\hat{g}}\frac{M_{\rm pl}^2}{2}\hat{R} - \frac{1}{2}G(\phi)^2(\nabla\phi)^2 - \hat{V}(\phi)\,, \tag{2.200}$$

where we introduced an hat for the quantities defined in the EF, and we used:

$$G(\phi) \equiv \frac{d\hat{\phi}}{d\phi} = \sqrt{\frac{3}{2}\left(\frac{F'}{F}\right)^2 + \frac{\omega}{F}}\,, \tag{2.201}$$

where $\hat{\phi}$ is the kinetic term of the scalar field in the canonical form in the EF, and the potential in the EF is:

$$\hat{V}(\phi) = \frac{V(\phi)}{\Omega^2(\phi)}\,. \tag{2.202}$$

The HFFs calculated up to the second order in slow-roll in EF are:

$$\epsilon_1 \simeq \frac{M_{\rm pl}^2}{2}\left(\frac{d\phi}{d\hat{\phi}}\right)\frac{V_{,\hat{\phi}}}{V} = \frac{8M_{\rm pl}^2}{\phi^2\left[1+(1+6\xi)\xi\frac{\phi^2}{M_{\rm pl}^2}\right]}\,, \tag{2.203a}$$

$$\epsilon_2 \simeq \frac{8M_{\rm pl}^2}{\phi^2}\frac{\left(1+\xi\frac{\phi^2}{M_{\rm pl}^2}\right)\left[1+2(1+6\xi)\xi\frac{\phi^2}{M_{\rm pl}^2}\right]}{\left[1+(1+6\xi)\xi\frac{\phi^2}{M_{\rm pl}^2}\right]^2}\,, \tag{2.203b}$$

$$\epsilon_3 \simeq \frac{8M_{\rm pl}^2}{\phi^2}\frac{1+(1+6\xi)\xi\frac{\phi^2}{M_{\rm pl}^2}\left[3+2(1+6\xi)\xi\frac{\phi^2}{M_{\rm pl}^2}\left(2+\xi\frac{\phi^2}{M_{\rm pl}^2}\right)\right]}{\left[1+2(1+6\xi)\xi\frac{\phi^2}{M_{\rm pl}^2}\right]\left[1+(1+6\xi)\xi\frac{\phi^2}{M_{\rm pl}^2}\right]^2}\,, \tag{2.203c}$$

and:

$$\phi_{\rm end} = \frac{4M_{\rm pl}}{\sqrt{1+\sqrt{(1+8\xi)(1+24\xi)}}}\,. \tag{2.204}$$

The predictions for the scalar spectral index and for the tensor-to-scalar ratio at first order in the slow-roll approximation are (see Fig. 2.10):

$$\begin{aligned} n_{\rm s}-1 \approx & -\frac{3\sqrt{(1+8\xi)(1+24\xi)}}{2\left(-1+N-6\xi+8N^2\xi\right)} - \frac{9\xi\sqrt{(1+8\xi)(1+24\xi)}}{-1+N-6\xi+8N^2\xi} \\ & - \frac{3(1+6\xi)(1+16N\xi)}{2\left(-1+N-6\xi+8N^2\xi\right)} - \frac{6\xi^2(1+8\xi)(1+24\xi)}{(1+4\xi(-1-6\xi+N(3+8N\xi)))^2} \\ & - \frac{18\xi^2\sqrt{(1+8\xi)(1+24\xi)}}{(1+4\xi(-1-6\xi+N(3+8N\xi)))^2} - \frac{96N\xi^3\sqrt{(1+8\xi)(1+24\xi)}}{(1+4\xi(-1-6\xi+N(3+8N\xi)))^2} \\ & + \frac{2\xi\sqrt{(1+8\xi)(1+24\xi)}}{1+4\xi(-1-6\xi+N(3+8N\xi))} + \frac{36\xi^2\sqrt{(1+8\xi)(1+24\xi)}}{1+4\xi(-1-6\xi+N(3+8N\xi))} \\ & + \frac{2\xi(3+2\xi(21+8N(1+18\xi)))}{1+4\xi(-1-6\xi+N(3+8N\xi))} \end{aligned} \tag{2.205a}$$

$$r \approx \frac{512\xi(1+6\xi)}{\left(-3-16N\xi+\sqrt{(1+8\xi)(1+24\xi)}\right)\left(-1-16N\xi+\sqrt{(1+8\xi)(1+24\xi)}\right)}\,, \tag{2.205b}$$

which behave in the strong coupling and weak coupling as:

$$n_{\rm s} - 1 \approx \begin{cases} -\frac{2}{N} & \text{for } \xi \gg 1 \\ -\frac{3}{N-1} & \text{for } \xi \ll 1 \end{cases}, \tag{2.206}$$

$$r \approx \begin{cases} \frac{12}{N^2} & \text{for } \xi \gg 1 \\ \frac{16}{N-1} & \text{for } \xi \ll 1 \end{cases}. \tag{2.207}$$

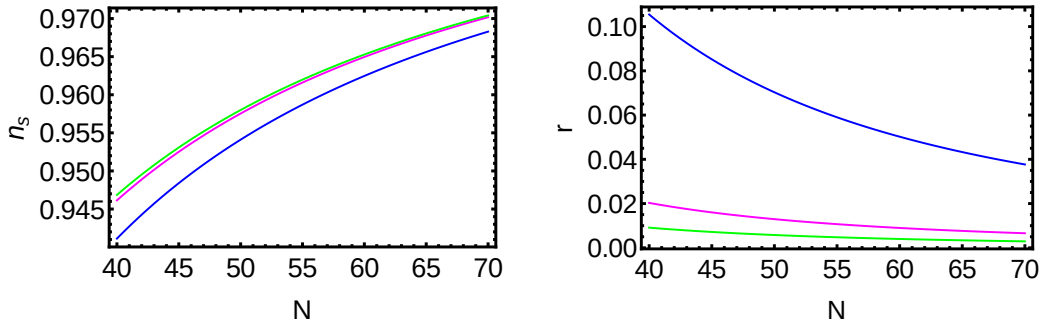

Figure 2.10: Predictions for the scalar spectral index $n_{\rm s}$ (left panel) and for the tensor-to-scalar ratio r (right panel) as function of the number of e-folds N for the non-minimally coupled quartic potential. Different lines represent different values of ξ: $\xi = 10^{-2}$ (blue line), $\xi = 10^{-1}$ (magenta line), and $\xi = 1$ (green line).

These predictions are given but not used yet in the comparison with observations.

2.7 Beyond slow-roll approximation

There are several theoretical motivations beyond violation of the slow-roll conditions. The theoretical interest in models beyond the slow-roll approximation is corroborated by observations as we will see in Sec. 4 where my contribution to the data analysis and scientific interpretation within the *Planck* Collaboration is presented.

Inflationary models violating the slow-roll approximation predict *features* in the PPS which can provide either a better fit to data or be constrained.

The slow-roll predictions previously given in this chapter are very convenient because they involve only the inflaton potential $V(\phi)$ and its derivatives evaluated at the epoch of the Hubble radius crossing, and they succesfully agree with cosmological data.

Eq. (2.117) holds exactly even if the slow-roll assumptions are violated and in general, for a given model, we can find the dominant and relevant term and solve the Mukhanov equation in this case.

A useful way to visualize the deviation from slow-roll is to rewrite the HFFs in terms of the inflaton field and its derivatives:

$$\epsilon_1 = 3\frac{\dot{\phi}^2/2}{\dot{\phi}^2/2 + V(\phi)} \tag{2.208}$$

$$\epsilon_2 = \frac{\ddot{H}}{H\dot{H}} - 2\frac{\dot{H}}{H^2} = 2\left(\frac{\ddot{\phi}}{H\dot{\phi}} + \epsilon_1\right), \tag{2.209}$$

where we used $\dot{H} = -\dot{\phi}^2/2M_{\rm pl}^2$, and $\ddot{H} = -\dot{\phi}\ddot{\phi}/M_{\rm pl}^2$.

In the following we will review the calculation of the scalar primordial spectrum for an archetypal model of violation of the slow-roll condition carried by a discontinuity in the first derivative of the potential, originally calculated by Starobinsky [110].

The first matching condition is the continuity of the curvature perturbations itself and the second one corresponds to the request of continuity of the generalized Newtonian potential [111] which is valid if the background expansion is continuous [112, 113]. They can be summarized on the mode function $v_{\mathbf{k}}$ as:

$$[v_{\mathbf{k}}]_{\pm} = 0 \tag{2.210}$$

$$\left[v'_{\mathbf{k}} - \frac{z'}{z}v_{\mathbf{k}}\right]_{\pm} = 0\,, \tag{2.211}$$

where $[X]_{\pm} = X_+ - X_-$.

At early time, i.e. $\eta \to -\infty$, we assume the Minkowsky positive frequency mode, which corresponds to the Bunch-Davies vacuum state. Before the transition, $\eta < \eta_0$, by considering for simplicity the de Sitter solution for massless minimally coupled test fields, we have:

$$v_{\mathbf{k}}^{(+)}(\eta) = \frac{\imath}{\sqrt{2c_{\rm s}^3k^3\eta^2}}(1 + \imath c_{\rm s}k\eta)e^{-\imath c_{\rm s}k\eta}\,. \tag{2.212}$$

After the transition, $\eta > \eta_0$, we have to consider the full solution (2.119), a superposition of wave functions:

$$v_{\mathbf{k}}^{(-)}(\eta) = \frac{\alpha_k}{\sqrt{2c_{\rm s}k}}e^{-\imath c_{\rm s}k\eta}\left(1 - \frac{\imath}{c_{\rm s}k\eta}\right) + \frac{\beta_k}{\sqrt{2c_{\rm s}k}}e^{\imath c_{\rm s}k\eta}\left(1 + \frac{\imath}{c_{\rm s}k\eta}\right). \tag{2.213}$$

By imposing the matching conditions (2.210)-(2.211), we determine the two Bogoliubov coefficients, α_k and β_k, to achive the contributions to the power spectrum which is given by:

$$\mathcal{P}_{\mathcal{R}}(\eta_0) \approx \mathcal{P}_{\mathcal{R},0}|\alpha_k - \beta_k|^2 \,, \tag{2.214}$$

where $\mathcal{P}_{\mathcal{R},0}$ is the featureless power spectrum.

2.7.1 Change in the slope of the potential

A microphysical representation of this scenario, with a sharp feature due to the transition of the slow-roll parameters ϵ_1, was proposed and studied originally in [110]. In the following we consider a canonical scalar field, i.e. $c_s = 1$.

In the Starobinsky model the inflaton rolls down to a linear potential written as:

$$V(\phi) = \begin{cases} V_0 + A_+(\phi - \phi_0) \,, & \phi \gg \phi_0 \\ V_0 + A_-(\phi - \phi_0) \,, & \phi \ll \phi_0 \end{cases} \tag{2.215}$$

with a sharp change in its slope, as depicted in the left panel of Fig. 2.11. We require

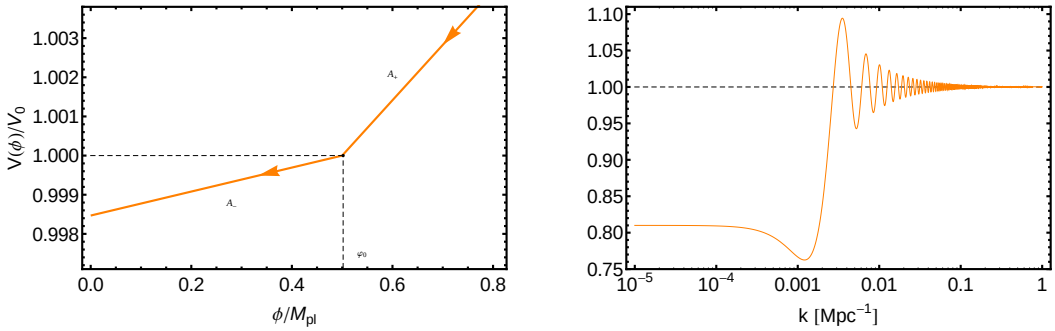

Figure 2.11: We plot the shape of the potential (left panel) for the model with a discontinuity in the first derivative of the potential and the correspondent spectrum of curvature perturbation at late times (right panel).

$|A_\pm| \ll |V_0|$ to avoid the end of inflation. Until the inflaton reaches the transition, i.e. for values $\phi^{(+)} > \phi_0$, we can assume that slow-roll holds.

The Starobinsky model assumes that near the transition the potential is constant

and $V \simeq V_0$, in this case we can solve the equation of the motion for the inflaton:

$$\phi^{(+)} \simeq \phi_{in} - \frac{A_+ M_{\rm pl}^2}{V_0} N \,, \tag{2.216a}$$

$$\phi^{(+)}_{,N} \simeq -\frac{A_+ M_{\rm pl}^2}{V_0} \,, \tag{2.216b}$$

$$\phi^{(+)}_{,NN} \simeq 0 \,, \tag{2.216c}$$

where ϕ_{in} is the initial value of the inflaton. The slow-roll parameters in the regime of linear potential are:

$$\epsilon_1^{(+)} = \frac{(\phi^{(+)}_{,N})^2}{2M_{\rm pl}^2} \,, \tag{2.217}$$

$$\epsilon_2^{(+)} = 2\left(\frac{\ddot{\phi}^{(+)}}{H\dot{\phi}^{(+)}} + \epsilon_1^{(+)}\right) \simeq 2\epsilon_1^{(+)} \,. \tag{2.218}$$

After the transition we allow the second slow-roll condition Eq. (1.32) to be violated, therefore ϵ_1 will continue to be small but ϵ_2 will become large for some time and after that, slow-roll will be recovered. In this case the KG equation Eq. (1.25e) can be solved out of slow-roll and ϕ'' contributes to ϵ_2. Thanks to ϕ'', ϵ_2 can become large even if ϵ_1 is still small and continuous at the transition, fast-roll phase. For $\phi^{(-)} \in (-\infty, \phi_0]$ we find:

$$\phi^{(-)} \simeq \phi_0 - \frac{A_- M_{\rm pl}^2}{V_0}(N - N_0) + \frac{\Delta A M_{\rm pl}^2}{3V_0}\left[1 - e^{-3(N-N_0)}\right] \,, \tag{2.219a}$$

$$\phi^{(-)}_{,N} \simeq \frac{\Delta A M_{\rm pl}^2}{V_0}\left[e^{-3(N-N_0)} - \frac{A_-}{\Delta A}\right] \,, \tag{2.219b}$$

$$\phi^{(-)}_{,NN} \simeq -\frac{3\Delta A M_{\rm pl}^2}{V_0} e^{-3(N-N_0)} \,, \tag{2.219c}$$

where $\Delta A \equiv A_- - A_+$ and $N_0 \simeq \frac{V_0}{A_+ M_{pl}^2}(\phi_{in} - \phi_0)$. Here we have required both ϕ and ϕ' to be continuous at the transition to solve the integration constant. The Bogoliubov coefficients in this case are:

$$\alpha_k = 1 - \frac{3\imath\Delta A(1 + k^2\eta_0^2)}{2A_+ k^3 \eta_0^3} \,, \tag{2.220}$$

$$\beta_k = \frac{3\imath\Delta A(1 - \imath k\eta_0)^2}{2A_+ k^3 \eta_0^3} e^{-2\imath k\eta_0} \,, \tag{2.221}$$

which correspond exactly to the gap in the second HFF, that is for this particular potential is:

$$\epsilon_2^{(+)} - \epsilon_2^{(-)} = 6\frac{\Delta A}{A_-}\,. \tag{2.222}$$

2.7.2 Variation in the speed of sound

In this section we will describe the case of a transition in the speed of sound at $\eta = \eta_0$, assuming slow-roll, i.e. ϵ_1 and ϵ_2 small and constant everywhere, in the context of k-inflation [71, 114].

By imposing the matching conditions Eqs. (2.210)-(2.211) at the transition time and $\epsilon_1^{(+)} = \epsilon_1^{(-)}$, $\epsilon_2^{(+)} = \epsilon_2^{(-)} = 0$, the Bogoliubov coefficients became:

$$\begin{aligned}\alpha_k =& \frac{e^{\imath(c_{\rm s}^{(-)} - c_{\rm s}^{(+)})k\eta_0}}{4(c_{\rm s}^{(-)}c_{\rm s}^{(+)})^{5/2}(k\eta_0)^3}\times \\ & \Big[\imath\left(c_{\rm s}^{(+)2}s^{(-)} - c_{\rm s}^{(-)2}s^{(+)}\right) + (c_{\rm s}^{(-)} - c_{\rm s}^{(+)})\left(c_{\rm s}^{(+)2}s^{(-)} - c_{\rm s}^{(-)2}s^{(+)}\right)k\eta_0 \\ & + \imath c_{\rm s}^{(-)}c_{\rm s}^{(+)}\left(c_{\rm s}^{(+)2}s^{(-)} - c_{\rm s}^{(-)2}s^{(+)}\right)(k\eta_0)^2 + 2c_{\rm s}^{(-)2}c_{\rm s}^{(+)2}(c_{\rm s}^{(+)} + c_{\rm s}^{(-)})(k\eta_0)^3\Big]\,,\end{aligned} \tag{2.223}$$

$$\begin{aligned}\beta_k =& \frac{e^{-\imath\left(c_{\rm s}^{(-)} + c_{\rm s}^{(+)}\right)k\eta_0}}{4\left(c_{\rm s}^{(-)}c_{\rm s}^{(+)}\right)^{5/2}(k\eta_0)^3}\times \\ & \Big[\imath\left(c_{\rm s}^{(+)2}s^{(-)} - c_{\rm s}^{(-)2}s^{(+)}\right) - (c_{\rm s}^{(-)} + c_{\rm s}^{(+)})\left(c_{\rm s}^{(+)2}s^{(-)} - c_{\rm s}^{(-)2}s^{(+)}\right)k\eta_0 \\ & - \imath c_{\rm s}^{(-)}c_{\rm s}^{(+)}\left(c_{\rm s}^{(+)2}s^{(-)} - c_{\rm s}^{(-)2}s^{(+)}\right)(k\eta_0)^2 + 2c_{\rm s}^{(-)2}c_{\rm s}^{(+)2}(c_{\rm s}^{(+)} - c_{\rm s}^{(-)})(k\eta_0)^3\Big]\,,\end{aligned} \tag{2.224}$$

with $|\alpha_k|^2 - |\beta_k|^2 = 1$.

As first case, we assume now the situation in which we have two different and constant speed of sound before and after the transition with vanishing derivatives, i.e. $c_{\rm s}^{(+)} \neq c_{\rm s}^{(-)}$ and $s^{(+)} = s^{(-)}$. The Bogoliubov coefficients and the modulation of the power

spectra became:

$$\alpha_k = \frac{\left(c_{\rm s}^{(-)} + c_{\rm s}^{(+)}\right) e^{\imath\left(c_{\rm s}^{(-)} - c_{\rm s}^{(+)}\right)k\eta_0}}{2\sqrt{c_{\rm s}^{(-)} c_{\rm s}^{(+)}}}\,, \tag{2.225}$$

$$\beta_k = \frac{\left(-c_{\rm s}^{(-)} + c_{\rm s}^{(+)}\right) e^{\imath\left(c_{\rm s}^{(-)} + c_{\rm s}^{(+)}\right)k\eta_0}}{2\sqrt{c_{\rm s}^{(-)} c_{\rm s}^{(+)}}}\,, \tag{2.226}$$

and:

$$|\alpha_k - \beta_k|^2 = \frac{c_{\rm s}^{(-)2} + c_{\rm s}^{(+)2} + \left(c_{\rm s}^{(-)} + c_{\rm s}^{(+)}\right)\left(c_{\rm s}^{(-)} - c_{\rm s}^{(+)}\right)\cos\left(2c_{\rm s}^{(-)}k\eta_0\right)}{2c_{\rm s}^{(-)} c_{\rm s}^{(+)}}\,. \tag{2.227}$$

If we define a new variable A and k_0, as in Ref. [115]:

$$c_{\rm s}^{(-)} = A c_{\rm s}^{(+)}\,, \tag{2.228}$$

$$c_{\rm s}^{(-)} = -\frac{1}{k_0\eta_0}\,, \tag{2.229}$$

we can rewrite the modulation of the power spectrum as:

$$|\alpha_k - \beta_k|^2 = A + \left(\frac{1}{A} - A\right)\sin^2\left(\frac{k}{k_0}\right)\,, \tag{2.230}$$

which is the identical constant modulation found in Ref. [115, Eq. 4.27]. Note that oscillations are not suppressed.

Another interesting limit, in analogy to the Starobisky model developed in the previous section, is obtained by assuming the continuity of the speed of sound during the transition, $c_{\rm s}^{(+)} = c_{\rm s}^{(-)}$ at $\eta = \eta_0$. In this case the features will be driven by the derivative of the speed of sound, i.e. s. The Bogoliubov coefficients are:

$$\alpha_k = 1 + \frac{\imath\left(s^{(-)} - s^{(+)}\right)\left(1 + c_{\rm s}^2 k^2\eta_0^2\right)}{4(c_{\rm s}k\eta_0)^3}\,, \tag{2.231}$$

$$\beta_k = e^{-2\imath c_{\rm s}k\eta_0}\frac{\imath\left(s^{(-)} - s^{(+)}\right)\left(1 + \imath c_{\rm s}k\eta_0\right)^2}{4(c_{\rm s}k\eta_0)^3}\,. \tag{2.232}$$

Note that this form is completely analogous to Eqs. (2.220)-(2.221) with $\eta_0 \to \eta_0 c_{\rm s}$ and:

$$\frac{s^{(+)} - s^{(-)}}{2} = \frac{3\Delta A}{A_+}\,. \tag{2.233}$$

Therefore the modulation of the power spectrum, such as the Bogoliubov coefficients, are the same as in the Starobinsky model Eqs. (2.220)-(2.221). We have found a degeneracy which could be disentangled considering the tensor sector of the power spectrum or considering higher-order correlators [116].

3 Cosmological observations

Current measurements of the CMB anisotropies angular power spectrum (APS) have reached high precision in constraining the parameters of the concordance cosmological model (ΛCDM). Since the first detection of these anisotropies by the Cosmic Background Explorer (COBE) satellite [117] (lunched in 1990), there has been an intense activity to map the microwave sky at increasing level of sensitivity and angular resolution by ground-based, balloon, and space missions.

These different measurements of the largest angular scales and acoustic peaks of the CMB APS, both in temperature and polarization, were joined in 2003 by the first results from NASA's Wilkinson Microwaves Anisotropy Probe (WMAP) [118] (launched in 2001), which were then improved upon by analyses of the 3-year, 5-year, 7-year, and final 9-year WMAP data [119–122]. WMAP precision has been improved upon through the first and second cosmological results from ESA's *Planck* satellite [123–125]. With the cosmic variance (CV) limit measurement of the CMB temperature APS made by *Planck* we entered in the era of high precision polarization experiments. The ongoing ground-based Stage-II CMB experiments such as ACTpol [126], BICEP2 and Keck Array [127, 128], POLARBEAR [129], and SPTpol [130] should reach a sensitivity of $10^{-2}\mu$K in the power spectrum, and this will be significantly improved by the future ground-based Stage-III experiments such as Advanced ACTpol [131], BICEP3 and Keck Array [132], Simons Array [133], SPT3G [134], CLASS [135], and the proposed Stage-IV [136, 137] up to $10^{-4}\mu$K. Moreover, the proposed space CMB missions LiteBIRD [138] and CORE [139] are planned to perform a CV-limited measurement of the E-mode polarization power spectrum (only CORE will provide a self-consistent CV-limited measure of all the CMB APS).

In the coming years, an enormous effort will be put in the realization of large galaxy surveys having the primary goal of hunting for primordial B-mode polarization exploiting the information contained in the clustering properties. With this information we can hope to learn much about structure formation and the late time cosmology. To date, the CMB has been the dominant source of information about primordial perturbations. Nevertheless, galaxy surveys have a fundamental role when combined with CMB anisotropies in breaking degeneracy in the cosmological parameters, e.g. when a non-vanishing spatial curvature $\Omega_{\rm K}$ or the parameter of state of the DE $w_{\rm DE}$ are

considered.

Several LSS wide-field surveys currently planned have the potential to constrain cosmological parameters and the physics of cosmological perturbations.

For spectroscopic survey, the SDSS-III's Baryonic Oscillation Spectroscopic Survey (**BOSS**) was completed in 2014 and mapped the redshift of 2.5 million galaxies over 9376 $\deg^2$ to $z < 0.7$ (the survey has been splitted in two samples: LOWZ with $z < 0.4$, and CMASS with $0.4 < z < 0.7$). The latest generation of the SDSS (SDSS-IV, $2014 - 2020$), named **eBOSS**) [140], is extending cosmological measurements to a critical early phase of cosmic history mapping the Universe over the redshift range $0.6 < z < 2.2$, a range of distances (redshifts) currently left completely unexplored by other 3D maps of LSS in the Universe.

The Dark Energy Spectroscopic Instrument (**DESI**) ground-based experiment [141] is expected to start observations in 2018 and to complete in 4 years a 14000 $\deg^2$ redshift survey of galaxies and quasars. DESI will also obtain a sample of bright galaxies at lower redshifts ($0.05 < z < 0.4$) and one of higher-redshift ($2.1 < z < 3.5$) quasars looking for the Lyman-α forest absorption features in their spectra.

The ESA Cosmic Vision mission **Euclid** [142] is scheduled to be launched in 2020, with the goal of characterising the dark sector of our Universe. This will be done mostly measuring the cosmic shear in a photometric surveys of billions of galaxies and the galaxy clustering in a spectroscopic survey of tens of millions of Hα emitting galaxies over an area of 15000 $\deg^2$ and will cover a redshift range $0.9 < z < 1.8$.

SPHEREx [143] is a NASA proposed small explorer satellite having the goal of providing the first near-infrared spectro-photometric image of the complete sky, thanks to its coverage of 40000 $\deg^2$ in the wide wavelength range $0.75 < \lambda\ \mu\mathrm{m}^{-1} < 4.8$.

With photometric surveys the redshift (true redshift) is inferred from broadband galaxy colours and will be estimated from a number of broad bans (photometric redshifts). On scales larger than the redshift error length, all the physical information is preserved. This makes photometric surveys good to test the largest scales of the matter power spectrum. Large Synoptic Survey Telescope (**LSST**) represents the widest ($\sim$ 18000 $\deg^2$) and deeper photometric survey with a sample of ten billion galaxies over a huge volume, planned in the foreseeable future (planned to start in 2020) [144, 145].

Radio surveys will map out the redshift-space matter distribution over a huge volume, providing precision data over a significant wide area of the sky. Thanks to the prospect to the Square Kilometre Array (**SKA**), a planned general-purpose array split over two main sites in South-Africa and Australia, using the 21 emission line and the radio continuum surveys will be possible to tackle several challeges of modern cosmology.

The SKA will survey LSS primarily by detecting the redshifted neutral hydrogen

(HI) 21-cm emission line from a large number of galaxies out to high redshift. This can be achieved by HI galaxy survey, intensity mapping and radio continuum survey [146–148].

3.1 The Cosmic Microwave Background anisotropies

The CMB anisotropies pattern is the best observable for the physics of the early Universe. We now give the essentials of the decomposition of the CMB temperature field $T(\hat{\mathbf{n}})$ in spherical harmonics ($\hat{\mathbf{n}}$ denotes the direction on the sky).

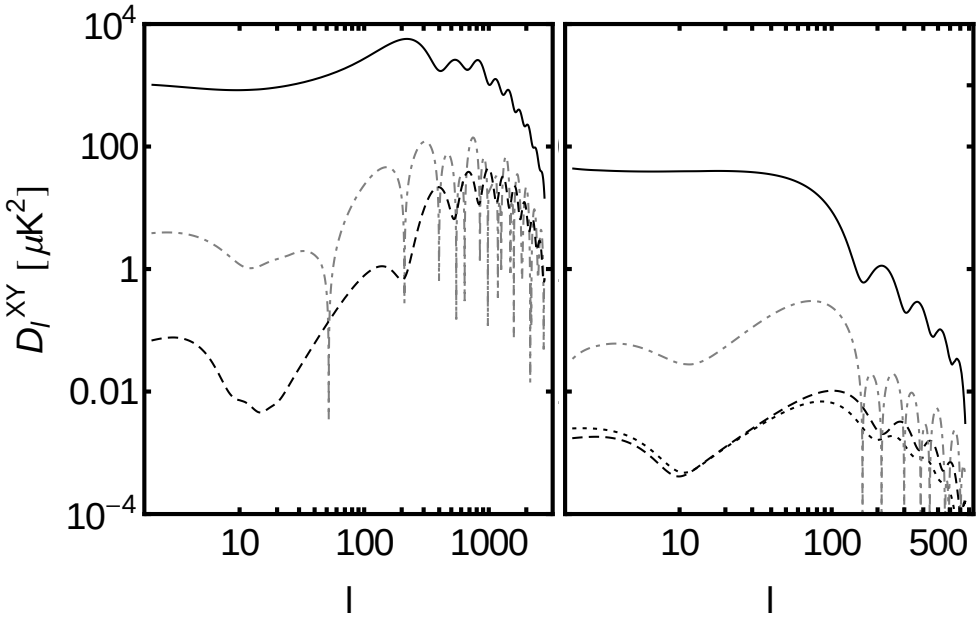

Figure 3.1: Scalar (left panel) and tensor (right panel) CMB anysotropies bandpasses $\mathcal{D}_\ell^{\rm XY}$ with tensor-to-scalar ratio r=0.1. Different curves represent: temperature (solid line), E-mode polarization (dashed line), cross-correlation between temperature and E-mode polarization (gray dot-dashed line), and B-mode polarization (dotted line).

The observed temperature, and its anisotropies, with respect to the observer located at $(\eta_0, \mathbf{x}_0)$, is:

$$T(\eta_0, \mathbf{x_0}, \hat{\mathbf{n}}) = T(\eta_0)\left[1 + \Theta(\eta_0, \mathbf{x_0}, \hat{\mathbf{n}})\right] , \tag{3.1}$$

where we defined the *adimensional temperature anisotropy field* as:

$$\Theta(\hat{\mathbf{n}}) \equiv \frac{\delta T(\hat{\mathbf{n}})}{T} = \sum_{\ell} \sum_{\mathrm{m}=-\ell}^{\ell} a_{\ell \mathrm{m}} Y_{\ell \mathrm{m}}(\hat{\mathbf{n}}) \,, \tag{3.2}$$

with the *multipole moments* defined as:

$$a_{\ell \mathrm{m}} = \int d\Omega \, Y^*_{\ell \mathrm{m}}(\hat{\mathbf{n}}) \Theta(\hat{\mathbf{n}}) \,. \tag{3.3}$$

By assuming rotation invariance, the variance of the multipole moments is connected to the *angular power spectrum*:

$$\langle a^*_{\ell \mathrm{m}} a_{\ell' \mathrm{m}'} \rangle = \delta_{\ell \ell'} \delta_{\mathrm{m} \mathrm{m}'} C_\ell \,. \tag{3.4}$$

In the above the angle bracket $\langle \, , \rangle$ denotes an average over an ensamble of realizations of the fluctuations. If we were given an ideal (i.e. noise free) measurement over the full sky, the CMB power spectrum could be estimated as:

$$\hat{C}_\ell = \frac{1}{2\ell + 1} \sum_{\mathrm{m}=-\ell}^{\ell} |a_{\ell \mathrm{m}}|^2 \,. \tag{3.5}$$

$\hat{C}_\ell$ is an unbiased estimator of the true ensemble C_ℓ, but has an irremovable *cosmic variance* due to the finite numer of modes, i.e. $2\ell + 1$.

The multipole moment in Eq. (3.3) gives the relation between the PPS and the temperature fluctuation:

$$a_{\ell \mathrm{m}} = 4\pi (-\imath)^\ell \int \frac{d^3k}{(2\pi)^3} \, \Theta_\ell(k) \mathcal{P}_{\mathcal{R}}(k) Y_{\ell \mathrm{m}}(k) \,. \tag{3.6}$$

The transfer function $\Theta_\ell(k)$ provides the map from the PPS of curvature perturbations to the APS of temperature anisotropies and can be written as the *line-of-sight* solution of the Boltzmann equation [149]:

$$\begin{aligned} \Theta_\ell(k) = & \left(\Phi + \frac{1}{4} \delta_\gamma \right) \Big|_{\eta_{\mathrm{rec}}} j_\ell(k(\eta_0 - \eta_{\mathrm{rec}})) + v_\gamma(\eta_{\mathrm{rec}}) j'_\ell(k(\eta_0 - \eta_{\mathrm{rec}})) \\ & + 2 \int_{\eta_{\mathrm{rec}}}^{\eta_0} d\eta \, \dot{\Phi} j_\ell(k(\eta_0 - \eta)) \,, \end{aligned} \tag{3.7}$$

where we assumed instantaneous recombination. We can now obtain an expression for C_ℓ in terms of $\Theta_\ell(k)$:

$$C_\ell = \frac{2}{\pi} \int k^2 dk \, \mathcal{P}_\mathcal{R}(k) \Theta_\ell^2(k) \,. \tag{3.8}$$

Substituting Eq. (3.7) into Eq. (3.8) we get six terms: the Sachs-Wolfe (SW) term [150], the Doppler term, the Integrated Sachs-Wolfe (ISW) term [150, 151], and three cross spectra. The cross-spectra and the ISW contribution are small.

The SW effect describes the evolution of the primordial perturbations into perturbations in the matter (δ_γ) and the metric (Φ) perturbations at recombination. On the scales which were outside the Hubble radius at recombination, the SW is the main contributed to the anisotropies. It predicts a plateau for the band power $\mathcal{D}_\ell \equiv \ell(\ell+1)C_\ell/2\pi$ with a slope connected to the scalar spectral index, flat for $n_\mathrm{s} = 1$. On scales below the sound horizon at the last scattering, the photon-baryon fluid had time to undergo acoustic oscillation. The form of the photon initial condition set the oscillation mostly in the $\cos(k\chi_\mathrm{s})$, which rise the SW power spectrum in particular to phases $k\chi_\mathrm{s}(\eta_\mathrm{rec}) = n\pi$.

The photon velocity v_γ oscillates as $\sin(k\chi_\mathrm{s})$, so the Doppler term tends to fill in powers between the acoustic peaks (dipole contribution).

The ISW effect is described by the last term in Eq. (3.7). It is an additional source to anisotropy due to the temporal variation of the gravitational potentials along the line of sight. The ISW receives contributions from late times as the potential decays during the Λ-dominated phase, and at early times around last scattering from the residual radiation at a_eq. The late ISW effect is the only way to probe the growing of structure at low redshift in linear CMB anisotropies, and distinguish between different DE models. It contributes mainly to large angular scales and therefore at low multipoles, i.e. $\ell \lesssim 10$, since there is a little power in the potentials at late times on scales that entered the Hubble radius during radiation domination. This contribution modifies the strict connection between the large scales SW effect and the scalar spectral index. Therefore, in order to measure n_s, we needs to include also small scales due to the variation on the plateau injected by the ISW effect, plus a contribution from the dipole at recombination. Moreover, the late ISW effect produces correlations between the large scale temperature fluctuations and other tracers of the potential in the local Universe [152]. The early time ISW effect adds coherently to the SW anisotropies near the first peak, boosting it significantly [153].

At very small scales, we have to consider the fact that photons have a finite mean path by going beyond the perfect tight coupling approximations and a finite duration of recombination. The effect of a finite mean free path for the photons would lead to the

damping of small scale fluctuations. This effect could be reproduce phenomenologically by adding a UV cutoff in the integral (3.8) [154].

The last fundamental effect that we would like to mention is *reionization*. The free electron density generated after the Universe began to reionize could re-scatter CMB photons, and this could smooth the CMB by averaging the anisotropies. In practice, the visibility function is not perfectly sharp at reionization and the integral through the finite re-scattering distance tends to decrease the Doppler term. The anisotropies get suppressed by a factor of $e^{-\tau}$.

3.1.1 Tensor perturbations

Tensor modes, describing GWs, represent the transverse trace-free perturbations to the spatial metric Eq. (2.3). Their evolution is given by the transfer function:

$$\Theta(\hat{\mathbf{n}}) = -\frac{1}{2}\int_0^{\eta_0} d\eta\, e^{-\tau}\dot{h}_{\mathrm{ij}}\hat{n}^{\mathrm{i}}\hat{n}^{\mathrm{j}}\,. \tag{3.9}$$

This quadrupole perturbation to the expansion produces an anisotropic redshifting of the CMB photons and an associated temperature anisotropy. GWs damp as they oscillate inside the Hubble radius, so the significant contribution is from long wavelengths at last scattering, i.e. $\ell \sim 60$, see Fig. 3.1 (right panel).

3.1.2 CMB polarization

Scattering processes during recombination generated linear polarization [155]. In addition, large-angle polarization was generated by subsequent re-scattering as the Universe reionized (Thomson scattering of the photons from free electron).

Polarization is conveniently described in terms of the Stokes parameters T (or I), the total intensity, Q and U, describe the linear polarization, and V describes the circular polarization, which is expected undetectably small for the CMB. The temperature anisotropy field T is invariant under rotation in the plane perpendicular to $\hat{\mathbf{n}}$ and can be expandend in terms of scalar spherical harmonics as in Eq. (3.2). Instead, the quantities Q and U trasform under rotation as a spinor field and therefore can be expanded on the sphere in terms of tensor spherical harmonics [156]:

$$(Q \pm \imath U)(\hat{\mathbf{n}}) = \sum_{\ell}\sum_{\mathrm{m}=-\ell}^{\ell} a_{\ell\mathrm{m}}^{(\pm 2)}Y_{\ell\mathrm{m}}^{(\pm 2)}(\hat{\mathbf{n}})\,. \tag{3.10}$$

Instead of the momentum $a_{\ell \mathrm{m}}^{(\pm 2)}$ and of the Stokes parameters Q and U, it is convenient to introduce:

$$a_{\ell \mathrm{m}}^{\mathrm{E}} \equiv -\frac{1}{2}\left(a_{\ell \mathrm{m}}^{(+2)} + a_{\ell \mathrm{m}}^{(-2)}\right), \qquad a_{\ell \mathrm{m}}^{\mathrm{B}} \equiv -\frac{1}{2i}\left(a_{\ell \mathrm{m}}^{(+2)} - a_{\ell \mathrm{m}}^{(-2)}\right), \tag{3.11a}$$

$$E(\hat{\mathbf{n}}) = \sum_{\ell} \sum_{\mathrm{m}=-\ell}^{\ell} a_{\ell \mathrm{m}}^{\mathrm{E}} Y_{\ell m}(\hat{\mathbf{n}}), \qquad B(\hat{\mathbf{n}}) = \sum_{\ell} \sum_{\mathrm{m}=-\ell}^{\ell} a_{\ell \mathrm{m}}^{\mathrm{B}} Y_{\ell m}(\hat{\mathbf{n}}). \tag{3.11b}$$

E-mode polarization is curl-free with polarization vectors that are radial around cold spots and tangential around hot spots. B-mode polarization is divergence-free with polarization vectors which vortic around any point.

There are four types of correlations between temperature and polarization anisotropies: three autocorrelations denoted by TT, EE, and BB, as well as the cross-correlation between temperature fluctuations and E-modes denoted by TE. All other cross-correlations, i.e. TB and EB, vanish under parity symmetry.

The generalization of the APS (3.4) is defined as:

$$C_{\ell}^{\mathrm{XY}} \equiv \frac{1}{2\ell+1} \sum_{\mathrm{m}=-\ell}^{\ell} \langle a_{\ell \mathrm{m}}^{\mathrm{X}\,*} a_{\ell \mathrm{m}}^{\mathrm{Y}} \rangle, \tag{3.12}$$

where X,Y = T,E,B and the multipole moments are now sourced by scalars $\mathcal{R}$ and tensors h. The scalar perturbations do not produce magnetic polarization in linear perturbation theory, while tensor perturbations produce both electric and magnetic polarization [156, 157].

Reionization does produce significant large scales polarization [158]. The position of the bump is controlled by the epoch of reionization, and the height by the fraction of photons that scatter there, i.e. τ.

3.1.3 Quantum coherence

Once inside the Hubble radius, the curvature perturbation $\mathcal{R}$ sources density fluctuations δ which evolves under the influence of gravity and pressure. At last scattering surface, assuming that fluctuations with different wavelengths are captured at the same moment, if all Fourier modes of a given wavelength have the same phases they interfere coherently and the spectrum of all Fourier produces a series of peaks and throughs in the CMB power spectrum as seen on the last scattering surface. Without this coherence the CMB power spectrum would be white noise [159].

Because fluctuations freeze when they exit horizon, the phase for all Fourier modes were well set before the modes of interest entered the Hubble radius. Inflation does predict the same initial phase for all Fourier modes.

CMB polarization states the strength of this results. Even if we build a theory which succeeds to produce a cosine mode and predicts the acoustic peaks in the CMB temperature APS, we still have to explain the negative peak around $100 < \ell < 200$ in the cross-correlation between CMB temperature fluctuations and E-mode polarization. This anti-correlation signal is the result of phase coherence at scales outside the Hubble radius at recombination. Hence, it requires a mechanism which shrinks the comoving horizon as inflation does.

3.1.4 CMB lensing

Weak lensing (WL) is characterized by a deflection field $\mathbf{d}$ which maps the shift in the direction of a photon path from the last scattering surface [160–162]:

$$\widetilde{\Theta}(\hat{\mathbf{n}}) = \Theta(\hat{\mathbf{n}} + \mathbf{d}(\hat{\mathbf{n}}))\,, \tag{3.13}$$

$$(\widetilde{Q} \pm \imath\widetilde{U})(\hat{\mathbf{n}}) = (Q \pm \imath U)(\hat{\mathbf{n}} + \mathbf{d}(\hat{\mathbf{n}}))\,, \tag{3.14}$$

where we mean with a tilde the lensed fields. At leading order this field can be written as the gradient of the lensing potential, i.e. $\mathbf{d} = \nabla\phi$. The lensing potential map and the deflection map can be expanded in harmonic space as [163, 164]:

$$\phi(\hat{\mathbf{n}}) = 2\int_0^{z_{\rm rec}} \frac{dz}{H(z)} \left(\frac{1}{\chi(z)} - \frac{1}{\chi(z_{\rm rec})}\right) \Phi(\hat{\mathbf{n}}, z)\,, \tag{3.15}$$

$$= \sum_\ell \sum_{\mathrm{m}=-\ell}^{\ell} \phi_{\ell\mathrm{m}} Y_{\ell\mathrm{m}}(\hat{\mathbf{n}})\,, \tag{3.16}$$

$$d_{\ell\mathrm{m}} = -\imath\sqrt{\ell(\ell+1)}\phi_{\ell\mathrm{m}}\,, \tag{3.17}$$

and the corresponding APS are:

$$C_\ell^{dd} = \langle d^*_{\ell\mathrm{m}} d_{\ell\mathrm{m}}\rangle\,, \tag{3.18}$$

$$= \ell(\ell+1)\, C_\ell^{\phi\phi}\,. \tag{3.19}$$

3.1.5 Primordial B-mode polarization

GWs are expected to leave an unambiguous imprint in the pattern of CMB polarization called the *B-mode polarization* [157, 165]. Inflation and the standard model of

cosmology predict that the primordial B-mode polarization power spectrum has two characteristic scales: one peak at large angular scales (low multipoles, $\ell < 10$), and another peak at $\ell \approx 80$. These peaks originate from different epochs: the former from the epoch of cosmic reionization when the Universe was a few hundred million years old, and the latter from the epoch of last scattering of CMB photons when the Universe was only 400,000 years old.

We have not yet detected a non-zero value of r. The latest 95 % CL upper bound is $r < 0.07$ [166–168]. This measurement has ruled out a host of once popular, textbook examples of inflation models such as those based upon a monomial potential, $V(\phi) \propto \phi^n$, with $n \geq 2$.

There are two major contaminants of the primordial B-mode signal. One is from gravitational lensing, an effect that can be removed to some extent by *delensing* (see Sec. 3.4.1 for more details). Another contaminant are *foregrounds*. CMB polarized foregrounds arise due to free-free, synchrotron, and dust emission, as well as extra-galactic sources.

3.2 Cosmological parameters from CMB

The ΛCDM is called the concordance cosmological model since it fits to current cosmological observations.

The ΛCDM model is based on six parameters: the physical CDM density parameter $\omega_{\rm c} \equiv \Omega_{\rm c} h^2$, the physical baryon density parameter $\omega_{\rm b} \equiv \Omega_{\rm b} h^2$, the age of the Universe expressed through the Hubble parameter measured today H_0 or alternatively the ratio between the sound horizon and the angular diameter distance at decoupling $\theta_{\rm s}$, the reionization optical depth τ, the scalar spectral index $n_{\rm s}$, and the curvature fluctuation amplitude $A_{\rm s}$.

Other possible parameters are fixed, e.g. the geometry of the spatial sections $\Omega_{\rm K} = 0$, the DE equation of state $w_{\rm DE} = -1$. However, in light of the new precise data, some of the assumptions made in the six parameters approach can be relaxed, but no impelling evidence of extra parameters is found.

3.2.1 Energy density content in the Universe

Parameters that determine the energy content of the Universe before recombination, such as the critical energy density of non-relativistic matter $\Omega_{\rm m}$ and relativistic components $\Omega_{\rm rel}$, play an important role in the physics of the acoustic peaks.

The critical energy density of baryons $\Omega_{\rm b}$ affects the acoustic oscillations through baryon inertia and the dependence of the photon mean-free path on the electron den-

sity. Their different inertia enhances the amplitude of the oscillations. Increasing the baryon density tends to decrease the damping processes (decrease the diffusion length). Increasing the baryon density reduces the speed of sound and pushes the acoustic peaks to smallest scales by moving the last scattering surface at early times. All these three effects can be appreciated from Fig. 3.2 (right panels).

The anisotropies on small angular scales decrease with matter density.

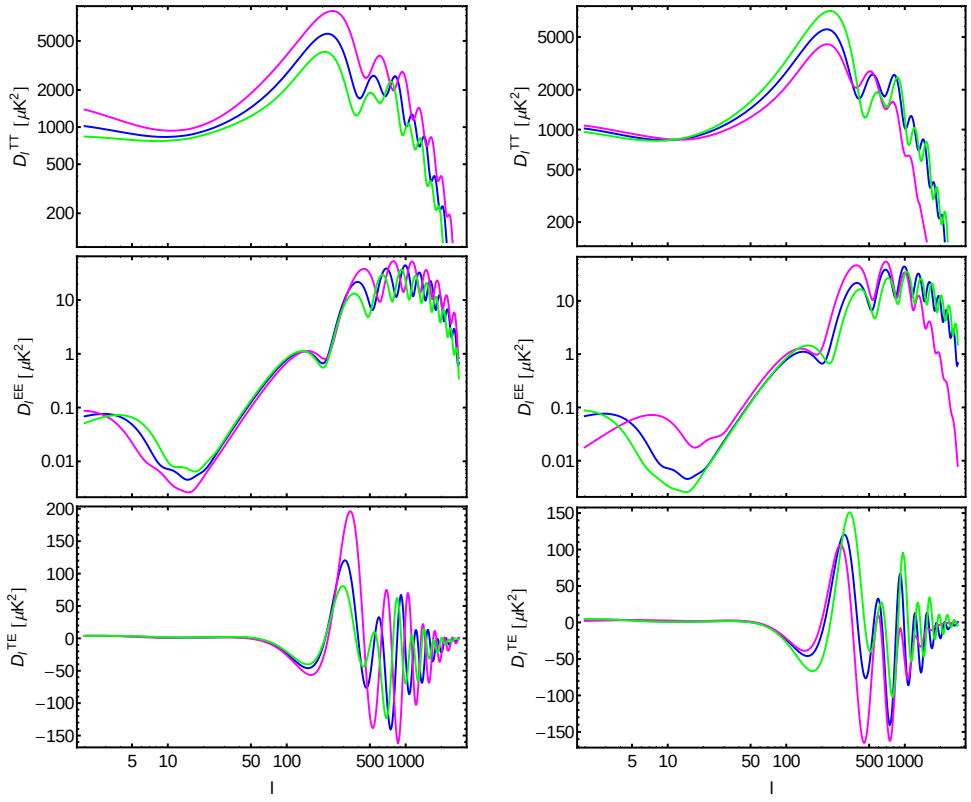

Figure 3.2: Dependence of $\mathcal{D}_\ell^{\rm X} \equiv \ell(\ell+1)C_\ell^{\rm X}/2\pi$ on the physical density in CDM (left panels) and baryons (right panels), for X=TT,TE,EE. The spectra on the left are for $\omega_{\rm c} = 0.045$ (magenta line), 0.12 (blue line), 0.23 (green line), and on the right for $\omega_{\rm b} = 0.0045$ (magenta line), 0.022 (blue line), 0.045 (green line).

Some fundamental parameters missing in the ΛCDM model are the neutrino mass and the number of relativistic degrees of freedom. The standard neutrino sector has

three flavors and lower limit of 0.06 eV on the total mass, when the direct hierarchy of neutrinos masses is considered. The effect of a total "small" mass could have a potentially observable effect on the formation of structure, as neutrino free-streaming damps the growth of perturbations. Present cosmological observations have shown no convincing evidence for a non-zero neutrino mass so far.

Under the standard assumptions of an exactly flat Universe, the cosmological constant energy density is fixed by a combination of the other cosmological parameters, where the radiation density is usually neglected.

The radiation density is dominated by the energy in the CMB background, and the COBE FIRAS experiment has determined its temperature to $T = 2.72548 \pm 0.00057$ K [169], corresponding to $\Omega_{\rm rad} = 2.47 \times 10^{-5} h^{-2}$.

3.2.2 Reionization

As scattering takes place between the free electrons and the CMB photons, primordial fluctuations are damped. This effect can be added directly to Eq. (3.1):

$$T = T \left[1 + \Theta e^{-\tau}\right] , \tag{3.20}$$

that would affect those scales within the Hubble scale at the time of reionization, small ℓ will be unaffected (see Fig. 3.3).

Due to the Eq. (3.20) ,measurements of the temperature APS provide a highly accurate measurement of the amplitude $A_{\rm s} e^{-2\tau}$. In order to break this degeneracy, large scale polarization measurements or CMB lensing information are required.

3.2.3 Early-Universe physics

As can be seen from Eq. (3.6), the CMB power spectrum is proportional to $A_{\rm s}$. The amplitude of the primordial power spectrum $A_{\rm s}$ moves the spectra up or down, it is the only one of all the parameters which can rise the amplitude of the APS (see Fig. 3.4).

The scalar spectral index $n_{\rm s}$ has the most distinctive shape and will be better and better characterized with the inclusion of smaller scales probe (see Fig. 3.4).

Since there is no observational evidence for the existence of primordial tensor perturbations, in the standard cosmological model they are set to zero. Tensors affect anisotropies only on scales larger than the Hubble scale at recombination, $\ell \lesssim 100$. Once they enter the Hubble radius, the amplitude of primordial GWs are damped. Therefore, the temperature and polarization power spectra are identical to the ΛCDM model on scales $\ell > 100$ where only scalars remain. Nevertheless, the tensor amplitude is degenerate with other cosmological parameters, as $n_{\rm s}$, $A_{\rm s}$ and τ.

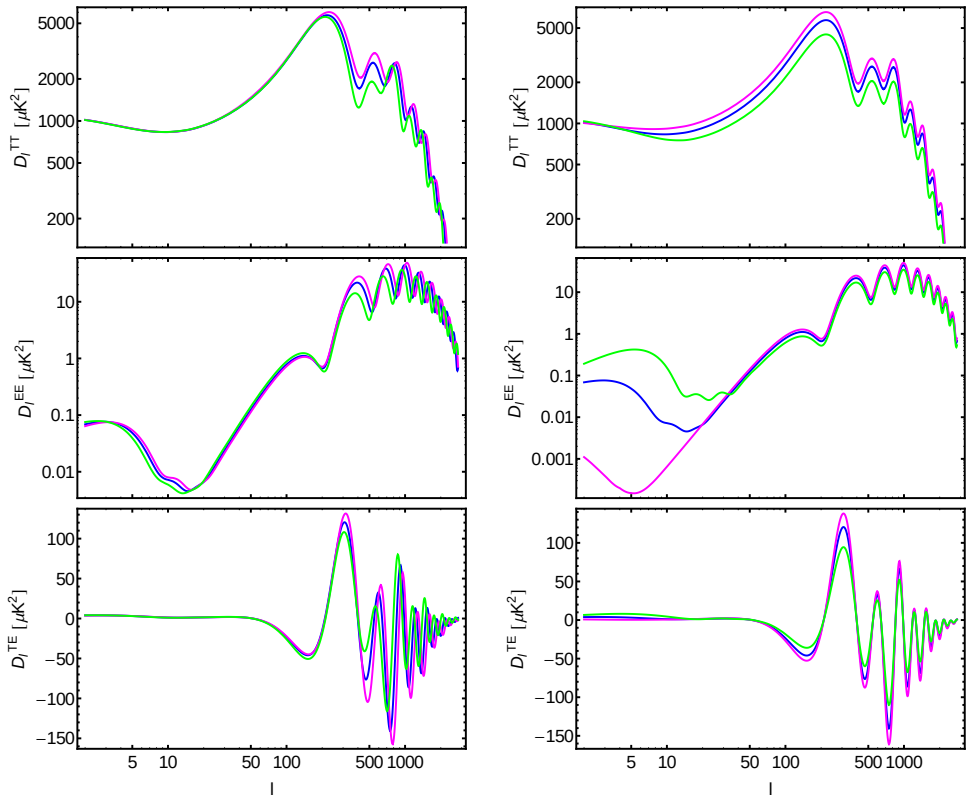

Figure 3.3: Dependence of $\mathcal{D}_\ell^{\rm X} \equiv \ell(\ell+1)\mathrm{C}_\ell^{\rm X}/2\pi$ on the Hubble parameter (left panels) and optical depth (right panels), for X=TT,TE,EE. The spectra on the left are for $H_0 = 60$ (magenta line), 67 (blue line), 80 (green line), and on the right for $\tau = 0.001$ (magenta line), 0.078 (blue line), 0.1 (green line).

3.3 Galaxy clustering

Within the CDM paradigm, the shape of the power spectrum depends primarily on the PPS and on the combination $\Omega_{\rm m}h$ which determines the horizon scale at matter-radiation equality, with a subdominant dependence on the baryon density. It does not matter how small initial overdensity was, as time evolves matter accumulates in initially overdense region.

The matter distribution is most easily probed by observing the galaxy distribution, but this must be done with care as the galaxies do not perfectly trace the DM distri-

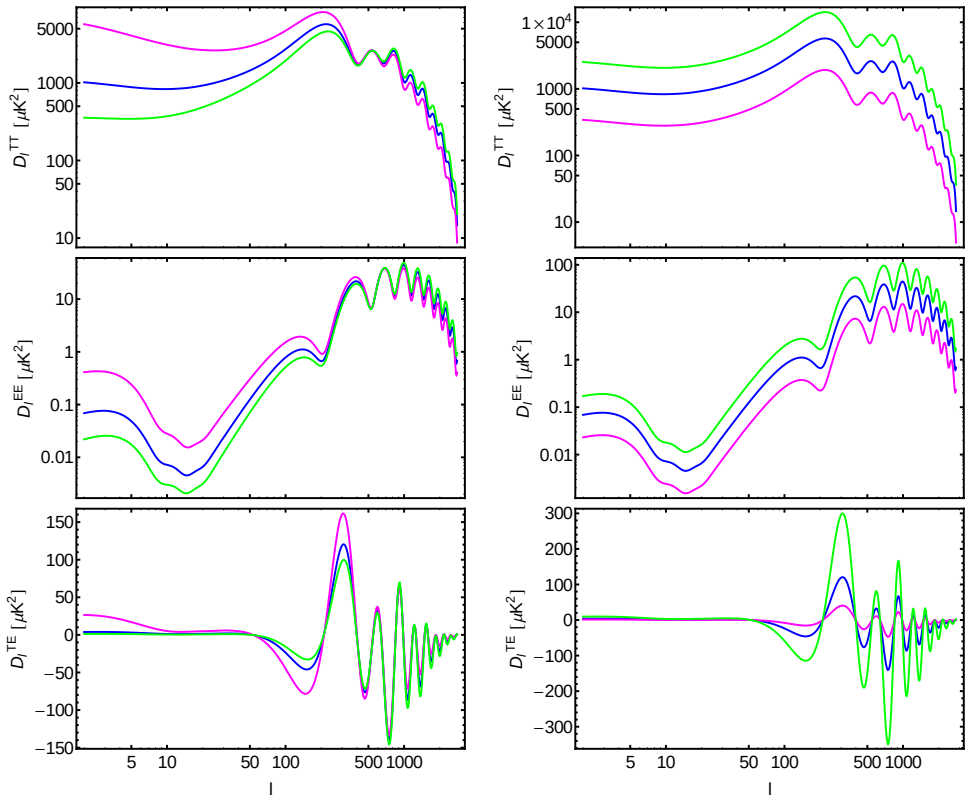

Figure 3.4: Dependence of $\mathcal{D}_\ell^{\rm X} \equiv \ell(\ell{+}1)\mathrm{C}_\ell^{\rm X}/2\pi$ on the scalar spectral index (left panels) and the amplitude of the primordial curvature fluctuations (right panels), for X=TT,TE,EE. The spectra on the left are for $n_{\rm s} = 0.6$ (magenta line), 0.96 (blue line), 1.2 (green line), and on the right for $\ln\left(10^{10}\,A_{\rm s}\right) = 2$ (magenta line), 3.1 (blue line), 4 (green line).

bution: they are a *biased tracer* of the DM. Moreover, different types of galaxies are characterized by different bias.

The observed 3D galaxy distribution is in redshift space, where the observed redshift is the combination of the Hubble expansion and the line-of-sight peculiar velocity, leading to linear and non-linear dynamical effects which also depend on the cosmological parameters.

3.3.1 The matter power spectrum

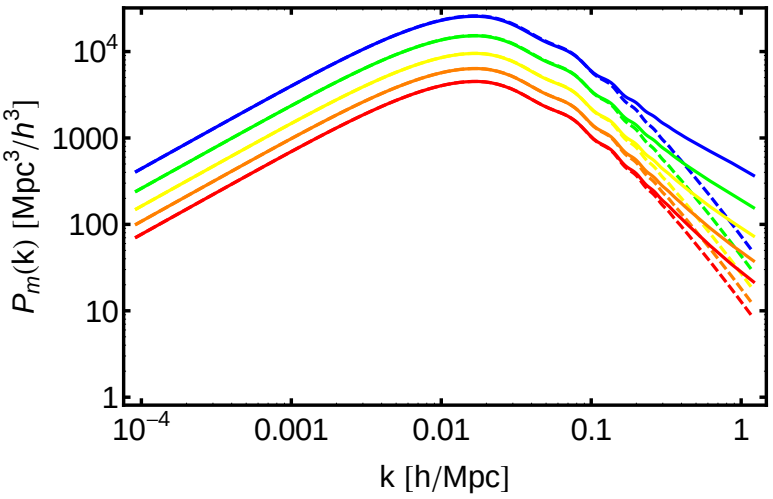

Figure 3.5: From top to bottom, we plot the matter power spectrum for z=0, 0.5, 1.0, 1.5, 2.0, respectively. Dashed lines represent the linear matter power spectrum.

Matter perturbations are connected to the metric fluctuations by the Einstein equations (see Sec. 2.1.4). The Newtonian potential at low redshift can be written:

$$\Phi(k,a) = \Phi_0(k)T(k)D(a)\,, \tag{3.21}$$

where the transfer function $T(k)$ accounts for wavelength's Hubble radius crossing and the effect of the transition from radiation to matter phase, $D(a)$ is the *growth factor*. So we have:

$$\Phi(k,a) = \frac{9}{10}\Phi_0(k)T(k)\frac{D(a)}{a}\,, \tag{3.22}$$

where the potential drops by a factor 9/10 as the Universe goes from radiation to matter domination. On small scales, the density perturbation in DM can be relate to the gravitational potential through the Poisson equation:

$$4\pi G\rho_{\rm m}a^2\delta_{\rm m} = -k^2\Phi(k,a)\,, \tag{3.23}$$

and we get:

$$\delta_{\rm m}(\mathbf{k},a) = \frac{3}{5}\frac{k^2}{\Omega_{\rm m}H_0^2}\Phi_0(k)T(k)D(a)\,. \tag{3.24}$$

What we actually observe today is the isotropic two-point correlation function of the matter density perturbations $\delta_{\rm m}$, or its Fourier transform matter power spectrum $P_{\rm m}(k)$:

$$\langle\delta_{\rm m}(\mathbf{k},a)\delta^*_{\rm m}(\mathbf{k}',a)\rangle = (2\pi)^3\delta^{(3)}_{\rm D}(\mathbf{k}-\mathbf{k}')P_{\rm m}(k)\,. \tag{3.25}$$

On small scales the DM dimensionless power spectrum, assuming a power-law PPS, is:

$$\mathcal{P}_{\rm m}(k) = \frac{4}{25}\frac{A_{\rm s}}{\Omega_{\rm m}H_0^2}\left(\frac{k}{k_*}\right)^{n_{\rm s}+3}T^2(k)D^2(a)\,, \tag{3.26}$$

since in conformal Newtonian gauge, after inflation, $\mathcal{R} = 3\Phi/2$ thus $P_{\mathcal{R}} = 9P_\Phi/4$.

3.3.2 The galaxy power spectrum

Observations of galaxies can be used to trace the invisible DM distribution in order to estimate the matter and the primordial power spectra.

On the largest scales, the galaxies are expected to trace the presence of DM, except for a constant multiplier to the power spectrum, known as *linear bias*, which is a multiplicative factor for:

$$\delta_{\rm g} \simeq b \times \delta_{\rm m}\,. \tag{3.27}$$

In addition, *redshift space distortions* (RSD) increase the real power spectrum due to peculiar velocities, in the radial direction, not associated with the Hubble flow:

$$\delta_{\rm RSD}(\mathbf{k}) \simeq \beta\mu_{\rm k}^2\,\delta_{\rm m}(\mathbf{k})\,. \tag{3.28}$$

In the linear regime, the redshift-space power spectrum can be modelled as [170, 171]:

$$P_{\rm m}^{\rm RSD}(k,\mu_{\rm k}) = (1+\beta\mu_{\rm k}^2)^2P_{\rm m}(k)\,, \tag{3.29}$$

where $\mu_{\rm k}$ is the cosine of the angle between the line of sight direction and the wavenumber direction within the survey $\mu_{\rm k} = \hat{k}\cdot\hat{r}$, and the real-space power spectrum can be

reconstructed by a linear combination of different redshift-space multipoles to characterize the quantity β, defined as $\beta = f/b$ with f, the *growth rate*, defined as the logarithmic derivative of the growth factor:

$$f(k,z) \equiv \frac{d \ln D(k,z)}{d \ln a} \,. \tag{3.30}$$

On small scales, non-linear collapse and random motions in virialized objects stretch systems along the line-of-sight, givin rise to the *Fingers of God* (FoG) effect, which inflates overdense regions and depresses their density constrast. We model the FoG and the error in the determination of the redshift sources respectively as [172]:

$$G_{\rm FoG}(k,\mu_{\rm k},z) = e^{-k^2\mu_{\rm k}^2\sigma_{\rm v}^2} \times e^{-k^2\mu_{\rm k}^2\sigma_{\rm r}^2} \,, \tag{3.31}$$

where $\sigma_{\rm v}^2$ is the square of the velocity dispersion, which depends on the velocity power spectrum, and the expected error in the determination of the redshift z, which depends on the survey specifications, is:

$$\sigma_{\rm r} = \sigma(z) c/H(z) \,. \tag{3.32}$$

In this thesis we choose a value of $\sigma_{\rm v} = 7$ Mpc for our fiducial value as in Refs. [173, 174], which corresponds to a velocity dispersion of ~ 500 km/s. We define $\sigma_{\rm tot}$ as $\sqrt{\sigma_{\rm v}^2 + \sigma_{\rm r}^2}$.

Simple Poisson sampling correction is included by adding a shot noise contribution corresponding to the inverse of the galaxy number density at that redshift.

The observed galaxy power spectrum is also affected by geometrical effects due to the incorrect assumption of the reference cosmology with respect to the true/fiducial one [175, 176]:

$$\begin{aligned} P_{\rm obs}(k^{\rm ref},\mu_{\rm k}^{\rm ref},z) = \left(\frac{D_{\rm A}^{\rm ref}(z)}{D_{\rm A}(z)}\right)^2 \frac{H(z)}{H^{\rm ref}(z)} b^2(z) \left[1+\beta(k,z)\mu_k^2\right]^2 P_{\rm m}(k,z)\, G_{\rm FoG}(k,\mu_{\rm k},z) \\ + P_{\rm shot}(z) \,, \end{aligned} \tag{3.33}$$

where the prefactor encapsulates the geometrical distortions due to the Alcock-Paczynski effect [177] and the distorted coordinates are defined as [175]:

$$k = k^{\rm ref} \sqrt{\left(\frac{H\mu_{\rm k}^{\rm ref}}{H^{\rm ref}}\right)^2 + \left(\frac{D_{\rm A}^{\rm ref}}{D_{\rm A}}\right)^2 \left[1 - \left(\mu_{\rm k}^{\rm ref}\right)^2\right]} \,, \tag{3.34}$$

and

$$\mu_{\rm k} = \mu_{\rm k}^{\rm ref} \left(\frac{H}{H^{\rm ref}}\right)^2 \frac{k^{\rm ref}}{k} \,. \tag{3.35}$$

For the case of current galaxy surveys, the gauge where the matter power spectrum is calculated does not matter since gauge effects start to become important on scales approaching the Hubble radius scale. Perturbation are of the order of the Hubble radius at the epoch of the observed source, which is much larger than the turnover for observed redshift $z \in [0, 10]$. For example, at z=2 the angular extent of the Hubble radius is $\theta_H \equiv H^{-1}/D_{\rm A} \simeq 50^\circ$.

Moreover, lightcone effects affect the inferred $P(k)$ since constant-time slices are in principle unobservable for significant redshifts and, for a given observer, are not uniquely associated with redshift.

These correction have been analyzed in detail [178–184] and now results obtained in different gauge, i.e. synchronous, Newtonian and gauge invariant, agree to first oder correction in GR.

3.4 Comparison with data

We start our consideration recalling the Bayes' theorem:

$$P(\theta|d) \propto P(\theta)P(d|\theta)\,, \tag{3.36}$$

where $P(\theta|d)$ is the probability of the parameters θ given the data. Note that we drop the normalization factor since it is irrelevant to obtain the confidence levels (CL). CL for each parameter are defined as the regions in which the probability exceeds a given value.

In order to analyze data, both real and simulated ones, the key ingredient is to specify a likelihood function to compare them with a theory and determine best estimate parameters of the theoretical model where the posterior probability peaks along with errors (determinated by the width of the posterior function). In case the data are Gaussian distributed, the likelihood function is:

$$P(d|\theta) \propto \mathcal{L} = \frac{1}{|2\pi\mathbf{C}|^{1/2}} \exp\left\{-\frac{1}{2}\mathbf{d}^\dagger\mathbf{C}^{-1}\mathbf{d}\right\}\,, \tag{3.37}$$

where $\mathbf{C}$ is the signal plus noise covariance matrix, and $\mathbf{d}$ is data vector.

3.4.1 CMB

If the CMB is Gaussian, as expected in linear theory, the corresponding harmonic components $a^X_{\ell \rm m}$ are Gaussian variables with mean zero. We consider n Gaussian fields defined by an n-dimensional vector $\mathbf{a}_{\ell \rm m}$ with covarince matrix $\mathbf{C}_\ell \equiv \langle \mathbf{a}^\dagger_{\ell \rm m}\mathbf{a}_{\ell \rm m}\rangle$ and

estimator $\hat{\mathbf{C}}_\ell$ given by Eq. (3.12) [185, 186]. Since the $\mathbf{a}_{\ell\mathrm{m}}$ are assumed to be Gaussian and statistically isotropic they have a Gaussian likelihood:

$$\begin{aligned} -2\ln(P(\{\mathbf{a}_{\ell\mathrm{m}}\}|\mathbf{C}_\ell)) &= \sum_{\mathrm{m}} \left[\mathbf{a}^\dagger_{\ell\mathrm{m}}\mathbf{C}_\ell^{-1}\mathbf{a}_{\ell\mathrm{m}} + \ln|2\pi\mathbf{C}_\ell|\right] , \\ &= (2\ell+1)\left(\mathrm{Tr}\left[\hat{\mathbf{C}}_\ell\mathbf{C}_\ell^{-1}\right] + \ln|\mathbf{C}_\ell|\right) + \mathrm{const}\,. \end{aligned} \tag{3.38}$$

Normalizing with respect to $\hat{\mathbf{C}}_\ell$ we obtain:

$$P(\hat{\mathbf{C}}_\ell|\mathbf{C}_\ell) \propto \frac{|\hat{\mathbf{C}}_\ell|^{\frac{2\ell-n}{2}}}{|\mathbf{C}_\ell|^{\frac{2\ell+1}{2}}}\exp\left\{-\frac{2\ell+1}{2}\mathrm{Tr}\left[\hat{\mathbf{C}}_\ell\mathbf{C}_\ell^{-1}\right]\right\} . \tag{3.39}$$

When $n = 1$, for example when only the temperature is considered, the likelihood function (3.38) reduces to:

$$-2\ln(P(\hat{C}_\ell|C_\ell)) = (2\ell+1)\left[\frac{\hat{C}_\ell}{C_\ell} + \ln(C_\ell) - \frac{2\ell-1}{2\ell+1}\ln(\hat{C}_\ell)\right] + \mathrm{const}\,. \tag{3.40}$$

In general, we can rewrite Eq. (3.38) as:

$$-2\ln(P(\left\{\hat{\mathbf{C}}_\ell\right\}|\mathbf{C}_\ell)) = \sum_\ell (2\ell+1)\left\{\mathrm{Tr}\left[\hat{\mathbf{C}}_\ell\mathbf{C}_\ell^{-1}\right] - \ln|\hat{\mathbf{C}}_\ell\mathbf{C}_\ell^{-1}| - n\right\} , \tag{3.41}$$

where we have normalized the likelihood function so that $\ln\mathcal{L} = 0$ when $\mathbf{C}_\ell = \hat{\mathbf{C}}_\ell$.

Including temperature and polarization, the data vector is $\mathbf{a}_{\ell\mathrm{m}} = (a^T_{\ell\mathrm{m}}, a^E_{\ell\mathrm{m}}, a^B_{\ell\mathrm{m}})^\dagger$ and the covariance matrix:

$$\mathbf{C}_\ell = \begin{pmatrix} C_\ell^{TT} & C_\ell^{TE} & 0 \\ C_\ell^{TE} & C_\ell^{EE} & 0 \\ 0 & 0 & C_\ell^{BB} \end{pmatrix} , \tag{3.42}$$

where we assumed $C_\ell^{TB} = C_\ell^{EB} = 0$ for invariance under parity transformation.

Instead of computing the exact likelihood function, we can find alternative ways to approximate it on minimal information. Now, the errors associated with each parameter θ_i can be derived from a *Fisher matrix*:

$$\mathbf{F}_{\mathrm{ij}} = \left\langle \frac{\partial^2\mathcal{L}}{\partial\theta_\mathrm{i}\partial\theta_\mathrm{j}} \right\rangle = \sum_\ell \frac{2\ell+1}{2} f_{\mathrm{sky}}\mathrm{Tr}\left[\mathbf{C}_\ell^{-1}\mathbf{C}_{\ell,\mathrm{i}}\mathbf{C}_\ell^{-1}\mathbf{C}_{\ell,\mathrm{j}}\right] , \tag{3.43}$$

computed in the vicinity of the best-fit model. Indeed, after marginalization over all other free parameters, the $1\,\sigma$ error (68 % CL) on a parameter $\theta_{\rm i}$, the so called *conditional error*, would be larger or equal to:

$$\sigma(\theta_{\rm i}) = \sqrt{(F^{-1})_{\rm ii}}\,, \tag{3.44}$$

which is called Cramer-Rao bond.

Due to lensing effect, CMB data are not exactly Gaussian. However, the difference between the un-lensed and lensed power spectra for (TT,TE,EE) is small that Eq. (3.43) remains a good approximation, at least when the B-mode is not included. Therefore, the map of the lensing potential can be added in the data vector:

$$\mathbf{C}_\ell = \begin{pmatrix} C_\ell^{TT} & C_\ell^{TE} & C_\ell^{Td} \\ C_\ell^{TE} & C_\ell^{EE} & 0 \\ C_\ell^{Td} & 0 & C_\ell^{dd} \end{pmatrix}\,, \tag{3.45}$$

where the cross-correlation between the temperature map and the lensing map C_ℓ^{Td} does not vanish because of the late time ISW effect.

In presence of isotropic and uncorrelated noise $n_{\ell \rm m}$ with known power spectrum N_ℓ, the observed field $\mathbf{a}_{\ell \rm m} + \mathbf{n}_{\ell \rm m}$ is just another Gaussian field with power spectrum $\bar{C} = C_\ell + N_\ell$, which can be straightforwardly substituted in all the equations above. We include the noise power spectrum with Gaussian beam profile [187]:

$$N_\ell^X = w_X^{-1} b_\ell^{-2}\,, \tag{3.46}$$

where $N_\ell^{\rm TE} = 0$, and $N_\ell^{\rm EE} = N_\ell^{\rm BB}$. Here b_ℓ^2 is the beam window function, assumed Gaussian, with $b_\ell = e^{-\ell(\ell+1)\theta^2_{\rm FWHM}/16\ln 2}$; $\theta_{\rm FWHM}$ is the full width half maximum (FWHM) of the beam in radians; $w_{\rm TT}$ and $w_{\rm EE}$ are the inverse square of the detector noise level on a steradian patch for temperature and polarization, respectively. For multiple frequency channels, $w_X b_\ell^2$ is replaced by the sum of this quantity for each channel:

$$N_\ell^X = \left[\sum_{\rm channels} \frac{1}{N^X_{\ell,{\rm i}}}\right]^{-1}\,. \tag{3.47}$$

The noise for the lensing potential from the CMB EB estimator is given as [163, 188]:

$$N_\ell^{\phi\phi} = \left[\frac{1}{2\ell+1}\sum_{\ell_1}\sum_{\ell_2} |f^{EB}_{\ell_1\ell_2\ell}|^2 \left(\frac{1}{\bar{C}^{BB}_{\ell_1}}\right)\left(\frac{\left(C^{EE}_{\ell_2}\right)^2}{\bar{C}^{EE}_{\ell_2}}\right)\right]^{-1}\,, \tag{3.48}$$

with:

$$f^{EB}_{\ell_1\ell_2\ell} = \frac{F^{-2}_{\ell_1\ell_2\ell} - F^{2}_{\ell_1\ell_2\ell}}{2\imath}\,, \tag{3.49}$$

and:

$$F^{s}_{\ell_1\ell_2\ell} = [-\ell_1(\ell_1{+}1){+}\ell_2(\ell_2{+}1){+}\ell_3(\ell_3{+}1)]\sqrt{\frac{(2\ell_1+1)(2\ell_2+1)(2\ell_3+1)}{16\pi}}\begin{pmatrix}\ell_1 & \ell_2 & \ell_3\\ -s & s & 0\end{pmatrix}, \tag{3.50}$$

where the matrix represents the Wigner 3-j symbol. The coupling coefficient (3.49) gives the B-mode APS generated by the unlensed E-mode at first order in the lensing potential, and allows to calculate an analytical expression for the estimate B-mode APS [189, 190]:

$$C^{BB,estimated}_{\ell} = \left[\frac{1}{2\ell+1}\sum_{\ell_1}\sum_{\ell_2}|f^{EB}_{\ell_1\ell_2\ell}|^2\left(\frac{(C^{EE}_{\ell_1})^2}{\bar{C}^{EE}_{\ell_1}}\right)\left(\frac{(C^{\phi\phi}_{\ell_2})^2}{\bar{C}^{\phi\phi}_{\ell_2}}\right)\right]^{-1}, \tag{3.51}$$

and this intuitively allows to extract the unlensed signal, so called delensed, by:

$$C^{BB,delens}_{\ell} = C^{BB}_{\ell} - C^{BB,estimated}_{\ell}\,. \tag{3.52}$$

3.4.2 Galaxy survey

Under the assumption that the density field has a Gaussian statistics and uncorrelated Fourier modes, the Fisher matrix for the broadband power spectrum in Eq. (3.33), for a given redshift bin with $\bar{z}$ as centroid value, is [191]:

$$\mathbf{F}^{\rm gg}_{\rm ij}(\bar{z}) = \int_{k_{\rm min}}^{k_{\rm max}}\frac{{\rm d}^3\mathbf{k}}{2(2\pi)^3}\frac{\partial\ln P_{\rm obs}(\mathbf{k}|\bar{z})}{\partial\theta_{\rm i}}\Big|_{\bar{\theta}}\frac{\partial\ln P_{\rm obs}(\mathbf{k}|\bar{z})}{\partial\theta_{\rm j}}\Big|_{\bar{\theta}}V_{\rm eff}(\mathbf{k}|\bar{z}) \tag{3.53}$$

$$= \int_{k_{\rm min}}^{k_{\rm max}}\frac{k^2dk}{(2\pi)^2}\int_0^1 d\mu\frac{\partial\ln P_{\rm obs}(k,\mu|\bar{z})}{\partial\theta_{\rm i}}\Big|_{\bar{\theta}}\frac{\partial\ln P_{\rm obs}(k,\mu|\bar{z})}{\partial\theta_{\rm j}}\Big|_{\bar{\theta}}V_{\rm eff}(k,\mu|\bar{z})\,, \tag{3.54}$$

where the effective volume of the survey in Fourier space, which determines the mode counts, is [192]:

$$V_{\rm eff}(k,\mu|\bar{z}) \simeq \left[\frac{\bar{n}_{\rm g}(\bar{z})P_{\rm obs}(k,\mu|\bar{z})}{\bar{n}_{\rm g}(\bar{z})P_{\rm obs}(k,\mu|\bar{z})+1}\right]^2 V_{\rm surv}(\bar{z})\,, \tag{3.55}$$

which depends on the geometrical volume of the survey:

$$V_{\rm surv}(\bar{z}) = \frac{4\pi f_{\rm sky}}{3}\left[\chi^3(\bar{z}+\Delta z/2) - \chi^3(\bar{z}-\Delta z/2)\right] , \tag{3.56}$$

and on the average number density, $\bar{n}_{\rm g}$, of tracers in a specific redshift bin.

At large scales different wavelengths are correlated. This effect on the observed power spectrum is due to the beam of the instrument and to the limit, given by the volume of the survey, on the largest accessible wavelengths. To avoid this correlation, we take a discrete number of wavenumber by considering top-hat bins in the linear k-space. We set $k_{\rm min}(\bar{z}) = 2\pi/\sqrt[3]{V_{\rm surv}(\bar{z})}$, which depends on the volume of the z-bin considered, and on the width for the k-bin $\Delta k(\bar{z}) = 1.4/\sqrt[3]{V_{\rm surv}(\bar{z})}$, as in Ref. [193]. Eq. (3.53) can be rewritten as a binned sum over k and μ:

$$\mathbf{F}^{gg}_{\rm ij}(\bar{z}) = \sum_{k,\mu} \frac{\partial \ln P_{\rm obs}(k,\mu|\bar{z})}{\partial\theta_{\rm i}}\Big|_{\bar{\theta}} \left[{\rm Cov}_{\mathbf{k}}(\bar{z})\right]^{-1} \frac{\partial \ln P_{\rm obs}(k,\mu|\bar{z})}{\partial\theta_{\rm j}}\Big|_{\bar{\theta}} , \tag{3.57}$$

where

$${\rm Cov}_{\mathbf{k}}(\bar{z}) = \frac{(2\pi)^2}{k^2\Delta k\Delta\mu}\frac{1}{V_{\rm eff}(k,\mu|\bar{z})} . \tag{3.58}$$

The derivative in Eq. (3.57) is [194, 195]:

$$\begin{aligned}\frac{{\rm d}\ln P_{\rm obs}}{{\rm d}\theta_{\rm i}}(k,\mu_{\rm k}|z_{\rm i}) \simeq{}& \frac{\partial \ln P_m(k|z_{\rm i})}{\partial\theta_{\rm i}} + \frac{2\mu_{\rm k}^2}{1+\beta(k|z_{\rm i})\mu_{\rm k}^2}\frac{\partial\beta(k|z_{\rm i})}{\partial\theta_{\rm i}} \\ &+ \left[1 + \frac{4\beta(k|z_{\rm i})\mu_{\rm k}^2}{1+\beta(k|z_{\rm i})\mu_{\rm k}^2}\left(1-\mu_{\rm k}^2\right) + \mu_{\rm k}^2\frac{\partial\ln P_{\rm m}(k|z_{\rm i})}{\partial\ln k}\right]\frac{\partial\ln H(z_{\rm i})}{\partial\theta_{\rm i}} \\ &+ \left[-2 + \frac{4\beta(k|z_{\rm i})\mu_{\rm k}^2}{1+\beta(k|z_{\rm i})\mu_{\rm k}^2}\left(1-\mu_{\rm k}^2\right) - \left(1-\mu_{\rm k}^2\right)\frac{\partial\ln P_{\rm m}(k|z_{\rm i})}{\partial\ln k}\right]\frac{\partial\ln D_{\rm A}(z_{\rm i})}{\partial\theta_{\rm i}} \\ &+ \frac{2}{1+\beta(k|z_{\rm i})\mu_{\rm k}^2}\frac{\partial\ln b(z_{\rm i})}{\partial\theta_{\rm i}} + \frac{1}{P_{\rm obs}(k,\mu_{\rm k}|z_{\rm i})}\frac{\partial P_{\rm shot}(z_{\rm i})}{\partial\theta_{\rm i}} - k^2\mu_{\rm k}^2\frac{\partial\sigma^2_{\rm tot}}{\partial\theta_{\rm i}} .\end{aligned} \tag{3.59}$$

4 The *Planck* results

In 1992, two space-based CMB experiments (COBRAS and SAMBA) were proposed to ESA. In 1996, following assessment studies, ESA selected a combined mission called COBRAS/SAMBA as the third Medium-Size Mission (M3) of the Horizon 2000 Scientific Programme. The merging of the two proposals was subsequently renamed as *Planck*.

The COBRAS instrument (led by the PI Nazzareno Mandolesi), which covers the frequencies 30, 44, and 70 GHz in temperature and polarization with radiometers, has been renamed LFI (Low Frequency Instrument). The SAMBA instrument (led by the PI Jean Loup Puget), which covers the frequencies from 100 to 857 GHz (from 100 to 353 GHz both in temperature and polarization) with bolometers, has been renamed HFI (High Frequency Instrument).

The *Planck* satellite was launched in May 2009 togheter with Hershel. With an improved angular resolution (3 times that of WMAP), enhanced sensitivity (more than 5 times the sensitivity of WMAP), lower noise at the CMB frequencies and wide frequency coverage (30-857 GHz), *Planck* measured the CMB temperature power spectrum with an accuracy set by fundamental astrophysical limits, and the polarization pattern at frequencies not covered by WMAP.

At the time this thesis has been written, two cosmological releases has been published, the first one on nominal mission temperature data in 2013 [124] and a second one in 2015 [125] including full mission temperature data and a first set of polarization data. In both releases lensing maps and likelihood have also been released.

In the next sections, we will present in more details implications for single field inflation and for the simplest scalar-tensor dark energy model.

4.0.3 Maps

Planck has produced full sky maps at nine frequency channels in temperature and at seven frequencies in polarization [196, 197]. These nine channels span over a decade in frequency, mapping out not only the CMB, but also synchrotron, dust emission and anomalous dust, and extragalactic point sources, called foregrounds.

In order to separate the different components of the sky and extract the CMB in

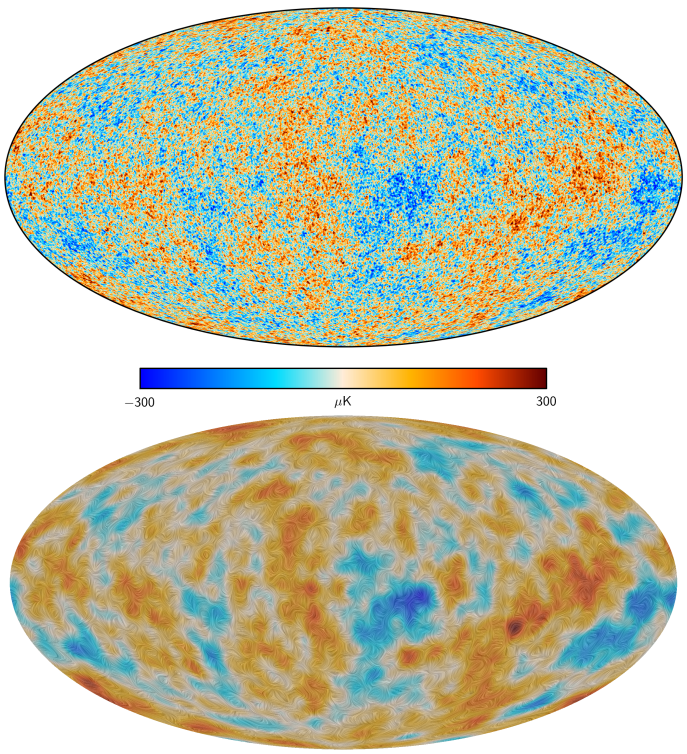

Figure 4.1: Top: Map of CMB temperature from SMICA. Bottom: CMB Polarization filtered around 5 degrees. Reproduced with permission from Astronomy & Astrophysics, ESO; original source ESA and the Planck Collaboration.

temperature and polarization *Planck* has used four different component separation methods all giving very consistent CMB maps [198]. In Fig. 4.1 we show the results of one of the method (SMICA) in temperature and polarization [1].

4.0.4 Power Spectra

In Fig. 4.2 and Fig. 4.3 we show the *Planck* 2015 APS in temperature and polarization. The spectra shown are the temperature TT autocorrelation, the E-mode autocorrelation EE, the cross-correlation between temperature and E-mode polarization TE.

[1] In the 2015 release the lowest multipoles ($\ell \lesssim 50$) of the polarization map have been filtered out, since systematic effects were not satisfactorily understood since systematic effects were not satisfactorily understood. For a recent update on the low-ℓ polarization see [24, 199]

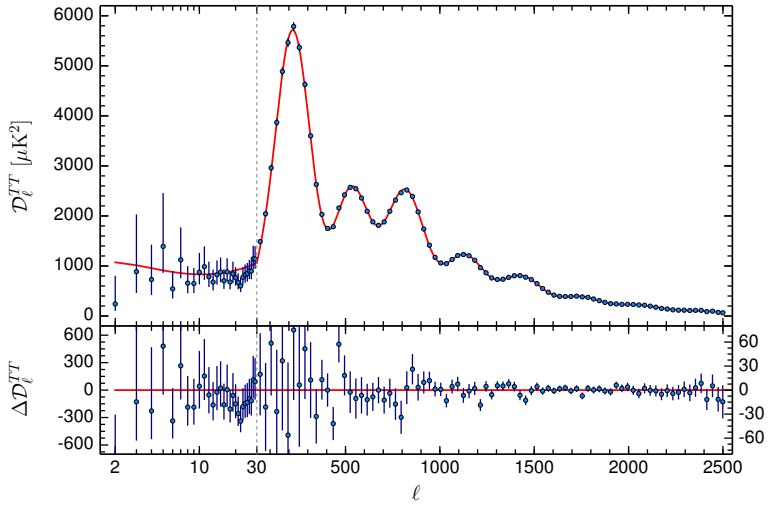

Figure 4.2: The *Planck* 2015 temperature power spectrum. Residuals with respect to the best-fit for the theoretical ΛCDM model are shown in the lower panel. Reproduced with permission from Astronomy & Astrophysics, ESO; original source ESA and the Planck Collaboration. Taken from [168].

4.0.5 Lensing

Gravitational lensing distoces the pattern of CMB anisotropies, providing information on the geometry of our Universe and structure formation, which would be otherwise degenerate in the information imprinted on the last scattering surface. The CMB lensing has distinctive signatures on the angular power spectra and has a non-Gaussian contribution to the CMB anisotropies. The lensing induce a smoothing of the acoustic peaks in temperature anisotropies, and generates a secondary non-zero B-mode polarization by lensing the primordial E-mode of the last scattering surface. This signal represents one of the main contaminants for the detection of the primordial B-mode polarization from inflation. Using its non-Gaussian contribution to CMB anisotropies *Planck* detected the lensing with a statistical significance of more than $40\,\sigma$ and was expected to reconstruct a full-sky map of the projected mass distribution. We show the lensing map in Fig. 4.4 and the power spectrum of the deflection field in Fig. 4.5.

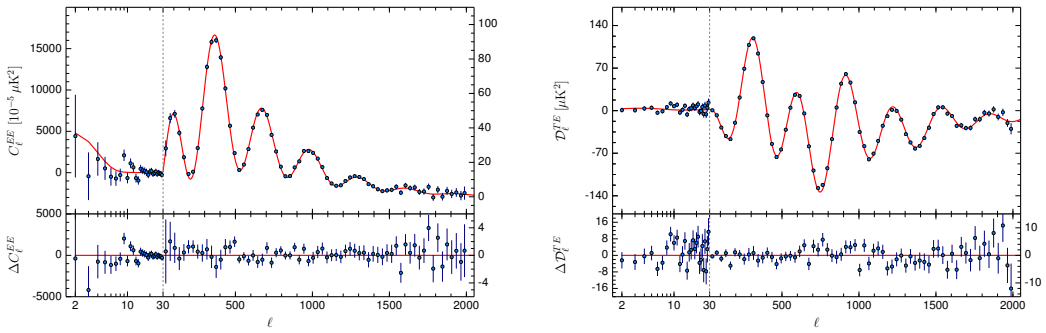

Figure 4.3: The *Planck* 2015 TE and EE spectra. The theoretical TE and EE spectra (plotted in red) are computed from the *Planck* TT+lowP best-fit model.Residuals with respect to the best-fit for the theoretical ΛCDM model are shown in the lower panel. Reproduced with permission from Astronomy & Astrophysics, ESO; original source ESA and the Planck Collaboration. Taken from [168]

4.1 Likelihood and cosmological parameters

The *Planck* 2015 likelihoods [168] are used to derive the constraints on the parameters of the standard cosmological model and its extensions. The *Planck* likelihood use a hybrid approach with the combination of one likelihood dedicated to low-ℓ and another to high-ℓ. The *Planck* low-ℓ likelihood is a fully pixel-based likelihood with temperature and polarization with an ℓ-range $2 < \ell < 29$ in TT, TE, EE, and BB. This low-ℓ likelihood is based on the foreground-cleaned LFI maps at 70 GHz and the temperature map derived by the component separation method `Commander` [168]. The polarization part of this likelihood is denoted as lowP in the following. The *Planck* high-ℓ likelihood is based on a multi-variante Gaussian approximation and covers the multipoles range $30 < \ell < 2500$. It uses the half-mission cross-power spectra of the 100 GHz, 143 GHz, and 217 GHz channels. The likelihood takes foregrounds and secondary anisotropies into account [168]. The high-ℓ likelihood with the inclusion of the $\ell = 2 - 29$ temperature multipoles of the low-ℓ likelihood is denoted *Planck* TT for temperature, and *Planck* TT,TE,EE when including polarization.

The *Planck* 2015 results for the cosmological parameters of ΛCDM model are summarized in Tab. 4.1, which also shows the consistency of temperature (TT), and po-

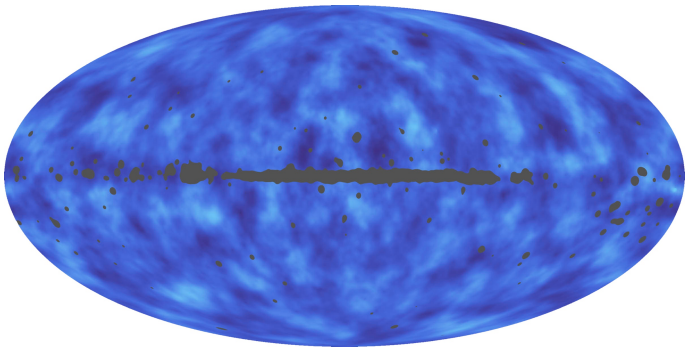

Figure 4.4: *Planck* 2015 lensing potential map. Reproduced with permission from Astronomy & Astrophysics, ESO; original source ESA and the Planck Collaboration.

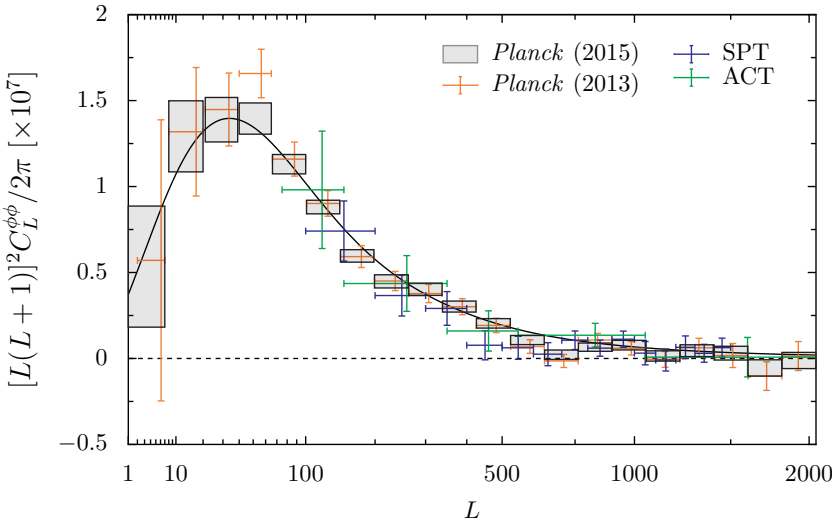

Figure 4.5: Lensing potential power spectrum estimate from the 2015 data release [200], based on the SMICA CMB map, as well as previous reconstructions from Planck and other experiments for comparison. Reproduced with permission from Astronomy & Astrophysics, ESO; original source ESA and the Planck Collaboration.

larization (EE), and the cross-correlation high-ℓ data separatly. [2] In the rest of this

[2]Note that the results including polarization at high-ℓ may be considered preliminary due to un-

section, we will present in more details the implications of *Planck* 2015 data for simple field inflation and for the simplest scalar-tensor DE model.

Table 4.1: Parameters of the base ΛCDM cosmology computed from the 2015 baseline *Planck* likelihoods, illustrating the consistency of parameters determined from the temperature and polarization spectra at high multipoles. Columns [2] and [3] use only the TE and EE spectra at high multipoles, and only polarization at low multipoles. Column [4] uses the full likelihood. This is extracted from Tab. 3 of [23].

Parameters	*Planck* TT+lowP	*Planck* TE+lowP	*Planck* EE+lowP	*Planck* TT,TE,EE+lowP
$\Omega_{\rm b}h^2$	0.02222 ± 0.00023	0.02228 ± 0.00025	0.0240 ± 0.0013	0.02225 ± 0.00016
$\Omega_{\rm c}h^2$	0.1197 ± 0.0022	0.1187 ± 0.0021	$0.1150^{+0.0048}_{-0.0055}$	0.1198 ± 0.0015
$100\theta_{\rm MC}$	1.04085 ± 0.00047	1.04094 ± 0.00051	1.03988 ± 0.00094	1.04077 ± 0.00032
τ	0.078 ± 0.019	0.053 ± 0.019	$0.059^{+0.022}_{-0.019}$	0.079 ± 0.017
$\ln(10^{10}A_{\rm s})$	3.089 ± 0.036	3.031 ± 0.041	$3.066^{+0.046}_{-0.041}$	3.094 ± 0.034
$n_{\rm s}$	0.9655 ± 0.0062	0.965 ± 0.012	0.973 ± 0.016	0.9645 ± 0.0049
H_0	67.31 ± 0.96	67.73 ± 0.92	70.2 ± 3.0	67.27 ± 0.66
$\Omega_{\rm m}$	0.315 ± 0.013	0.300 ± 0.012	$0.286^{+0.027}_{-0.038}$	0.3156 ± 0.0091
σ_8	0.829 ± 0.014	0.802 ± 0.018	0.796 ± 0.024	0.831 ± 0.013
$10^9 A_{\rm s}e^{-2\tau}$	1.880 ± 0.014	1.865 ± 0.019	1.907 ± 0.027	1.882 ± 0.012

The *Planck* 2015 results are consistent with the ΛCDM cosmology and no compelling evidence for extensions have been found. We refer to Tab. 4.2 for the constraints on the most interesting one parameter extensions of the ΛCDM model. [3]

In addition, the *Planck* sky surveys has produced a wealth of information on the properties of extragalactic sources and on the dust and gas in our own galaxy. One specific notable result is the measurement of the Sunyaev-Zeldovich effect in hundreds of galaxy clusters [201].

accounted systematics such as temperature to polarization leakage. For this reason in the next sections we will consider the temperature data as baseline.

[3] More recently results based on low-ℓ polarization HFI data have been presented in Refs. [24, 199]. Although consistent with 2015 results, the value of the optical depth is now low.

Table 4.2: Constraints on one-parameter extensions to the base ΛCDM model for combinations of *Planck* power spectra. All limits and confidence regions quoted here are 95 %. This is extracted from Tab. 5 of [23].

Parameters	*Planck* TT+lowP	*Planck* TT,TE,EE+lowP
Ω_K	$-0.052^{+0.049}_{-0.055}$	$-0.040^{+0.038}_{-0.041}$
Σm_ν [eV]	< 0.715	< 0.492
$N_{\rm eff}$	$3.13^{+0.64}_{-0.63}$	$2.99^{+0.41}_{-0.39}$
$Y_{\rm P}$	$0.252^{+0.041}_{-0.042}$	$0.250^{+0.026}_{-0.027}$
w	$-1.54^{+0.62}_{-0.50}$	$-1.55^{+0.58}_{-0.48}$

4.1.1 Primordial non-Gaussianity

In the *Planck* 2015 release has been used for the first time polarization information to constrain non-Gaussianity signals left by primordial physics. The *Planck* 2015 results for the local, equilateral and orthogonal shapes, from the 2015 combined analysis of temperature and polarization data, are respectively [202]:

$$f_{\rm NL}^{\rm local} = 0.8 \pm 5.0\,, \qquad f_{\rm NL}^{\rm equil.} = -4 \pm 43\,, \qquad f_{\rm NL}^{\rm ortho.} = -26 \pm 21\,. \quad (4.1)$$

In addition, *Planck* bispectrum constraints lead to important implications for inflationary model building, such as a lower bound on the sound speed in effective single field inflationary theory.

The main conclusion from *Planck* is that consistency with Gaussianity is found in all cases.

4.2 The Early Universe seen by *Planck*

We now present some of the implications of *Planck* 2015 data for the physics of the Early Universe following closely [44].

In addition to the likelihoods described in Sec. 4.0.5 and Sec. 4.1, we consider the CMB B-mode polarization contraints provided by the 2014 cross-correlation analysis of 353 GHz *Planck* channel, BICEP2 and Keck Array [167] (we refer to this dataset as BKP). [4]

[4]Note that the updated contraint on the tensor-to-scalar ratio from the BKP dataset with the includion of Keck Array observations at 95 GHz and 23 GHz WMAP channel [166].

In combination with CMB data we use measurements of $D_V/r_{\rm drag}$ by 6dFGRS at $z_{\rm eff} = 0.106$ [203], SDSS-MGS at $z_{\rm eff} = 0.15$ [204], SDSS-DR11 CMASS and LOWZ at $z_{\rm eff} = 0.57$ and $z_{\rm eff} = 0.32$ respectively [205]. The inclusion of BAO data and the inclusion of the high-ℓ polarization are compatible even if the high-ℓ polarization is still not fully understood and can contain unaccaunted systematics such as temperature to polarization leakege [168].

4.2.1 Constraints on the scalar spectral index

For the base ΛCDM model with a power-law power spectrum of curvature perturbations, the constraint on the scalar spectral index, $n_{\rm s}$, with the *Planck* 2015 data is:

$$n_{\rm s} = 0.9655 \pm 0.0062 \qquad (68\,\%\ \text{CL, } \textit{Planck}\ \text{TT+lowP})\,. \tag{4.2}$$

The shift towards slightly smaller values of the spectral index is driven by the smaller values of the optical depth to reionization. Given that the temperature data provide a sharp constraint on the combination $A_{\rm s}e^{-2\tau}$, a slightly lower $A_{\rm s}$ requires a smaller τ. *Planck* lensing data [200] have a marginal preference for a smaller primordial amplitude, with $\tau = 0.066 \pm 0.016$ (68 % CL). [5]

One of the *Planck* main result is the robust statistical significance evidence of $n_{\rm s} \neq 1$. The Harrison-Zeldovich (HZ) scale-invariant spectrum, i.e. $n_{\rm s} = 1$, [206–208] is disfavoured at $5.6\,\sigma$ da 2015 data. If extensions to the ΛCDM model are considered, we have $n_{\rm s} \neq 1$ at $2.8\,\sigma$ ΛCDM+$N_{\rm eff}$, and $3.0\,\sigma$ ΛCDM+$Y_{\rm P}$. The inclusion of *Planck* high-ℓ polarization data further disfavours the HZ model [44].

4.2.2 Constraints on the running of the spectral index

The running of the scalar spectral index, measured at $k_* = 0.05$ Mpc^{-1}, is constrained by the *Planck* 2015 data to:

$$\frac{{\rm d}n_{\rm s}}{{\rm d}\ln k} = -0.0084 \pm 0.0082 \qquad (68\,\%\ \text{CL, } \textit{Planck}\ \text{TT+lowP})\,. \tag{4.3}$$

A slightly negative running of the scalar spectral index is found in data, but with low statistical significance lower ($< 1\,\sigma$) with respect to previous CMB data release, i.e. $1.5\,\sigma$ *Planck* 2013 and $2.0\,\sigma$ WMAP9-yr. An important result achieved by *Planck* has

[5] HFI-based τ posterior distribution from E-mode polarization only gives a value $\tau = 0.058 \pm 0.009$ (68 % CL) when combined with CMB temperature APS.

been to show that a (negative) running of the spectral index is no more able to account simultaneously for the deficit of power at low-ℓ and for the high-ℓ acoustic peaks.

The running of the spectral index, for a single-field slow-roll inflation model with a featureless potential is at second-order in the slow-roll parameters:

$$\frac{\mathrm{d}n_\mathrm{s}}{\mathrm{d}\ln k} = -2\xi_\mathrm{V}^2 + 4\eta_\mathrm{V}^2 + \frac{3}{2}(n_\mathrm{s}-1)^2\,. \tag{4.4}$$

In order to achieve negative running compatible with the mean value inferred by *Planck* 2015 data, the running must be dominated by the first term in Eq. (4.4), i.e. by ξ_V^2.

The detection of the running will gives the opportunity to confirm slow-roll inflation and to the test its prediction up to second order. However, the best-fit value of the scalar running exceeds the standard slow-roll predictions. A measure of the running at the level of $\approx |n_\mathrm{s}-1|^2$ is out of reach even for the proposed experiments CMB-S4 [209] and CORE [139]. For these experiments the forecasted uncertainty is $\sigma(\alpha_\mathrm{s}) \sim 0.002 - 0.003$.

4.2.3 Constraints on the tensor-to-scalar ratio

The constraints on the tensor-to-scalar ratio inferred from the *Planck* 2015 data, for the ΛCDM+r model:

$$r_{0.05} < 0.11 \qquad (95\,\%\ \mathrm{CL},\ \textit{Planck}\ \mathrm{TT{+}lowP})\,, \tag{4.5}$$

obtained by assuming the slow-roll consistency condition at the first order on the tensor spectral index, $n_\mathrm{t} \approx -r/8$. These constraints are relaxed when a scale dependence of the scalar and tensor spectral indexes and when we consider extensions of the ΛCDM model, see [44] for the details.

The combined analysis from the cross-correlation of the BICEP2 and Keck Array data with the Planck maps gives:

$$r_{0.05} < 0.08 \qquad (68\,\%\ \mathrm{CL},\ \textit{Planck}\ \mathrm{TT{+}lowP{+}BKP})\,. \tag{4.6}$$

The constraints derived from B-mode polarization are less dependent on the cosmology, with respect to the ones TT derived, and they remove the degeneracies between the tensor-to-scalar ratio and other parameters. In Fig. 4.6 we show also the B-mode polarization which has been derived with a joint analyisis of the *Planck* and BICEP2/Keck data [167].

The constraints on r can be translated into upper bounds on the energy scale of inflation, when the pivot scale exits the Hubble radius, using:

$$V_* = \frac{3\pi^2 A_\mathrm{s}}{2}\, r_*\, M_\mathrm{pl}^4 = (1.88\times 10^{16}\ \mathrm{GeV})^4 \frac{r_*}{0.10}\,. \tag{4.7}$$

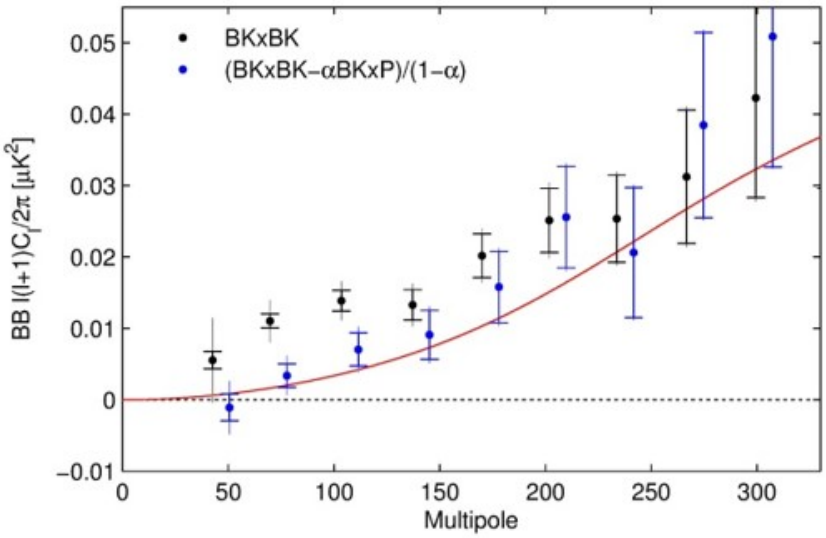

Figure 4.6: BB spectrum of the BICEP2/Keck Array maps before and after subtraction of the dust contribution, estimated from the cross-spectrum with *Planck* 353 GHz. Taken from [167].

This gives an upper bound, at $k_* = 0.05$ Mpc^{-1}, of:

$$V_*^{1/4} < 1.8 \times 10^{16} \text{ GeV} \qquad (68\,\% \text{ CL, } \textit{Planck} \text{ TT+lowP+BKP})\,. \quad (4.8)$$

4.2.4 Constraints on the slow-roll parameters

Both hierarchies of slow-roll parameters defined in Sec. 1.3.3 encode a wealth of information on the physics of inflation compared to the standard phenomenological parameters n_s, $\mathrm{d}n_\mathrm{s}/\mathrm{d}\ln k$, and r. Indeed, the potential slow-roll paramers describe the slow-roll condition which occurs for $\epsilon_\mathrm{V} \ll 1$ and $|\eta_\mathrm{V}| \ll 1$. The HFFs measure instead the deviation from an exact exponential expansion during inflation.

We first present the *Planck* 2015 constraints on slow-roll parameters obtained through the analytic perturbative expansion in terms of HFFs ϵ_i for the primordial spectra of cosmological fluctuations during slow-roll inflation [73, 210, 211] and derived constraints by using Eqs. (1.36a)-(1.36b). This analysis follows the same methodology in

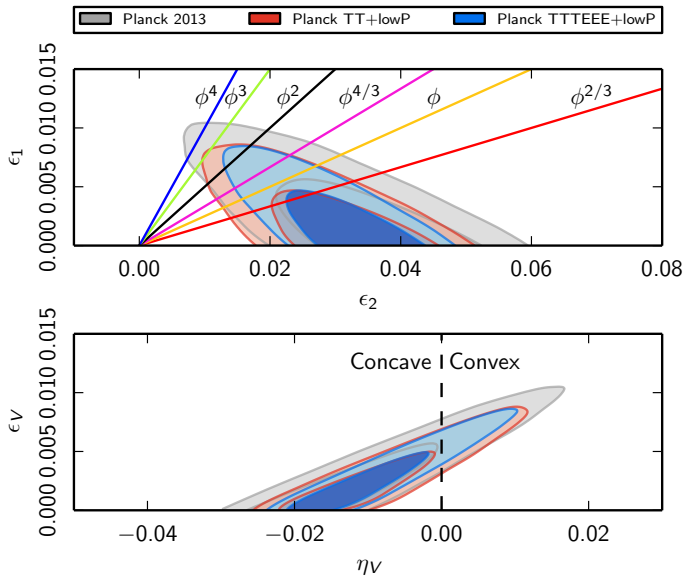

Figure 4.7: Marginalized joint 68 % and 95 % CL regions for (ϵ_1, ϵ_2) (top panel) and (ϵ_V, η_V) (bottom panel) for *Planck* TT+lowP (red contours), *Planck* TT,TE,EE+lowP (blue contours), and compared with the *Planck* 2013 results (gray contours). Reproduced with permission from Astronomy & Astrophysics, ESO; original source ESA and the Planck Collaboration. Taken from [44].
We add the predictions in the (ϵ_1, ϵ_2) plane for some selected power-law potentials (2.144), i.e. $\epsilon_1 = 2n\epsilon_2$.

[26, 212]. When restricting to first order in ϵ_i, we obtain:

$$\epsilon_1 < 0.0068 \qquad (95\,\%\ \text{CL}, \textit{Planck}\ \text{TT+lowP})\,, \tag{4.9}$$

$$\epsilon_2 = 0.029^{+0.008}_{-0.007} \qquad (68\,\%\ \text{CL}, \textit{Planck}\ \text{TT+lowP})\,. \tag{4.10}$$

When high-ℓ polarization is included we obtain $\epsilon_1 < 0.0066$ at 95 % CL and $\epsilon_2 = 0.030^{+0.007}_{-0.006}$ at 68 % CL.

By using Eqs. (1.36a)-(1.36b) with $\epsilon_3 = \epsilon_4 = 0$ and the PPS to lowest order in the HFFs, the derived constraints for the first two slow-roll potential parameters are:

$$\epsilon_V < 0.0068 \qquad (95\,\%\ \text{CL}, \textit{Planck}\ \text{TT+lowP})\,, \tag{4.11}$$

$$\eta_V = -0.010^{+0.005}_{-0.009} \qquad (68\,\%\ \text{CL}, \textit{Planck}\ \text{TT+lowP})\,. \tag{4.12}$$

When high-ℓ polarization is included we obtain $\epsilon_V < 0.0067$ at 95 % CL and $\eta_V = -0.010^{+0.004}_{-0.009}$ at 68 % CL.

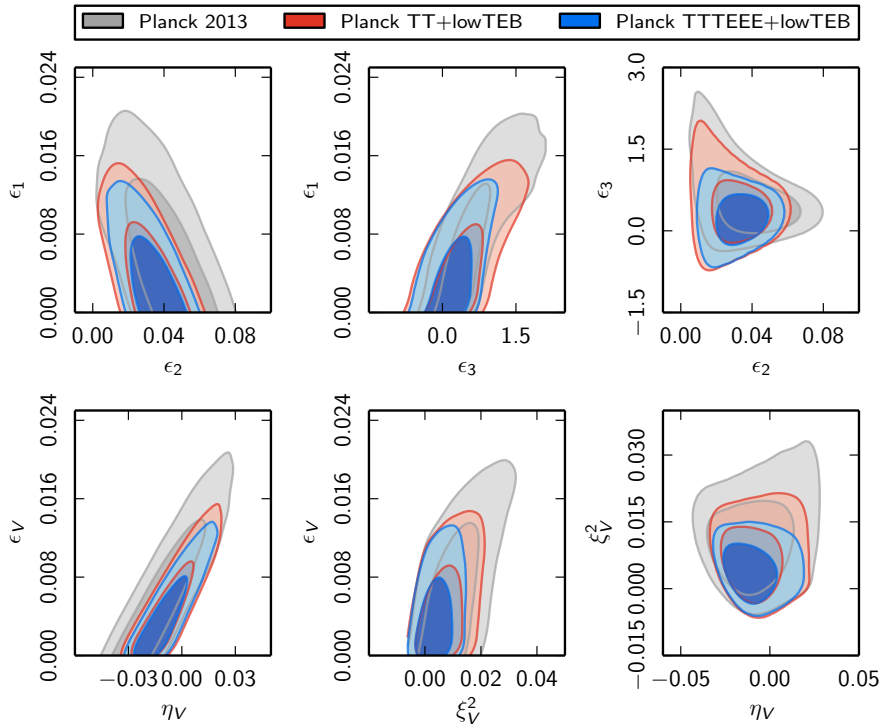

Figure 4.8: Marginalized joint 68 % and 95 % CL regions for $(\epsilon_1, \epsilon_2, \epsilon_3)$ (top panels) and $(\epsilon_V, \eta_V, \xi^2_V)$ (bottom panels) for *Planck* TT+lowP (red contours), *Planck* TT,TE,EE+lowP (blue contours), and compared with the *Planck* 2013 results (gray contours). Reproduced with permission from Astronomy & Astrophysics, ESO; original source ESA and the Planck Collaboration. Taken from [44].

When second-order contributions in the HFFs are included we obtain:

$$\epsilon_1 < 0.012 \qquad (95\,\%\ \text{CL, } \textit{Planck}\ \text{TT+lowP})\,, \tag{4.13}$$

$$\epsilon_2 = 0.031^{+0.013}_{-0.011} \qquad (68\,\%\ \text{CL, } \textit{Planck}\ \text{TT+lowP})\,, \tag{4.14}$$

$$-0.41 < \epsilon_3 < 1.38 \qquad (95\,\%\ \text{CL, } \textit{Planck}\ \text{TT+lowP})\,. \tag{4.15}$$

When high-ℓ polarization is included we obtain $\epsilon_1 < 0.011$ at 95 % CL, $\epsilon_2 = 0.032^{+0.011}_{-0.009}$

at 68 % CL, and $-0.32 < \epsilon_3 < 0.89$ at 95 % CL.

By using Eqs. (1.36a)-(1.36b)-(1.36c) with $\epsilon_4 = 0$ and the PPS to second-order in the HFFs, the derived constraints for the slow-roll potential parameters are:

$$\epsilon_V < 0.012 \qquad (95\,\%\ \text{CL}, \textit{Planck}\ \text{TT+lowP})\,, \tag{4.16}$$

$$\eta_V = -0.0080^{+0.0088}_{-0.0146} \qquad (68\,\%\ \text{CL}, \textit{Planck}\ \text{TT+lowP})\,, \tag{4.17}$$

$$\xi^2_V = 0.0070^{+0.0045}_{-0.0069} \qquad (68\,\%\ \text{CL}, \textit{Planck}\ \text{TT+lowP})\,. \tag{4.18}$$

When high-ℓ polarization is included we obtain $\epsilon_V < 0.011$ at 95 % CL, and $\eta_V = -0.0092^{+0.0074}_{-0.0127}$ and $\xi^2_V = 0.0044^{+0.0037}_{-0.0050}$, both at 68 % CL.

In Figs. 4.7 and 4.8 we show the 68 % CL and 95 % CL of the HFFs and the derived potential slow-roll parameters with and without the inclusion of high-ℓ polarization, comparing with the *Planck* 2013 results.

Using the BKP likelihood strengthens even more the constraints discussed above. If we set $\epsilon_3 = 0$, the first slow-roll parameter is constrained to $\epsilon_1 < 0.0055$ at 95 % CL by *Planck* TT+lowP+BKP, to be compared with Eq. (4.9).

4.2.5 Models comparison and Bayes factor

During the last decades, a massive amount of statistical tools in cosmology has been used in order to obtain accurate and robust conclusions from the data.

Bayesian inference is the basic method to derive constraints on physical models from experiments/observations. To be useful, the model must fit the data, and simple enough to be predictive.

The essence of Bayesian methodology is to assign probabilities to all quantities of interest, and to manipulate those probabilities according to a series of rules, among which the Bayes theorem (Thomas Bayes 1763 [213]) is the most important. The Bayes theorem can be written as:

$$P(\theta|d) = \frac{P(d|\theta)P(\theta)}{P(d)}\,, \tag{4.19}$$

where $P(\theta)$ is the prior probability, indicating different probabilities of different values of θ, assumed before employing the data d, θ is the N-dimensional vector of parameters of the model, $P(\theta|d)$ is the posterior probability of the parameters given the data, and $\mathcal{L} \equiv P(d|\theta)$ the likelihood function.

In cosmological parameter estimation, we have to figure out the parameter values that give the best fit to the data. This is achivable by looking for the maximum likelihood value and exploring the shape of the likelihood around the maximum. One

Table 4.3: Modified Jeffreys' scale for the strength of evidence.

$\lvert \ln B \rvert$	Relative odds	Number of σ	Interpretation
<1.0	< 3:1	< 1.15	not worth mentioning
<2.5	< 12:1	1.77	weak
<5.0	< 150:1	2.7	moderate
>5.0	> 150:1	> 2.7	strong

of the main method used is the Markov Chains Monte Carlo (MCMC). This method is defined as a random sampling in which the next step in the sequence depends only from the previous one. The Metropolis-Hasting (MH) algorithm is one of the simplest algorithm which implements this procedure: choose a starting point in the parameter space, propose a random jump, if the probability of the new point is higher than the probability of the starting point accept the jump anyhow stay at the same point and jump again. This until the probability distribution is mapped sufficiently well.

In general, we have several models competing to describe the data. In this case, discriminating between models becames important. The key quantity is the evidence:

$$\begin{aligned} E &\equiv P(d)\,, \\ &= \int d\theta\ P(d|M)(PM)\,, \end{aligned} \tag{4.20}$$

which is average likelihood of the parameters averaged over the prior. The ratio of the evidence of two models is know as *Bayes factor* [214]:

$$B_{0\mathrm{X}} \equiv \ln(E_0) - \ln(E_X)\,, \tag{4.21}$$

which is also defined just as the difference between of the evideces. To interprete the model probability with respect to another model, usually the Jeffreys' scale is used. In cosmology a slightly modified Jeffreys' scale is used to assess the strength of evidence, empirically calibrated (see Tab. 4.3) [215].

Computing the evidence is more demanding than mapping the dominant part of the posterior probability, because we have to be able to integrate the likelihood over the entire parameter space. The common method used in cosmology is *Nested sampling*. Nested sampling, introduced by Skilling [216], explores parameters space with large collection of points and deletes the lowest likelihood point by replacing it with a randomly-drawn point of higher likelihood.

4.2.6 Inflationary models comparison

We first discuss the implications of *Planck* TT+lowP+BAO data for the slow-roll inflationary models studied in Sec. 2.6 by taking into account the uncertainties in the reheating phase. For the number of e-folds to the end of inflation we use Eq. (2.143) with the pivot scale $k_* = 0.002$ Mpc^{-1}, $g_{\rm reh} = 10^3$, $\epsilon_1^{\rm end} = 1$, and $\rho_{\rm reh} \in [(10^3 {\rm GeV})^4, \rho_{\rm end}]$ (uniformly sampling in its logarithm). We choose the same prior $\ln\left(10^{10}\, A_{\rm s}\right) \in [2.7, 3.4]$ for all the models. We consider the two different cases with a dust equation of state during the reheating phase, i.e. $w_{\rm reh} = 0$, and $w_{\rm reh} \in [-1/3, 1/3]$. See Tab. 4.4 for the priors of the extra parameters of each model. The following discussion rely heavily on Sec. 2.6 for the peculiarity of each inflationary model considered.

The predictions to lowest order in the slow-roll approximation for $(n_{\rm s}, r)$ of a few inflationary models with a representative uncertainty for the entropy generation stage ($50 < N_* < 60$) are shown in Fig. 4.9.

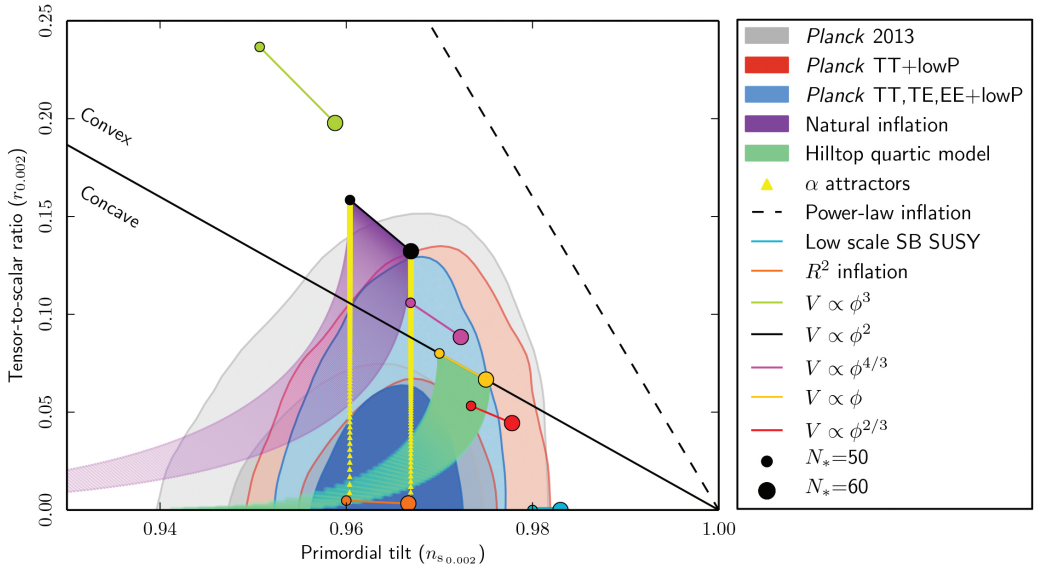

Figure 4.9: Marginalized joint 68 % and 95 % CL regions for $n_{\rm s}$ and $r_{0.002}$ from *Planck*, compared to theoretical predictions of selected inflationary models. Reproduced with permission from Astronomy & Astrophysics, ESO; original source ESA and the Planck Collaboration. Taken from [44].

The results on the tensor-to-scalar ratio imply that models such as ϕ^2 and natural

Table 4.4: Potential shape and prior for the selection of slow-roll inflationary models studied.

Inflationary Model	Potential	Prior(s)
$R + R^2/(6M^2)$	$V(\phi) = \Lambda^4 \left(1 - e^{\sqrt{2/3}\phi/M_{\rm pl}}\right)^2$	...
Power law potentials	$V(\phi) = \Lambda^4 \left(\frac{\phi}{M_{\rm pl}}\right)^p$	$0 \leq p \leq 6$
Natural Inflation	$V(\phi) = \Lambda^4 \left[1 + \cos\left(\frac{\phi}{f}\right)\right]$	$0.3 < \log_{10}(f/M_{\rm pl}) < 2.5$
Hilltop quadratic model ($p = 2$)	$V(\phi) = \Lambda^4 \left(1 - \frac{\phi^2}{\mu^2} + ...\right)$	$0.3 < \log_{10}(\mu/M_{\rm pl}) < 4.85$
Hilltop quartic model ($p = 4$)	$V(\phi) = \Lambda^4 \left(1 - \frac{\phi^4}{\mu^4} + ...\right)$	$-2 < \log_{10}(\mu/M_{\rm pl}) < 2$
Doble well	$V(\phi) = \Lambda^4 \left(1 - \frac{\phi^2}{2\mu^2}\right)$	$0.3 < \log_{10}(\mu/M_{\rm pl}) < 4.85$
D-brane inflation ($p = 2$)	$V(\phi) = \Lambda^4 \left(1 - \frac{\mu^2}{\phi^2} + ...\right)$	$-6 < \log_{10}(\mu/M_{\rm pl}) < 0.3$
D-brane inflation ($p = 4$)	$V(\phi) = \Lambda^4 \left(1 - \frac{\mu^4}{\phi^4} + ...\right)$	$-6 < \log_{10}(\mu/M_{\rm pl}) < 0.3$
Potential with exponential tails	$V(\phi) = \Lambda^4 \left(1 - e^{q\phi/M_{\rm pl}} + ...\right)$	$-3 < \log_{10}(q) < 3$
Spontaneously broken SUSY	$V(\phi) = \Lambda^4 \left(1 + \alpha_h \log(\phi/M_{\rm pl} + ...)\right)$	$-2.5 < \log_{10}(\alpha_h) < 1$
Supersymmetric α-attractor	$V(\phi) = \Lambda^4 \left(1 - e^{-\sqrt{2}\phi/\left(\sqrt{3\alpha}M_{\rm pl}\right)}\right)^2$	$0 < \log_{10}(\alpha^2) < 4$
Superconformal α-attractor	$V(\phi) = \Lambda^4 \tanh^{2m}\left(\frac{\phi}{\sqrt{6\alpha}M_{\rm pl}}\right)$	$0 < \log_{10}(\alpha^2) < 4$ $0 < m < 2$

Table 4.5: Results of the inflationary model comparison for *Planck* TT+lowP+BAO. We provide $\Delta\chi^2$ with respect to base ΛCDM and Bayes factors with respect to R^2 inflation. Taken from [44].

Inflationary model	$\Delta\chi^2$		$\ln B$	
	$w_{\rm int}=0$	$w_{\rm int}\neq 0$	$w_{\rm int}=0$	$w_{\rm int}\neq 0$
$R+R^2/(6M^2)$	+0.8	+0.3	...	+0.7
$n=2/3$	+6.5	+3.5	−2.4	−2.3
$n=1$	+6.2	+5.5	−2.1	−1.9
$n=4/3$	+6.4	+5.5	−2.6	−2.4
$n=2$	+8.6	+8.1	−4.7	−4.6
$n=3$	+22.8	+21.7	−11.6	−11.4
$n=4$	+43.3	+41.7	−23.3	−22.7
Natural	+7.2	+6.5	−2.4	−2.3
Hilltop ($p=2$)	+4.4	+3.9	−2.6	−2.4
Hilltop ($p=4$)	+3.7	+3.3	−2.8	−2.6
Double well	+5.5	+5.3	−3.1	−2.3
Brane inflation ($p=2$)	+3.0	+2.3	−0.7	−0.9
Brane inflation ($p=4$)	+2.8	+2.3	−0.4	−0.6
Exponential tail inflation	+0.8	+0.3	−0.7	−0.9
SB SUSY	+0.7	+0.4	−2.2	−1.7
Supersymmetric α-model	+0.7	+0.1	−1.8	−2.0
Superconformal α-model ($m=1$)	+0.9	+0.8	−2.3	−2.2
Superconformal α-model ($m\neq 1$)	+0.7	+0.5	−2.4	−2.6

inflation are disfavoured compared to models which predict a smaller tensor-to-scalar ratio. R^2 inflation has the strongest evidence among the models considered here. The models closest to R^2 in terms of evidence are brane inflation and exponential tail inflation, which have one more parameter than R^2. Both brane inflation considered in Eq. (2.168) and the potential with the exponential tail in Eq. (2.169) approximate the linear potential for a large portion of parameter space (for $\mu/M_{\rm pl}\gg 1$ and $q\gg 1$, respectively). For this reason these models have a higher evidence (although not at

a statistically significant level) compared to those approximate a quadratic potential, for instance α attractors in Eq. (2.176). Monomial potentials with integer $n > 2$ are strongly disfavoured at more than $2\,\sigma$ with respect to R^2. The Bayes factor prefers R^2 over chaotic inflation with monomial quadratic potential by odds of 110:1. When we allow the variation of $w_{\rm reh}$ the obtained $\Delta\chi^2$ changes a little, i.e. less than approximately 1.8 and the gain in the logarithm of the Bayesian evidence is even smaller, since an extra parameter is added.

Table 4.6: Results of inflationary model comparison using the cross-correlation between BICEP2/Keck Array and *Planck*. This table is the analogue to Tab. 4.5, which did not use the BKP likelihood. Taken from [44].

Inflationary model	$\Delta\chi^2$		$\ln B$	
	$w_{\rm int} = 0$	$w_{\rm int} \neq 0$	$w_{\rm int} = 0$	$w_{\rm int} \neq 0$
$R + R^2/(6M^2)$	+2.1	+1.6	...	+0.3
$n = 2/3$	+3.4	+3.0	−1.9	−1.2
$n = 1$	+5.1	+5.1	−1.6	−1.8
$n = 4/3$	+7.1	+6.6	−2.1	−2.5
$n = 2$	+12.3	+11.8	−6.0	−5.6
$n = 3$	+29.7	+29.6	−16.0	−15.6
$n = 4$	+58.1	+58.0	−30.1	−29.9
Natural	+6.0	+5.2	−5.6	−5.0
Hilltop ($p = 2$)	+1.6	+1.2	−0.7	−0.4
Hilltop ($p = 4$)	+1.5	+1.0	−0.6	−0.9
Double well	+3.2	+3.1	−4.3	−4.2
Brane inflation ($p = 2$)	+2.3	+2.2	+0.2	0.0
Brane inflation ($p = 4$)	+2.2	+2.2	+0.1	−0.1
Exponential tail inflation	+2.2	+1.4	−0.1	0.0
SB SUSY	+3.4	+1.6	−1.8	−1.5
Supersymmetric α-model	+1.6	+1.1	−1.1	+0.1
Superconformal α-model ($m = 1$)	+1.8	+1.3	−1.9	−1.4
Superconformal α-model ($m \neq 1$)	+1.8	+0.9	−2.5	−2.2

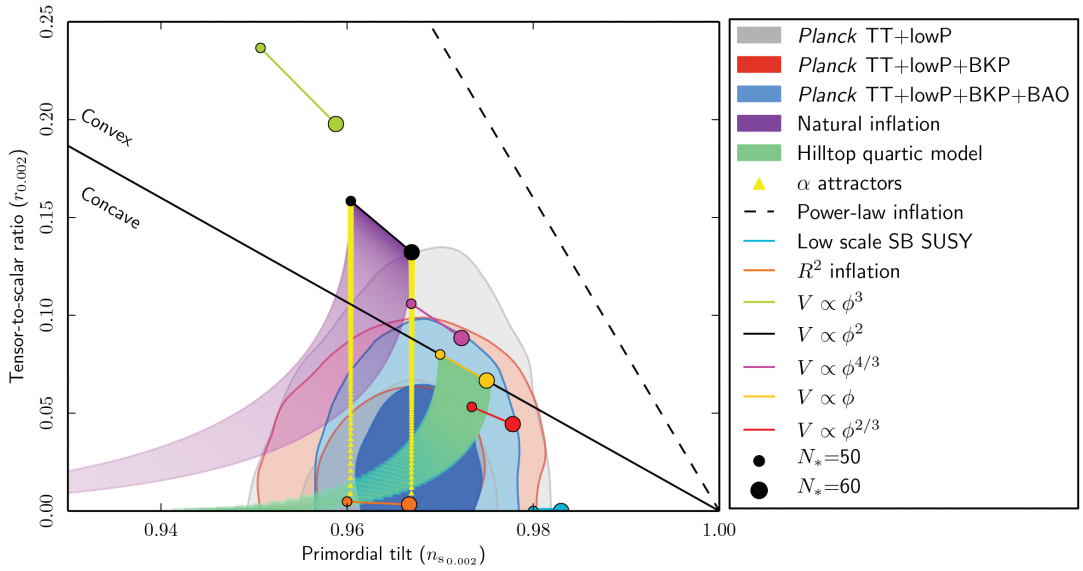

Figure 4.10: Marginalized joint 68 % and 95 % CL regions for n_s and $r_{0.002}$ from *Planck* alone and in combination with its cross-correlation with BKP and/or BAO data compared to theoretical predictions of selected inflationary models. Reproduced with permission from Astronomy & Astrophysics, ESO; original source ESA and the Planck Collaboration. Taken from [44].

Using the BKP likelihood further strengthens the constraints on the inflationary parameters and models discussed in Sect. 6, as seen

In Fig. 4.10 we shown the predictions to lowest order in the slow-roll approximation for (n_s, r) of the same inflationary models in in Fig. 4.9, with the inclusion of the BKP likelihood.

The combination with the BKP likelihood gives a Bayes factor preferring R^2 over chaotic inflation with monomial quadratic potential and natural inflation by odds of 403:1 and 270:1, respectively, under the assumption of a dust equation of state during the entropy generation stage. The combination with the BKP likelihood further penalizes the double-well model compared to R^2 inflation. However, adding BKP reduces the Bayes factor of the hilltop models compared to R^2, because these models can predict a value of the tensor-to-scalar ratio that better fits the non statistically insignificant peak at $r \approx 0.05$.

The results for the Bayes factors on the models with respect to R^2 and the results for

the $\Delta\chi^2$ with respect to the ΛCDM model are summarized in Tab. 4.5, and in Tab. 4.6 the BKP likelihood is included (for the Bayes factors of other inflationary models obtained from *Planck* 2013 and *Planck* 2015 data see respectively Refs. [217, 218] and Refs. [219, 220]).

4.3 Parametrized features

Although a spatially flat ΛCDM model with a tilted power-law spectrum of primordial fluctuations provides a good fit to *Planck* data, there are intriguing features in the temperature power spectrum, such as a dip at $\ell \sim 20$, a smaller average amplitude at $\ell \lesssim 40$ and other outliers at higher multipoles. The features at $\ell \lesssim 40$ in the CMB temperature power spectrum generate a particular pattern at $k \lesssim 0.008$ Mpc^{-1}, which roughly corresponds to $\ell \sim 20$, as also shown consistently by three different methods used to reconstruct the PPS of curvature perturbations with *Planck* data [44].

There are several theoretically well motivated mechanisms during inflation which support deviations from a simple power law for primordial fluctuations providing a better fit to the CMB temperature power spectrum. Some of these mechanisms are based on a temporary violation of the slow-roll regime for the inflaton field and include punctuated inflation [221], a short inflationary stage preceded by a kinetic stage [222] or by a bounce from a contracting stage [223], a string theory-motivated climbing phase prior to inflation [224], a sharp edge in the first derivative of the inflaton potential [110], a step in the inflaton potential [225, 226], a variation in the effective speed of sound [227–229], or a burst of particle production during inflation [230, 231]. On the other hand, resonant models include periodic oscillations in the potential and therefore super-imposed periodic features to the PPS [232] (see [233] for a review on primordial features). The case of periodic oscillations in axion monodromy inflation [234, 235] falls in this broad class of models [236]. These features in the power spectrum are accompanied by specific templates in the bispectrum (see [237] for a review): therefore, primordial features can also be searched in the bispectrum [202] or jointly in the power spectrum and bispectrum [238–240].

In the following we will consider various coses discussed in Ref. [44].

4.3.1 Phenomenological suppression of power on the largest scales

The lack of power in the *Planck* temperature power spectrum at low multipoles, already mentioned in the *Planck* 2013 release, could potentially be explained by a primordial spectrum having a suppression of power *only* at large wavelengths. Here we investigate two examples of such models.

We first update the analysis (already presented in [43]) of a power-law spectrum multiplied by an exponential cut-off:

$$\mathcal{P}_{\mathcal{R}}(k) = \mathcal{P}_{\mathcal{R},0}(k) \left\{ 1 - \exp\left[- \left(\frac{k}{k_{\rm c}} \right)^{\lambda_{\rm c}} \right] \right\}. \tag{4.22}$$

Here, Eq. (4.22) reproduces a suppression of the curvature power spectrum at large scales by introducing two extra parameters: the first one, $k_{\rm c}$, selects the relevant scale where the deviation from the smooth curvature power spectrum starts, while the second parameter, $\lambda_{\rm c}$, adjusts the stiffness of the suppression. We choose prior ranges $\lambda_{\rm c} \in [0, 10]$ and $\ln(k_{\rm c}/{\rm Mpc}^{-1}) \in [-12\,, -3]$.

This simple parameterization is motivated by models with a kinetic stage followed by a short inflationary phase in which the onset of the slow-roll phase coincides with the time when the largest observable scales exited the Hubble radius during inflation. On these largest scales, the curvature power spectrum is then strongly suppressed due to the kinetic energy of the inflaton, and so the CMB APS at the lowest multipoles. Note that the exact derivation of the PPS obtained through a matching of an initial kinetic-dominated regime with a quasi de-Sitter stage shows that the large scale suppression is connected to the smooth nearly scale-invariant power spectrum by oscillations [222].

For *Planck* TT+lowP (*Planck* TT,TE,EE+lowP), the best-fit model has $\lambda_{\rm c} = 0.50$ (0.53), $\ln(k_{\rm c}/{\rm Mpc}^{-1}) = -7.98$ (-7.98), $n_{\rm s} = 0.9647$ (0.9649).

As a second model, we consider a broken-power-law spectrum for curvature perturbations:

$$\mathcal{P}_{\mathcal{R}} = \begin{cases} A_{\rm low} \left(\frac{k}{k_*} \right)^{n_{\rm s}-1+\delta} & \text{if } k \leq k_{\rm b}, \\ A_{\rm s} \left(\frac{k}{k_*} \right)^{n_{\rm s}-1} & \text{if } k \geq k_{\rm b}, \end{cases} \tag{4.23}$$

with $A_{\rm low} = A_{\rm s}(k_{\rm b}/k_*)^{-\delta}$ to ensure continuity at $k = k_{\rm b}$. Hence this model, like the previous one, has two parameters, and also suppresses power at large wavelengths when $\delta > 0$. We assume top-hat priors on $\delta \in [0, 2]$ and $\ln(k_{\rm b}/{\rm Mpc}^{-1}) \in [-12\,, -3]$, and standard uniform priors for $\ln(10^{10} A_{\rm s})$ and $n_{\rm s}$. The best fit to *Planck* TT+lowP (*Planck* TT,TE,EE+lowP) is found for $n_{\rm s} = 0.9658$ (0.9647), $\delta = 1.14$ (1.14), and $\ln(k_{\rm b}/{\rm Mpc}^{-1}) = -7.55$ (-7.57).

We conclude that neither of these two models with two extra parameters is preferred over the base ΛCDM model.

4.3.2 Discontinuity in the first derivative of the potential

We consider a transition in the first derivative of the potential, which leads to a localized imprint in the PPS, at the scales where the transition occurred [110, 241]. This specific model assumes a sharp change in the slope of the inflaton potential $V(\phi)$:

$$V(\phi) = \begin{cases} V_0 + A_+(\phi - \phi_0)\,, & \phi \gg \phi_0 \\ V_0 + A_-(\phi - \phi_0)\,, & \phi \ll \phi_0 \end{cases} . \tag{4.24}$$

The two different slopes of the potential lead to different asymptotic values of the curvature power spectrum, plus an oscillatory pattern in between. The curvature power spectrum can be obtained analitically under the approximation $|A_+\phi|\,, |A_-\phi| \ll V_0$ [110]:

$$\mathcal{P}_\mathcal{R}(k) = \mathcal{P}_{\mathcal{R},0}(k) \times \mathcal{D}(y, \Delta)\,, \tag{4.25}$$

with:

$$\begin{aligned} \mathcal{D}(y,\Delta) =& 1 + \frac{9\Delta^2}{2}\left(\frac{1}{y} + \frac{1}{y^3}\right)^2 + \frac{3\Delta}{2}\left(4 + 3\Delta - \frac{3\Delta}{y^4}\right)^2 \frac{1}{y^2}\cos(2y) \\ &+ 3\Delta\left(1 - \frac{1+3\Delta}{y^2} - \frac{3\Delta}{y^4}\right)^2 \frac{1}{y}\sin(2y)\,, \end{aligned} \tag{4.26}$$

where $y = k/k_s$ and $\Delta = (A_+ - A_-)/A_+$. Here k_s is the scale of the transition.

4.3.3 Step in the inflaton potential

A step in the inflationary potential [225] predicts localized oscillations in the power spectrum. In this case the parameterization for the PPS is derived from the potential:

$$V(\phi) = \frac{1}{2}m^2\phi^2\left[1 + c\tanh\left(\frac{\phi - \phi_0}{b}\right)\right]\,, \tag{4.27}$$

where c is the height and d the width of the step localized at $\phi = \phi_0$. This step-like feature in the inflaton potential leads to a localized oscillatory pattern with a negligible difference in the asymptotic amplitudes of the PPS. An analytic approximation for the PPS describing the step in the potential has been obtained in Refs. [242, 243]:

$$\mathcal{P}_\mathcal{R}(k) = \exp\left\{\ln\mathcal{P}_{\mathcal{R},0}(k) + \mathcal{I}_0(k) + \ln\left[1 + \mathcal{I}_1^2(k)\right]\right\}\,, \tag{4.28}$$

where the first-order term is:

$$\mathcal{I}_0(k) = \mathcal{A}_{\rm st} W'\left(\frac{k}{k_{\rm st}}\right) \mathcal{D}\left(\frac{k}{k_{\rm st} x_{\rm st}}\right) , \tag{4.29}$$

and the second-order contribution is [243]:

$$\sqrt{2}\mathcal{I}_1(k) = \frac{\pi}{2}\left(1 - n_{\rm s}\right) + \mathcal{A}_{\rm st} X'\left(\frac{k}{k_{\rm st}}\right) \mathcal{D}\left(\frac{k}{k_{\rm st} x_{\rm st}}\right) , \tag{4.30}$$

where $k_{\rm st}$ is the mode corresponding to the time of the transition and $x_{\rm st}$ is related to the duration of the violation of slow-roll. The window functions in Eqs. (4.29) and (4.30) are:

$$W(x) = \frac{3\sin(2x)}{2x^3} - \frac{3\cos(2x)}{x^2} - \frac{3\sin(2x)}{2x} , \tag{4.31}$$

$$X(x) = \frac{3}{x^3}\left(\sin x - x\cos x\right)^2 ; \tag{4.32}$$

in this context the prime denotes $\mathrm{d}/\mathrm{d}\ln x$ and the damping envelope is:

$$\mathcal{D}(x) = \frac{x}{\sinh x} . \tag{4.33}$$

We can rewrite the full power spectrum of curvature perturbation as [242, 243]:

$$\begin{aligned}
\mathcal{P}_{\mathcal{R}}(k) = \exp\Bigg\{ & \ln \mathcal{P}_{\mathcal{R},0}(k) \\
& + \frac{\mathcal{A}_{\rm st} k_{\rm st}^3}{2k^3}\left[\left(18\frac{k}{k_{\rm st}} - 6\frac{k^3}{k_{\rm st}^3}\right)\cos\left(2\frac{k}{k_{\rm st}}\right) + \left(15\frac{k^2}{k_{\rm st}^2} - 9\right)\sin\left(2\frac{k}{k_{\rm st}}\right)\right]\frac{k\cosh\left(\frac{k}{k_{\rm st}x_{\rm st}}\right)}{k_{\rm st}x_{\rm st}} \\
& + \ln\Bigg[1 + \frac{1}{2}\Bigg(\frac{\pi}{2}(1-n_{\rm s}) - \frac{3\mathcal{A}_{\rm st}k_{\rm st}^3}{k^3}\left[\frac{k}{k_{\rm st}}\cos\left(\frac{k}{k_{\rm st}}\right) - \sin\left(\frac{k}{k_{\rm st}}\right)\right] \\
& \quad \cdot \left[3\frac{k}{k_{\rm st}}\cos\left(\frac{k}{k_{\rm st}}\right) + \left(2\frac{k^2}{k_{\rm st}^2} - 3\right)\sin\left(\frac{k}{k_{\rm st}}\right)\right]\frac{k\cosh\left(\frac{k}{k_{\rm st}x_{\rm st}}\right)}{k_{\rm st}x_{\rm st}}\Bigg)^2\Bigg]\Bigg\} ,
\end{aligned} \tag{4.34}$$

where $\mathcal{A}_{\rm st}$ tunes the amplitude of the feature.

In DBI-models the step in the potential could also afflicts the non-standard kinetic term of the Lagrangian, this is the case of the *warp features* [244].

4.3.4 Super-imposed oscillations

We study the case of logarithmic super-imposed oscillations to the PPS:

$$\mathcal{P}_{\mathcal{R}} = \mathcal{P}_{\mathcal{R},0}(k)\left[1 + \mathcal{A}_{\log}\cos\left(\omega_{\log}\ln\left(\frac{k}{k_*}\right) + \phi_{\log}\right)\right] . \tag{4.35}$$

This pattern can be generated by different mechanisms. Axion monodromy inflation [234] motivates periodic oscillations on a large field inflaton potential leading to an approximated analytic PPS as in Eq. (4.35) [236]. See also [245] for the most recent developments including drifting oscillations. Logarithmic super-imposed oscillations can also be generated by initial quantum states different from Bunch-Davies [246].

A linear modulation in k can be obtained in boundary effective filed theory models [247]. We adopt the parameterization used in Ref. [248] which allows for a scale-dependent modulation amplitude:

$$\mathcal{P}_{\mathcal{R}}(k) = \mathcal{P}_{\mathcal{R},0}(k)\left[1 + \mathcal{A}_{\rm lin}\left(\frac{k}{k_*}\right)^{n_{\rm lin}}\cos\left(\omega_{\rm lin}\frac{k}{k_*} + \phi_{\rm lin}\right)\right] . \tag{4.36}$$

4.3.5 Results

All the models described above have been analysed in Ref. [44] (see also [243, 249–255] for a non-exhaustive list of works analyzing features with *Planck* data).

Table 4.7: Improvement in fit and Bayes factors with respect to power-law base ΛCDM for *Planck* TT+lowP and *Planck* TT,TE,EE+lowP data. Negative Bayes factors indicate a preference for the power-law model. This is extracted from Tab. 12 of [44].

Model	*Planck* TT+lowP		*Planck* TT,TE,EE+lowP	
	$\Delta\chi^2$	$\ln B$	$\Delta\chi^2$	$\ln B$
Broken power-law	−1.9	...	−1.6	...
Cutoff	−3.4	−1.4	−3.4	−1.4
Step	−8.6	−0.3	−7.3	−0.6
Logarithmic osc.	−10.6	−1.9	−10.1	−1.5
Linear osc.	−8.9	−1.9	−10.9	−1.3

We present the Bayes factors with respect to the power-law ΛCDM model and the improvement in χ^2 over the power-law in Tab. 4.7. While the model with a discontinuity

in the first derivative of the potential and step model best-fits reproduce the large-scale suppression at $\ell \approx 20 - 30$ also obtaind by the running of the spectral index and by the cutoff model, the oscillation models prefer relatively higher frequencies. In Fig. 5.2 we show these angular power spectra for the four best-fits and the relative differences with respect to the baseline ΛCDM model.

The inclusion of high-ℓ polarization data does not add much to the model with a discontinuity in the first derivative of the potential and step model since the $\ell < 30$ treatments are the same in all cases. The two oscillation models', on the other hand, also predict a non-negligible signature in the polarization spectra at high-ℓ. However, though the linear oscillation model's $\Delta\chi^2$ does increase, it occurs at different frequencies compared to their *Planck* TT+lowP counterparts.

4.4 Induced Gravity

In this section we present the results for the induced gravity dark energy models with a monomial potential studies in [62], which updates the paper on the quartic potential using *Planck* 2013 nominal mission data [60]. These two papers use publicly available *Planck* data and are published as papers external to the *Planck* Collaboration.

Following the background cosmology introduced in Sec. 1.5.2, we first describe cosmological fluctuations in Sec 4.4.1 and then the cosmological constraints in the other sections.

4.4.1 The evolution of cosmological fluctuations

We study linear fluctuations in the Jordan frame in the longitudinal gauge for the background cosmologies discussed in Sec. 1.5.2. The perturbed Einstein equations for

our IG model in the longitudinal gauge are:

$$3H(\dot{\Phi}+H\Psi)+\frac{k^2}{a^2}\Phi+3\frac{\dot{\sigma}}{\sigma}(\dot{\Phi}+2H\Psi)-\frac{\dot{\sigma}^2}{2\gamma\sigma^2}\Psi= \\ -\frac{1}{2\gamma\sigma^2}\Big[3\dot{\sigma}\,\delta\dot{\sigma}-6H^2\gamma\sigma\,\delta\sigma-6H\gamma(\dot{\sigma}\,\delta\sigma+\sigma\,\dot{\delta\sigma})-\frac{2\gamma k^2}{a^2}\delta\sigma+\sum_i\delta\rho_i+V_\sigma\delta\sigma\Big], \tag{4.37a}$$

$$\dot{\Phi}+\Psi\Big(H+\frac{\dot{\sigma}}{\sigma}\Big)=\frac{a}{2k^2}\frac{\sum_i(\rho_i+p_i)\theta_i}{\gamma\sigma^2}+\frac{\delta\sigma}{\sigma}\Big[\Big(1+\frac{1}{2\gamma}\Big)\frac{\dot{\sigma}}{\sigma}-H\Big]+\frac{\delta\dot{\sigma}}{\sigma}, \tag{4.37b}$$

$$\Phi-\Psi=\frac{2\delta\sigma}{\sigma}+\frac{3a^2}{2k^2}\frac{\sum_i(\rho_i+p_i)\bar{\sigma}_i}{\gamma\sigma^2}\,. \tag{4.37c}$$

In the above $\rho_i\,, p_i$ ($\delta\rho_i\,, \delta p_i$) denote the energy and (longitudinal) pressure density perturbations for each matter component, respectively. For each component, the velocity potential and the anisotropic stress are denoted by θ_i and $\bar{\sigma}_i$. We refer to Ref. [68] for the conservation of the CDM, baryons, photons and neutrino energy-momentum tensors, since these equations are unchanged from those in Einstein gravity.

The Klein-Gordon equation at linear order in the longitudinal gauge is:

$$\ddot{\delta\sigma}+\dot{\delta\sigma}\Big(3H+2\frac{\dot{\sigma}}{\sigma}\Big)+\Big[\frac{k^2}{a^2}+\Big(V_{\sigma\sigma}+4\frac{V}{\sigma^2}-4\frac{V_\sigma}{\sigma}\Big)-\frac{\dot{\sigma}^2}{\sigma^2}+\frac{\sum_i(\rho_i-3p_i)}{(1+6\gamma)\sigma^2}\Big]\delta\sigma \\ =\frac{2\Psi\sum_i(\rho_i-3p_i)}{(1+6\gamma)\sigma}+\frac{\sum_i(\delta\rho_i-3\delta p_i)}{(1+6\gamma)\sigma}+\dot{\sigma}\Big(3\dot{\Phi}+\dot{\Psi}\Big)\,. \tag{4.38}$$

We note that the terms in the potential and its derivatives in the effective mass of $\delta\sigma$ vanish only for $n=4$. We therefore expect a non-trivial dependence of $\delta\sigma$ on large scales since the onset of accelerated expansion for different n.

We have extended our previous modification [60] of the publicly available Einstein-Boltzmann code CLASS [6] [256, 257] to a generic potential. We therefore test our numerical results obtained by initializing fluctuations in the adiabatic initial conditions deep in the radiation era to the quasi-static approximation beyond the case of a quartic potential, which was studied previously [60]. We consider the parameters $\mu(k,a)$ and $\delta(k,a)$:

$$k^2\Psi = -4\pi Ga^2\mu(k,a)\left[\Delta+3(\rho+p)\bar{\sigma}\right]\,, \tag{4.39}$$

$$k^2[\Phi-\delta(k,a)\Psi] = 12\pi Ga^2\mu(k,a)(\rho+p)\bar{\sigma}\,, \tag{4.40}$$

[6] www.class-code.net

where $\Phi\,,\Psi$ are the Newtonian potentials in the longitudinal gauge, Δ is the total comoving energy perturbation (excluding the contribution from $\bar{\sigma}$) and $\bar{\sigma}$ is the anisotropic stress [60]. In the quasi-static approximation, for generic n, the two parameters are approximated as:

$$\mu(k,a) = \frac{\sigma_0^2}{\sigma^2}\frac{1+6\gamma}{1+8\gamma}\frac{1+8\gamma-2m_{\rm eff}^2/k^2}{1+6\gamma-2m_{\rm eff}^2/k^2} \tag{4.41}$$

$$\delta(k,a) = \frac{1+4\gamma-2m_{\rm eff}^2/k^2}{1+8\gamma-2m_{\rm eff}^2/k^2} \tag{4.42}$$

where

$$m_{\rm eff}^2 = \frac{d}{d\sigma}\left(\sigma^4\frac{d}{d\sigma}\left(\frac{V}{\sigma^4}\right)\right)\,. \tag{4.43}$$

Our exact numerical results are compared with the quasi-static approximation in Fig. 4.11 for $k = 0.005$ Mpc^{-1} and $\gamma = 10^{-2}$ when n is varied. As already established for the quartic potential [60], the quasi-static approximation for $\mu(k,a)$ is accurate only for sub-Hubble scales also in the general case, i.e. $n \neq 4$. The parameter $\delta(k,a)$ depends on time when $n \neq 4$, but depends on n weakly compared to $\mu(k,a)$.

The power spectra of the CMB temperature and polarization anisotropies for different values of γ are shown in the left panel of Fig. 4.12 for $n = 4$. The relative differences with respect to the ΛCDM reference model are shown in the top-right panel of Fig. 4.12.

4.4.2 Cosmological constraints on Induces Gravity

We performed the MCMC analysis by using the publicly available code Monte Python [7] [258] connected to our modified version of the code CLASS [8] [60, 256, 257]. We sampled on the quantity ζ, according to [60, 259], defined as:

$$\zeta \equiv \ln(1+4\gamma) = \ln\left(1+\frac{1}{\omega_{\rm BD}}\right)\,, \tag{4.44}$$

with the prior $[0, 0.039]$, where γ is the extra parameter related to the coupling with the Ricci curvature in Eq. (1.70).

[7] https://github.com/baudren/montepython_public
[8] www.class-code.net

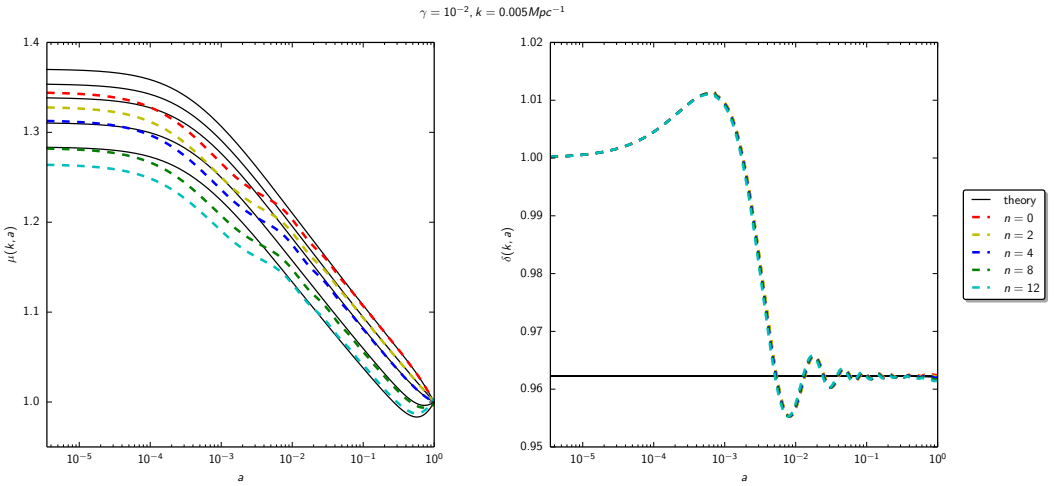

Figure 4.11: Comparison of the theoretical quasi-static approximations for $\mu(k, a)$ and $\delta(k, a)$ parameters (black lines) with our exact numerical results for $k = 0.005$ Mpc^{-1} and $\gamma = 10^{-2}$ when n is varied. Taken from [62].

The constraints obtained from CMB and BAO data with $n = 4$, for different combinations of data sets are summarized in Tab. 4.8. These results update those presented in Ref. [60] based on the *Planck* nominal mission temperature data, and use the same compilation of BAO data. See also [259–261] for other works studying *Planck* 2013 constraints on BD-like models. In combination with the same BAO data, the full mission temperature data improve the 95 % CL constraint on the coupling to the Ricci curvature γ by 25 % compared to the nominal mission data (see also Fig. 4.13) to:

$$\gamma < 0.00089 \qquad (95\,\%\ \text{CL},\ \textit{Planck}\ \text{TT+lowP+BAO})\,. \tag{4.45}$$

As from Tab. 4.8 and Fig. 4.13, in this model there is a positive correlation between γ and H_0, and therefore H_0 in this class of models is higher that ΛCDM.

Now we discuss the impact of the *Planck* lensing data [200]. One of the effects of the CMB lensing is to slightly favour smaller values of the amplitude of fluctuations A_s and therefore of the optical depth thanks to the accurate determination of $A_\mathrm{s}e^{-2\tau}$ by the CMB temperature power spectrum measured by *Planck*. We show in Fig. 4.14 how the addition of *Planck* lensing improves either the determination of τ and the constraint on γ.

In Tab. 4.9 we show the results with the inclusion of *Planck* high-ℓ polarization data. The IG dark energy model with a quartic potential provide a better fit of the

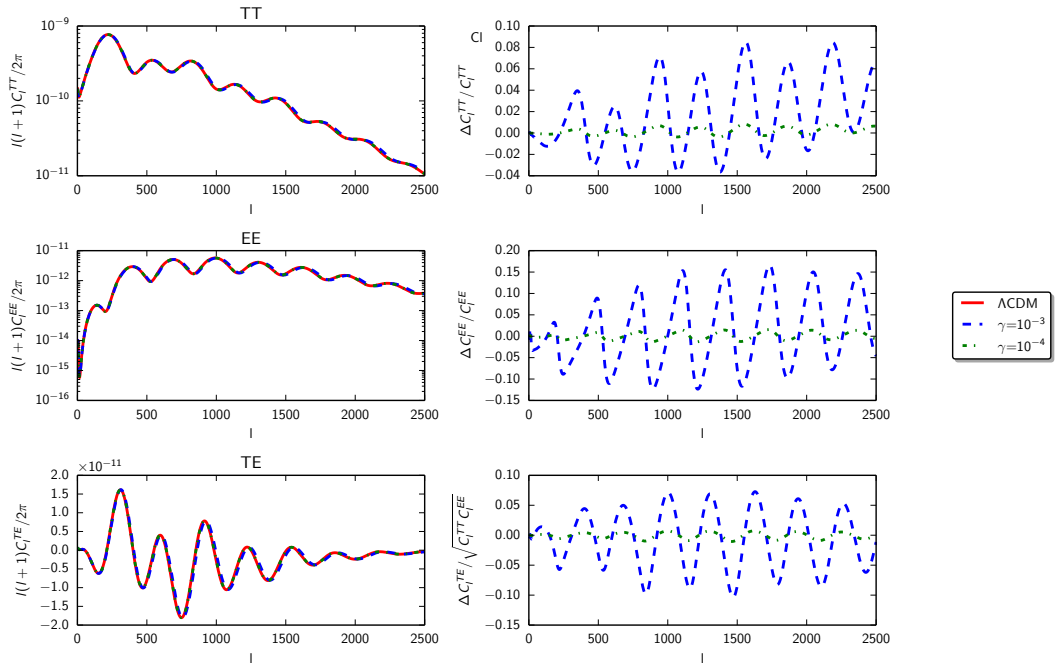

Figure 4.12: To the left, from the upper to the lower panel respectively, CMB TT, EE and TE power spectra for $\gamma = 10^{-3}, 10^{-4}$ and $n = 4$. In the upper and middle right panels, we show the relative differences for TT and EE spectra with respect to a reference ΛCDM model. In the lower right panel we show the differences for C_ℓ^{TE} normalized to $\sqrt{C_\ell^{TT} C_\ell^{EE}}$. Taken from [62].

data compared to ΛCDM, but not at a statistically significant level - $\Delta\chi^2 \simeq -1.2$ for *Planck* TT+lowP+BAO and $\Delta\chi^2 \simeq -2.3$ for *Planck* TT,TE,EE+lowP+lensing. It is important to note that all the information from *Planck* alone, i.e. temperature, polarization and lensing, are now capable to constrain γ:

$$\gamma < 0.0017 \qquad (95\,\%\ \text{CL, } \textit{Planck}\ \text{TT,TE,EE+lowP+lensing})\,. \quad (4.46)$$

We quote the following *Planck* TT,TE,EE+lowP+lensing+BAO at the 95 % CL constraint on the coupling to the Ricci curvature:

$$\gamma < 0.00075 \qquad (95\,\%\ \text{CL, } \textit{Planck}\ \text{TT,TE,EE+lowP+lensing+BAO})\,.$$

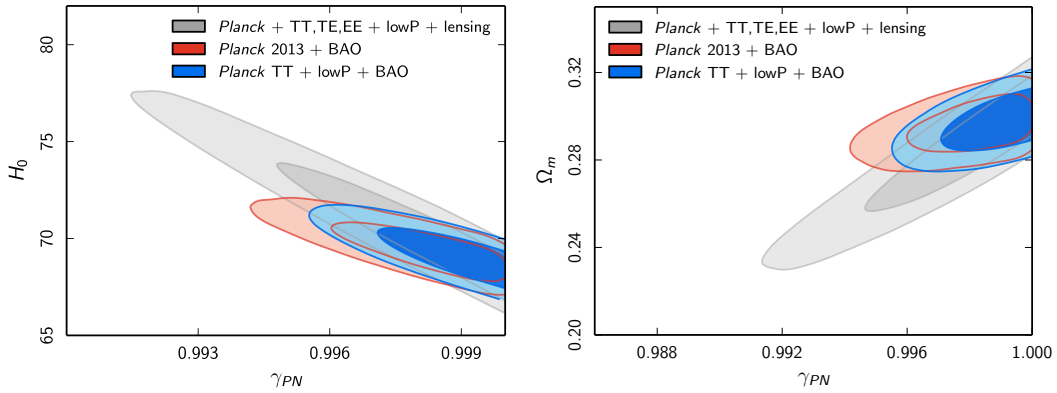

Figure 4.13: Marginalized joint 68 % and 95 % CL regions for ($\gamma_{\rm PN}$, H_0) on the left and ($\gamma_{\rm PN}$, $\Omega_{\rm m}$) on the right for *Planck* TT,TE,EE+lowP+lensing (gray), *Planck* 2013+BAO (red) and *Planck* TT+lowP+BAO (blue). Taken from [62].

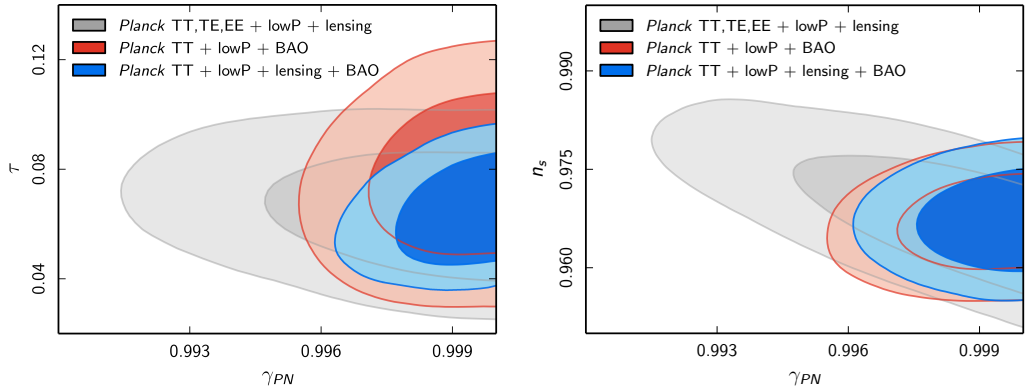

Figure 4.14: 2-dimentional marginalized confidence levels at 68 % and 95 % for ($\gamma_{\rm PN}$, τ) on the left and ($\gamma_{\rm PN}$, $n_{\rm s}$) on the right for *Planck* TT,TE,EE+lowP+lensing (gray), *Planck* 2013+BAO (red) and *Planck* TT+lowP+BAO (blue). Taken from [62].

(4.47)

We also quote the derived constraints on the change of the effective Newton's con-

Table 4.8: Constraints on main and derived parameters for *Planck* TT+lowP+BAO (at 68 % CL if not otherwise stated). In the first column we report the results obtained with the previous *Planck* 2013 data from Ref. [60]. Taken from [62].

Paramters	*Planck* 2013 +BAO	*Planck* TT + lowP +BAO	*Planck* TT + lowP +lensing+BAO
$10^5\Omega_{\rm b}h^2$	2203 ± 25	2224 ± 21	2224^{+20}_{-21}
$10^4\Omega_{\rm c}h^2$	1207^{+18}_{-22}	1198^{+16}_{-17}	1191 ± 14
H_0 [km s^{-1} Mpc^{-1}]	$69.5^{+0.9}_{-1.2}$	$69.4^{+0.8}_{-1.0}$	$69.4^{+0.7}_{-0.9}$
τ	$0.088^{+0.012}_{-0.013}$	$0.076^{+0.019}_{-0.018}$	$0.063^{+0.012}_{-0.014}$
$\ln\left(10^{10}A_{\rm s}\right)$	$3.090^{+0.024}_{-0.026}$	3.087 ± 0.036	$3.059^{+0.022}_{-0.026}$
$n_{\rm s}$	0.9611 ± 0.0053	0.9665 ± 0.0046	$0.9669^{-0.0042}_{-0.0047}$
ζ	< 0.0047 (95% CL)	< 0.0036 (95% CL)	< 0.0031 (95% CL)
$10^3\gamma$	< 1.2 (95% CL)	< 0.89 (95% CL)	< 0.75 (95% CL)
γ_{PN}	> 0.9953 (95% CL)	> 0.9965 (95% CL)	> 0.9970 (95% CL)
$\Omega_{\rm m}$	0.295 ± 0.009	0.295 ± 0.008	0.294 ± 0.008
$\delta G_{\rm N}/G_{\rm N}$	$-0.015^{+0.013}_{-0.006}$	$-0.011^{+0.010}_{-0.004}$	$-0.009^{+0.003}_{-0.009}$
$10^{13}\dot{G}_{\rm N}(z=0)/G_{\rm N}$ [yr^{-1}]	$-0.61^{+0.55}_{-0.25}$	$-0.45^{+0.43}_{-0.16}$	$-0.37^{+0.34}_{-0.12}$
$10^{23}\ddot{G}_{\rm N}(z=0)/G_{\rm N}$ [yr^{-2}]	$0.86^{+0.33}_{-0.78}$	$0.63^{+0.22}_{-0.58}$	$0.52^{+0.17}_{-0.50}$

stant between the radiation era and the present time $\delta G_{\rm N}/G_{\rm N} \equiv (\sigma_i^2 - \sigma_0^2)/\sigma_0^2$:

$$\frac{\delta G_{\rm N}}{G_{\rm N}} = -0.002^{+0.002}_{-0.037} \qquad (95\,\%\ \text{CL, } \textit{Planck}\ \text{TT,TE,EE+lowP+BAO})\,, \quad (4.48)$$

and the constraint on its derivatives ($\dot{G}_{\rm N}/G_{\rm N} \equiv -2\dot{\sigma}_0/\sigma_0$) at present time:

$$\frac{\dot{G}_{\rm N}}{G_{\rm N}}(z=0) = -0.08^{+0.08}_{-0.55}\ [\times 10^{-13}\ \text{yr}^{-1}] \quad (95\,\%\ \text{CL, } \textit{Planck}\ \text{TT,TE,EE+lowP+BAO})\,, \quad (4.49)$$

$$\frac{\ddot{G}_{\rm N}}{G_{\rm N}}(z=0) = 0.36^{+0.26}_{-0.36}\ [\times 10^{-23}\ \text{yr}^{-1}] \quad (95\,\%\ \text{CL, } \textit{Planck}\ \text{TT,TE,EE+lowP+BAO})\,. \quad (4.50)$$

Table 4.9: Constraints on main and derived parameters for *Planck* TT,TE,EE+lowP with different combination of other datasets (at 68 % CL if not otherwise stated). Taken from [62].

Parameters	*Planck* TT,TE,EE +lowP+lensing	*Planck* TT,TE,EE +lowP+BAO	*Planck* TT,TE,EE +lowP+lensing+BAO
$10^5\Omega_{\rm b}h^2$	2234 ± 17	2231 ± 14	2223 ± 20
$10^4\Omega_{\rm c}h^2$	1189 ± 14	1194 ± 12	1191^{+15}_{-14}
H_0 [km s^{-1} Mpc^{-1}]	$71.0^{+1.4}_{-3.0}$	$69.4^{+0.6}_{-1.1}$	$69.4^{+0.5}_{-1.0}$
τ	$0.066^{+0.012}_{-0.013}$	$0.079^{+0.017}_{-0.016}$	$0.063^{+0.012}_{-0.014}$
$\ln\left(10^{10}A_{\rm s}\right)$	$3.066^{+0.024}_{-0.028}$	$3.095^{+0.031}_{-0.033}$	$3.059^{+0.021}_{-0.026}$
$n_{\rm s}$	0.9695 ± 0.0056	0.9675 ± 0.0041	$0.9669^{-0.0043}_{-0.0048}$
ζ	< 0.0068 (95% CL)	< 0.0030 (95% CL)	< 0.0030 (95% CL)
$10^3\gamma$	< 1.7 (95% CL)	< 0.76 (95% CL)	< 0.75 (95% CL)
γ_{PN}	> 0.9933 (95% CL)	> 0.9970 (95% CL)	> 9970 (95% CL)
$\Omega_{\rm m}$	0.281 ± 0.009	0.295 ± 0.015	0.294 ± 0.008
$\delta G_{\rm N}/G_{\rm N}$	$-0.020^{+0.019}_{-0.005}$	$-0.010^{+0.004}_{-0.009}$	$-0.009^{+0.003}_{-0.009}$
$10^{13}\dot{G}_{\rm N}(z=0)/G_{\rm N}$ [yr^{-1}]	$-0.77^{+0.43}_{-0.27}$	$-0.39^{+0.35}_{-0.15}$	$-0.37^{+0.34}_{-0.12}$
$10^{23}\ddot{G}_{\rm N}(z=0)/G_{\rm N}$ [yr^{-2}]	$1.2^{+0.4}_{-1.1}$	$0.56^{+0.21}_{-0.50}$	$0.52^{+0.17}_{-0.50}$

4.4.3 Combination with local measurements

We analyze the combination of the local measurements of the Hubble constant with *Planck* TT + lowP by considering the impact of two different local estimates of H_0, such as: $H_0 = 73.8 \pm 2.4$ km s^{-1} Mpc^{-1} [262], denoted as H_0^*, and $H_0 = 70.6 \pm 3.0$ km s^{-1} Mpc^{-1} [263], denoted as $H_0^\dagger$. We find:

$$H_0 = 73.1^{+2.1}_{-2.3}\ [\text{km s}^{-1}\ \text{Mpc}^{-1}] \qquad (68\,\%\ \text{CL},\ \textit{Planck}\ \text{TT+lowP+H}_0^*)\,, \qquad (4.51)$$

$$\gamma = 0.0011 \pm 0.0010 \qquad (95\,\%\ \text{CL},\ \textit{Planck}\ \text{TT+lowP+H}_0^*)\,, \qquad (4.52)$$

and

$$H_0 = 71.3^{+1.8}_{-2.8}\ [\text{km s}^{-1}\ \text{Mpc}^{-1}] \qquad (68\,\%\ \text{CL},\ \textit{Planck}\ \text{TT+lowP+H}_0^\dagger)\,, \qquad (4.53)$$

$$\gamma < 0.0017 \qquad (95\,\%\ \text{CL},\ \textit{Planck}\ \text{TT+lowP+H}_0^\dagger)\,. \qquad (4.54)$$

We note that the degeneracy of H_0 with higher value of γ has been reduced with the improved accuracy of the *Planck* full mission temperature data, compared to the nominal mission data [60]. In combination with BAO, we find:

$$H_0 = 69.4^{+0.8}_{-1.0}\ [\mathrm{km\ s^{-1}\ Mpc^{-1}}] \qquad (68\,\%\ \mathrm{CL},\ \textit{Planck}\ \mathrm{TT{+}lowP{+}BAO})\,, \quad (4.55)$$

which is larger than the value obtained for the ΛCDM model with three massless neutrinos, i.e. 67.8 ± 0.6 km s^{-1} Mpc^{-1}, for the same combination of datasets.

4.4.4 BBN consistency relation on G_{N}

The value of the effective gravitational constant determines the expansion rate in the radiation era and therefore can affect the cosmological abundances of the light elements during Big Bang Nucleosynthesis (BBN). Therefore, BBN was used to provide limits to the variation of the effective Newton's constant [264, 265].

In the following we investigate the impact of the modification of the BBN consistency condition implemented in the public code PArthENoPE [266] due to the different value of the effective Newton's constant during nucleosynthesis. We consider the effect of a different gravitational constant as a source of extra radiation in $Y_{\mathrm{P}}^{\mathrm{BBN}}(\omega_b,\, N_{\mathrm{eff}})$, [267]. It is interesting to note that with this improved BBN consistency condition the posterior probabilities for the primary cosmological parameters are unaffected, and we just observe a small shift for the primordial Helium abundance towards higher values.

4.4.5 Cosmological constraints for $n \neq 4$

We consider also the case with a generalized monomial potential $V(\sigma) = \sigma^n$. Such potentials with a positive power are easily motivated at fundamental level or within particle physics, as happens for the analogous case of a non-minimally coupled scalar field [268], and in higher dimensions theories [269].

Current data cannot discriminate at a statistical significant level between different values of n, and the posterior probabilities for the seven primary cosmological parameters hardly change for these different values of n.

On the opposite, we note that the posterior probabilities for $\dot{G}_{\mathrm{N}}/G_{\mathrm{N}}$ and $\ddot{G}_{\mathrm{N}}/G_{\mathrm{N}}$ at present time depend on n. This dependence on n must be kept in mind when comparing cosmological bounds on $\dot{G}_{\mathrm{N}}/G_{\mathrm{N}}(z=0)$ and $\ddot{G}_{\mathrm{N}}/G_{\mathrm{N}}(z=0)$ (which depend on the form of the potential) with Solar System constraints on the same time variations (which are obtained extrapolating from the massless case since the effect of the potential is considered negligible on such smaller scales detached from the cosmological expansion).

Table 4.10: Constraints on the variation of the gravitational constant and its time derivatives (at 95 % CL) for different values of n with *Planck* TT+lowP+BAO. Taken from [62].

Parameters	$n = 0$	$n = 2$	$n = 4$	$n = 6$	$n = 8$
$\delta G_{\rm N}/G_{\rm N}$	> -0.028	> -0.027	> -0.026	> -0.026	> -0.025
$10^{13}\dot{G}_{\rm N}(z=0)/G_{\rm N}$ [yr^{-1}]	> -3.9	> -2.5	> -0.11	< 0.4	< 1.9
$10^{23}\ddot{G}_{\rm N}(z=0)/G_{\rm N}$ [yr^{-2}]	< 0.077	< 0.78	< 1.5	< 2.3	< 3.0

The bound on the shift of the scalar field between today and the radiation era is the same however it's evolution show a strong dependence from the choice of the potential as summarized in Table 4.10.

Let us conclude this Sec. 4.4 by mentioning future developments for these studies. We obviously wish to update these results with the final *Planck* data release, but in particular we wish to forecast Euclid capabilities of clustering and weak lensing in combination with CMB anisotropies measurements.

5 Primordial features with future galaxy surveys

In the previous chapter, we have discussed the implications of *Planck* 2015 data either for slow-roll inflation and for models of inflation which contains temporary violation of the slow-roll condition. Beyond the handle of better measurements of CMB polarization, the current snapshot of the PPS taken by *Planck* [23, 44] will be also further refined by future galaxy surveys as DESI [1] [141, 270], Euclid [2] [142, 271], SPHEREx [3] [143], LSST [4] [144], SKA [5] [272] and others. Thanks to the different sensitivity of the matter power spectrum to cosmology, future galaxy surveys will be useful to break the degeneracy among cosmological parameters encoded in the CMB angular power spectra of temperature and polarization.

We present a Fisher matrix forecast for several different types of surveys to probe departures from a power-law spectrum for primordial fluctuations. We consider the information from the galaxy clustering power spectrum up to quasi-linear scales, i.e. $k < 0.1$ h Mpc^{-1}, taking into account the error of the sample variance, the shot noise and spectroscopic/photometric redshift uncertainties (as discussed in Sec. 3.4.2).

We assume a fiducial cosmology described by the minimal flat ΛCDM model and we study the dependence on the following set of parameters: the cosmological parameters $\theta_0 = \{\Omega_{\rm c}, \Omega_{\rm b}, h_0, \tau, n_{\rm s}, \ln\left(10^{10} A_{\rm s}\right)\}$, the extra parameters which describe the parametrization of the PPS $\theta_{\rm ext}$ for some selected models described in the previous chapter, and the nuisance parameters $\theta_{\rm nui} = \{b, P_{\rm shot}, \sigma^2_{\rm tot}\}$ according to Ref. [194]. We consider a set of nuisance parameters per redshift bin in order to avoide any possible prior information about them. In this analysis we marginalize over $\theta_{\rm nui}$, and we assume that they do not depend on the cosmological parameters, θ_0, and over the extra ones, $\theta_{\rm ext}$.

We present the forecasts in combination with the CMB Fisher matrix information

[1] http://desi.lbl.gov/
[2] http://sci.esa.int/euclid/
[3] http://spherex.caltech.edu/
[4] http://www.lsst.org/
[5] http://www.skatelescope.org/

(as discussed in Sec. 3.4.1), with $\mathbf{F}_{ij}^{\rm CMB}$ representing the CMB measurements. We restrict ourselves to noise sensitivity and angular resolution to characterize the uncertainties in the CMB temperature and polarization spectra, although we know that the accuracy of CMB anisotropies measurements are not governed only by noise sensitivity and angular resolution, but limited in temperature at high multipoles by foreground residuals/secondary anisotropies and at low multipoles in polarization by the Galactic emission. Since the time scales of the surveys are different, not only the *Planck* final data in temperature and polarization, but also other measurements of CMB E-mode polarization on a large fraction of the sky, such as from Advcanced ACTpol, CLASS, LSPE [273], will be available. Therefore, we consider two settings, one more conservative (hereafter CMB-1) and another one with better sensitivity and angular resolution (CMB-2). We take into account the *Planck* 143 GHz channel as CMB-1 and the inverse noise weighted combination of the *Planck* 70, 100, 143 and 217 GHz channels as CMB-2. We consider the information from the TT, TE, and EE APS with updated full mission sensitivities and angular resolution as given in [125]. We use a sky fraction of $f_{\rm sky} = 0.75$, and a sum up to $\ell_{\rm max} = 2500$ in Eq. (3.43).

We study in the following representative classes of models: a cutoff model described by Eq. (4.22), in which depletion of power at large wavelengths is parametrized, sharp feature models, in which the inflation model contains a discontinuity in the first derivative of the potential (see Sec. 4.3.2) and a step in the inflaton potential (see Sec. 4.3.3); resonance feature models with logarithmic oscillation described by Eq. (4.35), in which the inflation model contains features that are periodic in time. For the fist three models deviations from a power-law spectrum are confined to the largest scales, whereas for the fourth one oscillations are on all scales.

We plot in Fig. 5.1 the PPS for the four representative inflationary models studied in this chapter and the baseline ΛCDM model. For each models the best-fit parameters for the standard cosmological parameters and for the extra parameters have been obtained with *Planck* TT+lowP [44]. In Fig.5.2 we show the lensed TT, EE, and TE, angular power spectra for this four models, and the relative differences with respect to the ΛCDM model. In Fig. 5.3, we plot the non-linear matter power spectrum at $z = 0$ for the four representative models, and their relative differences with respect to the baseline ΛCDM model.

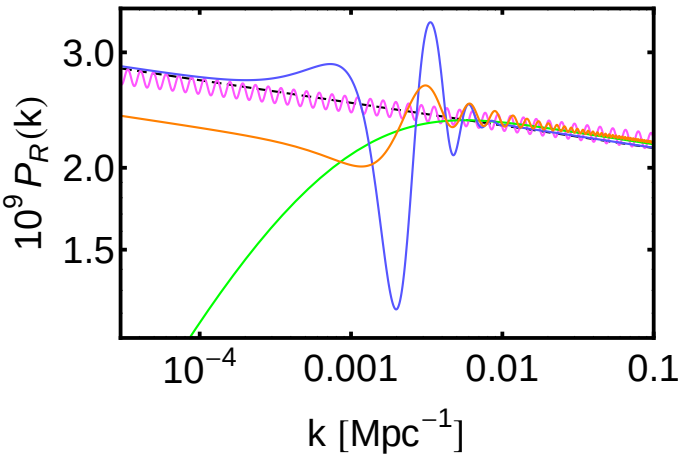

Figure 5.1: We show the PPS for a power-law spectrum (dashed black line), for the cutoff model (green solid line), for the model with a discontinuity in the first derivative of the potential (orange solid line), for the model with a step in the inflaton potential (blue solid line), and the model with logarithmic wiggles (magenta solid line). Taken from [274].

5.1 Spectroscopic and photo-spectroscopic surveys

5.1.1 A DESI catalog

In our analysis, for DESI, we use the specifications from Ref. [270] (cf. Tabs. 2.3 and Tab. 3.1 in Ref. [270]). In particular, we consider a coverage of 14000 deg^2 spanned over a redshift range from z=0.6 to 1.9.

We consider the combined galaxy clustering information for different tracers observed by DESI. We use a simplified picture in which we assume that the different populations of LRGs, ELGs and QSOs are contributing to an effective unique population, covering thirteen redshift bins between $z = 0.6$ and 1.9 with width of $\Delta z = 0.1$, and having an effective bias given by [275]:

$$b_{\rm eff}(z) = \frac{\bar{n}_{\rm LRG}(z) b_{\rm LRG}(z) + \bar{n}_{\rm ELG}(z) b_{\rm ELG}(z) + \bar{n}_{\rm QSO}(z) b_{\rm QSO}(z)}{\bar{n}_{\rm LRG}(z) + \bar{n}_{\rm ELG}(z) + \bar{n}_{\rm QSO}(z)}\,, \tag{5.1}$$

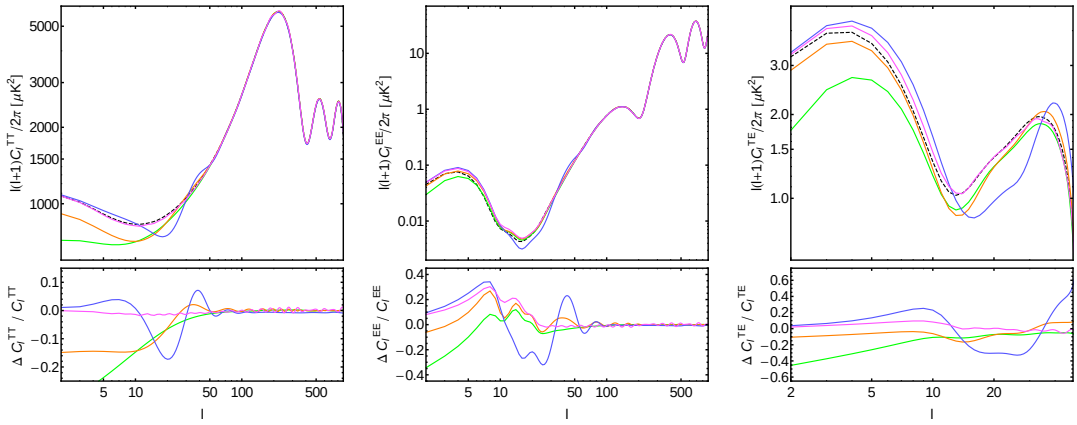

Figure 5.2: Lensed angular power spectra TT (left panel), EE (middle panel), TE (right panel) for the baseline ΛCDM model (black dashed line), for the cutoff model (green solid line), for the model with a discontinuity in the first derivative of the potential (orange solid line), for the model with a step in the inflaton potential (blue solid line), and the model with logarithmic wiggles (magenta solid line). In the bottom panels we display the corresponding relative differences of the models with respect to the baseline ΛCDM model. Taken from [274].

where we assume:

$$b_{\rm LRG}(z) = 1.7\ D(0)/D(z)\,, \tag{5.2}$$

$$b_{\rm ELG}(z) = 0.84\ D(0)/D(z)\,, \tag{5.3}$$

$$b_{\rm QSO}(z) = 1.34\ D(0)/D(z)\,. \tag{5.4}$$

This description is a good approximation of the exact multi-tracers approch in the limit of independent tracers [275]. For this purpose, we have also reduced the number of objects in the total sample as in [275] to include the effects of the target selection resulting in a good redshift definition and in a minimization of confusion between different tracers and other astrophysical objects (see the right panel of Fig. 5.4). The resulting effective bias is shown on the left panel in Fig. 5.4. As error for the DESI spectroscopic redshift we use $\bar{\sigma}_{\rm z} \sim 0.001$ [270]. As a reference, we obtain $k_{\rm min}$ ranging between $(3.59 - 4.71) \times 10^{-3}$ h Mpc^{-1} for the different redshift bins here considered.

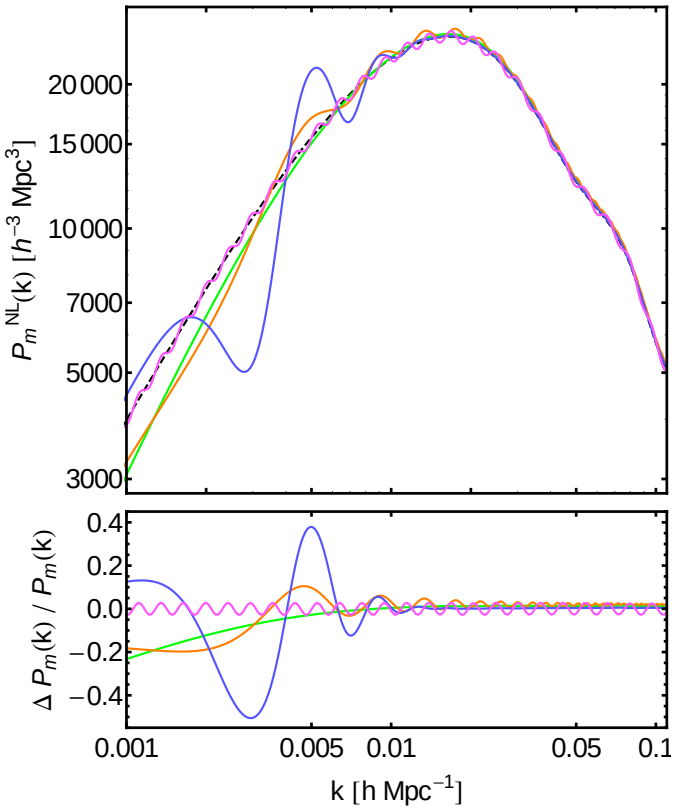

Figure 5.3: In the top panel we show the non-linear matter power spectrum for ΛCDM (dashed black line), for the cutoff model (green solid line), for the model with a discontinuity in the first derivative of the potential (orange solid line), for the model with a step in the inflaton potential (blue solid line), and the model with logarithmic wiggles (magenta solid line). In the bottom panel we display the corresponding relative differences of the models with respect to the baseline ΛCDM model. Taken from [274].

5.1.2 A Euclid catalog

According to the updated predictions obtained by [276], the Euclid wide single-grism survey will reach a flux limit $F_{\mathrm{H}\alpha} > 2 \times 10^{-16}$ erg cm^{-2} s^{-1} and will cover a redshift range $0.9 < z < 1.8$. We consider nine redshift bins in this redshift range with the same width of $\Delta z = 0.1$, over an area of 15000 deg^2. With these specifications and

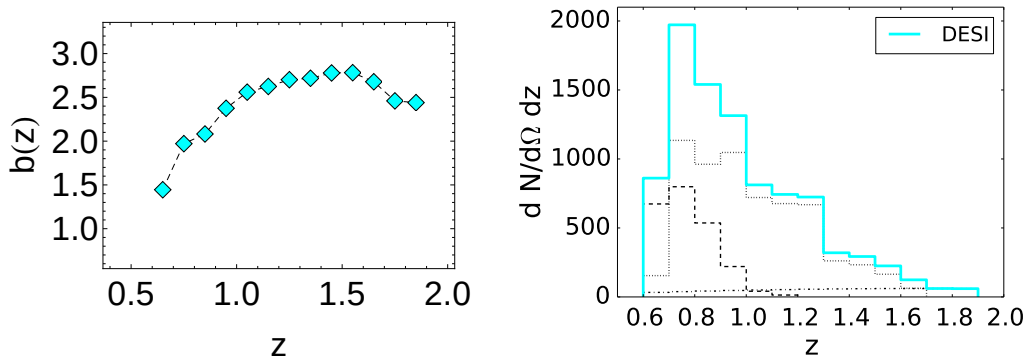

Figure 5.4: We show the linear bias (left panel) calculated according to Eq. (5.1) and the number density of objects (right panel) per unit of redshift bin Δz and per square degree according to Ref. [270], used for the analysis with DESI. We show the distribution for each single tracers and the cumulative one: LRGs (dashed), ELGs (dotted), QSOs (dot-dashed), and the total population (cyan).

assuming a completeness of 70 %, the expected density number of Hα emitters is about 4000 objects/deg^2, the redshift distribution of which (cf. Tab. 3 in Ref. [276]) is shown in the right panel of Fig. 5.5.

We can safely assume that the galaxy sample is composed by a single tracer, ELGs, and then that the bias follows Eq. (5.3). Finally, we adopt as redshift accuracy $\bar{\sigma}_z \sim 0.001$ [271]. As a reference, we obtain $k_{\rm min}$ in a range $(3.59 - 4.01) \times 10^{-3}$ h Mpc^{-1} in the different redshift bins.

5.1.3 A SPHEREx catalog

SPHEREx [143] is a NASA proposed small explorer satellite having the goal of providing the first near-infrared spectro-photometric image of the complete sky, thanks to its coverage of 40000 deg^2 in the wavelength range $0.75 < \lambda\ \mu$m$^{-1} < 4.8$.

SPHEREx will collect spectra of galaxies at $z < 1$, covering the redshift range for clustering studies that are not covered by IR telescopes like Euclid and WFIRST-AFTA [6]. Moreover, it will observe high-redshift quasars in its deep fields. In our analysis we will consider only the galaxy sample, assuming that the fraction of sky usable for

[6] http://wfirst.gsfc.nasa.gov/

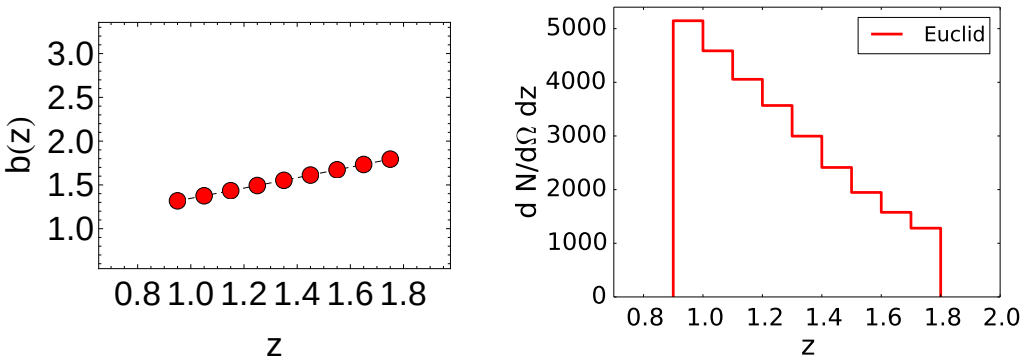

Figure 5.5: We show the linear bias (left panel) calculated according to Eq. (5.3) and the number density of objects (right panel) per unit of redshift bin Δz and per square degree according to Ref. [276], used for the analysis of with Euclid.

clustering studies is 75 % of the whole sky, in strict analogy to what is done in CMB analyses.

We consider two different configurations for SPHEREx [7], with $\bar{\sigma}_z \sim 0.003$ (hereafter SPHEREx1) and $\bar{\sigma}_z \sim 0.01$ (hereafter SPHEREx2).

For the two different configurations we consider five redshift bins, between $z = 0.0$ and 1.0, and one redshift bin, between $z = 1.0$ and 1.6, with a width of $\Delta z = 0.2$ between 0 and 1 and of $\Delta z = 0.6$ for higher redshifts. The adopted bias is shown in the left panel of Fig. 5.6. As a reference, for SPHEREx we obtain $k_{\rm min}$ in the range $(1.60 - 7.51) \times 10^{-3}$ h Mpc^{-1}.

5.1.4 Results

We now discuss the uncertainties in the cosmological parameters obtained as result of our combined CMB and LSS Fisher approach for DESI, Euclid, and SPHEREx.

For the ΛCDM model the uncertainties in the cosmological parameters are reported in Tab. 5.1. Our results for the uncertainties from CMB and LSS are broadly consistent with the ones in the literature. However, possible discrepancies can arise from our conservative cut at $k < 0.1$ h Mpc^{-1} for each redshift bins and from different assumptions for CMB specifications.

[7] We wish to thank Olivier Doré and Roland de Putter for making available the SPHEREx specifications to us, according to the simulations described in Ref. [277].

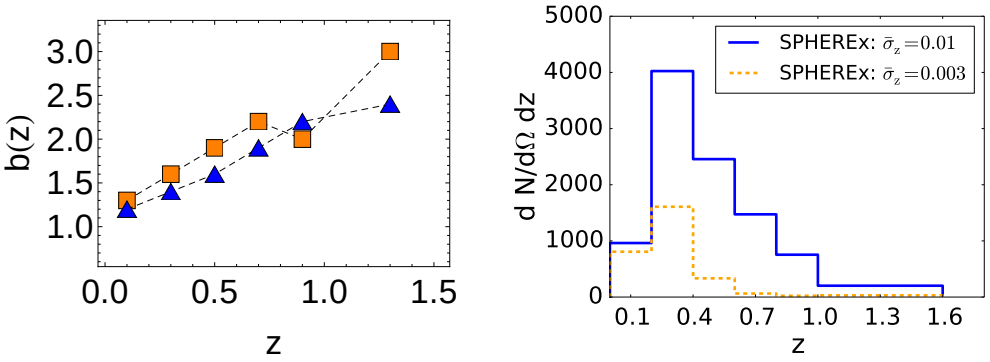

Figure 5.6: We show the linear bias (left panel) calculated and the number density of objects (right panel) per unit of redshift bin Δz used for the analysis of with SPHEREx. In the right panel we show two galaxy populations obtained for SPHEREx by considering different redshift uncertainty: the dashed (solid) line represents the observed objects considering a redshift uncertainty $\bar{\sigma}_z \sim 0.003$ (0.01) with a redshift bin of $\Delta z = 0.2$ between 0 and 1 and of $\Delta z = 0.6$ for higher redshifts.

Table 5.1: Forecasts for the marginalized 68 % uncertainties for the cosmological parameters in the ΛCDM model with our Fisher approach. The two results in the parentheses include the constraints obtained in combination with the CMB Fisher matrix for the two configurations (CMB-1 and CMB-2, respectively). We do not list the forecasted uncertainty for τ since it does not benefit from the inclusion of LSS. We refer to Tab. 4.1 for the *Planck* 2015 uncertainties. Taken from [274].

	DESI	Euclid	SPHEREx1	SPHEREx2
$10^3\ \sigma\,(\Omega_\mathrm{c})$	11.6 (2.6/2.5)	9.6 (2.1/2.0)	13.1 (2.9/2.7)	7.1 (1.8/1.6)
$10^3\ \sigma\,(\Omega_\mathrm{b})$	4.1 (0.28/0.26)	3.0 (0.25/0.23)	4.6 (0.30/0.29)	2.5 (0.23/0.21)
$\sigma\,(H_0)$	4.0 (0.21/0.20)	3.0 (0.17/0.16)	4.4 (0.23/0.22)	2.6 (0.15/0.14)
$10^2\ \sigma\,(n_\mathrm{s})$	6.7 (0.26/0.24)	5.3 (0.25/0.22)	7.5 (0.26/0.23)	4.2 (0.24/0.22)
$10^2\ \sigma\left(\ln\left(10^{10}A_\mathrm{s}\right)\right)$	35.5 (0.80/0.71)	32.9 (0.74/0.67)	37.9 (0.83/0.74)	21.2 (0.74/0.67)

We have also analyzed the case in which the dependence in the wavelength of the spectral index is allowed to vary, by fixing the fiducial model to $(n_{\rm s}, {\rm d}n_{\rm s}/{\rm d}\ln k) = (0.9655, 0.0)$. We obtain the following uncertainties $(\sigma(n_{\rm s}), \sigma({\rm d}n_{\rm s}/{\rm d}\ln k))$: $(0.0026, 0.0049)$ for DESI, $(0.0025, 0.0047)$ for Euclid, $(0.0026, 0.0046)$ for SPHEREx1, and $(0.0024, 0.0031)$ SPHEREx2, when the CMB-1 Fisher information for the more conservative configuration is added. When combining the Fisher information for the second CMB configuration with the LSS one, the errors are slightly decreased as can be seen in Fig. 5.7. The parameter space with ${\rm d}n_{\rm s}/{\rm d}\ln k$ exceeding the standard slow-roll predictions $\approx (n_{\rm s}-1)^2$ will be further probed by future galaxy surveys.

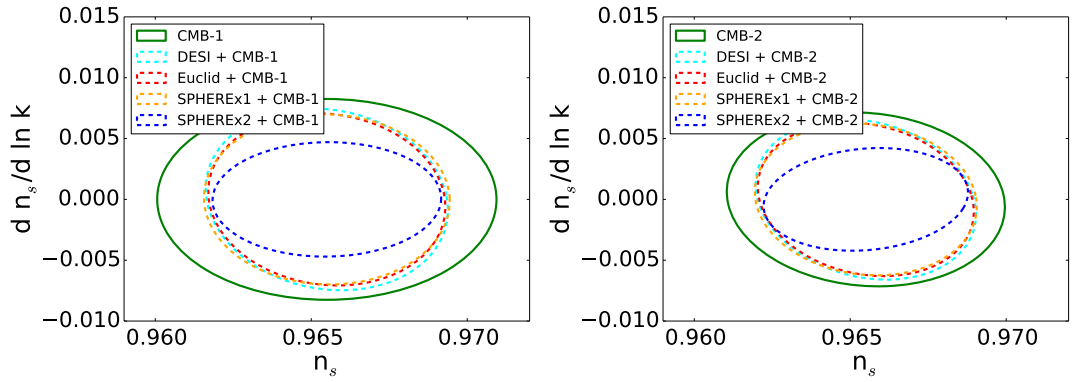

Figure 5.7: CMB and LSS combined constraints on $(n_{\rm s}, {\rm d}n_{\rm s}/{\rm d}\ln k)$ at 68 % CL. Different lines refer to CMB only (solid green), DESI (dashed cyan), Euclid (dashed red) and SPHEREx (dashed orange). The configuration CMB-1 (CMB-2) is considered in the left (right) panel. Taken from [274].

Geometrical distortions to the galaxy power spectrum due to the changes in $H(z)$ and $D_{\rm A}(z)$ will cause both a horizontal and vertical shift in the observed power spectrum and introduce new degeneracies in the measured power spectrum [278]. The AP effect instead has a main impact on the late-time parameters [279].

Overall, the impact of the geometrical distortions and of the AP term included in the analysis, see Eqs. (3.33)-(3.34)-(3.35), mainly affect the uncertainties of the standard cosmological parameters of the ΛCDM model and to a smaller extent the running of the spectral index. They have a small impact on the uncertainties of the extra parameters of the models with features in the PPS, in particular after having marginalized over the several nuisance parameters.

We now discuss our results for the four inflationary models with features considered. The results are summarized in Tab. 5.2.

Table 5.2: Forecasts for the marginalized 68 % uncertainties for the features parameters for any survey considered in combination with CMB-1 (CMB-2 in parenthesis). Taken from [274].

Model	Parameter (Best-fit)		DESI + CMB-1 (CMB-2)	Euclid + CMB-1 (CMB-2)	SPHEREx1 + CMB-1 (CMB-2)	SPHEREx2 + CMB-1 (CMB-2)
MI	λ_c	(0.5)	0.17 (0.21)	0.14 (0.21)	0.14 (0.22)	0.17 (0.20)
	$\log_{10}(k_c \text{ Mpc})$	(-3.47)	0.74 (0.39)	0.65 (0.39)	0.74 (0.39)	0.33 (0.35)
MII	Δ	(0.089)	0.050 (0.048)	0.042 (0.041)	0.053 (0.051)	0.032 (0.031)
	$\log_{10}(k_s \text{ Mpc})$	(-3.05)	0.10 (0.079)	0.090 (0.072)	0.11 (0.081)	0.071 (0.062)
MIII	$\mathcal{A}_{st}$	(0.374)	0.35 (0.28)	0.34 (0.28)	0.34 (0.28)	0.34 (0.28)
	$\log_{10}(k_{st} \text{ Mpc})$	(-3.10)	0.051 (0.050)	0.040 (0.039)	0.055 (0.053)	0.040 (0.039)
	$\ln x_{st}$	(0.342)	0.52 (0.46)	0.49 (0.43)	0.53 (0.48)	0.49 (0.43)
MIV	$\mathcal{A}_{log}$	(0.0278)	0.0035 (0.0032)	0.0030 (0.0028)	0.0038 (0.0035)	0.0025 (0.0024)
	$\log_{10}(\omega_{log})$	(1.51)	0.0087 (0.0079)	0.0077 (0.0071)	0.0094 (0.0084)	0.0062 (0.0059)
	$\phi_{log}/(2\pi)$	(0.634)	0.020 (0.018)	0.017 (0.016)	0.021 (0.019)	0.014 (0.013)

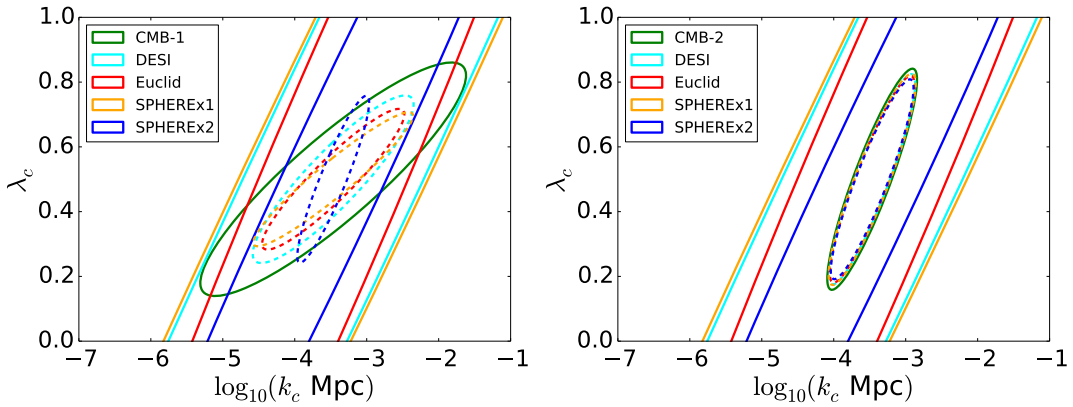

Figure 5.8: Marginalized 2D 68 % CL contours for the parameters $(\log_{10}(k_c \text{ Mpc}), \lambda_c)$ of MI for CMB only (solid green), DESI (solid cyan), Euclid (solid red), SPHEREx1 (solid orange), and SPHEREx2 (solid blue). The dashed contours represent the 2D 68 % CL CMB and LSS combined results. The configuration CMB-1 (CMB-2) is considered in the left (right) panel. Taken from [274].

The effective very large scale of the cutoff model obtained as a best-fit for *Planck*

2015 [44] is a challenge for the future galaxy surveys here considered (see Fig. 5.8). Such a modification on large scales seems a better target for high-sensitivity CMB polarization experiments covering a large fraction of the sky, such as *Planck*, Advanced ACTpol, CLASS, LSPE, which will provide an improved measurement of the E-mode polarization on large scales.

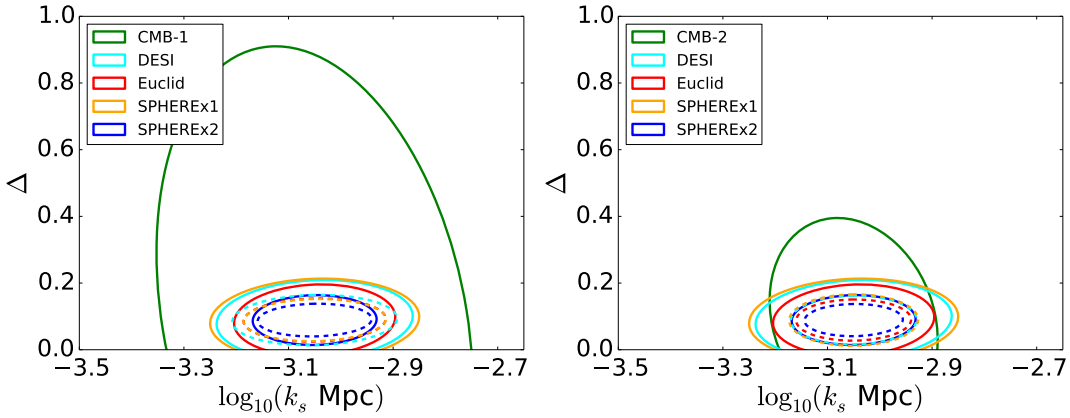

Figure 5.9: Marginalized 2D 68 % CL contours for the parameters $(\log_{10}(k_s \text{ Mpc}), \Delta)$ of MII for CMB only (green), DESI (solid cyan), Euclid (solid red), SPHEREx1 (solid orange), and SPHEREx2 (solid blue). The dashed contours represent the 2D 68 % CL CMB and LSS combined results. The configuration CMB-1 (CMB-2) is considered in the left (right) panel. Taken from [274].

The model with a discontinuity in the first derivative of the potential [110], has also two parameters as the first model, but the resulting power spectrum has super-imposed oscillations accompanying the change in the amplitude of the PPS. These oscillations are non-zero at scales smaller than the change in amplitude and can be therefore a target for future galaxy surveys. Whereas CMB is sensitive to the preferred scale of the model, the matter power spectrum from galaxy surveys is also more sensitive to the change in the amplitude of the power spectrum: for this model the complementarity of CMB and LSS is quite striking. As from Fig. 5.9, the scale of the feature would also be probed at higher statistical significance.

The model with a step in the potential benefits from the addition of LSS, as it can be seen from Fig. 5.10. In this case the power spectrum of galaxy surveys is sensitive to either the amplitude and the width of the ringing features in the primordial fluctuations; again, the scale of the feature would be probed at higher statistical significance.

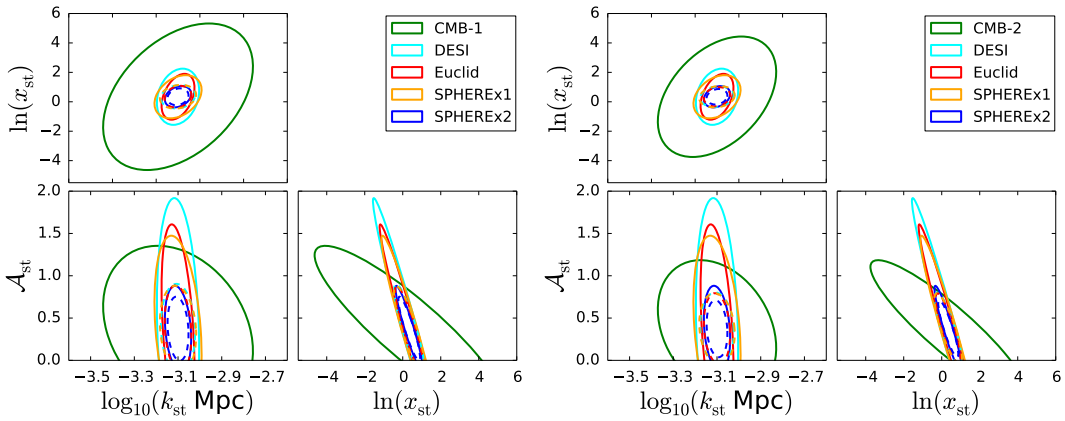

Figure 5.10: Triangle plot with marginalized 2D 68 % CL contours for the parameters $\mathcal{A}_{\rm st}, \log_{10}(k_{\rm st}\ {\rm Mpc}), \ln(x_{\rm st})$ of MIII for CMB only (solid green), DESI (solid cyan), Euclid (solid red), SPHEREx1 (solid orange), and SPHEREx2 (solid blue). The dashed contours represent the 2D 68 % CL CMB and LSS combined results. The configuration CMB-1 (CMB-2) is considered in the left (right) panel. Taken from [274].

For the model with super-imposed oscillations considered, CMB and LSS can probe the amplitude of periodic oscillations at high statistical significance: we obtain $\mathcal{A}_{\log} = 0.0278 \pm 0.0030$ ($\mathcal{A}_{\log} = 0.0278 \pm 0.0028$) at 68 % for CMB-1 (CMB-2) combined with Euclid. We also checked that our fiducial frequency, $\omega_{\log} \sim 32$, does not disappear in ℓ-space (keeping the frequency fixed) due the acoustic transfer function. By decreasing the amplitude of the periodic oscillations, the relative weight of the LSS increases with respect to CMB in the combined constraints; we have explicitly checked that half of the amplitude can still be detected at $3\,\sigma$ by CMB-2 + Euclid (see for details Ref. [274]).

By considering four representative deviations from a simple power-law PPS and including CMB uncertainties compatible with future measurements, we have shown that any of the galaxy surveys considered here with either a wide sky coverage and an accurate determination of redshift will be useful to decrease significantly the uncertainties in the features parameters, as is clear from Figs. 5.8-5.9-5.10-5.11.

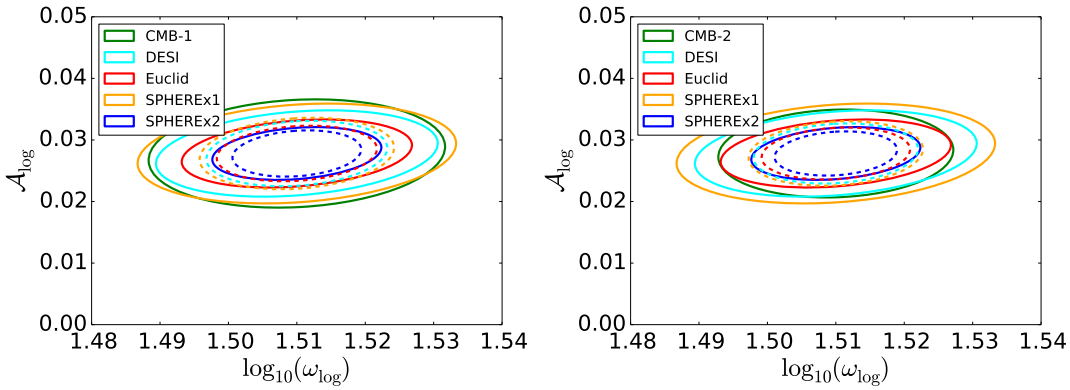

Figure 5.11: Marginalized 2D 68 % CL contours for the parameters $(\log_{10}(\omega_{\log}), \mathcal{A}_{\log})$ of MIV for CMB only (green), DESI (solid cyan), Euclid (solid red), SPHEREx1 (solid orange), and SPHEREx2 (solid blue). The dashed contours represent the 2D 68 % CL CMB and LSS combined results. The configuration CMB-1 (CMB-2) is considered in the left (right) panel. Taken from [274].

5.2 Photometric and radio surveys

The possibility to observe larger and larger volumes of the Universe is particularly important since the features for three of the four models studied here seem effectively located at scales which are at the edge of those probed by DESI, Euclid and SPHEREx. The LSST and SKA will carry out higher volume suveys than ever before of the LSS of the Universe (see Fig. 5.12).

With photometric surveys the redshift (true redshift) is inferred from broadband galaxy colours and will be estimated from a number of broad bans (photometric redshifts). Because the source galaxies are faint and numerous, multi-band imaging data allow to alleviate the problems of the shot noise by collecting a bigger number of objects rather than from spectroscopic data. Moreover, even the volume coverage problem is alleviated in photometric surveys.

The drawback is that the accuracy in determining the redshift of each galaxy with respect to spectroscopic surveys. However, on scales larger than the redshift error length, all the physical information is preserved. This makes photometric surveys good to test the largerst scales of the matter power spectrum.

LSST represents the widest and deepest photometric survey planned in the foreseeable future (to start in 2020) [144, 145]. With a sample of ten billion galaxies over a

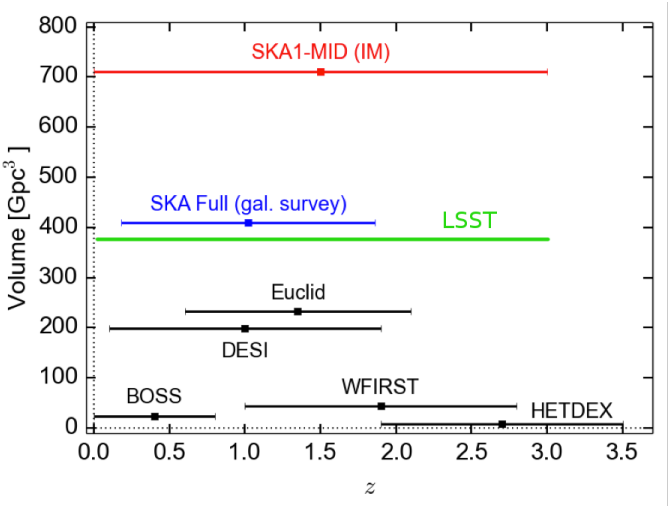

Figure 5.12: Survey volumes (at the midpoint of the redshift range) for various current and future surveys. Modified version of Fig. 2 from [272].

huge volume, LSST will be the largest photometric galaxy sample of its time for studies of large scale structure of the Universe, and will characterize the distribution and evolution of matter on extragalactic scales through observations of baryonic matter at a broad range of wavelengths.

The first phase of construction of SKA, to be finished around 2023, will consist of two sub-arrays: SKA1-LOW, a low-frequency aperture array operating at $\lesssim 350$ MHz, and SKA1-MID, a conventional mid-frequency array of 130 dishes equipped with low noise receivers covering $\sim 350 - 1400$ MHz. A second phase, scheduled for completion around 2030, will improve the overall sensitivity by a factor ~ 10.

The sensitivity and field of view of SKA will allow to map the galaxy distribution, by using HI as a tracer, putting to high redshifts over most of the sky.

The 21 cm line mapped by SKA will allow to measure redshift of many individual-detected galaxies, by using HI as a tracer, to high accuracy across a large redshift range [146], and to study the large-scale fluctuations of the integred 21 cm intensity from many unresolved galaxies [147] thanks to the intensity mapping of the neutral hydrogen (HI) method.

5.2.1 A LSST catalog

For LSST, we consider a full galaxy (single-tracer) survey area of 18000 deg^2 and spanning between redshift 0.15 and 3.0, with an underlying galaxy redshift distribution chosen to have the form:

$$n(z) \propto z^{\alpha} e^{-\left(\frac{z}{z_0}\right)^{\beta}} , \tag{5.5}$$

where $\alpha = 2$, $\beta = 1$ and $z_0 = 0.5$, and the galaxy redshift distribution is normalized in order to have 50 gal/deg^2 according to Ref. [144, 145].

To consider the effect of errors in photometric redshifts of source galaxies tomography, the true distribution of galaxy is multiplied with the photometric redshift error distribution:

$$n_{\rm i}(z) = \int_{z_{\rm i}}^{z_{\rm i}+\Delta z} d\tilde{z}\; n(z) P(\tilde{z}|z) \, . \tag{5.6}$$

Following Ref. [280], given the true redshift, the distribution of photometric redshifts can be well approximated with a Gaussian at each redshift bin:

$$P(z_{\rm ph}|z) = \frac{1}{\sqrt{2\pi}\sigma(z)} e^{-\frac{(z-z_{\rm ph}+z_{\rm bias})^2}{2\sigma(z)^2}} , \tag{5.7}$$

where $\sigma_{\rm z}$ is the redshift scattering and $z_{\rm bias}$ the photometric redshift bias. For redshift error we adopt $\sigma(z) = \bar{\sigma}_{\rm z}(1+z)$ with a conservative upper limit on the rms as fiducial of $\bar{\sigma}_{\rm z} = 0.05$ and for the photometric redshift bias $z_{\rm bias} = 0$ since any photometric redshift bias known a priori can be taken out [144].

We follow Ref. [144, 281] for the clustering bias with its redshift dependence:

$$b(z) = 1 + 1.84z \, , \tag{5.8}$$

and for simplicity we consider the same bias for all the galaxies (see the left panel of Fig. 5.13).

5.2.2 SKA1-MID HI intensity mapping

The HI intensity mapping signal is completely specified once we find a prescription for the HI density and bias. This can be obtained by making use of the halo mass function, i.e. $n(M, z)$, and relying on a model for the amount of HI mass in a DM halo

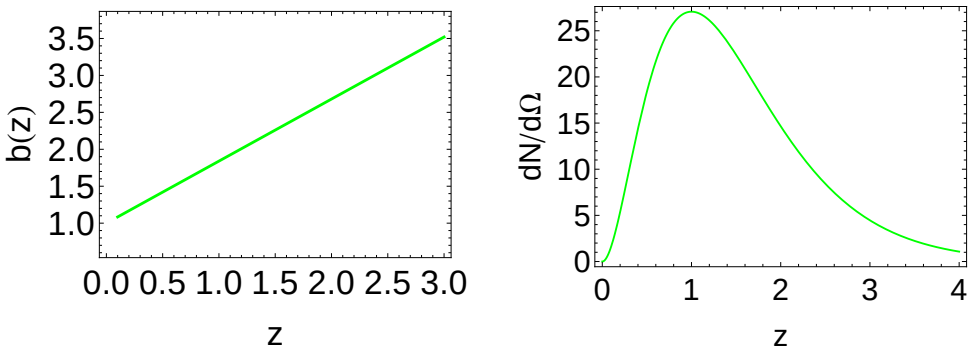

Figure 5.13: We show the linear bias (right panel) calculated according to Eq. (5.8) and the number density of objects (left panel) per unit of redshift bin Δz used for the analysis of with LSST.

of mass M, i.e. $M_{\rm HI}(M)$. We use the analytic predictions from [282, 283] for the HI density and bias:

$$\rho_{\rm HI}(z) = \int dM\, n(M,z) M_{\rm HI}(M,z)\,, \tag{5.9}$$

$$b_{\rm HI}(z) = \rho_{\rm HI}(z)^{-1} \int dM\, n(M,z) M_{\rm HI}(M,z) b(M,z)\,, \tag{5.10}$$

where the two integrals run in the mass range between $\left(5\times10^9 - 10^{12}\right)$ $\mathrm{M}_\odot$ [147], and:

$$M_{\rm HI}(M,z) = A M^\alpha\,, \tag{5.11}$$

where A is normalized to the result in Ref. [284] at $z\sim0.8$ that finds $\Omega_{\rm HI} b_{\rm HI} = 4.3\pm1.1\times10^{-4}$ at 68 % CL. We adopt as fiducial value $\Omega_{\rm HI}(z=0) = 4.86\times10^{-4}$ according to Ref. [174].

The shot noise power spectrum due to Poisson fluctuations in the halo number is given by:

$$P_{\rm HI}^{\rm shot}(z) = \left(\frac{\bar{T}_{\rm b}(z)}{\rho_{\rm HI}(z)}\right)^2 \int dM\, n(M,z) M_{\rm HI}^2(M,z)\,, \tag{5.12}$$

but for HI IM we can neglect shot noise according to Ref. [285].

The most efficient use of SKA1-MID for intensity mapping is the single-dish mode [147, 272]. We consider a constant noise at all scales with a variance per steradian in the i-th frequency channel is [174]:

$$N_{\rm HI}(\nu_{\rm i}) = \frac{T^2_{\rm sys}(\nu_{\rm i}) 4\pi f_{\rm sky}}{2 N_{\rm dish} t_{\rm tot} \Delta\nu}\,, \tag{5.13}$$

with no correlation between the noises in different frequency channels. The total system temperature has two main contributes:

$$T_{\rm sys} = T_{\rm inst} + T_{\rm sky}\,, \tag{5.14}$$

the instrument temperature $T_{\rm inst}$ and a component $T_{\rm sky}$ which takes into account other radio emissions (atmospheric and background):

$$T_{\rm sys} = 25 + 60 \left(\frac{300\ {\rm MHz}}{\nu}\right)^{2.55}\ {\rm K}\,. \tag{5.15}$$

We assume as specifications for SKA1-MID: $N_{\rm dish} = 200$ and $D_{\rm dish} = 15$ m, $t_{\rm tot} = 10^4$ hours for IM surveys with a total area of 25000 deg^2 in the redshift range $0.15 < z < 3$.

5.2.3 Intensity mapping

The hydrogen line 21-cm line, or HI line, refers to the electromagnetic radiation spectral line that is created by a change in the energy state of neutral hydrogen atoms. The electromagnetic radiation is at the frequency of $\nu_{21} = 1420.406$ MHz.

The flux density measure from radio telescope can be converted into an effective brightness temperature of the HI emission which can be split into a homogeneous part and a fluctuating one as $T_{\rm b} = \bar{T}_{\rm b}(1 + \delta_{\rm HI})$ where [174]:

$$\bar{T}_{\rm b} \approx 566 h \frac{\Omega_{\rm HI}(z)}{0.003} (1+z)^2 \frac{H_0}{H(z)}\ \mu{\rm K}\,, \tag{5.16}$$

where $\Omega_{\rm HI}(z) = (1+z)^{-3}\rho_{\rm HI}(z)/\rho_{\rm c,0}$.

We expect HI to be a bias tracer of the DM distribution, just as galaxies are, because the neutral hydrogen content of the Universe is expected to be localized within the galaxies. We can write the HI density contrast as:

$$\delta_{\rm HI} = b_{\rm HI} \times \delta_{\rm m}\,. \tag{5.17}$$

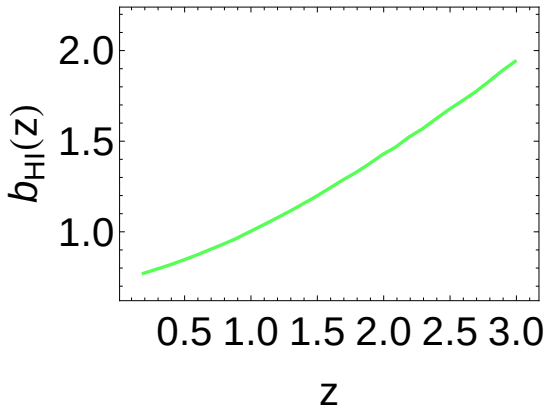

Figure 5.14: We show the linear bias (right panel) calculated with Eq. (5.10) for the analysis of with SKA1 IM.

Assuming that the signal is linear with respect to the underlying DM fluctuations, the fluctuations in the brightness temperature at a given position on the sky and frequency will be:

$$\delta T_{\rm b} = \bar{T}_{\rm b}\,\hat{\delta}_{\rm HI}(\mathbf{k}) = \bar{T}_{\rm b} b_{\rm HI}(1+\beta\mu_{\rm k}^2)\hat{\delta}_{\rm m}(\mathbf{k})\,, \tag{5.18}$$

and so the power spectrum of the HI is:

$$\langle \delta T_{\rm b}(\mathbf{k})\delta T_{\rm b}^*(\mathbf{k}')\rangle \equiv (2\pi)^3\delta^{(3)}(\mathbf{k}-\mathbf{k}')P_{\rm HI}(\mathbf{k})\,, \tag{5.19}$$

and can be connected with the observed galaxy power spectrum (3.33) through the brigtness temperature as:

$$P_{\rm HI}(\mathbf{k}) = \bar{T}_{\rm b}^2 \times P_{\rm obs}(\mathbf{k})\,. \tag{5.20}$$

5.2.4 SKA2 HI galaxy redshift survey

The models for the number density and bias of the HI galaxy distribution are obtained by fitting the simulated data in Refs. [286, 287], and are:

$$\frac{d\ N(z)}{d\ z} = 10^{c_1} z^{c_2} e^{-c_3 z}\,, \tag{5.21}$$

$$b = c_4 e^{c_5\, z}\,, \tag{5.22}$$

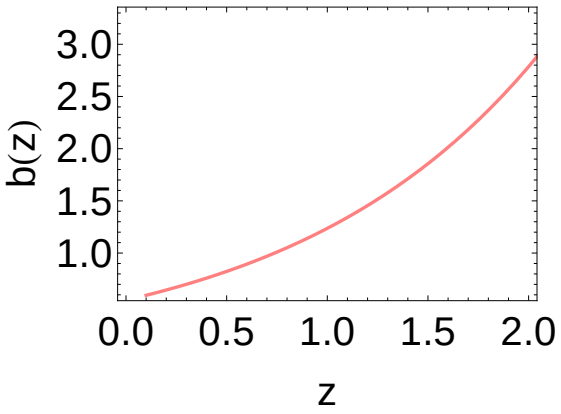

Figure 5.15: We show the linear bias (right panel) calculated and the number density of objects (left panel), per unit of redshift bin Δz used for the analysis of with SKA2.

and the coefficients $c_{\rm i}$ depend on the flux limit of the experiment.

For SKA2 [286], we consider specification for a flux rms, constant across the band, with $S^{\rm ref}_{\rm rms} = 5.4$ μJy. Specifications, with sensitivities obtained for a total observation time of 10^5 hours, and survey area of 30000 deg^2. The redshift interval for SKA2 is 0.1-2. According to HI galaxy simulations performed in Ref. [286], the number density and bias interpolation functions Eqs. (5.21) and (5.22) correspond for the flux rms considered to the best-fit: $c_1 = 6.555$, $c_2 = 1.932$, $c_3 = 6.378$, $c_4 = 0.549$, and $c_5 = 0.812$.

5.2.5 Results

We forecast the LSST and SKA capabilities for the model with a discontinuity in the first derivative of the potential (described in Sec. 4.3.2) and the model with the step in the inflaton potential (described in Sec. 4.3.3) only. [8] In Fig. 5.16 we compare the performance of these two surveys on detecting the amplitude of these two models taking their *Planck* 2015 best-fits, in combination with the Fisher information from CMB-2. Results are easy to understand by looking at Fig. 5.12: the constraining power

[8] This is an anticipation of a work in progress [288].

on such models scale with the volume of the survey. [9]

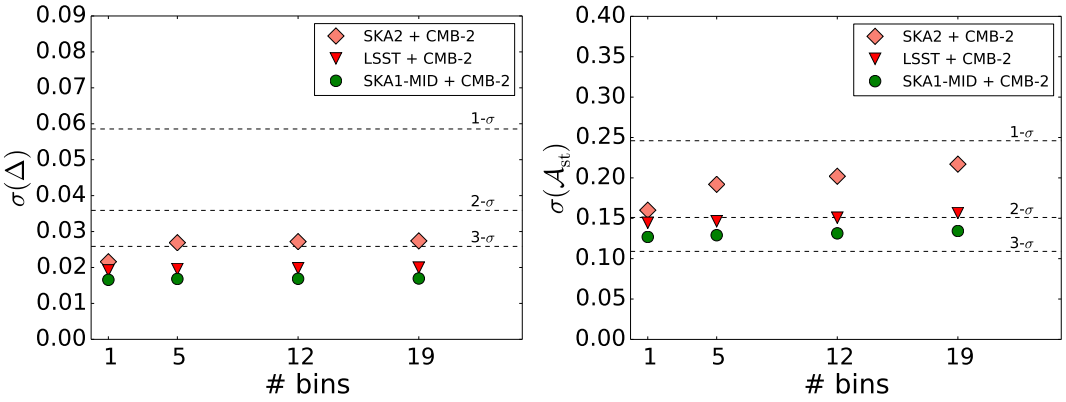

Figure 5.16: Marginalized $1\,\sigma$ error on the amplide Δ of the model with a discontinuity in the first derivative of the potential (left panel) and on the amplitude $\mathcal{A}_{\rm st}$ of the step model (right panel) for the galaxy power spectrum measurement from SKA2 and LSST, and for the HI power spectrum from SKA1-MID. The bullets are function of the number of redshift bins of the survey.

Moreover, we consider different binning schemes in redshift for the same surveys in order to understand the optimal configuration for the two models. By starting with a unique volume, with no division in redshift bin, we increase the number of slices by keeping more or less the same comoving radial content in the redshift slices. In particular, we consider LSST and SKA1-MID in the same redshift range, i.e. $z \in [0.15, 3]$, and the SKA2 HI galaxy survey in the redshift range $z \in [0.1, 2]$. We divide the three surveys in 1, 5, 12, 19 bins.

Note that there is a trade-off between the number of bins which usually imply a gain in information in the hypothesis of vanishing correlation and their size. A larger size indeed give accessibility of smaller $k_{\rm min}$ where some of the features are.

The deviations from a simple power law of primordial perturbations studied here can be accompanied by imprints in the CMB and/or galaxy shear, as well as in the CMB and/or galaxy bispectrum; these imprints in higher-order correlation functions can add to the ones we have considered here to further test primordial features. Moreover, since

[9] Note that from this analysis LSST seems to perform better than SKA2, for the two models considered here, even if it has a small volume. The different linear bias profiles cosidered, according to the ones provided by the two Collaborations, are responsible for that.

LSST and SKA will carry out their observations over a very similar region of the sky, the benefits of cross-correlating both experiments will be immense in study cosmology on these large scales.

Conclusions

The most recent cosmological observations, among which the CMB ansitropies data in temperature and polarization from *Planck*, have provided a description of our Universe consistent with the concordance ΛCDM model, whose parameters are estimated at the percent level. This picture will be refined by the final release of *Planck* data in 2017, but also by the several upcoming galaxy surveys which will probe our Universe at low redshift at unprecedent noise sensitivities level and wide sky coverage.

In this thesis we have studied the implications of the current precision of cosmological observations for cosmic inflation and what is probably the simplest model of modified gravity. In my Ph.D. work I have also explored the perspectives of future galaxy surveys for these two interesting aspects of fundamental physics, quantifying the cosmological information of future clustering data on non-standard model of cosmic inflation which may explain some hints of deviation from a smooth primordial power spectrum in the *Planck* temperature anisotropy data.

The main results that we found during this work, in the framework of *Planck* 2015 data, for slow-roll inflation, parametrized features and Induced Gravity dark energy models, respectively, are:

1. *Planck* 2015 data are consistent with a power-law power spectrum of Gaussian primordial fluctuations as generically predicted by the simplest models of inflation. *Planck* measures at more than $5\,\sigma$ $n_{\rm s}$ and does not evidence of a running spectral index. The tight bounds on isocurvature fluctuations imply that there is no evidence that inflation was driven by more than one field.

   The constraint on the tensor-to-scalar ratio in combination with BICEP2/Keck Array B-mode polarization data ($r_{0.05} < 0.08$ at $95\,\%$ CL) lands to tighter constraints on inflationary models. A careful Bayesian comparison shows that R^2 inflationary model is the simplest model among preferred. Moreover, monomial potentials with index $n > 2$ are strongly disfavoured with respect R^2, and models which approximate the linear potential have higher evidence compared to those that aprroximate a quartic potential.

2. *Planck* has imposed particularly strong constraints on features for wavenumbers

$0.008 < k$ Mpc < 0.1. However, a dip at $\ell \approx 20 - 40$ in the temperature power spectrum was found, although at weak statistical significance due to the large cosmic variance at low-ℓ.

We studied selected theoretically motivated parametrizations of the primordial power spectrum with departure from the near scale invariance providing a better fit to the CMB temperature power spectrum with respect to the simplest slow-roll inflationary models. These models lead to an improved fit, up to $\Delta\chi^2 \approx -10$, not large enough to consider these two/three extra parameters' models statistically significant.

3. We have studied a simple class of modified gravity models alternative to ΛCDM, based on Induced Gravity, or Brans-Dicke like, with a monomial potential with positive values of the exponent. In this class of models the scalar field increases from the constant value during the radiation era and the effective Newton's constant decreases in time during the matter dominated era. Despite its semplicity, this class of models leads to distinct effects compared to ΛCDM for values of the coupling γ compatible with observations, such as a slightly larger value of H_0 because of the modification of the expansion history due to the coupling of the scalar field to the Ricci curvature γ.

   The full information of *Planck* alone, i.e. temperature, polarization and lensing, is now capable to constrain $\gamma < 0.0017$ at 95 % CL for $n = 4$; by adding a compilation of BAO data this 95 % CL constraint is further tightened to $\gamma < 0.00075$.

   We have shown how there is a positive correlation between H_0 and γ and quantified the impact of adding H_0 local measurements.

My thesis work can be continued in variour contexts.

As a *Planck* Core Team member, I am involved in updating the results for the analysis of slow-roll inflation, the Bayesian comparison of inflationary models, the search of parametrized features with the final *Planck* release. We expect that the results shown in this thesis will be further refined by the improvement of the *Planck* polarization data in the final release. The *Planck* policy does not allow for an update of the current results in this thesis, but the methodology presented in this thesis will be used again for the final legacy papers of the *Planck* Collaboration.

I am also a member of the collaboration which has proposed a CMB space mission in reply to the ESA call of opportunity for a medium M5 mission. It would be interesting to see a comparison of inflationary models with the CORE capabilities with

few reference cosmologies which could foresee the status of cosmological observations in ten years from now. Work on these aspects is ongoing.

Concerning primordial features I can mention a couple of interesting questions which can be a follow-up of what presented here. The first one is to assess the importance of weak lensing for the Euclid forecasts: we have considered only clustering mock data, but weak lensing from Euclid might help in reducing uncertainties in the standard cosmological parameters and therefore constraint better the features' parameters. The second one would be to combine the information from higher order statistics with the forecasts of the clustering power spectrum: indeed the inflationary models with violation of the slow-roll condition have definite predictions for the bispectrum and a joint analysis of the power spectrum and bispectrum have been already presented in the context of CMB. We intend to explore these possibilities for future galaxy surveys. Another important aspect is what we can expect from CORE for the models studied in this thesis.

I am currently working with a Fisher methodology on the implications of the Euclid capabilities for the class of scalar-tensor models studied here. This analysis does not include only the clustering mock data expected from Euclid spectroscopic data used here for the study of primordial features, but also weak lensing data. Among the many results expected from this analysis, it will be very interesting to provide the Euclid constraint in combination with CMB on the post-Newtonian parameter. It will be extremely interesting at which level the cosmological bounds will get closer to the Solar System constraints. Another interesting aspect is the Euclid capability in discriminating among different power-law potentials for the scalar field. We have seen that current CMB data cannot discriminate among different power-law potentials and I can anticipate by my Fisher analysis that this will persist with CMB data with more sensitivity than *Planck*.

Publication list

The following works have been considered as part of the thesis:

- **M. Ballardini**, D. Sapone, C. Umiltà, F. Finelli, D. Paoletti, "Testing Brans-Dicke-like dark energy models with Euclid", in preparation.
- **M. Ballardini**, A. Davoli, F. Finelli, "Disentangling the origin of sharp features in primordial power spectrum", in preparation.
- **M. Ballardini**, F. Finelli, R. Maartens, L. Moscardini, "Probing primordial features with the next-generation ultra-large surveys", in preparation.
- **M. Ballardini**, F. Finelli, C. Fedeli, L. Moscardini, "Probing primordial features with future galaxy surveys", (2016).
  [arXiv: 1606.03747[astro-ph.CO]] (accepted by JCAP).
- **M. Ballardini**, F. Finelli, C. Umiltà, D. Paoletti, "Cosmological constraints on induced gravity dark energy models", JCAP 05 (2016), 067.
  [arXiv: 1601.03387[astro-ph.CO]].
- C. Umiltà, **M. Ballardini**, F. Finelli, D. Paoletti, "CMB and BAO constraints on an induced gravity dark energy model with broken scale invariance", JCAP 08 (2015), 017.
  [arXiv: 1507.00718[astro-ph.CO]].
- Planck Collaboration, "Planck 2015. XX. Constraints on inflation", Astron.Astrophys. 594 (2016) A20.
  [arXiv: 1502.02114[astro-ph.CO]] .
- Planck Collaboration, "Planck 2015. XVII. Constraints on primordial non-Gaussianity", Astron.Astrophys. 594 (2016) A17.
  [arXiv: 1502.01592[astro-ph.CO]].

- Planck Collaboration, "Planck 2015. II. Low Frequency Instrument data processing", Astron.Astrophys. 594 (2016) A2.
  [arXiv: 1502.01583[astro-ph.IM]].

- Planck Collaboration, "Planck 2015. I. Overview of products and scientific results", Astron.Astrophys. 594 (2016) A1.
  [arXiv: 1502.01582[astro-ph.CO]].

Additional publications related to the thesis:

- Planck Collaboration, "Planck intermediate results. LI. Features in the cosmic microwave background temperature power spectrum and shifts in cosmological parameters", (2016).
  [arXiv: 1608.02487[astro-ph.CO]] (submitted to A&A).

- Planck Collaboration, "Planck intermediate results. L. Evidence for spatial variation of the polarized thermal dust spectral energy distribution and implications for CMB B-mode analysis", (2016).
  [arXiv: 1606.07335[astro-ph.CO]] (submitted by A&A).

- Planck Collaboration, "Planck intermediate results. XLIX. Parity-violation constraints from polarization data", (2016).
  [arXiv: 1605.08633[astro-ph.CO]] (accepted by A&A).

- Planck Collaboration, "Planck intermediate results. XLVIII. Disentangling Galactic dust emission and cosmic infrared background anisotropies", (2016).
  [arXiv: 1605.09387[astro-ph.CO]] (accepted by A&A).

- Planck Collaboration, "Planck intermediate results. XLVII. Planck constraints on reionization history", (2016).
  [arXiv: 1605.03507[astro-ph.CO]] (accepted by A&A).

- Planck Collaboration, "Planck intermediate results. XLVI. Reduction of large-scale systematic effects in HFI polarization maps and estimation of the reionization optical depth, (2016).
  [arXiv: 1605.02985[astro-ph.CO]] (accepted by A&A).

- Planck Collaboration, "Planck intermediate results. XLIV. The structure of the Galactic magnetic field from dust polarization maps of the southern Galactic

cap", (2016).
[arXiv: 1604.01029[astro-ph.GA]] (accepted by A&A).

- N. Masi, **M. Ballardini**, "On dark matter annihilation cross section: a comparison between AMS-02 and Planck constraints", (2015).
[arXiv: 1509.00058[astro-ph.CO]] (accepted by IJMPD).

- Planck Collaboration, "Planck 2015. XIX. Constraints on primordial magnetic fields", Astron.Astrophys. 594 (2016) A19.
[arXiv: 1502.01594[astro-ph.CO]].

- **M. Ballardini**, F. Finelli, D. Paoletti, "CMB anisotropies generated by a stochastic background of primordial magnetic fields with non-zero helicity", JCAP 10 (2015), 031.
[arXiv: 1412.1836[astro-ph.CO]].

Bibliography

[1] Andrew R. Liddle and D. H. Lyth. *Cosmological inflation and large scale structure*. 2000.

[2] Scott Dodelson. *Modern Cosmology*. Academic Press, Amsterdam, 2003.

[3] Daniel Baumann. Inflation. In *Physics of the large and the small, TASI 09, proceedings of the Theoretical Advanced Study Institute in Elementary Particle Physics, Boulder, Colorado, USA, 1-26 June 2009*, pages 523–686, 2011.

[4] G. Gamow. Expanding universe and the origin of elements. *Phys. Rev.*, 70:572–573, 1946.

[5] R. A. Alpher, H. Bethe, and G. Gamow. The origin of chemical elements. *Phys. Rev.*, 73:803–804, 1948.

[6] Ralph A. Alpher and Robert C. Herman. On the relative abundance of the elements. *Phys. Rev.*, 74:1737–1742, Dec 1948.

[7] Ralph A. Alpher and Robert C. Herman. Remarks on the evolution of the expanding universe. *Phys. Rev.*, 75:1089–1095, Apr 1949.

[8] A. A. Penzias and R. W. Wilson. A Measurement of Excess Antenna Temperature at 4080 Mc/s. *Astrophys. J*, 142:419–421, July 1965.

[9] A. A. Penzias and R. W. Wilson. Measurement of the Flux Density of CAS a at 4080 Mc/s. *Astrophys. J*, 142:1149, October 1965.

[10] R. H. Dicke, P. J. E. Peebles, P. G. Roll, and D. T. Wilkinson. Cosmic Black-Body Radiation. *Astrophys. J.*, 142:414–419, 1965.

[11] Adam G. Riess et al. Observational evidence from supernovae for an accelerating universe and a cosmological constant. *Astron. J.*, 116:1009–1038, 1998.

[12] S. Perlmutter et al. Measurements of Omega and Lambda from 42 high redshift supernovae. *Astrophys. J.*, 517:565–586, 1999.

[13] D. N. Spergel et al. First year Wilkinson Microwave Anisotropy Probe (WMAP) observations: Determination of cosmological parameters. *Astrophys. J. Suppl.*, 148:175–194, 2003.

[14] P. A. R. Ade et al. Planck 2013 results. XVI. Cosmological parameters. *Astron. Astrophys.*, 571:A16, 2014.

[15] Daniel J. Eisenstein et al. Detection of the baryon acoustic peak in the large-scale correlation function of SDSS luminous red galaxies. *Astrophys. J.*, 633:560–574, 2005.

[16] H. P. Robertson. Kinematics and World-Structure. *Astrophys. J*, 82:284, November 1935.

[17] H. P. Robertson. Kinematics and World-Structure II. *Astrophys. J*, 83:187, April 1936.

[18] H. P. Robertson. Kinematics and World-Structure III. *Astrophys. J*, 83:257, May 1936.

[19] A. G. Walker. On milne's theory of world-structure. *Proceedings of the London Mathematical Society*, s2-42(1):90–127, 1937.

[20] Albert Einstein. Cosmological Considerations in the General Theory of Relativity. *Sitzungsber. Preuss. Akad. Wiss. Berlin (Math. Phys.)*, 1917:142–152, 1917.

[21] A. Friedman. On the Curvature of space. *Z. Phys.*, 10:377–386, 1922. [Gen. Rel. Grav.31,1991(1999)].

[22] Georges Lemaitre. A Homogeneous Universe of Constant Mass and Growing Radius Accounting for the Radial Velocity of Extragalactic Nebulae. *Annales Soc. Sci. Brux. Ser. I Sci. Math. Astron. Phys.*, A47:49–59, 1927.

[23] P. A. R. Ade et al. Planck 2015 results. XIII. Cosmological parameters. *Astron. Astrophys.*, 594:A13, 2016.

[24] N. Aghanim et al. Planck intermediate results. XLVI. Reduction of large-scale systematic effects in HFI polarization maps and estimation of the reionization optical depth. 2016.

[25] W. de Sitter. Einstein's theory of gravitation and its astronomical consequences, Third Paper. *Mon. Not. Roy. Astron. Soc.*, 78:3–28, 1917.

[26] Fabio Finelli, Jan Hamann, Samuel M. Leach, and Julien Lesgourgues. Single-field inflation constraints from CMB and SDSS data. *JCAP*, 1004:011, 2010.

[27] Marco Baldi, Fabio Finelli, and Sabino Matarrese. Inflation with violation of the null energy condition. *Phys. Rev.*, D72:083504, 2005.

[28] Jinn-Ouk Gong and Misao Sasaki. A new parameter in attractor single-field inflation. *Phys. Lett.*, B747:390–394, 2015.

[29] Alexei A. Starobinsky. A New Type of Isotropic Cosmological Models Without Singularity. *Phys. Lett.*, B91:99–102, 1980.

[30] Alexei A. Starobinsky. Spectrum of relict gravitational radiation and the early state of the universe. *JETP Lett.*, 30:682–685, 1979. [Pisma Zh. Eksp. Teor. Fiz.30,719(1979)].

[31] Viatcheslav F. Mukhanov and G. V. Chibisov. Quantum Fluctuation and Nonsingular Universe. (In Russian). *JETP Lett.*, 33:532–535, 1981. [Pisma Zh. Eksp. Teor. Fiz.33,549(1981)].

[32] A. A. Starobinsky. The Perturbation Spectrum Evolving from a Nonsingular Initially De-Sitter Cosmology and the Microwave Background Anisotropy. *Sov. Astron. Lett.*, 9:302, 1983.

[33] Alan H. Guth. The Inflationary Universe: A Possible Solution to the Horizon and Flatness Problems. *Phys. Rev.*, D23:347–356, 1981.

[34] S. W. Hawking, I. G. Moss, and J. M. Stewart. Bubble Collisions in the Very Early Universe. *Phys. Rev.*, D26:2681, 1982.

[35] Alan H. Guth and Erick J. Weinberg. Could the Universe Have Recovered from a Slow First Order Phase Transition? *Nucl. Phys.*, B212:321–364, 1983.

[36] Andrei D. Linde. A New Inflationary Universe Scenario: A Possible Solution of the Horizon, Flatness, Homogeneity, Isotropy and Primordial Monopole Problems. *Phys. Lett.*, B108:389–393, 1982.

[37] Andrei D. Linde. Scalar Field Fluctuations in Expanding Universe and the New Inflationary Universe Scenario. *Phys. Lett.*, B116:335–339, 1982.

[38] Andreas Albrecht and Paul J. Steinhardt. Cosmology for Grand Unified Theories with Radiatively Induced Symmetry Breaking. *Phys. Rev. Lett.*, 48:1220–1223, 1982.

[39] G. F. Mazenko, Robert M. Wald, and W. G. Unruh. Does a Phase Transition in the Early Universe Produce the Conditions Needed for Inflation? *Phys. Rev.*, D31:273–282, 1985.

[40] Andrei D. Linde. Chaotic Inflation. *Phys. Lett.*, B129:177–181, 1983.

[41] Lev Kofman, Andrei D. Linde, and Alexei A. Starobinsky. Towards the theory of reheating after inflation. *Phys. Rev.*, D56:3258–3295, 1997.

[42] Edward W. Kolb and Michael S. Turner. The Early Universe. *Front. Phys.*, 69:1–547, 1990.

[43] P. A. R. Ade et al. Planck 2013 results. XXII. Constraints on inflation. *Astron. Astrophys.*, 571:A22, 2014.

[44] P. A. R. Ade et al. Planck 2015 results. XX. Constraints on inflation. *Astron. Astrophys.*, 594:A20, 2016.

[45] Bharat Ratra and P. J. E. Peebles. Cosmological Consequences of a Rolling Homogeneous Scalar Field. *Phys. Rev.*, D37:3406, 1988.

[46] Sean M. Carroll. *Spacetime and geometry: An introduction to general relativity.* 2004.

[47] Ivaylo Zlatev, Li-Min Wang, and Paul J. Steinhardt. Quintessence, cosmic coincidence, and the cosmological constant. *Phys. Rev. Lett.*, 82:896–899, 1999.

[48] C. Armendariz-Picon, Viatcheslav F. Mukhanov, and Paul J. Steinhardt. Essentials of k essence. *Phys. Rev.*, D63:103510, 2001.

[49] Takeshi Chiba, Takahiro Okabe, and Masahide Yamaguchi. Kinetically driven quintessence. *Phys. Rev.*, D62:023511, 2000.

[50] P. Jordan. Zur neutrinotheorie des lichtes. *Z. Phys.*, 93:464–472, 1935.

[51] Paul A. M. Dirac. The Cosmological constants. *Nature*, 139:323, 1937.

[52] Pascual Jordan. The present state of Dirac's cosmological hypothesis. *Z. Phys.*, 157:112–121, 1959.

[53] C. Brans and R. H. Dicke. Mach's principle and a relativistic theory of gravitation. *Phys. Rev.*, 124:925–935, 1961.

[54] A. Zee. Spontaneously Generated Gravity. *Phys. Rev.*, D23:858, 1981.

[55] Fred Cooper and Giovanni Venturi. Cosmology and Broken Scale Invariance. *Phys. Rev.*, D24:3338, 1981.

[56] C. Wetterich. Cosmology and the Fate of Dilatation Symmetry. *Nucl. Phys.*, B302:668–696, 1988.

[57] F. Finelli, A. Tronconi, and Giovanni Venturi. Dark Energy, Induced Gravity and Broken Scale Invariance. *Phys. Lett.*, B659:466–470, 2008.

[58] A. Cerioni, F. Finelli, A. Tronconi, and G. Venturi. Inflation and Reheating in Induced Gravity. *Phys. Lett.*, B681:383–386, 2009.

[59] John D. Barrow and Kei-ichi Maeda. Extended inflationary universes. *Nucl. Phys.*, B341:294–308, 1990.

[60] C. Umiltà, M. Ballardini, F. Finelli, and D. Paoletti. CMB and BAO constraints for an induced gravity dark energy model with a quartic potential. *JCAP*, 1508:017, 2015.

[61] B. Boisseau, Gilles Esposito-Farese, D. Polarski, and Alexei A. Starobinsky. Reconstruction of a scalar tensor theory of gravity in an accelerating universe. *Phys. Rev. Lett.*, 85:2236, 2000.

[62] Mario Ballardini, Fabio Finelli, Caterina Umiltà, and Daniela Paoletti. Cosmological constraints on induced gravity dark energy models. *JCAP*, 1605(05):067, 2016.

[63] Alberto Nicolis, Riccardo Rattazzi, and Enrico Trincherini. The Galileon as a local modification of gravity. *Phys. Rev.*, D79:064036, 2009.

[64] Gregory Walter Horndeski. Second-order scalar-tensor field equations in a four-dimensional space. *International Journal of Theoretical Physics*, 10(6):363–384, 1974.

[65] C. Deffayet, Gilles Esposito-Farese, and A. Vikman. Covariant Galileon. *Phys. Rev.*, D79:084003, 2009.

[66] Miguel Zumalacárregui and Juan García-Bellido. Transforming gravity: from derivative couplings to matter to second-order scalar-tensor theories beyond the Horndeski Lagrangian. *Phys. Rev.*, D89:064046, 2014.

[67] Jérôme Gleyzes, David Langlois, Federico Piazza, and Filippo Vernizzi. Healthy theories beyond Horndeski. *Phys. Rev. Lett.*, 114(21):211101, 2015.

[68] Chung-Pei Ma and Edmund Bertschinger. Cosmological perturbation theory in the synchronous and conformal Newtonian gauges. *Astrophys. J.*, 455:7–25, 1995.

[69] James M. Bardeen. Gauge Invariant Cosmological Perturbations. *Phys. Rev.*, D22:1882–1905, 1980.

[70] Viatcheslav F. Mukhanov. Gravitational Instability of the Universe Filled with a Scalar Field. *JETP Lett.*, 41:493–496, 1985. [Pisma Zh. Eksp. Teor. Fiz.41,402(1985)].

[71] Jaume Garriga and Viatcheslav F. Mukhanov. Perturbations in k-inflation. *Phys. Lett.*, B458:219–225, 1999.

[72] Michael E. Peskin and Daniel V. Schroeder. *An Introduction to quantum field theory*. 1995.

[73] Ewan D. Stewart and David H. Lyth. A More accurate analytic calculation of the spectrum of cosmological perturbations produced during inflation. *Phys. Lett.*, B302:171–175, 1993.

[74] Milton Abramowitz and Irene A. Stegun, editors. *Handbook of mathematical functions : with formulas, graphs, and mathematical tables*. Dover, New York, 1965. Unaltered, unabridged republication of 55, National Bureau of Standards, Applied mathematics series (1964) corrected edition.–p. iv of cover.

[75] T. S. Bunch and P. C. W. Davies. Quantum Field Theory in de Sitter Space: Renormalization by Point Splitting. *Proc. Roy. Soc. Lond.*, A360:117–134, 1978.

[76] Andrew R Liddle and Samuel M Leach. How long before the end of inflation were observable perturbations produced? *Phys. Rev.*, D68:103503, 2003.

[77] Jerome Martin and Christophe Ringeval. First CMB Constraints on the Inflationary Reheating Temperature. *Phys. Rev.*, D82:023511, 2010.

[78] Lotfi Boubekeur and David.H. Lyth. Hilltop inflation. *JCAP*, 0507:010, 2005.

[79] Pierre Binétruy and Mary K. Gaillard. Candidates for the Inflaton Field in Superstring Models. *Phys. Rev.*, D34:3069–3083, 1986.

[80] Keith A. Olive. Inflation. *Phys. Rept.*, 190:307–403, 1990.

[81] Katherine Freese, Joshua A. Frieman, and Angela V. Olinto. Natural inflation with pseudo - Nambu-Goldstone bosons. *Phys. Rev. Lett.*, 65:3233–3236, 1990.

[82] Fred C. Adams, J. Richard Bond, Katherine Freese, Joshua A. Frieman, and Angela V. Olinto. Natural inflation: Particle physics models, power law spectra for large scale structure, and constraints from COBE. *Phys. Rev.*, D47:426–455, 1993.

[83] Jihn E. Kim, Hans Peter Nilles, and Marco Peloso. Completing natural inflation. *JCAP*, 0501:005, 2005.

[84] Juan Garcia-Bellido, Raul Rabadan, and Frederic Zamora. Inflationary scenarios from branes at angles. *JHEP*, 01:036, 2002.

[85] G. R. Dvali, Q. Shafi, and S. Solganik. D-brane inflation. In *4th European Meeting From the Planck Scale to the Electroweak Scale (Planck 2001) La Londe les Maures, Toulon, France, May 11-16, 2001*, 2001.

[86] Shamit Kachru, Renata Kallosh, Andrei D. Linde, Juan Martin Maldacena, Liam P. McAllister, and Sandip P. Trivedi. Towards inflation in string theory. *JCAP*, 0310:013, 2003.

[87] A. S. Goncharov and Andrei D. Linde. CHAOTIC INFLATION OF THE UNIVERSE IN SUPERGRAVITY. *Sov. Phys. JETP*, 59:930–933, 1984. [Zh. Eksp. Teor. Fiz.86,1594(1984)].

[88] Ewan D. Stewart. Inflation, supergravity and superstrings. *Phys. Rev.*, D51:6847–6853, 1995.

[89] G. R. Dvali and S. H. Henry Tye. Brane inflation. *Phys. Lett.*, B450:72–82, 1999.

[90] C. P. Burgess, P. Martineau, F. Quevedo, G. Rajesh, and R. J. Zhang. Brane - anti-brane inflation in orbifold and orientifold models. *JHEP*, 03:052, 2002.

[91] M. Cicoli, C. P. Burgess, and F. Quevedo. Fibre Inflation: Observable Gravity Waves from IIB String Compactifications. *JCAP*, 0903:013, 2009.

[92] F. Lucchin and S. Matarrese. Power Law Inflation. *Phys. Rev.*, D32:1316, 1985.

[93] Andrei D. Linde. Hybrid inflation. *Phys. Rev.*, D49:748–754, 1994.

[94] Edmund J. Copeland, Andrew R. Liddle, David H. Lyth, Ewan D. Stewart, and David Wands. False vacuum inflation with Einstein gravity. *Phys. Rev.*, D49:6410–6433, 1994.

[95] G. R. Dvali, Q. Shafi, and Robert K. Schaefer. Large scale structure and supersymmetric inflation without fine tuning. *Phys. Rev. Lett.*, 73:1886–1889, 1994.

[96] John Ellis, Dimitri V. Nanopoulos, and Keith A. Olive. No-Scale Supergravity Realization of the Starobinsky Model of Inflation. *Phys. Rev. Lett.*, 111:111301, 2013. [Erratum: Phys. Rev. Lett.111,no.12,129902(2013)].

[97] W. Buchmuller, V. Domcke, and K. Kamada. The Starobinsky Model from Superconformal D-Term Inflation. *Phys. Lett.*, B726:467–470, 2013.

[98] F. Farakos, A. Kehagias, and A. Riotto. On the Starobinsky Model of Inflation from Supergravity. *Nucl. Phys.*, B876:187–200, 2013.

[99] Sergio Ferrara, Renata Kallosh, and Antoine Van Proeyen. On the Supersymmetric Completion of $R + R^2$ Gravity and Cosmology. *JHEP*, 11:134, 2013.

[100] Sergei V. Ketov and Alexei A. Starobinsky. Embedding $(R + R^2)$-Inflation into Supergravity. *Phys. Rev.*, D83:063512, 2011.

[101] Renata Kallosh and Andrei Linde. Superconformal generalizations of the Starobinsky model. *JCAP*, 1306:028, 2013.

[102] Renata Kallosh, Andrei Linde, and Diederik Roest. Superconformal Inflationary α-Attractors. *JHEP*, 11:198, 2013.

[103] Sergio Ferrara, Renata Kallosh, Andrei Linde, and Massimo Porrati. Minimal Supergravity Models of Inflation. *Phys. Rev.*, D88(8):085038, 2013.

[104] Jerome Martin, Christophe Ringeval, and Vincent Vennin. Encyclopædia Inflationaris. *Phys. Dark Univ.*, 5-6:75–235, 2014.

[105] Eiichiro Komatsu and Toshifumi Futamase. Constraints on the chaotic inflationary scenario with a nonminimally coupled 'inflaton' field from the cosmic microwave background radiation anisotropy. *Phys. Rev.*, D58:023004, 1998. [Erratum: Phys. Rev.D58,089902(1998)].

[106] Shinji Tsujikawa and Burin Gumjudpai. Density perturbations in generalized Einstein scenarios and constraints on nonminimal couplings from the Cosmic Microwave Background. *Phys. Rev.*, D69:123523, 2004.

[107] Fedor L. Bezrukov and Mikhail Shaposhnikov. The Standard Model Higgs boson as the inflaton. *Phys. Lett.*, B659:703–706, 2008.

[108] A. O. Barvinsky, A. Yu. Kamenshchik, and A. A. Starobinsky. Inflation scenario via the Standard Model Higgs boson and LHC. *JCAP*, 0811:021, 2008.

[109] F. Bezrukov and M. Shaposhnikov. Standard Model Higgs boson mass from inflation: Two loop analysis. *JHEP*, 07:089, 2009.

[110] Alexei A. Starobinsky. Spectrum of adiabatic perturbations in the universe when there are singularities in the inflation potential. *JETP Lett.*, 55:489–494, 1992. [Pisma Zh. Eksp. Teor. Fiz.55,477(1992)].

[111] Mohammad Hossein Namjoo, Hassan Firouzjahi, and Misao Sasaki. Multiple Inflationary Stages with Varying Equation of State. *JCAP*, 1212:018, 2012.

[112] Robert Brandenberger and Fabio Finelli. On the spectrum of fluctuations in an effective field theory of the Ekpyrotic universe. *JHEP*, 11:056, 2001.

[113] Edmund J. Copeland and David Wands. Cosmological matching conditions. *JCAP*, 0706:014, 2007.

[114] C. Armendariz-Picon, T. Damour, and Viatcheslav F. Mukhanov. k - inflation. *Phys. Lett.*, B458:209–218, 1999.

[115] Masahiro Nakashima, Ryo Saito, Yu-ichi Takamizu, and Jun'ichi Yokoyama. The effect of varying sound velocity on primordial curvature perturbations. *Prog. Theor. Phys.*, 125:1035–1052, 2011.

[116] Mario Ballardini, Alessandro Davoli, and Fabio Finelli. Disentangling the origin of sharp features in primordial power spectrum.

[117] George F. Smoot et al. Structure in the COBE differential microwave radiometer first year maps. *Astrophys. J.*, 396:L1–L5, 1992.

[118] C. L. Bennett et al. First year Wilkinson Microwave Anisotropy Probe (WMAP) observations: Preliminary maps and basic results. *Astrophys. J. Suppl.*, 148:1–27, 2003.

[119] N. Jarosik et al. Three-year Wilkinson Microwave Anisotropy Pr (WMAP) observations: beam profiles, data processing, radiometer characterization and systematic error limits. *Astrophys. J. Suppl.*, 170:263, 2007.

[120] G. Hinshaw et al. Five-Year Wilkinson Microwave Anisotropy Probe (WMAP) Observations: Data Processing, Sky Maps, and Basic Results. *Astrophys. J. Suppl.*, 180:225–245, 2009.

[121] N. Jarosik et al. Seven-Year Wilkinson Microwave Anisotropy Probe (WMAP) Observations: Sky Maps, Systematic Errors, and Basic Results. *Astrophys. J. Suppl.*, 192:14, 2011.

[122] G. Hinshaw et al. Nine-Year Wilkinson Microwave Anisotropy Probe (WMAP) Observations: Cosmological Parameter Results. *Astrophys. J. Suppl.*, 208:19, 2013.

[123] J. A. Tauber et al. Planck Pre-Launch Status: The Planck Mission. *Astron. Astrophys.*, 520:A1, 2010.

[124] P. A. R. Ade et al. Planck 2013 results. I. Overview of products and scientific results. *Astron. Astrophys.*, 571:A1, 2014.

[125] R. Adam et al. Planck 2015 results. I. Overview of products and scientific results. 2015.

[126] M. D. Niemack, P. A. R. Ade, J. Aguirre, F. Barrientos, J. A. Beall, J. R. Bond, J. Britton, H. M. Cho, S. Das, M. J. Devlin, S. Dicker, J. Dunkley, R. Dünner, J. W. Fowler, A. Hajian, M. Halpern, M. Hasselfield, G. C. Hilton, M. Hilton, J. Hubmayr, J. P. Hughes, L. Infante, K. D. Irwin, N. Jarosik, J. Klein, A. Kosowsky, T. A. Marriage, J. McMahon, F. Menanteau, K. Moodley, J. P. Nibarger, M. R. Nolta, L. A. Page, B. Partridge, E. D. Reese, J. Sievers, D. N. Spergel, S. T. Staggs, R. Thornton, C. Tucker, E. Wollack, and K. W. Yoon. ACTPol: a polarization-sensitive receiver for the Atacama Cosmology Telescope. In *Millimeter, Submillimeter, and Far-Infrared Detectors and Instrumentation for Astronomy V*, 2010.

[127] BICEP2 Collaboration, P. A. R. Ade, R. W. Aikin, D. Barkats, S. J. Benton, C. A. Bischoff, J. J. Bock, J. A. Brevik, I. Buder, E. Bullock, C. D. Dowell, L. Duband, J. P. Filippini, S. Fliescher, S. R. Golwala, M. Halpern, M. Hasselfield, S. R. Hildebrandt, G. C. Hilton, V. V. Hristov, K. D. Irwin, K. S. Karkare, J. P. Kaufman, B. G. Keating, S. A. Kernasovskiy, J. M. Kovac, C. L. Kuo, E. M. Leitch, M. Lueker, P. Mason, C. B. Netterfield, H. T. Nguyen, R. O'Brient, R. W. Ogburn, A. Orlando, C. Pryke, C. D. Reintsema, S. Richter, R. Schwarz, C. D. Sheehy, Z. K. Staniszewski, R. V. Sudiwala, G. P. Teply, J. E.

Tolan, A. D. Turner, A. G. Vieregg, C. L. Wong, and K. W. Yoon. Detection of B-Mode Polarization at Degree Angular Scales by BICEP2. *Physical Review Letters*, 112(24):241101, June 2014.

[128] BICEP2 and Keck Array Collaborations, P. A. R. Ade, Z. Ahmed, R. W. Aikin, K. D. Alexander, D. Barkats, S. J. Benton, C. A. Bischoff, J. J. Bock, J. A. Brevik, I. Buder, E. Bullock, V. Buza, J. Connors, B. P. Crill, C. D. Dowell, C. Dvorkin, L. Duband, J. P. Filippini, S. Fliescher, S. R. Golwala, M. Halpern, S. Harrison, M. Hasselfield, S. R. Hildebrandt, G. C. Hilton, V. V. Hristov, H. Hui, K. D. Irwin, K. S. Karkare, J. P. Kaufman, B. G. Keating, S. Kefeli, S. A. Kernasovskiy, J. M. Kovac, C. L. Kuo, E. M. Leitch, M. Lueker, P. Mason, K. G. Megerian, C. B. Netterfield, H. T. Nguyen, R. O'Brient, R. W. Ogburn, IV, A. Orlando, C. Pryke, C. D. Reintsema, S. Richter, R. Schwarz, C. D. Sheehy, Z. K. Staniszewski, R. V. Sudiwala, G. P. Teply, K. L. Thompson, J. E. Tolan, A. D. Turner, A. G. Vieregg, A. C. Weber, J. Willmert, C. L. Wong, and K. W. Yoon. BICEP2/Keck Array V: Measurements of B-mode Polarization at Degree Angular Scales and 150 GHz by the Keck Array. *Astrophys. J.*, 811:126, October 2015.

[129] Z. D. Kermish, P. Ade, A. Anthony, K. Arnold, D. Barron, D. Boettger, J. Borrill, S. Chapman, Y. Chinone, M. A. Dobbs, J. Errard, G. Fabbian, D. Flanigan, G. Fuller, A. Ghribi, W. Grainger, N. Halverson, M. Hasegawa, K. Hattori, M. Hazumi, W. L. Holzapfel, J. Howard, P. Hyland, A. Jaffe, B. Keating, T. Kisner, A. T. Lee, M. Le Jeune, E. Linder, M. Lungu, F. Matsuda, T. Matsumura, X. Meng, N. J. Miller, H. Morii, S. Moyerman, M. J. Myers, H. Nishino, H. Paar, E. Quealy, C. L. Reichardt, P. L. Richards, C. Ross, A. Shimizu, M. Shimon, C. Shimmin, M. Sholl, P. Siritanasak, H. Spieler, N. Stebor, B. Steinbach, R. Stompor, A. Suzuki, T. Tomaru, C. Tucker, and O. Zahn. The POLARBEAR experiment. In *Millimeter, Submillimeter, and Far-Infrared Detectors and Instrumentation for Astronomy VI*, 2012.

[130] J. E. Austermann, K. A. Aird, J. A. Beall, D. Becker, A. Bender, B. A. Benson, L. E. Bleem, J. Britton, J. E. Carlstrom, C. L. Chang, H. C. Chiang, H.-M. Cho, T. M. Crawford, A. T. Crites, A. Datesman, T. de Haan, M. A. Dobbs, E. M. George, N. W. Halverson, N. Harrington, J. W. Henning, G. C. Hilton, G. P. Holder, W. L. Holzapfel, S. Hoover, N. Huang, J. Hubmayr, K. D. Irwin, R. Keisler, J. Kennedy, L. Knox, A. T. Lee, E. Leitch, D. Li, M. Lueker, D. P. Marrone, J. J. McMahon, J. Mehl, S. S. Meyer, T. E. Montroy, T. Natoli, J. P. Nibarger, M. D. Niemack, V. Novosad, S. Padin, C. Pryke, C. L. Reichardt,

J. E. Ruhl, B. R. Saliwanchik, J. T. Sayre, K. K. Schaffer, E. Shirokoff, A. A. Stark, K. Story, K. Vanderlinde, J. D. Vieira, G. Wang, R. Williamson, V. Yefremenko, K. W. Yoon, and O. Zahn. SPTpol: an instrument for CMB polarization measurements with the South Pole Telescope. In *Millimeter, Submillimeter, and Far-Infrared Detectors and Instrumentation for Astronomy VI*, 2012.

[131] S. W. Henderson et al. Advanced ACTPol Cryogenic Detector Arrays and Readout. *J. Low. Temp. Phys.*, 184(3-4):772–779, 2016.

[132] J. A. Grayson, P. A. R. Ade, Z. Ahmed, K. D. Alexander, M. Amiri, D. Barkats, S. J. Benton, C. A. Bischoff, J. J. Bock, H. Boenish, R. Bowens-Rubin, I. Buder, E. Bullock, V. Buza, J. Connors, J. P. Filippini, S. Fliescher, M. Halpern, S. Harrison, G. C. Hilton, V. V. Hristov, H. Hui, K. D. Irwin, J. Kang, K. S. Karkare, E. Karpel, S. Kefeli, S. A. Kernasovskiy, J. M. Kovac, C. L. Kuo, E. M. Leitch, M. Lueker, K. G. Megerian, V. Monticue, T. Namikawa, C. B. Netterfield, H. T. Nguyen, R. O'Brient, R. W. Ogburn, IV, C. Pryke, C. D. Reintsema, S. Richter, R. Schwarz, C. Sorensen, C. D. Sheehy, Z. K. Staniszewski, B. Steinbach, G. P. Teply, K. L. Thompson, J. E. Tolan, C. Tucker, A. D. Turner, A. G. Vieregg, A. Wandui, A. C. Weber, D. V. Wiebe, J. Willmert, W. L. K. Wu, and K. W. Yoon. BICEP3 performance overview and planned Keck Array upgrade. *ArXiv e-prints*, July 2016.

[133] K. Arnold, N. Stebor, P. A. R. Ade, Y. Akiba, A. E. Anthony, M. Atlas, D. Barron, A. Bender, D. Boettger, J. Borrill, S. Chapman, Y. Chinone, A. Cukierman, M. Dobbs, T. Elleflot, J. Errard, G. Fabbian, C. Feng, A. Gilbert, N. Goeckner-Wald, N. W. Halverson, M. Hasegawa, K. Hattori, M. Hazumi, W. L. Holzapfel, Y. Hori, Y. Inoue, G. C. Jaehnig, A. H. Jaffe, N. Katayama, B. Keating, Z. Kermish, R. Keskitalo, T. Kisner, M. Le Jeune, A. T. Lee, E. M. Leitch, E. Linder, F. Matsuda, T. Matsumura, X. Meng, N. J. Miller, H. Morii, M. J. Myers, M. Navaroli, H. Nishino, T. Okamura, H. Paar, J. Peloton, D. Poletti, C. Raum, G. Rebeiz, C. L. Reichardt, P. L. Richards, C. Ross, K. M. Rotermund, D. E. Schenck, B. D. Sherwin, I. Shirley, M. Sholl, P. Siritanasak, G. Smecher, B. Steinbach, R. Stompor, A. Suzuki, J. Suzuki, S. Takada, S. Takakura, T. Tomaru, B. Wilson, A. Yadav, and O. Zahn. The Simons Array: expanding POLARBEAR to three multi-chroic telescopes. In *Millimeter, Submillimeter, and Far-Infrared Detectors and Instrumentation for Astronomy VII*, 2014.

[134] B. A. Benson, P. A. R. Ade, Z. Ahmed, S. W. Allen, K. Arnold, J. E. Austermann, A. N. Bender, L. E. Bleem, J. E. Carlstrom, C. L. Chang, H. M. Cho, J. F.

Cliche, T. M. Crawford, A. Cukierman, T. de Haan, M. A. Dobbs, D. Dutcher, W. Everett, A. Gilbert, N. W. Halverson, D. Hanson, N. L. Harrington, K. Hattori, J. W. Henning, G. C. Hilton, G. P. Holder, W. L. Holzapfel, K. D. Irwin, R. Keisler, L. Knox, D. Kubik, C. L. Kuo, A. T. Lee, E. M. Leitch, D. Li, M. McDonald, S. S. Meyer, J. Montgomery, M. Myers, T. Natoli, H. Nguyen, V. Novosad, S. Padin, Z. Pan, J. Pearson, C. Reichardt, J. E. Ruhl, B. R. Saliwanchik, G. Simard, G. Smecher, J. T. Sayre, E. Shirokoff, A. A. Stark, K. Story, A. Suzuki, K. L. Thompson, C. Tucker, K. Vanderlinde, J. D. Vieira, A. Vikhlinin, G. Wang, V. Yefremenko, and K. W. Yoon. SPT-3G: a next-generation cosmic microwave background polarization experiment on the South Pole telescope. In *Millimeter, Submillimeter, and Far-Infrared Detectors and Instrumentation for Astronomy VII*, 2014.

[135] T. Essinger-Hileman, A. Ali, M. Amiri, J. W. Appel, D. Araujo, C. L. Bennett, F. Boone, M. Chan, H.-M. Cho, D. T. Chuss, F. Colazo, E. Crowe, K. Denis, R. Dünner, J. Eimer, D. Gothe, M. Halpern, K. Harrington, G. C. Hilton, G. F. Hinshaw, C. Huang, K. Irwin, G. Jones, J. Karakla, A. J. Kogut, D. Larson, M. Limon, L. Lowry, T. Marriage, N. Mehrle, A. D. Miller, N. Miller, S. H. Moseley, G. Novak, C. Reintsema, K. Rostem, T. Stevenson, D. Towner, K. U-Yen, E. Wagner, D. Watts, E. J. Wollack, Z. Xu, and L. Zeng. CLASS: the cosmology large angular scale surveyor. In *Millimeter, Submillimeter, and Far-Infrared Detectors and Instrumentation for Astronomy VII*, 2014.

[136] K. N. Abazajian et al. Neutrino Physics from the Cosmic Microwave Background and Large Scale Structure. *Astropart. Phys.*, 63:66–80, 2015.

[137] K. N. Abazajian et al. Inflation Physics from the Cosmic Microwave Background and Large Scale Structure. *Astropart. Phys.*, 63:55–65, 2015.

[138] T. Matsumura et al. Mission design of LiteBIRD. 2013. [J. Low. Temp. Phys.176,733(2014)].

[139] F. R. Bouchet et al. COrE (Cosmic Origins Explorer) A White Paper. 2011.

[140] Kyle S. Dawson et al. The SDSS-IV extended Baryon Oscillation Spectroscopic Survey: Overview and Early Data. *Astron. J.*, 151:44, 2016.

[141] Michael Levi et al. The DESI Experiment, a whitepaper for Snowmass 2013. 2013.

[142] R. Laureijs et al. Euclid Definition Study Report. 2011.

[143] Olivier Doré et al. Cosmology with the SPHEREX All-Sky Spectral Survey. 2014.

[144] Paul A. Abell et al. LSST Science Book, Version 2.0. 2009.

[145] Z. Ivezic, J. A. Tyson, R. Allsman, J. Andrew, and R. Angel. LSST: from Science Drivers to Reference Design and Anticipated Data Products. 2008.

[146] Filipe B. Abdalla et al. Cosmology from HI galaxy surveys with the SKA. 2015.

[147] Mario Santos et al. Cosmology from a SKA HI intensity mapping survey. *PoS*, AASKA14:019, 2015.

[148] Matt Jarvis, David Bacon, Chris Blake, Michael Brown, Sam Lindsay, Alvise Raccanelli, Mario Santos, and Dominik J. Schwarz. Cosmology with SKA Radio Continuum Surveys. *PoS*, AASKA14:018, 2015.

[149] Uros Seljak and Matias Zaldarriaga. A Line of sight integration approach to cosmic microwave background anisotropies. *Astrophys. J.*, 469:437–444, 1996.

[150] R. K. Sachs and A. M. Wolfe. Perturbations of a cosmological model and angular variations of the microwave background. *Astrophys. J.*, 147:73–90, 1967. [Gen. Rel. Grav.39,1929(2007)].

[151] M. J. Rees and D. W. Sciama. Large scale Density Inhomogeneities in the Universe. *Nature*, 217:511–516, 1968.

[152] Robert G. Crittenden and Neil Turok. Looking for Lambda with the Rees-Sciama effect. *Phys. Rev. Lett.*, 76:575, 1996.

[153] Wayne Hu and Naoshi Sugiyama. Anisotropies in the cosmic microwave background: An Analytic approach. *Astrophys. J.*, 444:489–506, 1995.

[154] Uros Seljak. A Two fluid approximation for calculating the cosmic microwave background anisotropies. *Astrophys. J.*, 435:L87–L90, 1994.

[155] Wayne Hu and Martin J. White. A CMB polarization primer. *New Astron.*, 2:323, 1997.

[156] Marc Kamionkowski, Arthur Kosowsky, and Albert Stebbins. Statistics of cosmic microwave background polarization. *Phys. Rev.*, D55:7368–7388, 1997.

[157] Uros Seljak and Matias Zaldarriaga. Signature of gravity waves in polarization of the microwave background. *Phys. Rev. Lett.*, 78:2054–2057, 1997.

[158] Matias Zaldarriaga. Polarization of the microwave background in reionized models. *Phys. Rev.*, D55:1822–1829, 1997.

[159] Scott Dodelson. Coherent phase argument for inflation. *AIP Conf. Proc.*, 689:184–196, 2003. [,184(2003)].

[160] A. Blanchard and J. Schneider. Gravitational lensing effect on the fluctuations of the cosmic background radiation. *Astron. Astrophys.*, 184:1–6, October 1987.

[161] F. Bernardeau. Weak lensing detection in CMB maps. *Astron. Astrophys.*, 324:15–26, 1997.

[162] Matias Zaldarriaga and Uros Seljak. Gravitational lensing effect on cosmic microwave background polarization. *Phys. Rev.*, D58:023003, 1998.

[163] Christopher M. Hirata and Uros Seljak. Reconstruction of lensing from the cosmic microwave background polarization. *Phys. Rev.*, D68:083002, 2003.

[164] Antony Lewis and Anthony Challinor. Weak gravitational lensing of the cmb. *Phys. Rept.*, 429:1–65, 2006.

[165] Marc Kamionkowski, Arthur Kosowsky, and Albert Stebbins. A Probe of primordial gravity waves and vorticity. *Phys. Rev. Lett.*, 78:2058–2061, 1997.

[166] P. A. R. Ade et al. Improved Constraints on Cosmology and Foregrounds from BICEP2 and Keck Array Cosmic Microwave Background Data with Inclusion of 95 GHz Band. *Phys. Rev. Lett.*, 116:031302, 2016.

[167] P. A. R. Ade et al. Joint Analysis of BICEP2/$Keck$fl$Array$ and $Planck$ Data. *Phys. Rev. Lett.*, 114:101301, 2015.

[168] N. Aghanim et al. Planck 2015 results. XI. CMB power spectra, likelihoods, and robustness of parameters. *Astron. Astrophys.*, 594:A11, 2016.

[169] D. J. Fixsen. The Temperature of the Cosmic Microwave Background. *Astrophys. J.*, 707:916–920, 2009.

[170] N. Kaiser. Clustering in real space and in redshift space. *Mon. Not. Roy. Astron. Soc.*, 227:1–27, 1987.

[171] A. J. S. Hamilton. Linear redshift distortions: A Review. In *Ringberg Workshop on Large Scale Structure Ringberg, Germany, September 23-28, 1996*, 1997.

[172] J. C. Jackson. Fingers of God: A critique of Rees' theory of primoridal gravitational radiation. *Mon. Not. Roy. Astron. Soc.*, 156:1P–5P, 1972.

[173] Cheng Li, Y. P. Jing, Guinevere Kauffmann, Gerhard Boerner, Xi Kang, and Lan Wang. Luminosity dependence of the spatial and velocity distributions of galaxies: Semi-analytic models versus the Sloan Digital Sky Survey. *Mon. Not. Roy. Astron. Soc.*, 376:984–996, 2007.

[174] Philip Bull, Pedro G. Ferreira, Prina Patel, and Mario G. Santos. Late-time cosmology with 21cm intensity mapping experiments. *Astrophys. J.*, 803(1):21, 2015.

[175] Hee-Jong Seo and Daniel J. Eisenstein. Probing dark energy with baryonic acoustic oscillations from future large galaxy redshift surveys. *Astrophys. J.*, 598:720–740, 2003.

[176] Yong-Seon Song and Will J. Percival. Reconstructing the history of structure formation using Redshift Distortions. *JCAP*, 0910:004, 2009.

[177] C. Alcock and B. Paczynski. An evolution free test for non-zero cosmological constant. *Nature*, 281:358–359, 1979.

[178] Christos G. Tsagas, Anthony Challinor, and Roy Maartens. Relativistic cosmology and large-scale structure. *Phys. Rept.*, 465:61–147, 2008.

[179] Jaiyul Yoo, Matias Zaldarriaga, and Lars Hernquist. Lensing reconstruction of cluster-mass cross-correlation with cosmic microwave background polarization. *Phys. Rev.*, D81:123006, 2010.

[180] Jaiyul Yoo. General Relativistic Description of the Observed Galaxy Power Spectrum: Do We Understand What We Measure? *Phys. Rev.*, D82:083508, 2010.

[181] N. Bartolo, S. Matarrese, and A. Riotto. Relativistic Effects and Primordial Non-Gaussianity in the Galaxy bias. *JCAP*, 1104:011, 2011.

[182] Camille Bonvin and Ruth Durrer. What galaxy surveys really measure. *Phys. Rev.*, D84:063505, 2011.

[183] Anthony Challinor and Antony Lewis. The linear power spectrum of observed source number counts. *Phys. Rev.*, D84:043516, 2011.

[184] Marco Bruni, Robert Crittenden, Kazuya Koyama, Roy Maartens, Cyril Pitrou, and David Wands. Disentangling non-Gaussianity, bias and GR effects in the galaxy distribution. *Phys. Rev.*, D85:041301, 2012.

[185] Andrew H. Jaffe, J. R. Bond, P. G. Ferreira, and L. Knox. CMB likelihood functions for beginners and experts. 1999.

[186] Samira Hamimeche and Antony Lewis. Likelihood Analysis of CMB Temperature and Polarization Power Spectra. *Phys. Rev.*, D77:103013, 2008.

[187] Lloyd Knox. Cosmic microwave background anisotropy observing strategy assessment. *Astrophys. J.*, 480:72, 1997.

[188] Wayne Hu and Takemi Okamoto. Mass reconstruction with cmb polarization. *Astrophys. J.*, 574:566–574, 2002.

[189] Anthony Challinor and Antony Lewis. Lensed CMB power spectra from all-sky correlation functions. *Phys. Rev.*, D71:103010, 2005.

[190] Kendrick M. Smith, Duncan Hanson, Marilena LoVerde, Christopher M. Hirata, and Oliver Zahn. Delensing CMB Polarization with External Datasets. *JCAP*, 1206:014, 2012.

[191] Max Tegmark. Measuring cosmological parameters with galaxy surveys. *Phys. Rev. Lett.*, 79:3806–3809, 1997.

[192] Hume A. Feldman, Nick Kaiser, and John A. Peacock. Power spectrum analysis of three-dimensional redshift surveys. *Astrophys. J.*, 426:23–37, 1994.

[193] L. Raul Abramo. The full Fisher matrix for galaxy surveys. *Mon. Not. Roy. Astron. Soc.*, 420:3, 2012.

[194] Martin White, Yong-Seon Song, and Will J. Percival. Forecasting Cosmological Constraints from Redshift Surveys. *Mon. Not. Roy. Astron. Soc.*, 397:1348–1354, 2008.

[195] Lado Samushia et al. Effects of cosmological model assumptions on galaxy redshift survey measurements. *Mon. Not. Roy. Astron. Soc.*, 410:1993–2002, 2011.

[196] P. A. R. Ade et al. Planck 2015 results. VI. LFI mapmaking. *Astron. Astrophys.*, 594:A6, 2016.

[197] R. Adam et al. Planck 2015 results. VIII. High Frequency Instrument data processing: Calibration and maps. *Astron. Astrophys.*, 594:A8, 2016.

[198] R. Adam et al. Planck 2015 results. IX. Diffuse component separation: CMB maps. *Astron. Astrophys.*, 594:A9, 2016.

[199] R. Adam et al. Planck intermediate results. XLVII. Planck constraints on reionization history. 2016.

[200] P. A. R. Ade et al. Planck 2015 results. XV. Gravitational lensing. *Astron. Astrophys.*, 594:A15, 2016.

[201] P. A. R. Ade et al. Planck 2015 results. XXIV. Cosmology from Sunyaev-Zeldovich cluster counts. *Astron. Astrophys.*, 594:A24, 2016.

[202] P. A. R. Ade et al. Planck 2015 results. XVII. Constraints on primordial non-Gaussianity. 2015.

[203] Florian Beutler, Chris Blake, Matthew Colless, D. Heath Jones, Lister Staveley-Smith, Lachlan Campbell, Quentin Parker, Will Saunders, and Fred Watson. The 6dF Galaxy Survey: Baryon Acoustic Oscillations and the Local Hubble Constant. *Mon. Not. Roy. Astron. Soc.*, 416:3017–3032, 2011.

[204] Ashley J. Ross, Lado Samushia, Cullan Howlett, Will J. Percival, Angela Burden, and Marc Manera. The clustering of the SDSS DR7 main Galaxy sample ,Äì I. A 4 per cent distance measure at $z = 0.15$. *Mon. Not. Roy. Astron. Soc.*, 449(1):835–847, 2015.

[205] Lauren Anderson et al. The clustering of galaxies in the SDSS-III Baryon Oscillation Spectroscopic Survey: baryon acoustic oscillations in the Data Releases 10 and 11 Galaxy samples. *Mon. Not. Roy. Astron. Soc.*, 441(1):24–62, 2014.

[206] Edward R. Harrison. Fluctuations at the threshold of classical cosmology. *Phys. Rev.*, D1:2726–2730, 1970.

[207] P. J. E. Peebles and J. T. Yu. Primeval adiabatic perturbation in an expanding universe. *Astrophys. J.*, 162:815–836, 1970.

[208] Ya. B. Zeldovich. A Hypothesis, unifying the structure and the entropy of the universe. *Mon. Not. Roy. Astron. Soc.*, 160:1P–3P, 1972.

[209] Kevork N. Abazajian et al. CMB-S4 Science Book, First Edition. 2016.

[210] Jinn-Ouk Gong and Ewan D. Stewart. The Density perturbation power spectrum to second order corrections in the slow roll expansion. *Phys. Lett.*, B510:1–9, 2001.

[211] Samuel M. Leach, Andrew R. Liddle, Jerome Martin, and Dominik J Schwarz. Cosmological parameter estimation and the inflationary cosmology. *Phys. Rev.*, D66:023515, 2002.

[212] Fabio Finelli, M. Rianna, and N. Mandolesi. Constraints on the Inflationary Expansion from Three Year WMAP, small scale CMB anisotropies and Large Scale Structure Data Sets. *JCAP*, 0612:006, 2006.

[213] Mr. Bayes and Mr. Price. An essay towards solving a problem in the doctrine of chances. by the late rev. mr. bayes, f. r. s. communicated by mr. price, in a letter to john canton, a. m. f. r. s. *Philosophical Transactions*, 53:370–418, 1763.

[214] Robert E. Kass and Adrian E. Raftery. Bayes factors, 1995.

[215] Roberto Trotta. Bayes in the sky: Bayesian inference and model selection in cosmology. *Contemp. Phys.*, 49:71–104, 2008.

[216] John Skilling. Nested sampling for general bayesian computation. *Bayesian Anal.*, 1(4):833–859, 12 2006.

[217] Jerome Martin, Christophe Ringeval, Roberto Trotta, and Vincent Vennin. The Best Inflationary Models After Planck. *JCAP*, 1403:039, 2014.

[218] Jerome Martin, Christophe Ringeval, and Vincent Vennin. Observing Inflationary Reheating. *Phys. Rev. Lett.*, 114(8):081303, 2015.

[219] Jerome Martin, Christophe Ringeval, Roberto Trotta, and Vincent Vennin. Compatibility of Planck and BICEP2 in the Light of Inflation. *Phys. Rev.*, D90(6):063501, 2014.

[220] Jerome Martin, Christophe Ringeval, and Vincent Vennin. Information Gain on Reheating: the One Bit Milestone. *Phys. Rev.*, D93(10):103532, 2016.

[221] Rajeev Kumar Jain, Pravabati Chingangbam, Jinn-Ouk Gong, L. Sriramkumar, and Tarun Souradeep. Punctuated inflation and the low CMB multipoles. *JCAP*, 0901:009, 2009.

[222] Carlo R. Contaldi, Marco Peloso, Lev Kofman, and Andrei D. Linde. Suppressing the lower multipoles in the CMB anisotropies. *JCAP*, 0307:002, 2003.

[223] Yun-Song Piao, Bo Feng, and Xin-min Zhang. Suppressing CMB quadrupole with a bounce from contracting phase to inflation. *Phys. Rev.*, D69:103520, 2004.

[224] E. Dudas, N. Kitazawa, S. P. Patil, and A. Sagnotti. CMB Imprints of a Pre-Inflationary Climbing Phase. *JCAP*, 1205:012, 2012.

[225] Jennifer A. Adams, Bevan Cresswell, and Richard Easther. Inflationary perturbations from a potential with a step. *Phys. Rev.*, D64:123514, 2001.

[226] Jan Hamann, Laura Covi, Alessandro Melchiorri, and Anze Slosar. New Constraints on Oscillations in the Primordial Spectrum of Inflationary Perturbations. *Phys. Rev.*, D76:023503, 2007.

[227] Ana Achucarro, Jinn-Ouk Gong, Sjoerd Hardeman, Gonzalo A. Palma, and Subodh P. Patil. Features of heavy physics in the CMB power spectrum. *JCAP*, 1101:030, 2011.

[228] Nicola Bartolo, Dario Cannone, and Sabino Matarrese. The Effective Field Theory of Inflation Models with Sharp Features. *JCAP*, 1310:038, 2013.

[229] Ana Achucarro, Jinn-Ouk Gong, Gonzalo A. Palma, and Subodh P. Patil. Correlating features in the primordial spectra. *Phys. Rev.*, D87(12):121301, 2013.

[230] Neil Barnaby, Zhiqi Huang, Lev Kofman, and Dmitry Pogosyan. Cosmological Fluctuations from Infra-Red Cascading During Inflation. *Phys. Rev.*, D80:043501, 2009.

[231] Teeraparb Chantavat, Christopher Gordon, and Joseph Silk. Large Scale Structure Forecast Constraints on Particle Production During Inflation. *Phys. Rev.*, D83:103501, 2011.

[232] Xingang Chen, Richard Easther, and Eugene A. Lim. Generation and Characterization of Large Non-Gaussianities in Single Field Inflation. *JCAP*, 0804:010, 2008.

[233] Jens Chluba, Jan Hamann, and Subodh P. Patil. Features and New Physical Scales in Primordial Observables: Theory and Observation. *Int. J. Mod. Phys.*, D24(10):1530023, 2015.

[234] Eva Silverstein and Alexander Westphal. Monodromy in the CMB: Gravity Waves and String Inflation. *Phys. Rev.*, D78:106003, 2008.

[235] Liam McAllister, Eva Silverstein, and Alexander Westphal. Gravity Waves and Linear Inflation from Axion Monodromy. *Phys. Rev.*, D82:046003, 2010.

[236] Raphael Flauger, Liam McAllister, Enrico Pajer, Alexander Westphal, and Gang Xu. Oscillations in the CMB from Axion Monodromy Inflation. *JCAP*, 1006:009, 2010.

[237] Xingang Chen. Primordial Non-Gaussianities from Inflation Models. *Adv. Astron.*, 2010:638979, 2010.

[238] J. R. Fergusson, H. F. Gruetjen, E. P. S. Shellard, and M. Liguori. Combining power spectrum and bispectrum measurements to detect oscillatory features. *Phys. Rev.*, D91(2):023502, 2015.

[239] J. R. Fergusson, H. F. Gruetjen, E. P. S. Shellard, and B. Wallisch. Polyspectra searches for sharp oscillatory features in cosmic microwave sky data. *Phys. Rev.*, D91(12):123506, 2015.

[240] P. Daniel Meerburg and M

[241] Jinn-Ouk Gong. Breaking scale invariance from a singular inflaton potential. *JCAP*, 0507:015, 2005.

[242] Cora Dvorkin and Wayne Hu. Generalized Slow Roll for Large Power Spectrum Features. *Phys. Rev.*, D81:023518, 2010.

[243] Vinicius Miranda and Wayne Hu. Inflationary Steps in the Planck Data. *Phys. Rev.*, D89(8):083529, 2014.

[244] Vinicius Miranda, Wayne Hu, and Peter Adshead. Warp Features in DBI Inflation. *Phys. Rev.*, D86:063529, 2012.

[245] Raphael Flauger, Liam McAllister, Eva Silverstein, and Alexander Westphal. Drifting Oscillations in Axion Monodromy. 2014.

[246] Jerome Martin and Robert Brandenberger. On the dependence of the spectra of fluctuations in inflationary cosmology on transPlanckian physics. *Phys. Rev.*, D68:063513, 2003.

[247] Mark G. Jackson and Gary Shiu. Study of the consistency relation for single-field inflation with power spectrum oscillations. *Phys. Rev.*, D88(12):123511, 2013.

[248] P. Daniel Meerburg and David N. Spergel. Searching for oscillations in the primordial power spectrum. II. Constraints from Planck data. *Phys. Rev.*, D89(6):063537, 2014.

[249] Micol Benetti. Updating constraints on inflationary features in the primordial power spectrum with the Planck data. *Phys. Rev.*, D88:087302, 2013.

[250] Richard Easther and Raphael Flauger. Planck Constraints on Monodromy Inflation. *JCAP*, 1402:037, 2014.

[251] Xingang Chen and Mohammad Hossein Namjoo. Standard Clock in Primordial Density Perturbations and Cosmic Microwave Background. *Phys. Lett.*, B739:285–292, 2014.

[252] Dhiraj Kumar Hazra, Arman Shafieloo, George F. Smoot, and Alexei A. Starobinsky. Wiggly Whipped Inflation. *JCAP*, 1408:048, 2014.

[253] Bin Hu and Jesús Torrado. Searching for primordial localized features with CMB and LSS spectra. *Phys. Rev.*, D91(6):064039, 2015.

[254] A. Gruppuso, N. Kitazawa, N. Mandolesi, P. Natoli, and A. Sagnotti. Pre-Inflationary Relics in the CMB? *Phys. Dark Univ.*, 11:68–73, 2016.

[255] Dhiraj Kumar Hazra, Arman Shafieloo, George F. Smoot, and Alexei A. Starobinsky. Primordial features and Planck polarization. *JCAP*, 1609(09):009, 2016.

[256] Julien Lesgourgues. The Cosmic Linear Anisotropy Solving System (CLASS) I: Overview. 2011.

[257] Diego Blas, Julien Lesgourgues, and Thomas Tram. The Cosmic Linear Anisotropy Solving System (CLASS) II: Approximation schemes. *JCAP*, 1107:034, 2011.

[258] Benjamin Audren, Julien Lesgourgues, Karim Benabed, and Simon Prunet. Conservative Constraints on Early Cosmology: an illustration of the Monte Python cosmological parameter inference code. *JCAP*, 1302:001, 2013.

[259] Yi-Chao Li, Feng-Quan Wu, and Xuelei Chen. Constraints on the Brans-Dicke gravity theory with the Planck data. *Phys. Rev.*, D88:084053, 2013.

[260] A. Avilez and C. Skordis. Cosmological constraints on Brans-Dicke theory. *Phys. Rev. Lett.*, 113(1):011101, 2014.

[261] Ji-Xia Li, Feng-Quan Wu, Yi-Chao Li, Yan Gong, and Xue-Lei Chen. Cosmological constraint on Brans-Dicke Model. *Res. Astron. Astrophys.*, 15(12):2151–2163, 2015.

[262] Adam G. Riess, Lucas Macri, Stefano Casertano, Hubert Lampeitl, Henry C. Ferguson, Alexei V. Filippenko, Saurabh W. Jha, Weidong Li, and Ryan Chornock. A 3% Solution: Determination of the Hubble Constant with the Hubble Space Telescope and Wide Field Camera 3. *Astrophys. J.*, 730:119, 2011. [Erratum: Astrophys. J.732,129(2011)].

[263] George Efstathiou. H0 Revisited. *Mon. Not. Roy. Astron. Soc.*, 440(2):1138–1152, 2014.

[264] Craig J. Copi, Adam N. Davis, and Lawrence M. Krauss. A New nucleosynthesis constraint on the variation of G. *Phys. Rev. Lett.*, 92:171301, 2004.

[265] Cosimo Bambi, Maurizio Giannotti, and F. L. Villante. The Response of primordial abundances to a general modification of G(N) and/or of the early Universe expansion rate. *Phys. Rev.*, D71:123524, 2005.

[266] O. Pisanti, A. Cirillo, S. Esposito, F. Iocco, G. Mangano, G. Miele, and P. D. Serpico. PArthENoPE: Public Algorithm Evaluating the Nucleosynthesis of Primordial Elements. *Comput. Phys. Commun.*, 178:956–971, 2008.

[267] Jan Hamann, Julien Lesgourgues, and Gianpiero Mangano. Using BBN in cosmological parameter extraction from CMB: A Forecast for PLANCK. *JCAP*, 0803:004, 2008.

[268] Takeshi Chiba, Masaru Siino, and Masahide Yamaguchi. Slow-roll Extended Quintessence. *Phys. Rev.*, D81:083530, 2010.

[269] M. D. Pollock. AN INFLATIONARY COSMOLOGICAL MODEL WITH INDUCED GRAVITY FROM HIGHER DIMENSIONS. *Phys. Lett.*, B160:47, 1985.

[270] DESI Collaboration. DESI Technical Design Report Part I: Science, Targeting, and Survey Design.

[271] Luca Amendola et al. Cosmology and Fundamental Physics with the Euclid Satellite. 2016.

[272] Roy Maartens, Filipe B. Abdalla, Matt Jarvis, and Mario G. Santos. Overview of Cosmology with the SKA. *PoS*, AASKA14:016, 2015.

[273] S. Aiola et al. The Large-Scale Polarization Explorer (LSPE). In *Instrumentation 2012 Conference - Ground-based and Airborne Instrumentation for Astronomy IV, Amsterdam 1-6 July 2012, paper #8446-277*, pages 8446–277, 2012.

[274] Mario Ballardini, Fabio Finelli, Cosimo Fedeli, and Lauro Moscardini. Probing primordial features with future galaxy surveys. 2016.

[275] David Alonso and Pedro G. Ferreira. Constraining ultralarge-scale cosmology with multiple tracers in optical and radio surveys. *Phys. Rev.*, D92(6):063525, 2015.

[276] L. Pozzetti, C. M. Hirata, J. E. Geach, A. Cimatti, C. Baugh, O. Cucciati, A. Merson, P. Norberg, and D. Shi. Modelling the number density of Hα emitters for future spectroscopic near-IR space missions. *Astron. Astrophys.*, 590:A3, 2016.

[277] Nathaniel R. Stickley, Peter Capak, Daniel Masters, Roland de Putter, Olivier Doré, and Jamie Bock. An Empirical Approach to Cosmological Galaxy Survey Simulation: Application to SPHEREx Low-Resolution Spectroscopy. 2016.

[278] Masatoshi Shoji, Donghui Jeong, and Eiichiro Komatsu. Extracting Angular Diameter Distance and Expansion Rate of the Universe from Two-dimensional Galaxy Power Spectrum at High Redshifts: Baryon Acoustic Oscillation Fitting versus Full Modeling. *Astrophys. J.*, 693:1404–1416, 2009.

[279] Alberto Bailoni, Alessio Spurio Mancini, and Luca Amendola. Improving the galaxy clustering Fisher matrix: window function, bin cross-correlation, and bin redshift uncertainty. 2016.

[280] Zhao-Ming Ma, Wayne Hu, and Dragan Huterer. Effect of photometric redshift uncertainties on weak lensing tomography. *Astrophys. J.*, 636:21–29, 2005.

[281] David H. Weinberg, Romeel Dave, Neal Katz, and Lars Hernquist. Galaxy clustering and galaxy bias in a lambda-CDM universe. *Astrophys. J.*, 601:1–21, 2004.

[282] Jeremy L. Tinker, Andrey V. Kravtsov, Anatoly Klypin, Kevork Abazajian, Michael S. Warren, Gustavo Yepes, Stefan Gottlober, and Daniel E. Holz. Toward a halo mass function for precision cosmology: The Limits of universality. *Astrophys. J.*, 688:709–728, 2008.

[283] Jeremy L. Tinker, Brant E. Robertson, Andrey V. Kravtsov, Anatoly Klypin, Michael S. Warren, Gustavo Yepes, and Stefan Gottlober. The Large Scale Bias of Dark Matter Halos: Numerical Calibration and Model Tests. *Astrophys. J.*, 724:878–886, 2010.

[284] E. R. Switzer et al. Determination of z 0.8 neutral hydrogen fluctuations using the 21 cm intensity mapping auto-correlation. *Mon. Not. Roy. Astron. Soc.*, 434:L46, 2013.

[285] Yan Gong, Xuelei Chen, Marta Silva, Asantha Cooray, and Mario G. Santos. The OH line contamination of 21 cm intensity fluctuation measurements for z=1 4. *Astrophys. J.*, 740:L20, 2011.

[286] S. Yahya, P. Bull, M. G. Santos, M. Silva, R. Maartens, P. Okouma, and B. Bassett. Cosmological performance of SKA HI galaxy surveys. *Mon. Not. Roy. Astron. Soc.*, 450(3):2251–2260, 2015.

[287] Mario Santos, David Alonso, Phil Bull, M. B. Silva, and Sahba Yahya. HI galaxy simulations for the SKA: number counts and bias. *PoS*, AASKA14:021, 2015.

[288] Mario Ballardini, Fabio Finelli, Roy Maartens, and Lauro Moscardini. Probing primordial features with the next-generation ultra-large surveys.